EFFECTS OF BIOMASS–BURNING AEROSOL LOADING ON SOUTHERN AFRICAN CLIMATE

Thesis submitted for the degree of Doctor of Philosophy

in the Department of Environmental and Geographical Sciences

UNIVERSITY OF CAPE TOWN

South Africa

by

Genito Amós Maúre

Supervisors: Dr. Mark Tadross

Prof. Bruce Hewitson

Cape Town, May 2013

I hereby:

(a) grant the University free license to reproduce the above thesis in whole or in part, for the purpose of research;

(b) declare that:

(i) the above thesis is my own unaided work, both in conception and execution, and that apart from the normal guidance of my supervisor, I have received no assistance apart from the stated below;

(ii) except as stated below, neither the substance nor any part of the thesis has been submitted in the past, nor is being, nor is to be submitted for a degree at this University or any other University.

(iii) I am now presenting the thesis for examination for the Degree of PhD.

Signed by candidate

Signature Removed

Genito Amós Maúre

2013

The dissertation of Genito Amós Maúre is approved.

Marker 1

Marker 2

Marker 3

TBA, Committee Chair

University of Cape Town, South Africa

2013

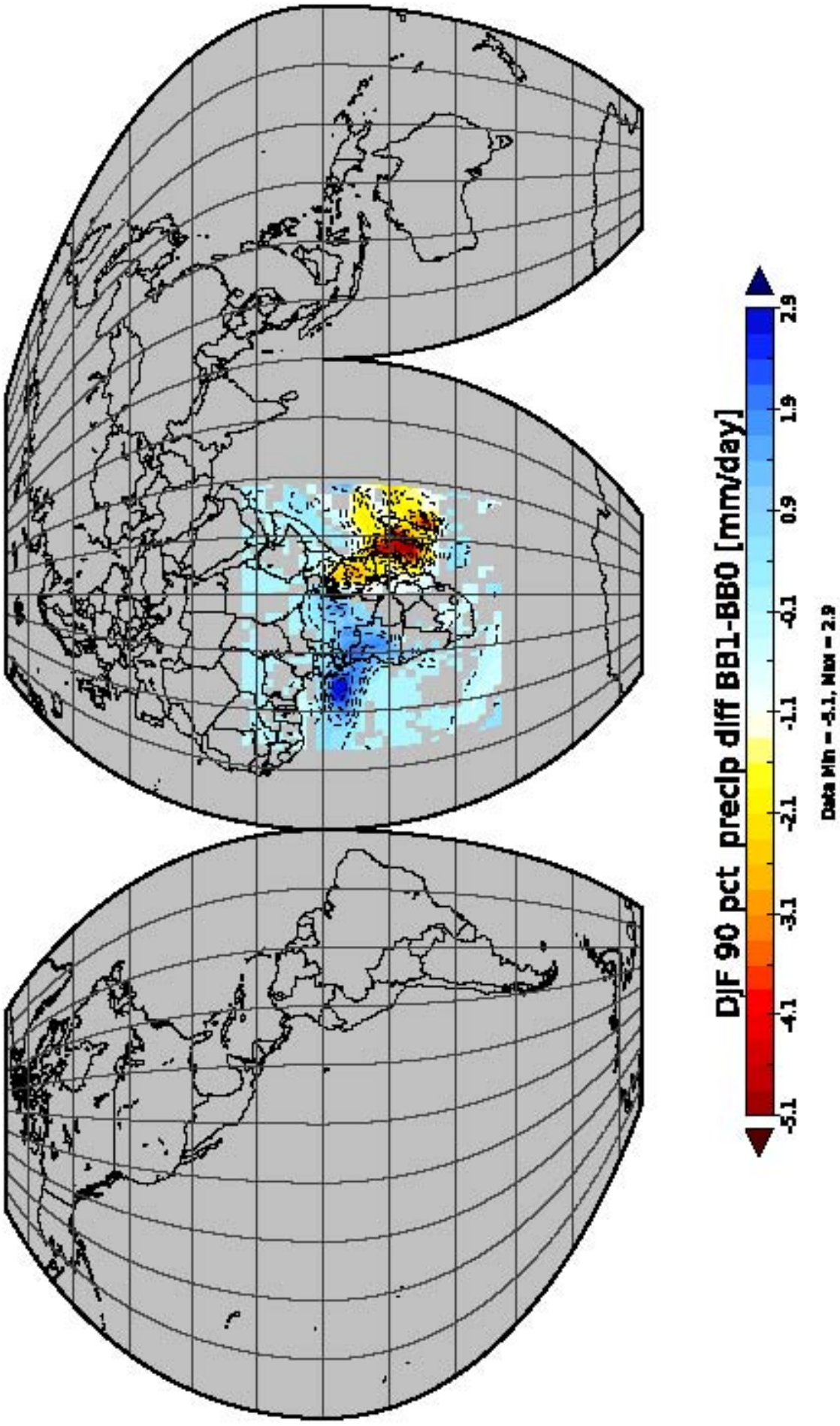
DJF 90 pct precip diff BB1-BB0 [mm/day]
2.9
1.9
0.9
-0.1
-1.1
-2.1
-3.1
-4.1
-5.1
Data Min = -5.1, Max = 2.9

Acronyms

Notation	Description
ACM2	Asymmetric Convective Model.
AE	Ångström exponent.
AEROCOM	Aerosol Inter Comparison project.
AERONET	AErosol RObotic NETwork.
AF	Asymetry Factor.
AI	Aerosol Index.
AIE	Aerosol Indirect Effect.
AMIP2	Atmospheric Model Inter-comparison Project 2.
ANN	Artificial Neural Network.
AOD	Aerosol Optical Depth.
APF	Aerosol Phase Function.
ARREX	Aerosol Recirculation and Rainfall Experiment.
ASD	Aerosol Size Distribution.
asl	above sea level.
AVHRR/LAC	the Advanced Very High Resolution Radiometer/Local Area Coverage.
BB	Biomass Burning.
BC	Black Carbon.
C	Carbon.
CAM	NCAR Community Atmosphere Model.
CBMZ	Carbon Bond Mechanism–Z.
CCN	Cloud Condensation Nuclei.
CDNC	Cloud Droplet Number Concentration.

Notation	**Description**
CH_4	Methane.
CN	Ice Nuclei.
CNC	Condensation Nuclei Counter.
CO	carbon monoxide.
CO_2	carbon dioxide.
COD	Cloud Optical Depth.
Combo CTM	Combined Stratosphere–Troposphere Chemistry and Transport Model.
CRU	University of East Anglia Climate Research Unit.
CSA	Critical Surface Albedo.
DISORT	the DIScrete Ordinate Radiative Transfer model.
DJF	December–January–February.
DMPS	Differential Mobility Particle Sizer.
DMS	DiMethyl Sulphide.
DRC	Democratic Republic of Congo.
DRE	direct radiative effect.
ECHAM5	5^{th} Version of the European Centre Hamburg Model.
ECHAM5-HAM	ECHAM5 with Hamburg Aerosol Module.
ECMWF	European Centre for Medium–Range Weather Forecasts.
EDGAR	Emission Database for Global Atmospheric Research.
ENSO	El-Niño Southern Oscillation.
EOF	Empirical Orthogonal Function.
EOS	Earth Observing System.
FLAME	Fire Lab At Missoula Experiment.
GAM	Generalised Additive Model.
GCM	Global Circulation Model.
GDE	*Aerosol General Dynamic Equation*.
GFDL-AGCM	Geophysical Fluid Dynamics Laboratory AGCM.

Notation	**Description**
GFED	Global Fire Emissions Database.
GFEDv2	Global Fire Emissions Database Version 2.
GHG	Greenhouse Gases.
GMI	Global Modeling Initiative.
GOCART	Georgia Institute of Technology – Goddard Chemistry Aerosol Radiation and Transport.
GRACES	Global Regional Atmospheric Chemistry Event Simulator.
H_2	molecular hydrogen.
HAM	Hamburg Aerosol Module.
HYSPLIT	HYbrid Single Particle Lagrangian Integrated Trajectory Model.
IGBP/IGAC	the International Geosphere-Biosphere Programme/International Global Atmospheric Chemistry.
IPCC	Intergovernmental Panel on Climate Change.
ITCZ	Intertropical Convergence Zone.
JJA	June–July–August.
lhs	left–hand side.
LIDAR	Light Detection And Ranging.
LOSU	Level of Scientific Understanding.
LSM	Land–Surface Model.
LW	longwave.
LWP	liquid water path.
MADE	Modal Aerosol Dynamics for Europe.
MAM	March–April–May.
MM5	Fifth-Generation NCAR/Penn State Mesoscale Model.
MODIS	Moderate Resolution Imaging Spectroradiometer.
MODTRAN	MODerate resolution atmospheric TRANsmission.

Notation	Description
MOM	Method of Moments.
MOSAIC	Model for Simulating Aerosol Interactions and Chemistry.
MPIMet	Max Planck Institute for Meteorology.
N_2O	nitrous oxide.
NCEP	National Centers for Environmental Prediction.
NDVI	Normalized Difference Vegetation Index.
NMHC	non–methane hydrocarbons.
NO_x	nitrogen oxides.
NOAA	National Oceanic and Atmospheric Administration.
OC	organic carbon.
OI	Optimum Interpolated.
OPC	Optical Particle Counters.
PBL	Planetary Boundary Layer.
PCA	Principal Component Analysis.
PDF	Probability Distribution Function.
PM	particulate matter.
POM	Particulate Organic Matter.
QMOM	Quadrature Method of Moments.
RCM	Regional Climate Model.
RegCM	ICTP Regional Climate Model.
RETRO	REanalysis of TROpospheric chemical composition database.
RF	Radiative Forcing.
rhs	right–hand side.
RMSE	Root Mean Squared Error.
RSD	Raindrop Size Distribution.
RTE	Radiative Transfer Equation.

Notation	Description
RUC	Rapid Update Cycle.
SAFARI-92	South African Fire–Atmosphere Research Initiative.
SAFARI2000	Southern African Regional Science Initiative.
SLP	Sea–Level Pressure.
SO_2	sulphur dioxide.
SOA	Secondary Organic Aerosol.
SOM	Self–Organising Map.
SON	September-October-November.
SORGAM	Secondary Organic Aerosol Model.
SSA	Single Scattering Albedo.
SST	sea surface temperature.
STD	Soil Thermal Diffusion.
SW	shortwave.
TC	total carbon.
TOA	Top–Of–Atmosphere.
TPM	Total particulate matter.
TRACE-A	Transport and Atmospheric Research Chemistry near the Equator-Atlantic.
UV	Ultra–Violet.
VOC	Volatile Organic Compound.
WPS	WRF Pre-processing System.
WRF	Weather Research and Forecast Model.
WRF/Chem	Weather Research and Forecast Model with Online Chemistry.

Contents

List of Figures

List of Tables

Dedication

This thesis is dedicated to:

- My wife Ana C C Rebelo–Maure, who became "CEO" and "Deputy CEO" of our family, and with gratitude for her unconditional support once I stopped being a father and husband and became a mere PhD student;
- Kaya, for asking me why I was still studying instead of just working, as I was a father and parents should just work!
- Kobe, for making me give up going to the first foreign workshop I was expected to attend as a PhD student – he was born a week later. In fact the model I was going to be trained in did not work as expected.
- My parents and siblings for being ready to assist me and my family whenever 100% of my brain was focused on my research.

Acknowledgements

I am highly indebted to the *Fondation Prince Albert II* of MONACO through the IPCC Scholarship Programme for Developing Countries and the Swedish International Development Cooperation Agency (Sida) who made this PhD project possible by funding the studies especially at both the initial and final stages.

I would like to thank my two supervisors, Dr. Mark Tadross and Professor Bruce Hewitson, for the guidance given throughout the years and their patience in following my sudden changes of research tools and for the many fruitful discussions.

I hereby express my deepest appreciation to Ulrich Schlese of the Max–Planck Institute for Meteorology, Hamburg, Germany, for being the link in the provision of the ECHAM5–HAM model.

I gratefully acknowledge the importance of the Climate System Analysis Group (CSAG) and its favourable research environment for catalysing my will to try to understand the complexities of climate systems.

The Center for High Performance Computing (CHPC) is hereby acknowledged for allowing me an unique opportunity of working in world–class computing facilities without having to travel overseas.

To my Mozambican friends and colleagues in Cape Town as well as the Mozambique Consulate, I owe immense gratitude for making me feel at home.

I also acknowledge the MODIS mission scientists and associated NASA personnel for access to some of the data and literature used in this research.

Last but not least, I would like to thank my colleagues at the Department of Physics – Faculty of Science – Eduardo Mondlane University, Maputo – Mozambique, for keeping up the pace of my subjects while I was busy studying in Cape Town.

Abstract

Aerosols are known to directly influence the climate system by scattering and absorbing solar radiation, and indirectly by acting as cloud condensation nuclei (CCN) and/or ice nuclei (CN) and thereby affecting the lifetime and extent of clouds. In this work, a *state–of–the–art* Global Circulation Model (GCM) incorporating both effects was used to assess how local communities are impacting the seasonality of regional climate by contributing to the release of massive amounts of aerosols through seasonal biomass burning. Except for localised biases (e.g. especially for the desert areas and over areas where observed data is scarce) overall validation of the model performance has shown that it was capable of capturing, with a good approximation, the observed climate variability in the study region. Simulations revealed that the largest pollution sources contributing to the aerosol burden found over Southern African atmosphere are local emissions. Minor external contributions come from the African tropical forest north of the Equator as well as south American pollution (especially during two seasons: March–to–May and December–to–February). The largest biomass burning aerosol concentrations tend to be found over low–pressure systems over the subcontinent. Model results have shown that aerosol impact in rainfall was small during the June–October period, as this period falls largely within the austral dry season. Additionally, results indicated not only negative changes of surface temperature can be induced, as previous studies have suggested, but positive changes can also be induced by the inclusion of biomass burning sulfur dioxide and sulfate aerosols nucleated thereofrom, which implied increased lower–level convergence over these regions, and, consequently, increased precipitation. The most significant impacts are an 80% increase in daily precipitation, for December–to–February, over the Atlantic Ocean (near the coast of Angola) and a prominent reduction (between 40–60%) found during the same season over central and northern Mozambique and Tanzania. This study highlights the importance of including all biomass burning emissions, from the aerosols directly released from fires to the precursor

gases, as different radiative forcings will be obtained from different chemical species, and, therefore, different circulation patterns are likely to be induced over all seasons, regardless of how large the emissions loading and/or concentrations are.

THESIS

Chapter 1

Introduction and motivation

Airborne aerosol particles impact the climate by absorbing or reflecting solar radiation, and/or serving as cloud condensation nuclei, thereby affecting the albedo and the lifetime of clouds [Andreae and Crutzen, 1997; IPCC-WGI, 2007; Ramanathan et al., 2001a]. While carbonaceous aerosols are efficient heat absorbers (thus warming the surrounding atmosphere and cooling the earth's surface), sulphate and organic aerosols play a different role by scattering solar radiation and acting as efficient Cloud Condensation Nuclei (CCN) [Menon, S., 2004; Penner et al., 2006]. Although carbonaceous aerosols are the most predominant type of aerosols directly released from biomass combustion processes, the impact of aerosol loading on climate in Southern Africa, where aerosol loadings are derived largely from biomass burning, is expected to be more complex than previous studies (particularly studies solely based on carbonaceous aerosols and/or studies on the aerosol radiative properties) have revealed. The transformation of sulphur dioxide – a by-product of biomass combustion – into sulphate particles, can counteract the effects of carbonaceous aerosols and, depending on their relative concentration, can sometimes even offset it at some locations [Charlson et al., 1992; Ramana et al., 2010].

Some of the primary factors impacting the climate on the global scale are well understood and well represented in climate models. However, current climate models often fail to accurately and faithfully reproduce observed climate patterns, partly because regional feedbacks are not fully understood or incorporated into these models [Colman, 2003; Colman and McAvaney, 2009; Raes et al., 2010; Ramanathan and Carmichael, 2008]

Accurately simulating observed climate variability and trends with climate models depends on how well the relevant forcings are known and how well the internal physical

relationships have been described in the models. Ideally, climate models should be able to simulate processes with spatial scales ranging from metres to planetary, and temporal scales ranging from minutes to multi–annual; models should include feedbacks between the different parameters. Figure 1.1 shows the relevant scales important for climate models.

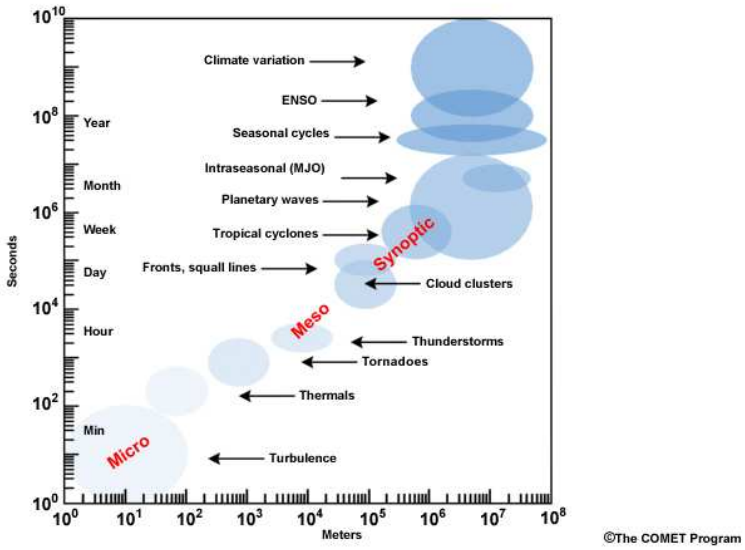

Figure 1.1: Atmospheric scales relevant for climate models. From `http://www.meted.ucar.edu/tropical/textbook_2nd_edition/print.htm`

Since models are limited by their spatial and temporal resolutions, processes ocurring in scales smaller than these resolutions must be parameterised to reflect their impact on the models' dynamics. Such processes include vegetation and soil–atmosphere feedbacks from the land surface, as well as regional ocean feedbacks and convection.

This study investigates one such important feedback – the seasonal Biomass Burning (BB) – and the impact on the atmosphere caused by the aerosols generated by the burning process. In Southern Africa, field campaigns have shown that these aerosols have impact on the regional climate [Ichoku et al., 2001, 2003; Scholes et al., 1996] and this study investigates these impacts, using a state–of–the–art aerosol–climate model.

1.1 Aerosols

Aerosols are tiny liquid and/or solid particles (Figure 1.2) suspended in the atmosphere with sizes ranging from tens of nanometres (nm) to tens of micrometres (μm).

Aerosol particles are generated by both anthropogenic and natural activities.

Anthropogenic aerosols are mainly released by combustion through fuel-wood consumption, industry, transport and forest fires ignited by man–made accidents; natural aerosols derive from volcanoes, lightning induced forest fires, desert dust, sea spray, and natural emissions from vegetation. The concentration of natural aerosols in the atmosphere is approximately 10^7–10^8 particles/m^3 [Seinfeld and Pandis, 1998; Seinfeld and Pandis, 2000].

Dependending on their origin, aerosols can further be classified as primary or secondary. Primary aerosols are those directly emitted to the atmosphere by volcanoes; through the effect of wind lifting dust particles in arid regions; from combustion during BB; from sea spray through bursting of water bubbles at sea surface; and from vegetation [Power, 2003]. Secondary Organic Aerosol (SOA) particles are those resulting from the chemical reactions of gas–to–particle conversion of hydrocarbons from plants, DiMethyl Sulphide (DMS) from the ocean and SO_2 from fossil fuel combustion [Buseck and Pósfai, 1999; Buseck and Schwartz, 2003; Power, 2003; Seinfeld and Pandis, 1998]. The most important example of this is the transformation of sulphur dioxide, a by–product of fossil fuel combustion, into sulphate particles. Hydroxyl radicals attack the sulphur dioxide and make gaseous sulphuric acid which may then condense within existing aerosol particles or nucleate through a direct gas–to–particle change of state in the presence of water vapour and ammonia to produce new particles [Binkowski and Roselle, 2003; Griffin et al., 2002].

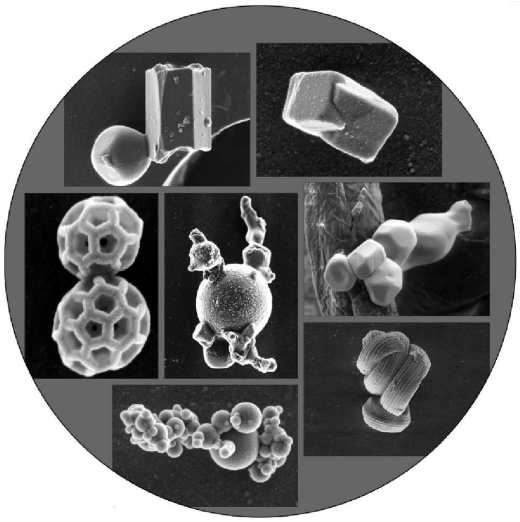

Figure 1.2: Sample microscopic picture of aerosols. Source: Pöschl [2005]

Chemical species composing aerosols are mainly sulphates, nitrates, organic material, elemental carbon and ammonium. Sulphates and organics typically constitute more than half of the mass concentrations of urban and suburban aerosols [Heintzenberg, 1989; Ho

et al., 2003]. It is also possible to trace the origins of aerosols based on their chemical nature. For instance, elemental carbon (also known as graphitic carbon) is a sub-product of combustion processes and thus can be used as a tracer for primary carbonaceous (rich in carbon) aerosols of combustion origin [Bhave et al., 2007; Turpin et al., 1991]. Generally, aerosols from fossil–fuel combustion and BB are mainly composed of black carbon, organic carbon (a form of carbon usually bound to hydrogen molecules) and sulphate nucleated from emitted SO_2 gas [Ramana et al., 2010; Ross et al., 1998].

Near urban and/or industrialised areas and deserts, aerosol concentrations are higher than over oceans [IPCC-WGI, 2001; Power, 2003]. The lifespan of aerosols varies: it can range from days to weeks within the atmosphere (a less stable environment) but can be up to years in the stratosphere (the latter environment is highly stable) [Power, 2003]. Studies by Turco et al. [1982], Power [2003], and Rampino and Self [1984], and also by Hobbs [2003], Magi et al. [2003], Garstang et al. [1996] and Murphy et al. [1998], all indicate the existence of two dominant layers of aerosols: one close to the surface of the Earth (i.e. within 0–3 km of the earth's surface); and the other in the stratosphere (i.e., approximately 15–25 km above the earth's surface). The latter layer is caused by volcanic emission; meteoric dust; gas–to–particle conversion of aircraft and volcanic gases; and penetrative convection from the troposphere.

The shape of the size distribution function is determined by the sources of the aerosols and also by aerosol removal processes [Heintzenberg, 1989; Jung, 1957; Sharma and Patil, 1992]. Radiation transmission through an aerosol–laden medium, as well as the aerosol hydrodynamic characteristics, are highly dependent on their shape and size [Friedlander, 1977]. Since atmospheric aerosol particles have heterogeneous aspects and are rarely spherical (Figure 1.2), a common physical parameter for describing them is the aerodynamic diameter (D_p) (which is the particle size determined from inertia or settling velocity, assuming their resistance as if they were spheres moving through a fluid) [DeCarlo et al., 2004; Spencer et al., 2007; Wilson and Liu, 1980].

The probability density function of sizes of most natural aerosols follows a log–normal distribution (Figure 1.3). Aerosol particles with D_p of less than 1 µm are known as fine mode; those above 1 µm are coarse mode particles. Additionally, subdivisions are found in the fine mode: the *Aitken* mode or nucleation mode (which refers to particles with $0.001\mu m < D_p < 0.1\mu m$) and the *accumulation* mode (with D_p above 0.1 µm and below

1µm) [Heintzenberg, 1989; Power, 2003; Whitby, 1978].

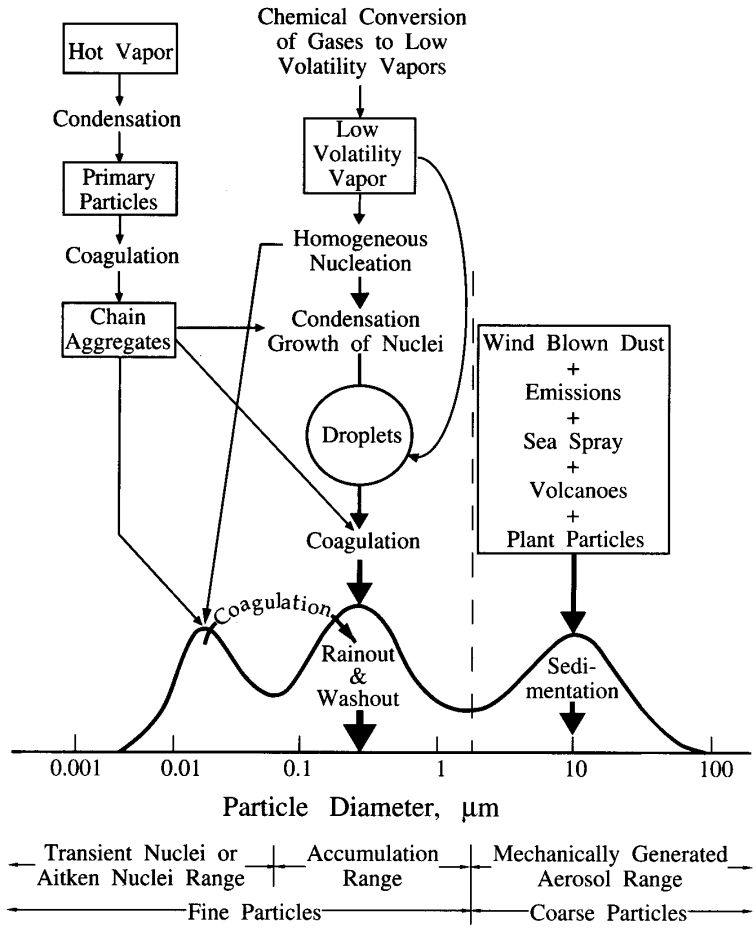

Figure 1.3: Aerosol modes, corresponding sources, formation and removal mechanisms. From Seinfeld and Pandis [1998]

Figure 1.3 shows atmospheric aerosol formation and removal mechanisms and their common size intervals. Particle formation processes can be subdivided in thermodynamical and mechanical. Primary aerosol particles are formed during high temperature combustion; by gas–to–particle conversion or by processes involving homogenous condensation of low–volatility vapours. The size of particles generated from such processes fall into the *Aitken* mode. The accumulation mode is generally composed of droplets formed by condensation of particles nucleated from low volatility vapours (as cloud–borne chemical processes) as well as by coagulation of *Aitken* mode particles. Particles generated from processes which involve the extraction of pre–existing particles from their "enclosure" to the atmosphere by mechanical processes (such as wind, volcanoes, sea spray, etc) dominate the composition of the coarse mode [Seinfeld and Pandis, 1998].

Several studies have presented the dependence of atmospheric aerosol residence time

on the particle size [Langmann et al., 2010; Maxey and Corrsin, 1986; Power, 2003; Sellegri et al., 2003]. Fine mode particles have a shorter residence time in the troposphere because they are quickly removed by diffusion (*Aitken* mode aerosols) and by scavenging and washout/rainout (accumulation mode aerosols). Coarse mode particles ($D_p > 1\mu m$) are mainly removed by gravitational settling (also referred to as sedimentation). In particular, accumulation mode aerosols tend to reside for a longer time because they are too large to be removed by diffusion processes and too small for sedimentation; they therefore become the targets for in–cloud nucleation scavenging in the upper levels [Andronache, 2003; Han et al., 2004; Power, 2003]. This latter range of sizes is also termed *The Greenfield Gap*, in acknowledgement of the work carried out by Greenfield [1957].

1.2 Effects of aerosols on climate

Apart from polluting the atmosphere, impairing visibility, health problems [Lave and Seskin, 1970; Pope, 2000; Schwarts and Marcus, 1990] and damage to agricultural crops [van Tienhoven et al., 2006; Zunckel et al., 2006], air pollution also impacts on global and regional climates [IPCC-WGI, 2001].

Much is known about the radiative influences of the Greenhouse Gasess (GHGs) in climate [IPCC-WGI, 2001]. However, the effect of aerosols remains a major uncertainty in understanding past and present climates and in predicting the future climate [Bergstrom et al., 2003; Haywood et al., 2003; IPCC-WGI, 2001; Rotstayn and Lohmann, 2002; Suzuki et al., 2004; Zakey et al., 2006]. Figure 1.4 is an illustration by the Intergovernmental Panel on Climate Change (IPCC) showing the estimated magnitude of the radiative forcing in W/m^2 (bars) and the corresponding Level of Scientific Understanding (LOSU) of each forcing of the climate system. A positive/negative radiative forcing implies a warming/cooling of the environment, respectively. According to IPCC-WGI [2007], the LOSU is an unavoidable subjective concept created in order to leverage the lack of sufficient quantitative data supporting estimates of a given climate forcing. This index indicates how well studies agree on quantifying the Radiative Forcing (RF) and how well observation-based studies agree with models. It is given by the 'Evidence' $\times$ 'Consensus' product, where "Evidence" ranges from A (strong evidence) to C (insufficient evidence); while "Consensus" ranges from 1 (good deal of consensus) to 3 (insufficient consensus).

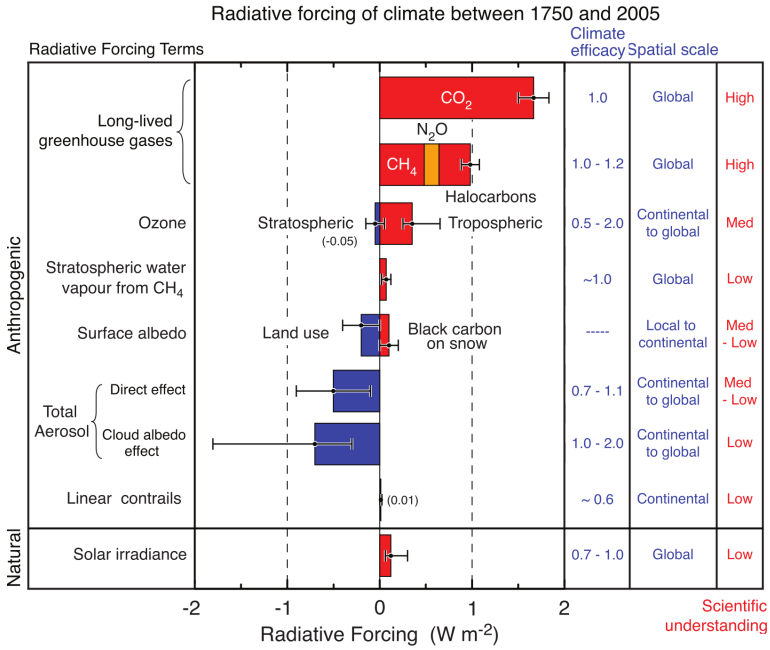

Figure 1.4: Global mean radiative forcing in W/m^2 (in bars) and the level of scientific understanding (in error bars). Adapted from IPCC-WGI [2007]

In Figure 1.4, the LOSU ranges from high to low. The very well established consensus that long–lived GHGs exert the single largest and positive forcing (i.e., warming of the atmosphere) to the global climate system is shown by the first bar on top of this figure. This consensus is indicated by a 'High' LOSU and a small size of the uncertainty value (the error bar). The magnitude of the stratospheric and tropospheric ozone forcings have also been thoroughly investigated and their LOSU is considered 'Medium'.

As indicated by IPCC-WGI [2007], strong evidence that aerosols have a negative RF on climate exists (based on ground–based and airborne observations, and from modeling studies). However, the corresponding LOSU is still medium to low because the determination of aerosol emission sources, their complex spatio–temporal distribution and optical properties, and the fact that aerosols are mixed with natural background particles raise uncertainties. For example, the effect of aerosols on cloud reflectivity (presented in Subsection 1.2.2), still lacks observational support [Boucher and Lohmann, 1995; IPCC-WGI, 2007].

1.2.1 Direct effects

Aerosols **directly** influence the climate system by scattering and absorbing solar radiation, which can cool both the atmosphere and surface by reflecting solar radiation back into space. At the same time, the direct effects can warm the atmosphere by absorbing solar radiation, depleting the solar radiation reaching the ground and therefore cooling the surface. These effects change the temperature structure and thus reduce the convective contribution to warming the atmosphere by increasing atmospheric stability [Abel et al., 2005; Andreae and Crutzen, 1997; Haywood and Boucher, 2000; Jacobson, 2001; Ramanathan et al., 2001a]. As shown by several authors [Kirkevåg et al., 1999; Kondratyev et al., 1998; Menon, S., 2004; Penner et al., 1998; Schult et al., 1997], absorptivity and/or reflectivity are highly dependent on the nature of aerosols. Black-carbon is an efficient heat absorber (i.e., exerts a positive forcing to the atmosphere); by contrast sulphate and organic aerosols play the opposite role. Therefore, the black-carbon/sulphate ratios play an important role in determining atmospheric warming [Ramana et al., 2010]. Additionally, the Greenfield Gap (referred to in Section 1.1) includes the peak wavelength of solar radiation (0.48 μm), which causes accumulation mode aerosols to interact efficiently with solar radiation [Tinsley et al., 2000].

1.2.2 Indirect effects

In a much more complex process than that of the direct effects (as indicated by Andreae and Crutzen [1997]; Andreae and Rosenfeld [2008]; Feichter et al. [2003]; Huang et al. [2007]; Quaas et al. [2004]; Ramanathan et al. [2001b]) scavenged aerosols **indirectly** affect climate in serveral ways:

- by acting as CCN and/or Ice Nuclei (CN), which modify the microphysics and radiative properties – termed "the first indirect effect" or *Twomey effect* [Chylek et al., 2006; Feingold et al., 2003; Ferrare et al., 2002; Previdi et al., 2003; Twomey, 1974];
- throught the lifetime and extent of clouds – termed "the second indirect effect" or *Albrecht effect* [Albrecht, 1989; Feichter et al., 2003; Lohmann and Feichter, 2005; Rosenfeld and Feingold, 2003].

An additional aerosol effect – the **semi–direct effect** [Hansen et al., 1997] – is associated with absorption of solar radiation by incloud carbonaceous aerosols, which causes reduction

of relative humidity because of increased heat in the surrounding environment and, eventually, evaporation of clouds [Johnson et al., 2004; Lohmann and Feichter, 2001, 2005; Ramanathan et al., 2001]. This effect also alters atmospheric stability and, again, cloud formation and lifetime. Figure 1.5 shows a schematic diagram of the various radiative mechanisms associated with aerosol–cloud interactions.

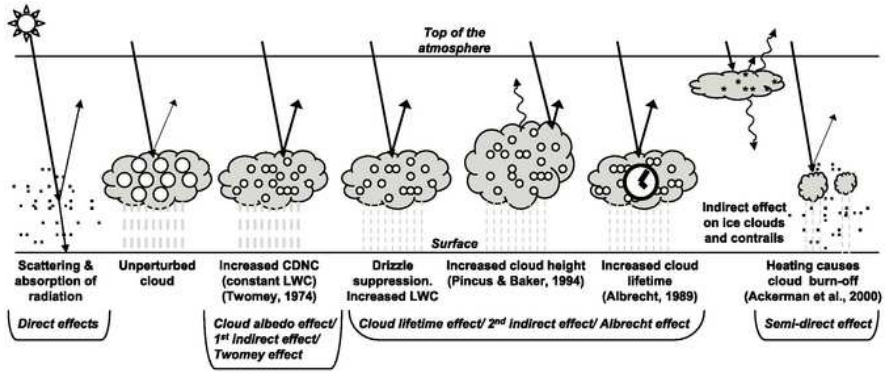

Figure 1.5: Schematic diagram of the multiple aerosol radiative mechanisms. The small black dots represent aerosol particles; the larger open circles cloud droplets. Straight lines represent the incident and reflected solar radiation, and wavy lines represent terrestrial radiation. The filled white circles indicate cloud droplet number concentration (CDNC). The unperturbed cloud contains larger cloud drops as only natural aerosols are available as cloud condensation nuclei, while the perturbed cloud contains a greater number of smaller cloud drops as both natural and anthropogenic aerosols are available as cloud condensation nuclei (CCN). The vertical grey dashes represent rainfall, and LWC refers to the liquid water content. After van Dorland et al. [2007]

The direct and indirect effects are believed to lead to a net reduction in the global annual mean surface temperature, thereby offsetting the positive forcing caused by the anthropogenic greenhouse gases [Coakley et al., 1983; IPCC-WGI, 2001; Quaas and Boucher, 2005]. However, possible future increases in aerosol loading and the resulting increase in concentration of cloud condensation nuclei, may saturate the cooling effect, allowing the heating effect to dominate [Kaufman et al., 1991].

1.3 Aerosol emissions in Southern Africa: The contribution of biomass burning

Southern Africa is dominated by savanna ecosystems, changing to subtropical and tropical zones toward the north, and to semiarid and arid zones toward the south-west

[Ichoku et al., 2003; Mason and Joubert, 1997].

Associated with human population pressures on regional ecosystems and related to agricultural and domestic fuel–wood consumption practices, most of the subcontinent savannah is periodically subjected to some of the highest levels of BB in the world (see, Figure 1.6), loading heavy amounts of aerosols into the atmosphere [Crutzen and Andreae, 1990; Helas and Pienaar, 1996; Kirchstetter et al., 2003; Liousse et al., 2007; Schmid et al., 2003; Scholes et al., 1996; Swap et al., 2003; Yokelson et al., 2003]. Already in 1979, Crutzen et al. mentioned that BB sometimes competed with fossil fuel from traffic and industry use as a source of atmospheric pollution in some regions of the globe. Such is the case with Southern Africa, where BB plays a major role on the total emissions of aerosols [Andreae and Merlet, 2001; Marufu et al., 2000].

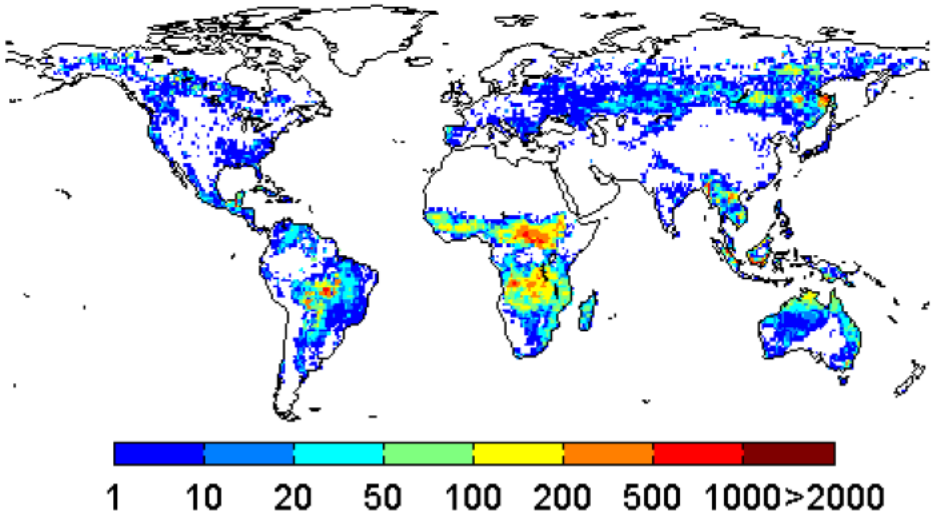

Figure 1.6: Mean annual fire emissions (g $Cm^{-2}year^{-1}$) averaged over 1997–2004. Source: van der Werf et al. [2006]

First systematic attempts to quantify fire emissions in Southern Africa and their likely impacts date back to 1992, when, as part of the the International Geosphere-Biosphere Programme/International Global Atmospheric Chemistry (IGBP/IGAC), an experiment called South African Fire–Atmosphere Research Initiative (SAFARI-92) [Lindesay et al., 1996] was carried out in the region. This experiment aimed at performing a comprehensive investigation of the role of vegetation fires, particularly savanna fires, in atmospheric chemistry, climate and ecology. SAFARI-92 resorted to the Advanced Very High Resolution Radiometer/Local Area Coverage (AVHRR/LAC) imagery, meteorology derived from aircraft–measurements and European Centre for Medium–Range Weather Forecasts

(ECMWF) products, as well as pyrogenic models, to reveal that the contribution of vegetation fires to the concentration of photochemical oxidants and haze over the subcontinent is large. According to Barnaba et al. [2011], in Europe (where the level of wildfires is far less than that of Southern Africa) wild land fires already represented the major source of atmospheric particles with diameters $< 1(\mu m)$.

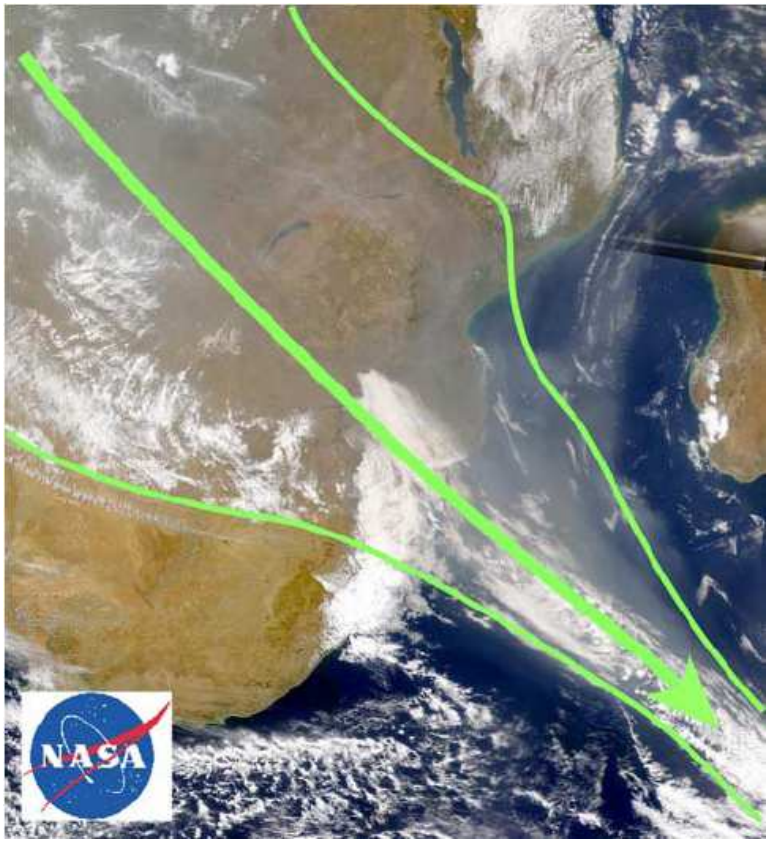

Figure 1.7: Southern African biomass burning smoke and haze exiting off the east coast on 4 September 2000, designated as the *River of Smoke*. Provided by the SeaWiFS Project, NASA/Goddard Space Flight Center, and ORBIMAGE. Satellite: OrbView-2, Sensor: SeaWiFS, Image Date: 09-04-2000. (Image captured by CSIR Satellite Application Center.). From: Swap et al. [2003]

Later, within the scope of the Southern African Regional Science Initiative (SAFARI2000) [Swap et al., 2003], a project aiming at investigating the generation, transport and fate of aerosols and trace gases over the subcontinent, and based on multi-annual calculations of monthly Aerosol Optical Depth (AOD), Eck [2003a], Eck [2003b], Queface et al. [2003] and Queface et al. [2011] showed that the seasonal variability of aerosol concentration over the subcontinent indicated September and April as the months with the highest and lowest aerosol loading respectively, coinciding with the highest and lowest peaks of BB in the region.

Figure 1.7 shows Southern African BB smoke and haze exiting off the east coast on 4 September 2000, designated as the *River of Smoke* [Annegarn et al., 2001]. Using the HYbrid Single Particle Lagrangian Integrated Trajectory Model (HYSPLIT), Kanyanga [2008] has shown that for air masses originating over tropical Southern Africa, the *River of Smoke* is a phenomenon occurring only during neutral El-Niño Southern Oscillation (ENSO) years.

1.4 Southern African circulation patterns and their relation to aerosol concentration in the region

Southern Africa is located between the south Atlantic and Indian ocean subtropical high–pressure cells and is influenced by the interaction of tropical easterly and extra–tropical westerly flows [Barry and Chorley, 1968; Tyson, 1981]. The seasonal longitudinal movement of the two the high–pressure cells determines most of the climate variability in the region [Tyson, 1981]. As the Atlantic high is more often 3° farther north than the Indian Ocean cell, it is responsible for bringing low level westerlies to Angola and the Democratic Republic of Congo (DRC) throughout the year; high–level westerlies are carried to central Angola during austral summer [Barry and Chorley, 1968; Tyson, 1981]. In turn, a larger impact on regional climate is caused by the westward movement and intensification of the Indian Ocean cell during the austral winter, bringing easterlies at all levels to most of the subcontinent [Barry and Chorley, 1968; Tyson, 1981].

Associated with the above, a very important feature of the atmospheric circulation pattern was shown to occur in Southern Africa by Tyson et al. [1996b]. In this work, analysis of a 7–year climatology revealed that aerosols and trace gases over the region are re–circulated. This type of circulation, occurring nearly 70% of the time during austral winter, is the so-called Southern African anticyclonic *gyre* [Swap et al., 1996]. Effectively, this means air masses do not directly exit the region, but are kept for variable period of time (on a time-scale ranging from hours to weeks) and on a spatial scale of tens to thousands of kilometres (generally below 500 hPa). This uncommon aerosol re–circulation pattern has triggered various subsequent studies by Gatebe et al. [2001]; Piketh et al. [1999]; Swap et al. [1996]; Tyson [1997]; Tyson et al. [1997], all of these studies identified and defined various circulation patterns in the region. Figure 1.8 illustrates major circulation patterns over

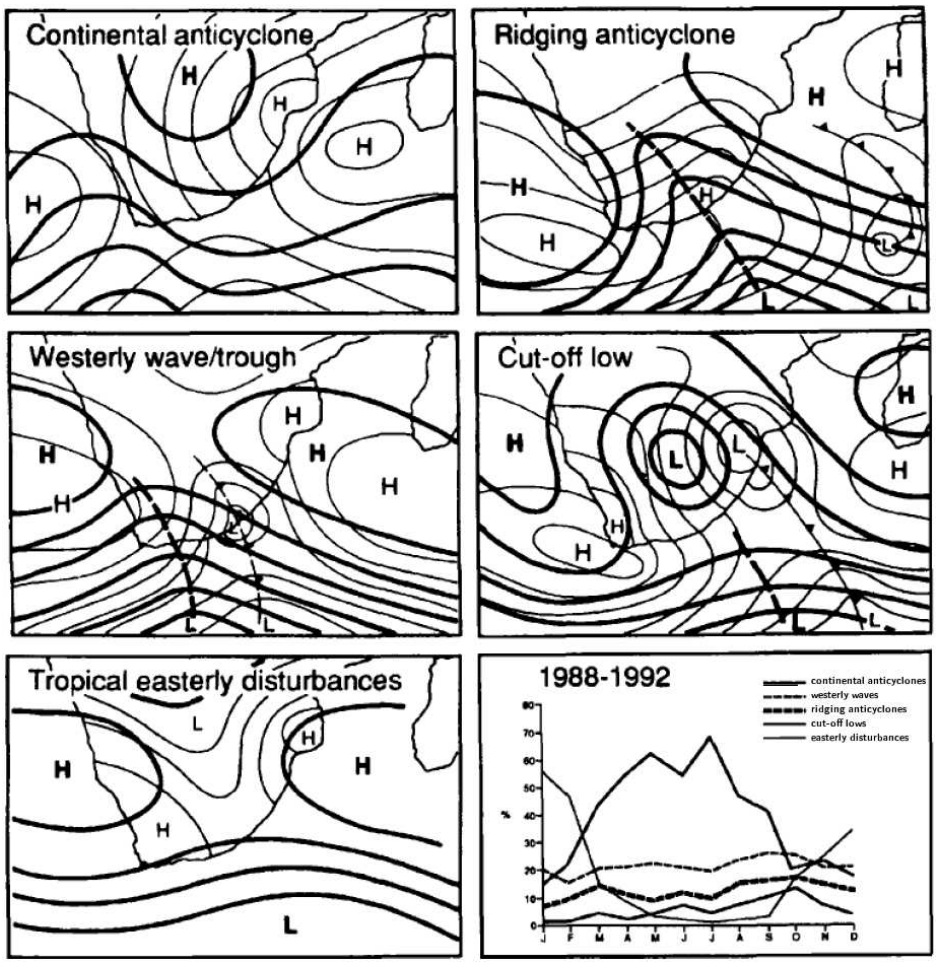

Figure 1.8: Predominant circulation patterns in Southern Africa calculated over a five–year period (1988–1992). Heavy lines represent conditions at 500 hPa; light lines give surface conditions (as sea-level isobars over the oceans and contours of the 850 hPa surface over the subcontinent). Following Tyson et al. [1996b]

Southern Africa, and the corresponding monthly frequencies, calculated over a five–year period (1988–1992).

Additionally, Garstang et al. [1996] and Tyson [1997] revealed that vertical motions of recirculated material in the region are inhibited by the presence of three persistent absolutely stable layers occurring close to the 850 hPa (approximately 1.5 km), 700 hPa (approximately 3 km) and 500 hPa(approximately 8 km) levels. They also found that the layer at 500 hPa, in particular, seems to cover large areas by the end of the dry season.

1.5 Modeling studies on biomass burning aerosols in Southern Africa

Modeling studies covering aerosols in the region are recent and, so far, most of them have only looked at the transport and/or direct radiative impacts of aerosols, omitting the important contribution of the aerosol nucleation processes and indirect effect. For instance, Gatebe et al. [2001]; Piketh et al. [1999]; Swap et al. [1996] investigated the long–range transport of aerosols emanating from Southern Africa. The Transport and Atmospheric Research Chemistry near the Equator-Atlantic (TRACE-A) experiment [Fishman et al., 1996] together with SAFARI-92, gathered numerous measurements and undertook complex modeling work to investigate the sources of the massive amounts of pollution observed by satellite between Southern Africa and Southern America during the dry season.

Duncan et al. [2007] and Trentmann et al. [2002] did similar work on the cross-tropopause transport of BB pollution for several regions of the world (including Southern Africa) using the Global Modeling Initiative (GMI) Combined Stratosphere–Troposphere Chemistry and Transport Model (Combo CTM). Again, Guan et al. [2008] investigated the transport aspects of BB aerosols using the NCAR Community Atmosphere Model (CAM). An interesting work on sources of pollution over Southern Africa was done by Chatfield et al. [1998] using the Global Regional Atmospheric Chemistry Event Simulator (GRACES) driven by the Fifth-Generation NCAR/Penn State Mesoscale Model (MM5), covering period September–October 1992. In this work the "Great African Plume" – a flow of agricultural burning smoke moving westward from a wind divergence line over Central Africa to pollute the Equatorial Atlantic Ocean – was identified. Additionally, an "inward" flow, named by the authors "Global Burning Plume", originating from tropical South America and flowing past South Africa above 8 km altitude was identified by the model. These plumes were found to influence the South Indian and Southern Oceans.

Using a global aerosol model and observations of CCN concentrations, Spracklen et al. [2011] concluded that fire emitted carbonaceous aerosol was responsible for forming more than half of the global cloud condensation nuclei. Conversely, Pierce et al. [2007] found that, dependent on the emissions inventory used, the addition of primary carbonaceous aerosol in a global aerosol microphysics model, increased concentrations of CCN at 0.2% super-saturation level by 65–90% in the surface layer.

In order to calculate the direct radiative impact of aerosols from biomass burning, Myhre et al. [2003] used meteorological data from the SAFARI2000 project to drive an off-line chemical transport model over Southern Africa, and found that the local radiative impact of biomass aerosols reached as much as 50 W/m^2 for September 2000. In 2005, Abel et al. applied a radiative transfer code to model the direct radiative effect of BB aerosols over Southern African during the peak burning season, and found that the inclusion of clouds in the model reduced the radiative impact of the BB aerosols by half to one third. More recently, Aghedo et al. [2007] used a coupled global chemistry–climate model to investigate the relative importance of African BB, biogenic Volatile Organic Compounds (VOCs), lightning and anthropogenic emissions to the tropospheric ozone budget over Africa and globally. This work demonstrated that more than 70% of the tropospheric ozone produced through continental African emissions is advected outside the continent; thereby impacting the Atlantic and Indian Oceans, Latin America, Oceania and the Middle Eastern regions.

Roeckner et al. [2006b] applied ECHAM5 with Hamburg Aerosol Module (ECHAM5-HAM) to assess the impact of varying carbonaceous aerosols on the globe, and found that the various regions respond differently to this perturbation, and that, regions located in low latitudes display the largest decreases in surface temperature and increases in precipitation and run–off.

Tummon et al. [2010] studied the direct and semi-direct aerosol effects on the Southern African climate during the austral winter season using the ICTP Regional Climate Model (RegCM). In this work, the authors found that aerosol direct radiative forcing, in the main biomass burning region, caused surface turbulent fluxes to decrease, resulting in reduced Planetary Boundary Layer (PBL) height and surface temperatures. Additionally, the resulting changes in surface temperature gradients caused the southern branch of the African Easterly Jet to be enhanced and shifted southward. In another study, Tummon [2010] found that aerosol emissions have much more influence on the radiative forcing than other parameters (e.g., sea surface temperatures (SSTs)). Additionally, Randles and Ramaswamy [2010] investigated the impact of radiation absorbing biomass burning aerosols on the climate of Southern Africa, using the Geophysical Fluid Dynamics Laboratory AGCM (GFDL-AGCM). As a result, they found that aerosols emitted by BB reduce the incoming solar radiation at the surface and locally heat the atmosphere. Another recent study looking

at the direct and semi-direct aerosol effects of the Southern African BB, was carried out by Sakaeda et al. [2011] using the CAM model, in which contrasting radiative feedbacks were identified over ocean and land: Over the ocean, where aerosols are predominantly above cloud layers, a negative Top–Of–Atmosphere (TOA) semi–direct radiative effect was found to be larger than positive all-sky direct radiative effect (DRE); over the land, where the aerosols are often below or within cloud layers, reductions in cloud liquid water path (LWP) led to a positive semidirect radiative effect that dominated over a negligible DRE.

Although there has been a growing understanding of the effects of aerosols on local climate (as described above), large uncertainties still remain especially on how small-scale feedbacks can modulate climate events [Feichter et al., 2003; Girard and Bekcic, 2005; Hulme et al., 2001; IPCC-WGI, 2001; Paeth and Feichter, 2006; Wang et al., 2004; Zhang, 2008]. The uncertainties remain partly because many features of short-time scale climate variability, are not adequately represented in climate models [Batjes, 2006; Lioubimtseva et al., 2005; Tews et al., 2006]. One such feedback is the inclusion of the aerosol indirect effect, a very important factor determining cloud–albedo and cloud lifetime, as described in Section 1.2.

Generally, because of model limitations or the scope of work undertaken, the above referenced modeling studies over Southern Africa did not look at the combined impact of both the direct and indirect effects of all types of aerosols on the Southern African regional climate. In other cases, because the studies were limited to their main points of focus, they did not (or could not) include all aerosols or precursors to aerosols and, thus, eventually failed to reveal important features associated with direct and indirect effects in the presence of all types of aerosols directly and indirectly generated by biomass burning processes. For instance, although using an advanced Global Circulation Model (GCM) able to simulate both direct and indirect effects, Roeckner et al. [2006b] only studied the impact of carbonaceous aerosols. On the other hand, Sakaeda et al. [2011] only accounted for the direct and semi–direct effects because the version of the CAM used in the study could not depict aerosol activation. In turn, Tummon [2010] and Tummon et al. [2010] used a version of RegCM which could only simulate the aerosol direct and semi–direct effects.

With the advent of *state–of–the–art* aerosol–climate models able to simultaneously simulate fully–coupled climate–chemistry–aerosol–radiation interactions (including secondary aerosol formation) [Baklanov et al., 2008; Grell et al., 2005; Jacobson, 2001;

Stier et al., 2005] and the availability of fairly comprehensive global emission inventory databases [van der Werf et al., 2006], alongside the existence of the computational power to handle such models, the opportunity to resolve small–scale processes and incorporate feedbacks (judged important for a region), and thus to more accurate representation of regional climate forcings opens up.

BB aerosols are in the accumulation mode range [Eck et al., 1999], and, according to results obtained by Ross et al. [2003] (using experimental data from Aerosol Recirculation and Rainfall Experiment (ARREX) and SAFARI2000), and those later obtained by Ghosh et al. [2007] and by Vestin et al. [2007] (during experiments in the Amazonian forest), these BB aerosols act as efficient CCNs. In an experiment conducted within the scope of Fire Lab At Missoula Experiment (FLAME), Petters et al. [2009] also suggested that BB aerosol emissions are CCN–active at the point of emission and do not require conversion in the atmosphere to more hygroscopic composition before they are able to participate in cloud formation and undergo wet deposition. Thus, the nucleation of CCN–active aerosols would add secondary particles to the existing burden, changing aerosol concentrations and/or residence time. These factors may lead to complex changes in climate variables only fully understandable through comprehensive aerosol–climate models. Among these changes, the following impacts are possible:

- a decrease in surface temperature in the region, because part of the solar radiation is reflected and/or absorbed by aerosols in the atmosphere;
- an increase in atmospheric temperature, because of the presence of absorbing aerosols (BB mainly produces black carbon, a known heat absorber);
- a further decrease in atmospheric temperature, because of the presence of scattering aerosols, especially because BB also generates SO_2 which then nucleates into sulphate particles, known to be highly scattering;
- changes in the circulation patterns induced by reduction in convection because of a reduction in solar radiation reaching the Earth's surface, thereby affecting precipitation patterns;
- a reduction of the rainfall intensity because of cloud burning by absorbing carbonaceous aerosols (i.e., the semi–direct effect);

- an increase in cloud albedo, caused by the increase in aerosols activating into CCN; and
- a reduction in precipitation efficiency and/or a delayed precipitation onset by nucleation of many small cloud droplets which coalesce inefficiently into raindrops, because mainly black carbon and organic carbon are emitted from BB processes, as described in Section 1.2.

1.6 Research objectives

This study aims to better understand the response of the Southern African climate to the presence of BB aerosols, in a context where sulphate particles formed by gas–to–particle conversion of BB SO_2 are added to the directly emitted carbonaceous aerosols.

The study applies the state–of–the–art ECHAM5-HAM and Weather Research and Forecast Model with Online Chemistry (WRF/Chem). These models incorporate both the direct and the indirect aerosol effects and are able to represent gas–to–particle conversion. The latter model is able to simulate chemistry, allowing for the production of additional aerosol species with different chemico–physical properties and, thus, may induce different radiative and microphysical responses on climate. Specifically, the objectives of this work are as follows:

- Quantify the contribution of local and external sources to BB concentration in Southern Africa throughout the year;
- Assess the relevance of the synoptic variables in determining the aerosol concentrations in Southern Africa during the biomass burning season;
- Estimate potential feedbacks between the BB aerosols and the large-scale thermodynamic structure during austral spring;
- Evaluate the impacts of BB aerosols on temperature and precipitation during austral spring and, their subsequent seasonal and inter–annual variability, when primary and secondary aerosols are included in the simulations.

1.7 Thesis outline

This work is structured in eight main chapters. An overview on how aerosols are incorporated in climate models is presented in Chapter Two. The methodology for verifying the models against observed temperature and precipitation datasets and well as a description of how the final results were obtained is presented in Chapter Three. The evaluation of the simulations against observed data is presented in Chapter Four, followed by the identification of the contribution of local and external sources to biomass burning aerosol concentrations in Southern African in Chapter Five. An assessment of the relevance of the synoptic variables in determining the aerosol concentrations in Southern Africa during the biomass burning season is presented in Chapter Six. The simulated response of the thermal structure, and the atmospheric circulation, and their implication on temperature and precipitation during austral spring, and their subsequent seasonal inter–annual variability, when primary and secondary BB aerosols are included in the simulations, is presented in Chapter Seven. A summary of the major findings and the limitations of this work and suggestions for prospective research are presented in Chapter Eight.

Chapter 2

Aerosols in climate models

To fully incorporate aerosol–climate interactions in climate models, modelers must be able to describe, in numerical expressions, aspects impacting the life–cycle of atmospheric aerosols (from emission to removal processes), and including chemistry at any given time and at any given location within the model domain. There are several important aerosol factors that need explicit description in a model: aerosol size–distribution; aerosol emissions; formation of secondary aerosols by gas–phase chemistry (also referred to as nucleation); the condensation of gas phase molecules; coagulation; formation of cloud droplets and their evaporation (termed cloud burning); wet deposition; and dry deposition. In this chapter, an overview is given on how the above–mentioned factors have been incorporated into climate models

2.1 Aerosol emissions

For aerosol emissions to be accounted for in climate models, a detailed knowledge of their complex source activity, chemical composition and particle mass size distribution is required [Binkowski and Roselle, 2003; Stier et al., 2005; van Dorland et al., 2007; Ward et al., 2010]. The above details must have both time and space resolution representative of the regions of interest. This necessitates the establishment of gridded aerosol emission inventory databases, which, in turn, require extensive validation to ensure the implication of their usage is secured with a minimum level of uncertainty [Lindley et al., 2000; Winiwarter and Schimak, 2005]

Several experiments to build emission inventories databases were carried out [Greenberg

et al., 2003; Otter et al., 2003]. The level of complexity of the methods ranged from local measurements of emissions to remote–sensing techniques assisted with numerical models and/or a combination thereof [French et al., 2004; King et al., 1999; Ward and Hardy, 1991]. Commonly, the gridded emission databases have been gouped in the following categories: Anthropogenic emissions; Biofuel usage and natural emissions; BB; DMS from sea; elementary and organic carbon; mineral dust emissions; sea salt emissions; ship emissions; and volcanic emissions [Schultz et al., 2008]. In general, information contained in these databases include burned area, fuel loads, combustion completeness, fire emissions Carbon (C); Black Carbon (BC); organic carbon (OC); sulphur dioxide (SO_2); Particulate Organic Matter (POM); carbon dioxide (CO_2); carbon monoxide (CO); Methane (CH_4); non–methane hydrocarbons (NMHC); molecular hydrogen (H_2); nitrogen oxides (NO_x); nitrous oxide (N_2O); particulate matter (PM); Total particulate matter (TPM); total carbon (TC); and other less dominant/less present substances.

A panoply of global emissions inventory databases exist nowadays, including:

- The REanalysis of TROpospheric chemical composition database (RETRO) [Schultz et al., 2008];
- The Global Fire Emissions Database (GFED) [Randerson et al., 2005, 2007; van der Werf et al., 2006];
- The Emission Database for Global Atmospheric Research (EDGAR) [Olivier et al., 1994];
- The Aerosol Inter Comparison project (AEROCOM) [Dentener et al., 2006] the most frequently used by the aerosol modeling community.

In fact, AEROCOM is a combination of the former emissions inventory databases. Details of the methodology used to develop these databases, including spatio–temporal resolutions, the period covered, and the sectors used to generate the emissions appear in the corresponding literature. A summary of the relevant aspects of each of the above–referenced databases is publicly available on the Internet (for example, `http://accent.aero.jussieu.fr/database_table_inventories.php`).

2.2 Aerosol size distribution functions

As stated in Section 1.1, knowledge of atmospheric aerosol size distribution and chemical composition is crucial for the derivation of direct and indirect atmospheric radiative properties [Haywood and Boucher, 2000; Morrison et al., 2005; Whitby et al., 1971]. Given their vast and complex spacio–temporal distributions, various authors have used several experimental methods to derive size distribution functions for aerosols. One such method is the so–called Differential Mobility Particle Sizer (DMPS) – in which particles are electrically charged and, subsequently, separated by size ranges (through the identification of their different electrical mobility) [Knutson and Whitby, 1975; Levin et al., 2010]. A second technique has been based on the optical properties of the atmospheric aerosols (See Section 2.6) – in this method Optical Particle Counters (OPC) are used to determine the size of particles based on the intensity of the scattered radiation [Chen et al., 1984; Jaenicke and Hanusch, 1993; Liu et al., 1974; Szymanski and Liu, 1986]. An additional technique, named the Condensation Nuclei Counter (CNC) (effectively a modified extension of OPC) is used for particles smaller than the visible range [Liu and Kim, 1977; Maring and Schwartze, 1994; Rashid and Mavliev, 2002]. In the latter method, particles are immersed in a super–saturated fluid vapour so that they are activated and grow to a certain size within the visible range, and so, become optically detectable.

Figure 2.1 shows typical aerosols species found in the atmosphere and the corresponding number and volume distributions as function of the particle diameter. The lower part of this figure indicates the number (left–hand side (lhs)) and volume (right–hand side (rhs)) distributions as a function of the aerosol particle diameter. In terms of number, particle concentration distribution peaks on the Aitken mode; in terms of volume, the peak is within the coarse mode. Porter and Clarke [1997] contains a good review of the aerosol size distributions for sulphate, sea–salt and dust and based on experimental measurement over the sea. These are the distributions that climate models need to replicate numerically, to accurately assess the aerosol interaction with climate.

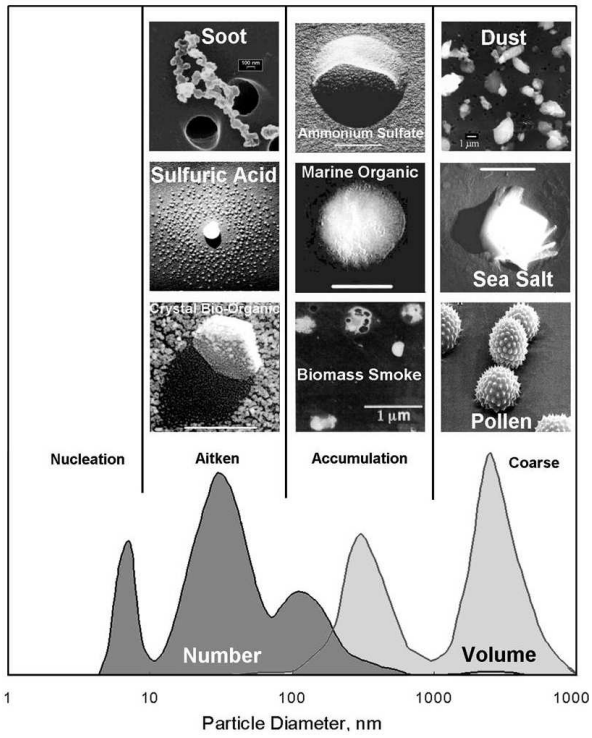

Figure 2.1: Aerosol number and volume size distributions ($dN/d\log r$, and $dV/d\log r$) for different atmospheric aerosols. From Seinfeld and Pandis [2000].

2.3 Aerosol formation and growth

2.3.1 Aerosol General Dynamic Equation (GDE)

Physico–chemical processes occurring in the atmosphere may change the aerosol formation and growth dynamics, and, therefore, the aerosol size distribution and magnitude of their interaction with climate [Wu and Biswas, 1998]. According to Whitby [1978], many attempts have been made to fit the aerosol size distributions with the results of the experiments (as described above) so that results could be used for practical cases. The basic criteria for such a distribution should include:

(a) Coverage of all particle size range (from 1 to 1000 nm);

(b) Accurate fit of particle number, surface area and volume;

(c) Correctly adhere to and be based on proven physical laws.

Basically, there are three processes associated with the aerosol formation and growth dynamics, namely nucleation; coagulation/agglomeration; and condensation/evaporation. For more details on these distributions, refer to Williams and Gage [2009].

In climate models, aerosol particle dynamics – from formation to growth of particles – is represented by a partial integro–differential equation named *Aerosol General Dynamic Equation* (GDE) [Talukdar and Swihart, 2004]. This equation describes coagulation, condensation, evaporation and nucleation processes, and, generally, has no analytic solution (except in simplified cases where particle growth has been neglected) [Friedlander, 1977]. Equation 2.1 is an example of the general form of the GDE. This equation represents the factors impacting the particle population balance in the volume interval limited by v and $v+dv$ [Friedlander, 1977; Talukdar and Swihart, 2004]

$$\begin{aligned}\frac{\partial n(v)}{\partial t} \quad + \quad & \underbrace{\nabla \cdot V n(v)}_{\text{flux divergence}} \; \underbrace{-\nabla \cdot D(v) \nabla n(v)}_{\text{diffusion}} + \underbrace{\nabla \cdot V_{\text{th}} n(v)}_{\text{external forces}} \\ = \quad & \underbrace{\frac{1}{2}\int_0^v \beta(\tilde{v}, v-\tilde{v}) n(\tilde{v}) n(v-\tilde{v}) d\tilde{v} - n(v)\int_0^\infty \beta(\tilde{v}, v) n(\tilde{v}) d\tilde{v}}_{\text{coagulation}} \\ & \underbrace{-\frac{\partial}{\partial v}\left[n(v)\frac{dv}{dt}\right]}_{\text{particle growth}} + \underbrace{\dot{n}(v)}_{\text{internal sources}} \quad ; \end{aligned} \tag{2.1}$$

where the underbraces refer the contribution of each factor to the change in the aerosol population, $\partial n(v)/\partial(t)$. Various solutions for the GDE have been presented in aerosol modeling history [e.g., Barrett and Webb, 1998; Debry and Sportisse, 2007; Gelbard and Seinfeld, 1979; Katoshevski and Seinfeld, 1997; Kourti and Schatz, 1998; Talukdar and Swihart, 2004; Tsang and Brock, 1982; Whitby and McMurry, 1997; Wu and Biswas, 1998]; each solution has demosntrable advantages and drawbacks. Advantages are mostly related to the precision and computational speed of the numerical solution; drawbacks are related to the ability to simultaneously account for condensation, nucleation, and coagulation [Barrett and Webb, 1998; Upadhyay and Ezekoye, 2003; Zhang et al., 1999]. A good comparison of the available numerical solutions of the GDE has been given by Whitby and McMurry [1997]. In summary, common methods used in aerosol–climate modeling for solving the GDE can be grouped as a) Bulk scheme; b) Sectional (bin) scheme; c) Method of Moments; and d) Modal scheme.

2.3.1.1 Method of Moments

An explicit method used to model the evolution of the Aerosol Size Distribution (ASD), the Method of Moments (MOM) uses volume/radial moments of the ASD, instead of the required *a priori* knowledge of particle size distribution function itself [Barrett and Webb,

1998; Thorpe et al., 1997; Yu et al., 2008]. The idea is to turn Equation 2.1 into a lower order differential equation by multiplying it by v^k (or by r^k, if radial moments are desired) and integrating for the size distribution [Hulburt and Katz, 1964; Pratsinis, 1988; Upadhyay and Ezekoye, 2003; Wu and Menon, 2001; Yu et al., 2008]. Thus, the moment μ_k is defined by:

$$\mu_k = \int_0^\infty v^k n(v) dv \tag{2.2}$$

Since Equation 2.2 involves integration of the unknown function $n(v)$, a mathematical closure problem arises [Hulburt and Katz, 1964]. Therefore, the MOM is only applicable for special cases where the growth function allows a closure of the equation [Barrett and Webb, 1998; Frenklach and Harris, 1987; McGraw, 1997], as is the case when ASD is assumed log–normal [Talukdar and Swihart, 2004].

2.3.1.2 Quadrature Method of Moments

Proposed by McGraw [1997], the Quadrature Method of Moments (QMOM) is an extension of the MOM in which the growth laws are arbitrary in order to overcome the closure problem described in 2.3.1.1. The integral moments are approximated by a sum of functions of abscissas (N) and weights (w_i) of the Gaussian quadrature [McGraw, 1997; Talukdar and Swihart, 2004] as

$$\mu_k = \int_0^\infty v^k n(v) dv \approx \sum_{i=1}^{N} v_i^k w_i \quad k = 0, 1, \ldots, 2N-1 \tag{2.3}$$

The number of moments in Equation 2.3 is determined by the number of abscissas N used. Results by Barrett and Webb [1998]; Marchisio et al. [2003] have shown that three nodes ($N = 3$; $k = 0, \ldots, 5$) are sufficient to describe moment evolutions using QMOM, and retain good accuracy at bearable computational costs.

2.3.1.3 Sectional (bin) method

In the sectional bin scheme, the continuous size distribution of particles is approximated by (n) discrete sections (bins) in each of which particle properties are constant [Gelbard and Seinfeld, 1979]:

$$n(v) \approx \sum_{i=1}^{i_{\max}} n_i \phi_i \tag{2.4}$$

where ϕ_i is the i^{th} section size distribution function. The size of each of the bins used to discretise size distribution determines the accuracy of this method [Whitby and McMurry, 1997; Wu and Biswas, 1998]. Time evolution is simulated with n equations for each time step. Since coagulation processes imply increasing the size of particles and, therefore, the overlapping of size bins, an increase in the number of calculations per bin per chemical compound is required; in turn this method becomes computationally demanding, especially where multidimensional fluid dynamic models are concerned [Talukdar and Swihart, 2004]. Some advances have been implemented for this method, in that the bins are allowed to be fixed during coagulation but can move to larger/smaller sizes during the condensation/evaporation processes [Jacobson, 1997; Kim and Seinfeld, 1990].

2.3.1.4 Modal method

In this method, each of the polydispersed aerosol populations is represented as an independent aerosol population – the *mode* [Whitby and McMurry, 1997]. According to Gelbard and Seinfeld [1979] and Whitby and McMurry [1997], the most common shapes of the modes used are mono–dispersed and log–normal – a determinant factor relating to the accuracy of the method (i.e., the number of modes will determine the accuracy of the method). In this method each process (nucleation, condensation and coagulation) in Equation 2.1 is represented by its own equation–the moment dynamic equations – and coagulation process is seen as collision of aerosols with the modes, thus resulting in intra–modal and intermodal coagulation processes [Whitby and McMurry, 1997]. The distribution moments are represented by

$$M_k = \int d_p^k n(d_p) \mathrm{d}d_p \tag{2.5}$$

where k is the k^{th} moment; $M_o = \int n(d_p) \mathrm{d}d_p$ is the total concentration of the particles in the mode. For the case of bimodal distribution, with the modes represented by represented

by indexes i and j, for the i^{th} mode we have:

$$\begin{aligned}\frac{\partial}{\partial t}\left(M_{k_i}\right) &= \nabla \cdot V M_{k_i} - \nabla \cdot \int_0^\infty d_p^k c(d_p) n_i(d_p) \mathrm{d}d_p + \nabla \cdot \int_0^\infty d_p^k D(d_p) \nabla n_i(d_p) \mathrm{d}d_p \\ &+ \frac{1}{2}\int_0^\infty \int_0^\infty \left(d_{p_1}^3 + d_{p_2}^3\right)^{k/3} \beta(d_{p_1}, d_{p_2}) n_i(d_{p_1}) n_i(d_{p_2}) \mathrm{d}d_{p_1} \mathrm{d}d_{p_2} \\ &- \underbrace{\int_0^\infty \int_0^\infty d_{p_1}^k \beta(d_{p_1}, d_{p_2}) n_i(d_{p_1}) n_i(d_{p_2}) \mathrm{d}d_{p_1}\ \mathrm{d}d_{p_2}}_{\text{intramodal coagulation}} \\ &- \underbrace{\int_0^\infty \int_0^\infty d_{p_1}^k \beta(d_{p_1}, d_{p_2}) n_i(d_{p_1}) n_j(d_{p_2}) \mathrm{d}d_{p_1}\ \mathrm{d}d_{p_2}}_{\text{intermodal coagulation}} \\ &+ \int_0^\infty \frac{\mathrm{d}d_p^k}{\mathrm{d}\upsilon_p} \frac{\partial d_p}{\partial t} n_i(d_p) \mathrm{d}d_p + \int_0^\infty d_p^k \dot{n}_{S_i}(d_p) \mathrm{d}d_p \end{aligned} \tag{2.6}$$

and a similar equation can be obtained for the j^{th} mode, by substituting i by j and *vice–versa* in Equation 2.6.

The log–normal distributions were the only instances that met all the criteria needed to characterise size distributions in models. One such distribution is given by

$$n(\ln d_p) = \sum_{i=1}^{n} \frac{N_i}{\sqrt{2\pi}\ln\sigma_g} \exp\left(-\frac{\ln d_p - \ln \overline{d_{pi}}}{2\ln^2 \sigma_i}\right) \tag{2.7}$$

where $n(\log d_p)$ is the number concentration of the particles with diameter, d_{pi} is the median diameter, and σ_i, is the standard deviation of the i^{th} log–normal mode [Seinfeld and Pandis, 1998; Whitby, 1978]. Because only three parameters are needed (namely particle concentration, geometric mean diameter and distribution standard deviation) in each mode to solve the GDE, log–normal distributions are those mostly used for solving Equation 2.6 [Whitby and McMurry, 1997]. The Modal Aerosol Dynamics for Europe (MADE) [Ingmar J. Ackermann and Heinz Hass and M. Memmesheimer and A. Ebel and Francis S. Binkowski and Uma Shankar, 1998], MADE–Secondary Organic Aerosol Model (SORGAM) [Schell et al., 2001] and Model for Simulating Aerosol Interactions and Chemistry (MOSAIC) [Zaveri et al., 2008] are examples of models using the modal method.

2.3.1.5 Bulk scheme

In a bulk scheme, aerosols are treated as being only one group, with total mass and number the only known variables, without any information on ASDs. This type of model is computationally fast; however, it can only be used to estimate aerosol particle dynamics (for instance without aerosol nucleation processes) for idealised cases [Whitby and McMurry,

1997]. This scheme is computationally efficient; however, ASD has to be assumed for the calculation of any undergoing physical process. The Georgia Institute of Technology – Goddard Chemistry Aerosol Radiation and Transport (GOCART) model [Chin et al., 2000] is an example of a model using a bulk scheme.

2.4 Aerosol activation of cloud droplets

For clouds to form, hygroscopic aerosol particles need to be present so that available super–saturated water vapour condenses onto them [Andreae and Crutzen, 1997; Martinsson et al., 1997]. The existing uncertainties in the assessment of the Aerosol Indirect Effect (AIE) (as reported by the IPCC) are mainly caused by the complex relationships between aerosol activation of cloud droplets and chemico–physical parameters (such as the number concentration, size distribution and chemical composition of the aerosol particles acting as CCN)s [Ghan et al., 1993; Lohmann and Feichter, 2005; McFiggans et al., 2006].

Several attempts have been made in order to relate CCN and Cloud Droplet Number Concentration (CDNC) in models. Köhler [1936], presented the well known *Köhler Theory* linking cloud droplet formation and growth with thermodynamic variables (especifically the saturation vapour pressure). This theory is also used to determine whether or not a droplet is activated and, if so, whether it will grow spontaneously [Laaksonen et al., 1998; Pruppacher and Klett, 1978]. In this theory, the saturation ratio S_w of an aqueous solution droplet of radius r is given by:

$$S_w \approx 1 + \frac{a_w}{r} - \frac{b_s}{r^3} \tag{2.8}$$

where a_w is related to the surface tension (surface curvature) within the Kelvin Effect[1]; and b_s is related to the vapour pressure reduction due to the solute in the Raoult's effect[2]. The concept is: for each dry soluble particle size there is a critical super–saturation point (S_c) at which the difference between the Raoult and Kelvin effect is at the maximum; i.e., if the droplet grows bigger than the critical size r_c, the droplet will grow spontaneously if the ambient super–saturation is greater or equal to that given by Equation 2.8, unless super–saturation reduces at r_c [Laaksonen et al., 1998; Lee et al., 2010; McFiggans et al., 2006].

[1] See Andreae and Rosenfeld [2008] and Seinfeld and Pandis [1998] for more details on this effect

[2] *Ibidem*

Because *Köhler Theory* assumes that the amount of solute in the droplets is fixed and that the CCN is either a highly soluble solid substance (such as NaCl $(NH_4)_2SO_4$) or a highly soluble liquid substance (such as H_2SO_4), it was later extended by several authors to include other substances and factors affecting activation not yet accounted for [Asa-Awuku and Nenes, 2007; Chen, 1994; Conant et al., 2002; Kulmala et al., 1997a, 1996; Laaksonen et al., 1998; Sotiropoulou et al., 2007]. For instance, Kulmala et al. [1996, 1997b] have shown that, depending on the acidity, vapours can behave differently in particle formation, with more acidic vapours contributing to the formation and growth of particles strongly enough to change the Cloud Optical Depth (COD) under specific conditions. Laaksonen et al. [1998] modified the Köhler equation to include the effect of soluble gases and slightly soluble aerosol. Abdul-Razzak and Ghan [2000] presented a parameterisation of cloud droplet activation by multiple aerosol types, in which the ASD is represented as multiple externally mixed log–normal modes, each composed of a uniform internal mixture of soluble and insoluble material. The latter parameterisation has been further extended by the same authors [Abdul-Razzak and Ghan, 2002], using a sectional approach. The errors of both methods did not exceed 10% when compared to idealised cases. Henning et al. [2005] found that the particle phase was also an important factor for the critical super–saturation for the activation of solid particles and solution droplets.

Nenes et al. [2002] assessed the role of the aerosol chemical effect (dissolution of soluble gases and slightly soluble substances, surface tension depression by organic substances and accommodation coefficient changes) *vis–à–vis* changes in droplet number from changes in aerosol number concentration, and found certain conditions exist under which the chemical effect competes with the Twomey effect for cloud droplet activation. Conversely, using size–resolved measurements of cloud condensation nuclei (CCN) spectra in a non-urban location in Germany, Dusek et al. [2006] showed that 84 to 96% of the variation in CCN concentrations were mainly determined by the aerosol number size distribution.

The several approaches being used for representing cloud droplet activation as a function of aerosol number concentration, can be grouped into two basic methods:

(a) An empirical method, relating observed aerosol mass [Jones et al., 1994] or sulphate mass [Boucher and Lohmann, 1995] and droplet number concentrations. The limitations of this method are related to extent of accessible observational data to validate GCMs. Additionally, the established relationships relate only sulphate and

sea–salt to CDNC [Pringle et al., 2009; Rap et al., 2009] and have no information on the microphysics controlling the nucleation of cloud droplets;

(b) A mechanistic method of droplet nucleation, which uses a model to simulate the relationship between CDNC and aerosol particles and droplets, determined at cloud base, based on the microphysics of the processes involved Abdul-Razzak and Ghan [2000]; Pringle et al. [2009]. In this method, the change in CDNC is associated with change in the total aerosol concentration, size distribution, aerosol composition, updraft velocity and/or activation parameters, together with an approximate solution of the Köhler equation [Lohmann et al., 2000; Nenes and Seinfeld, 2003; Penner and Chuang, 1999]. The limitation of this method is related to the solution of the microphyical equations and with the unresolved cloud parcel updraft velocity [Pringle et al., 2009]

The most common relationship between aerosol number concentration and droplet concentration – the CCN spectra – is the power–law size distribution of aerosol particles, derived by Twomey [1959], which relates the production of super–saturation due to adiabatic expansion in a vertically moving parcel, and the number of droplets activated from the CCN phase [Feingold et al., 1998; Khvorostyanov and Curry, 2006; Seinfeld and Pandis, 1998]:

$$N_{CCN}(s) = Cs^k \tag{2.9}$$

where $N_{CCN}(s)$ is the number of droplets activated, s is the maximum super–saturation produced near cloud base, and C and k are parameters determined by experimental measurements [Feingold et al., 1998]. For instance, $s = 1$ corresponds to 1% super–saturation, and C is the CCN concentration activated at 1% super–saturation.

2.5 Aerosol removal processes

As stated in Section 1.1, aerosols have a limited residence time in the atmosphere, dependent on their size and location. Aerosol removal processes are commonly represented in climate models by two mechanisms: dry and wet deposition [Thomas and Schumann, 1991]. In the following two sections, a short description of these removal mechanisms is presented.

2.5.1 Dry deposition

The process in which aerosols (and gases) are removed from the atmosphere to the surface of the Earth by air motions is called dry deposition. The paper by Wesely and Hicks [2000] contains a good review of the current/recent knowledge of dry deposition. For simple applications, dry deposition speed v_d is commonly represented by a formula devised by Chamberlain [1967], which relates it to the mass flux F and the particle concentration C at a reference height (generally 10m) above ground surface.

$$v_d = -F/C \tag{2.10}$$

In climate models dry deposition speed v_d is represented as a flux of electrical current through resistances connected in series. One example of this type of models is given by Equation 2.11 [Hicks et al., 1987; Seinfeld and Pandis, 1998]:

$$v_d = \frac{1}{r_a + r_b + r_c} + v_g \tag{2.11}$$

where r_a is the aerodynamic resistance (a function of atmospheric turbulence) [Businger, 1986]; r_b is the so–called quasi–laminar resistance (a function of the molecular diffusion) Wesely and Hicks [2000]; r_c is the surface resistance (a function of the surface type, physical structure of the colliding particles, hygroscopicity and other physico–chemical properties). When gravitational settling is important (i.e., when particles deposit themselves immediately after colliding with the surface), the term representing the settling speed v_g is included in Equation 2.11. The surface resistance is the most complex of the resistances.

2.5.2 Wet deposition

This is a process by which particles are swept from the air by hydrometeors (rain, fog or snow) [Seinfeld and Pandis, 1998] and is also the most effective way by which particles are removed from the atmosphere [Loosmore and Cederwall, 2004]. Often, climate models parameterise wet deposition in terms of two processes, namely *In–cloud scavenging* and *Below–cloud scavenging* [Harrison et al., 2001; Jung et al., 2002].

2.5.2.1 In–cloud scavenging

Also called 'rainout', this form of scavenging consists of two processes: a) the nucleation of CCN in cloud droplets, and b) the incorporation of the non–nucleated fraction of aerosols

by hydrometeors [Seinfeld and Pandis, 1998]. The first, in which particles are captured as CCN is the most important mechanism for the wet removal of aerosol particles [Ebert et al., 1998; J.M. and Pacyna, 2008].

$$\Delta C_{wet} = -C\frac{W_{in}P}{\Delta z \rho_w} \tag{2.12}$$

2.5.2.2 Below–cloud scavenging

Or 'washout' – is when particles are captured by falling raindrops. Several authors have defined various parameterisation schemes used to describe the below–cloud scavenging. In a recent work, Duhanyan and Roustan [2011] give a detailed review of these schemes, in which variables such as the Raindrop Size Distribution (RSD), the terminal velocity of raindrops, the below–cloud scavenging coefficient for gaseous and particulate pollutants, and particle–size distributions are taken into account. For instance, below–cloud wet scavenging can be written as a first–order differential equation representing the depletion of the aerosol number concentration $N(r,t)$ with time as a function of a scavenging coefficient λ [Chate et al., 2003]

$$\left.\frac{dN(r)}{dt}\right|_{\text{Bel.Cld.Scav}} = -\lambda N(r,t) \tag{2.13}$$

where, for particles, the coefficient λ is a function given by

$$\lambda = \int_0^R \pi R^2 v_t(R) E(R,r) N(R) dR \tag{2.14}$$

where R and r are, respectively, the raindrop and scavenged particle radii (in µm); $v_t(R)$ (in ms^{-1}), is the raindrops terminal velocity; $E(R,r)$ is the collision efficiency of an aerosol particle – i.e., the probability for an aerosol particle of radius r to collide with a raindrop of radius R; and $N(R)$ (in m^{-4}) represents the raindrops size distribution.

As shown by Loosmore and Cederwall [2004], for instance, when rain rate

$$J = \int_0^R \frac{\pi}{6} R^3 v_t(R) N(R) dR$$

is taken into account, then

$$\lambda = \frac{3}{2}\frac{E(R,r)}{R} J, \tag{2.15}$$

where the terminal velocity from a particle with diameter D can be given by [Mircea and Stefan, 1998; Pruppacher and Klett, 1978]

$$v_t = v_t^{\text{ground}} \times \left[\frac{\rho_{\text{air}}^{\text{ground}}}{\rho_{\text{air}}}\right] \tag{2.16}$$

Different types of RSDs can be found in literature: Gamma; Weibull; and log–normal distributions [Seinfeld and Pandis, 1998]. The latter is the most commonly used form of RSD in climate modeling, and is represented by:

$$N(D) = \frac{C_{\text{tot}}}{D\pi\sqrt{2(\ln\sigma_g)^2}} \exp\left[-\frac{\ln D - \ln \overline{D}_g}{2(\ln\sigma_g)^2}\right] \tag{2.17}$$

where D_g is the geometric mean of the diameters D of the raindrops; C_{tot} is total concentration of the raindrops; and σ_g the standard deviation of the distribution.

2.6 Aerosol optical properties

As stated in the introduction, the transmission of radiation through an aerosol–laden medium, as well as the aerosol hydrodynamic characteristics, are highly dependent on the shape and size of the aerosols [Friedlander, 1977]. Thus, to assess the characteristics of the aerosol–radiation interaction, aerosol optical characteristics relevant to the absorption and reflection of radiation need to be known.

In climate models, attenuation of the radiation by aerosols is represented in terms of absorption and Mie diffusion. The Mie diffusion theory is applicable when the wavelength of the incident radiation is comparable in magnitude to the size of the scattering particle, which is the case with atmospheric aerosols [Seinfeld and Pandis, 1998]. Thus, the attenuation of radiation of wavelength λ traversing the atmosphere is given by

$$dI_\lambda = -\alpha_\lambda I_\lambda dS \tag{2.18}$$

where dS is the length of the medium traversed by a beam of intensity I, and α is the extinction coefficient of the medium. When the latter parameter is vertically integrated over a unitary cross–section column of path length L, it leads to the AOD or thickness τ

$$\tau_\lambda = \int_0^L \alpha_\lambda dS \tag{2.19}$$

in which $\tau = 0$ implies no reduction in intensity; $\tau = 1$ implies an e–fold reduction in intensity and $\tau \gg 1$ means the observer will detect almost zero intensity.

Other optical parameters exist for describing aerosol–radiation:

- Aerosol Index (AI);

- Ångström exponent (AE);
- Single Scattering Albedo (SSA);
- Asymetry Factor (AF).

AI signals the Ultra–Violet (UV)–absorbing aerosols such as dust and soot [D'Alessio et al., 1998; Herman et al., 1997]. If AI is positive absorbing aerosols (dust and smoke) are dominant; small or negative values relate to non-absorbing aerosols and clouds. In turn AE is the exponent (α) used to parameterise the relationship between aerosol size and dependence of optical depth on wavelength [Eck et al., 1999]:

$$\frac{\tau}{\tau_1} = \left(\frac{\lambda}{\lambda_1}\right)^{-\alpha} \text{and, thus } \alpha = -\frac{\ln\left(\frac{\tau}{\tau_1}\right)}{\ln\left(\frac{\lambda}{\lambda_1}\right)} \tag{2.20}$$

where τ and τ_1 are AODs at the wavelengths λ and λ_1, respectively. Eck et al. [1999] showed that, in general, if $\alpha \leq 1$, then aerosol size distribution is mostly dominated by mechanically generated particles (coarse mode), and if $\alpha \geq 2$, size distribution is dominated by fine mode aerosols (produced by BB and industrial activity).

The SSA, designated ω_o, is the fraction of the aerosol light scattering over the extinction [Hess et al., 2010]:

$$\omega_o = \frac{\sigma_s}{\sigma_a + \sigma_s}, \tag{2.21}$$

where σ_a and σ_s are the absorption and scattering coefficients. One of the most relevant optical properties of aerosols is ω_o because the direct radiative effect is very sensitive to SSA [Hong et al., 2009; Montilla et al., 2011].

The angular distribution of light scattered from aerosol particles is called the Aerosol Phase Function (APF). When radiation is scattered by aerosols, it then points to either forward or backward direction. The AF, designated as g, indicates the predominant scattering direction. Thus, if $g \approx 1$, radiation is mainly scattered in a forward direction; when $g \approx -1$, the backwards direction is predominant. When $g = 0$, it indicates isentropic scattering [Ebert and Curry, 1992; Kaufman et al., 1994]

The interaction of radiation with aerosols is represented in models by a Radiative Transfer Equation (RTE) [van De Hulst, 1981], in which the diffuse solar intensity I in plane–parallel atmospheres has the form

$$\mu \frac{dI(\tau,\mu)}{d\tau} = I(\tau,\mu) - \frac{\omega_o}{2}\int_{-1}^{1} I(\tau,\mu')P(\mu,\mu')d\mu' - \frac{\omega_o}{4\pi}\pi F_0 P(\mu,-\mu_0)e^{-\tau/\mu_0} \tag{2.22}$$

where $\mu = \cos\theta$, θ is the zenith angle, πF_0 the solar flux on TOA, μ_0 the cosine of the solar zenith angle θ_0.

Currently, there are dedicated computer codes for solving the RTE, such as the the DIScrete Ordinate Radiative Transfer model (DISORT) [Stamnes et al., 2000] and MODerate resolution atmospheric TRANsmission (MODTRAN) [Berk et al., 2009]. This type of code is too computationally demanding to be directly incorporated into climate modeling, particularly where the numerical integration of the Fourier components of the scattering phase function is concerned [Menghua and Wang, 2003].

Among the aspects which add complexity to the solution of the RTE, Eq 2.22 needs to be solved for: a) all levels of the atmosphere; and b) all the frequencies in the electromagnetic spectrum [Clough et al., 1992]. Thus, a major challenge for climate models is to devise simple yet accurate numerical solutions of Equation 2.22 without compromising the computational demands of the other components within the model [Joseph et al., 1976].

As a trade–off, climate modelers use several assumptions in order to analytically solve and incorporate the RTE in model calculations [Coakley et al., 1983; Meador and Weaver, 1980]. The most widely known approximations for the integro–differential RTE are the so–called Eddington and Two-Stream approximations (or variants thereof) [Coakley and Chylek, 1975; Joseph et al., 1976]. In other instances, lookup–tables are used by climate models as source of information on aerosol optical properties and volume fraction for every wavelength of the radiation [Levy et al., 2005; Menghua and Wang, 2003; Strow et al., 1998; Wong et al., 2009].

Chapter 3

Research Methodology

This study employs the ECHAM5-HAM to assess the impact of biomass burning aerosol loading on Southern African climate. While ECHAM5-HAM is the main focus of the work, the WRF/Chem Regional Climate Model (RCM) is sporadically used as a support model to help in analysis required in finer scales and short periods. The two models run online simulations of aerosol-radiation-cloud interactions with global and regional coverages, respectively. These models were chosen for their different levels of complexity in dealing with aerosol climate feedbacks: ECHAM5-HAM is a GCM able to recirculate aerosols globally, with parameterizations of gas-to-particle conversion processes. WRF/Chem is an RCM that depends on the boundary conditions created by a GCM; nevertheless, it is capable of creating aerosols not only through processes of nucleation, but also through chemical reactions.

3.1 Description of the models

3.1.1 The aerosol–climate GCM ECHAM5–HAM

The ECHAM5-HAM is the fifth-generation climate model developed at the Max Planck Institute for Meteorology (MPIMet) and is a state–of–the–art coupled climate–aerosol GCM. The model uses a hybrid sigma–pressure terrain–following vertical coordinate system [Simmons and Burridge, 1981], and a flux form semi-Lagrangian transport scheme by Lin and Rood [1996] is used to represent transport of scalars in the gaussian grid. Time integration is performed with a semi-implicit leapfrog scheme [Robert et al., 1972].

The dynamics and physical parameterisation of the model are imported from the 5th

Version of the European Centre Hamburg Model (ECHAM5) model [Roeckner et al., 2003] and the aerosol component utilised is from the Hamburg Aerosol Module (HAM) [Stier et al., 2005]. The latter is a double–moment modal aerosol microphysics scheme which predicts the aerosol mixing state in addition to the aerosol mass and number concentrations, together with modifications in the cloud microphysics scheme and different aerosol emissions on aerosol and cloud properties in the present-day climate and for estimates of the total anthropogenic aerosol effect [Lohmann et al., 2007; Stier et al., 2005].

The size distribution in the HAM is represented by a superposition of seven log–normal modes, where four size classes of median radii $\overline{r}_i$ [in µm] are for mixed particles grouped into nucleation ($\overline{r}_i \leq 0.005$), *Aitken* ($0.005 < \overline{r}_i < 0.05$), accumulation ($0.05 < \overline{r}_i \leq 0.5$), and coarse mode ($\overline{r}_i > 0.5$), and three are for the insoluble (*Aitken*, accumulation, and coarse modes), which include the major global aerosol compounds sulphate, black carbon, particulate organic matter, sea salt and mineral dust [Stier et al., 2005] and is given by Equation 3.1:

$$n(\ln r) = \sum_{i=1}^{7} \frac{N_i}{\sqrt{2\pi}\ln\sigma_i} \exp\left[-\frac{(\ln r - \ln \overline{r_i})^2}{2\ln^2\sigma_i}\right] \tag{3.1}$$

Its dynamical core – the ECHAM5 GCM – evolved from the ECMWF model and solves prognostic equations for vorticity, divergence, surface pressure, and temperature represented in spherical harmonics with a triangular truncation in order to provide uniform spacial resolution over the globe [Roeckner et al., 2003]. Interaction with radiation is as in Fouquart and Bonnel [1980] with 4 spectral bands: 1 for the visible and ultra–violet, and 3 for the near–infrared. For the longwave radiation, the model uses 16 spectral bands [Mlawer et al., 1997]. More details on the available model physical parameterisations can be found in Stier et al. [2005].

3.1.2 The aerosol–climate model WRF/Chem

The WRF/Chem is a fully coupled climate-chemistry model designed to simulate climate–air quality interactions [Grell et al., 2005]. Its dynamic core is based on the non-hydrostatic mesoscale Weather Research and Forecast Model (WRF) [see description in Skamarok et al., 2007]. As a further extension of the "meteorology-only" WRF, the model is also scalar preserving, uses the same horizontal and vertical grids as well as the same parametrisation schemes for microphysics, convection, PBL, Land–Surface Model (LSM) and radiation. The model uses a terrain–following hydrostatic pressure coordinate and the

grid staggering is the Arakawa C-grid. Time integration is performed with higher–order integration schemes, which include 2^{nd} and 3^{rd} integration schemes, and 2^{nd} to 6^{th} –order advection schemes in both horizontal and vertical directions Skamarok et al. [2007].

Since its release WRF/Chem has undergone complex improvements in aspects such as gas–phase chemistry, aerosol treatments and photolysis scheme [Chapman et al., 2009; Fast et al., 2006; Gustafson et al., 2007]. The version 3.1.1 of the WRF/Chem used in this work comprises several coupled processes as emission, transport and deposition of chemical species; aerosol–climate interactions; photolysis; and radiation. The model applies the second–moment microphysical scheme of Lin et al. [1983] to derive prognosis of cloud droplet activation as a function of the ASD. Detailed description of the WRF/Chem model can be found in Grell et al. [2005].

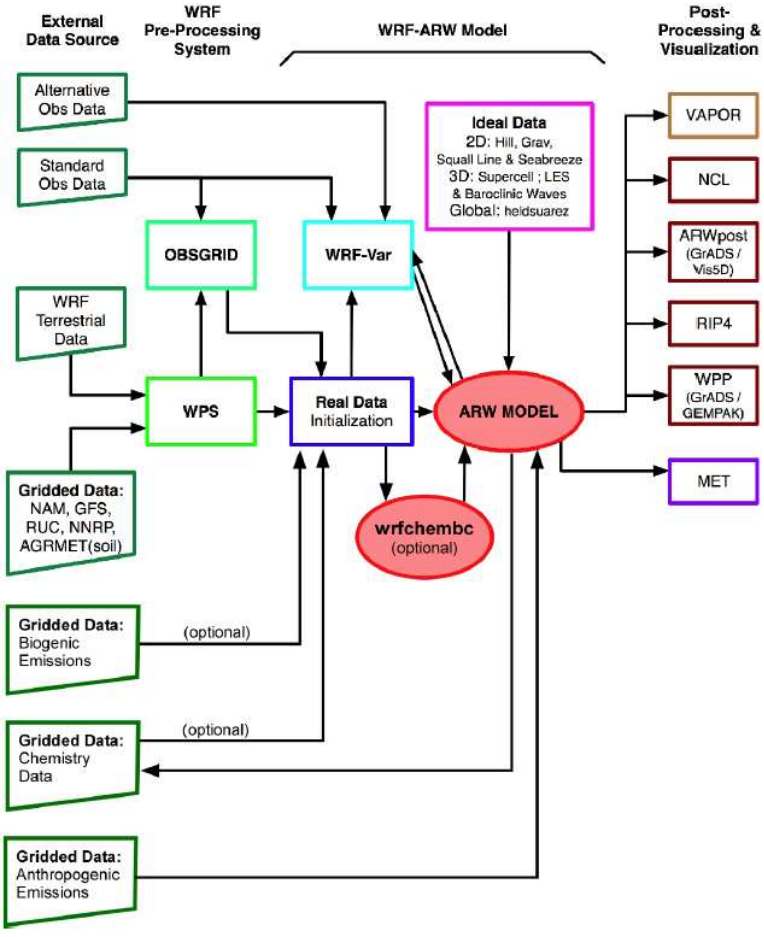

Figure 3.1: Structure of the WRF/Chem modeling system. From Peckham et al. [2010]

Figure 3.1 shows a schematic diagram of the WRF/Chem modeling system, which is composed by the WRF Pre-processing System (WPS); the WRF solver with chemistry; and the Post-processing and visualization tools. Aerosol size distriubution in WRF/Chem is

represented by a superposition of two overlapping modes of log–normal distributions given by the same distribution as in Equation 3.1. Description of additional processes such as nucleation, condensation, and coagulation as well as photolysis can be found in Grell et al. [2005].

3.2 Models setup and datasets

3.2.1 ECHAM5-HAM setup

ECHAM5-HAM is set to cover the whole globe and the period covered spans 1991–1996. Figure 3.2 shows the model domain used in these experiments. The resolution used in this work is L31/T63, which corresponds to a horizontal resolution approximately equivalent to 1.8×1.8 degrees and 31 hybrid sigma–pressure vertical levels from surface to 10 hPa.

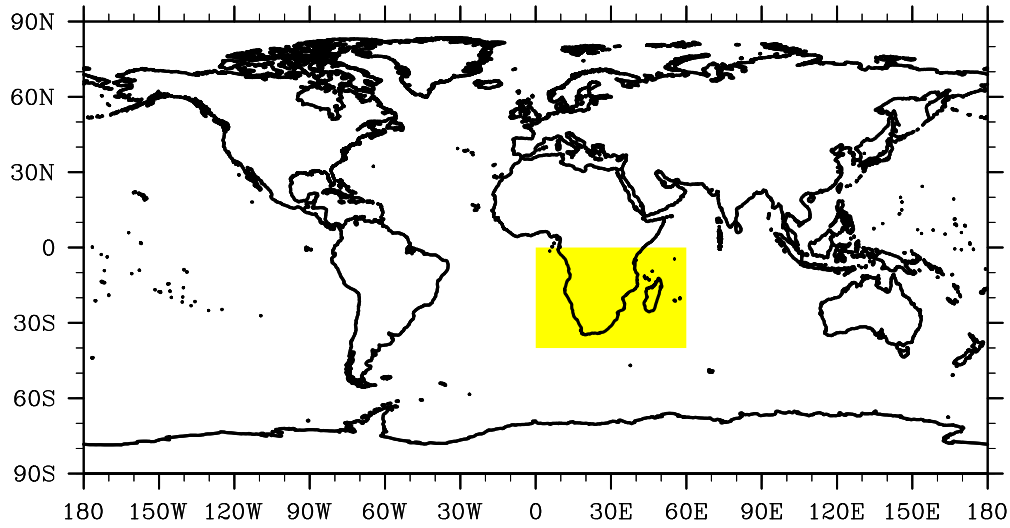

Figure 3.2: Domain size of ECHAM5-HAM. Box in yellow shows study area, where modification of wildfire emissions occur.

The model is run under four different wildfire aerosol emission settings summarised in Table 3.1. The use of each model to obtain desired results is described in Section 3.3. The simulations cover a six–year period, from 1991 to 1996, however, January to November 1991 results are considered adjustment period and, thus, not used in the analysis. The intention of using this period was to omit the ENSO signal (rainfall in particular) on the aerosol emissions [Tosca et al., 2010; Tummon, 2010] as this signal is the most dominant mode of climate variability over the region [see for example Janowiak, 1988; Nicholson and Entekhabi, 1986; Richard et al., 2000]. 1991 to 1996 is the longest period available

Table 3.1: Configuration of simulations of ECHAM5–HAM.

Simulation	Description
GLBLBB0	Global emissions from nature (volcanoes, lightning induced forest fires, desert dust, sea spray and natural emissions from vegetation); Global anthropogenic emissions from industrial activities; GFED emissions set to nil globally
GLBLBB1	Global emissions from nature; Global anthropogenic emissions from industrial activities; GFED emissions exist globally
RGNLBB0	Global emissions from nature; Global anthropogenic emissions from industrial activities; GFED emissions exist globally except for the shaded region shown in Figure 3.2

within the ECHAM5–HAM initial and boundary conditions received by the author from the MPIMet, in which the atmospheric aerosol layers are not likely to be removed by wet deposition and, therefore, their interaction with climate is not perceived.

The AEROCOM anthropogenic and BB emissions for year 2000 [Dentener et al., 2006] are used as source of information on emissions. These emissions use year 2000 monthly mean values as reference for all years, i.e., there will be no interannual variation of monthly emissions. The BB emissions are from the GFED database and are composed of BC and POM aerosols, as well as the sulphate aerosol precursor SO_2. The ECHAM5-HAM model is driven by prescribed SSTs and sea ice are based on the climatological data from the Atmospheric Model Inter-comparison Project 2 (AMIP2) [Gates et al., 1999]. A surface mixed-layer is coupled to the interior ocean in order to represent near–surface vertical mixing and to improve the response time-scales to atmospheric forcing, such as the aerosols, which is controlled by the mixed-layer thickness [Roeckner et al., 2003].

Differences between variable magnitudes in the GLBLBB1 and GLBLBB0 simulations give the impact of global BB on these variables; differences between variables in GLBLBB1 and RGNLBB0 give the impact of regional BB on the variables.

3.2.2 WRF/Chem setup

As an RCM, WRF/Chem is configured to cover the shaded region shown in Figure 3.3. This figure shows vegetation fraction valid for November 2001. Dimensions are 99 gridpoints

on the south–north direction, 137 on the west–east direction and 27 vertical levels, with a spatial resolution of $60\text{km} \times 60\text{km}$, in polar stereographic projection. These dimensions were chosen in order to optimise computation demand and model output data size. The model is set to run with adaptive time–step to guarantee numerical stability throughout the simulation [Hutchinson, 2005], and the map projection is set to polar stereographic to comply with one of the requirements of using global emissions data sets and/or wildfire emissions in this version of the model [as described in Peckham et al., 2010].

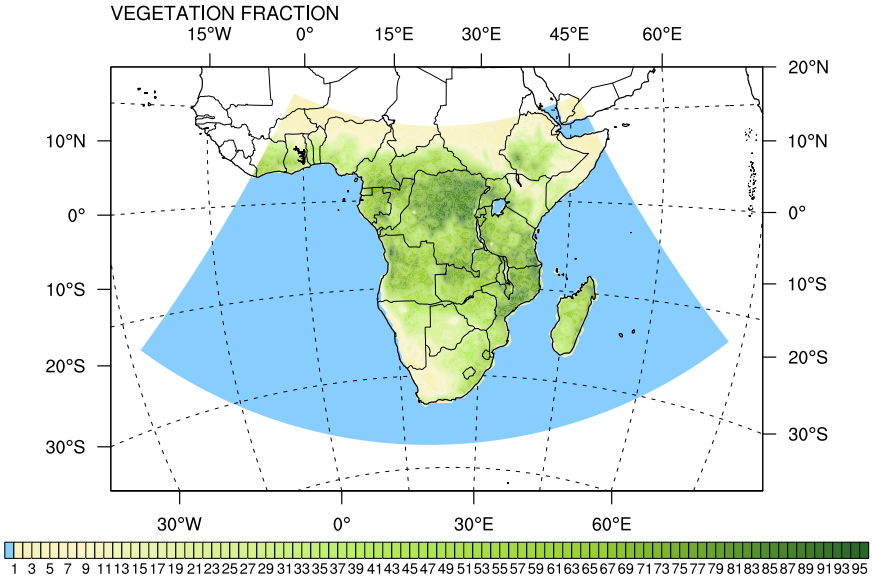

Figure 3.3: WRF/Chem model domain location in polar stereographic map projection. Shaded region over the continent depicts Leaf Area Index (LAI) for November 2001.

The WRF-Chem V3.1 model is forced by NCEP/DOE Reanalysis-II data [Kanamitsu et al., 2002] and SSTs from the weekly 1° spatial resolution Optimum Interpolated (OI) SST analysis from National Oceanic and Atmospheric Administration (NOAA) [Reynolds et al., 2002]. This version of WRF–Chem includes three LSM schemes, from the simple Soil Thermal Diffusion (STD) to the Noah LSM [Ek et al., 2003] and the Rapid Update Cycle (RUC) [Smirnova et al., 2000; Smirnova et al., 1997]. In our case, soil moisture estimates are based on model generated soil moisture fields from Noah LSM [Ek et al., 2003], a scheme with four temperature and moisture layers (with thicknesses of 10, 30, 60 and 100 cm) and fractional snow cover and frozen soil physics[1]. Although it is acknowledged that

[1]A comparison of the performance of available LSM schemes in WRF was carried out by Jin et al. [2010] over the United States of America

the performance of an LSM over a region is highly influenced by the available input fields and the highly variable surface water and energy states at the beginning of the simulation [Rodell et al., 2005], the Noah scheme option is used for it has extensively been tested and operationally used at the National Centers for Environmental Prediction (NCEP). The Noah LSM has 1 vegetation type per grid cell and uses monthly Normalized Difference Vegetation Index (NDVI) to represent seasonal vegetation dynamics. It uses initial conditions provided by the WPS to prognose total and liquid soil moisture and surface and skin temperatures in each layer by solving Eqs 3.2 and 3.3:

$$\frac{\partial \theta}{\partial t} = \frac{\partial}{\partial z}\left(D\frac{\partial \theta}{\partial z}\right) + \frac{\partial K}{\partial z} + F_\theta \tag{3.2}$$

$$C(\theta)\frac{\partial T}{\partial t} = \frac{\partial}{\partial z}\left(K_t(\theta)\frac{\partial T}{\partial z}\right) \tag{3.3}$$

where, where D, K, C and K_t are functions of soil texture and moisture and F_θ represents sources (rainfall) and sinks (evaporation) of moisture.

The WRF-Chem model is tuned with chemistry options and physical schemes which parameterise both the effects on radiation and on clouds, as shown in Table 3.2. The monthly averaged 1×1 degree Global Fire Emissions Database Version 2 (GFEDv2) [Randerson et al., 2005] from `http://daac.ornl.gov/` is used as source of information on regional emissions from vegetation fires. This dataset covers the time period January 1997 – December 2006, and is pre–processed to fit model settings by a special tool named `PREP-CHEM-SRC`, documented by Freitas et al. [2011]. Aerosols generated by global emissions and brought into Southern Africa through long–range transport mechanisms are provided by the GOCART model [Chin et al., 2000], referred to in Chapter 2. GOCART is a global three-dimensional chemistry–transport model, with a horizontal grid resolution of $2.5^\circ \times 2.5^\circ$, with 20–55 layers in the vertical. The model solves equations for advection, turbulent mixing, moist convection, dry deposition, wet removal and chemical transformations. Emissions treated in the model include sulfate precursors, organic carbon, black carbon, mineral dust and sea–salt particles.

Figure 3.4 shows 1997–2006 monthly OC emission anomalies from the GFEDv2 datasets for the region shaded in yellow in Figure 3.2. This figure is generated to help identify the simulation period. In this work, the period in which the emissions build up, reach their peak, and dissipate is targeted. The model is thus set up to simulate JJA and SON seasons,

Table 3.2: Summary of schemes used by WRF/Chem.

Process	Option/scheme
Convection	G3 – Improved Grell and Dévényi [2002]
Photolysis	Fast-J by Wild et al. [2000]
Shortwave radiation	Goddard Shortwave Scheme [Max and Suarez, 1994]
Longwave radiation	Scheme from CAM
Cloud microphysics	Lin et al. [1983]
PBL	Asymmetric Convective Model (ACM2) by Pleim [2007]
Land–surface	Noah LSM by Ek et al. [2003]
Cloud chemistry	TRUE

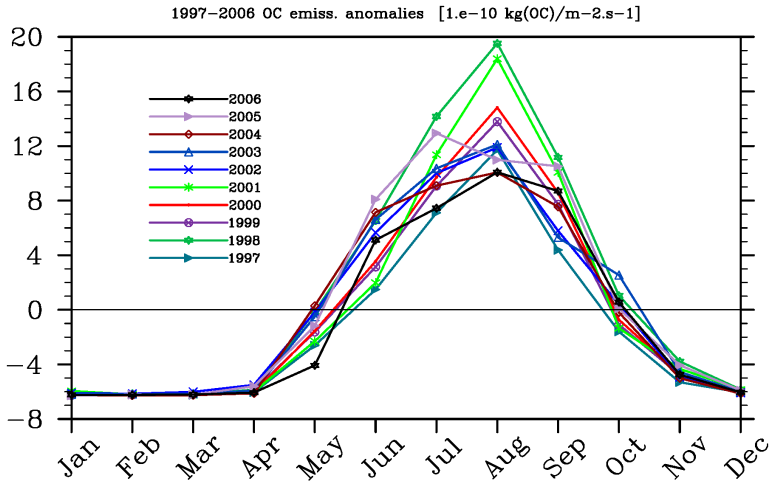

Figure 3.4: Ten-year (1997–2006) averaged emission anomalies of OC in Southern Africa (shaded region in Figure 3.2), based on GFEDv2 data.

including a spin–up period of 1 month (results of May are not used in the analysis).

In this part of the work, WRF/Chem simulation year is 2001, unambiguously one of the years with the highest emission rates in this period according to Figure 3.4. Two simulations are performed with prognostic cloud droplet number included in the microphysics (i.e., the indirect effect) namely

(a) WRF/Chem with BB aerosol emissions from GFED (`WRFCHEMBB1`)

(b) WRF/Chem without BB aerosol emissions (`WRFCHEMBB0`)

Differences between variable magnitudes of the `WRFCHEMBB1` and `WRFCHEMBB0` simulations give the impact of BB on these variables.

To increase the existing model complexity in WRF/Chem, gas–phase chemistry mechanism is turned on so that secondary aerosol formation is allowed during the simulations. The chosen mechanism is Carbon Bond Mechanism–Z (CBMZ) [Zaveri and Peters, 1999] combined with MOSAIC using the maximum number of sectional aerosol bins allowed (i.e., 8), including some aqueous reactions.

3.3 Methods

Verification of the models

Root Mean Squared Error (RMSE) and correlation maps are used to verify model performance against observed temperature and precipitation data in Southern Africa in monthly, seasonal and annual scales. Model performance for temperature and precipitation are compared to the corresponding $0.5^\circ \times 0.5^\circ$ resolution of the University of East Anglia Climate Research Unit (CRU) [Mitchell and Jones, 2005] gridded datasets. Although there are indications of biases of $0.5^\circ - 1.3^\circ$C and $10 - 25\%$ for temperature and precipitation respectively [see New et al., 1999, 2000], at the time the work was carried out, CRU datasets were the standard alternative to the both spatially and temporally scarce observed climate for some regions of the world and are found to be the datasets models are mostly verified with [see Giorgi et al., 2004; Tadross et al., 2006, for example]. WRF model performance over Southern Africa has extensively been verified against observed data by Crétat et al. [2012].

Observed datasets are regridded to the models' resolutions before any comparison is performed. Model AOD is compared to that observed by the ground–based global AErosol RObotic NETwork (AERONET) [Holben et al., 2001] available at `http://aeronet.gsfc.nasa.gov/`. This network, working since 1993, uses ground–based measurements of sun–photometers to measure extinction of incoming solar radiation by atmospheric pollution, and thus, determine AOD and AE, as shown in Section 2.6. Although it represents point observations, it is a quite well established quality assured dataset, validated in many regions of the world, and even used to validate products of the emerging airborne counterparts and models at the reference wavelength of 550nm [see Holben et al., 2001; Kim et al., 2008; Popp et al., 2007, for instance]. AERONET observations and model AOD are compared by their corresponding Probability Distribution Functions (PDFs).

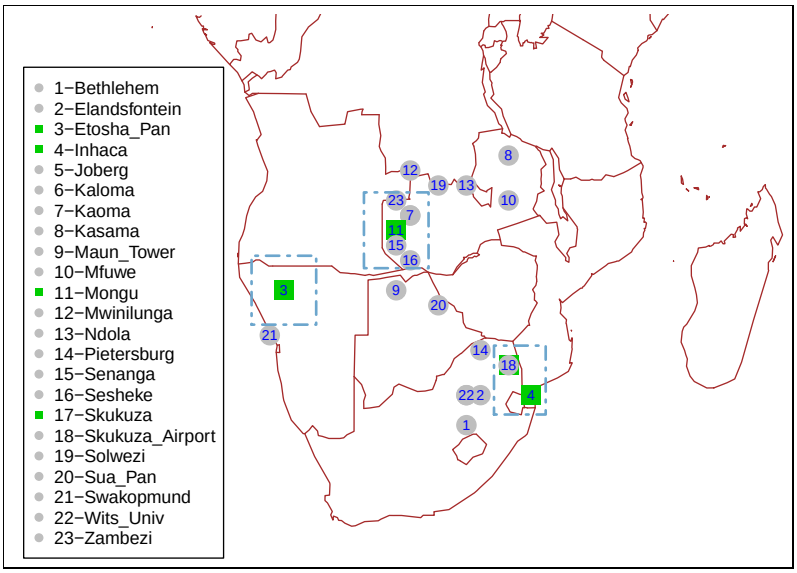

Figure 3.5: Available AERONET sites in Southern Africa. Green squares indicate the stations used to verify WRF/Chem model performance and light–blue rectangles around these are the areas where ECHAM5–HAM simulated AOD is compared to MODIS observations.

Over the continental Southern Africa, AERONET has 23 observing stations as shown in Figure 3.5, and most of them were set up on a permanent basis around the year 2000 during the SAFARI2000 project. For the current study only four sites in Southern Africa are used, namely Inhaca, Skukuza, Etosha and Mongu for they have relatively good temporal data coverage for 2001 (these stations are indicated in the map with green squares). Thus, only WRF/Chem results are compared to observed AOD, applying linear interpolation from model grid cell to AERONET station coordinates and, afterwards, comparing histograms of model interpolated daily data with observations to assess similarities on their probability distributions functions. Scatter plots are also drawn to indicate correlations between observed and modeled data.

The advent of satellite–based measurements of aerosol properties over southern Africa allows a refined spatio–temporal verification of simulated datasets. Thus, in order to assess how `GLBLBB1`, `WRFCHEMBB1` and `WRFCHEMBB0` settings of the models simulate AOD in the region, they are compared to the Moderate Resolution Imaging Spectroradiometer (MODIS) products. The MODIS instruments, launched in December 1999 onboard Terra Earth Observing System (EOS) platform and in May 2002 onboard Aqua spacecraft retrieve aerosol and cloud optical properties globally. Validation of MODIS products over land in Southern Africa using AERONET ground–based station data, as well as the retrieval

algorithms used by the former can be found, for example, in Platnick et al. [2003], Remer [2005], and Ichoku et al. [2001].

Because of the unavailability of systematic observations of AODs over Southern Africa for the 1991—1996 period, the performance of the `GLBLBB1` setting of the model in simulating AOD over this region is evaluated by comparing seasonal climatologies of 1991—1996 simulations with 2001–2010 MODIS observations, as well as monthly climatologies in the areas enclosing Inhaca, Skukuza, Etosha and Mongu AERONET stations, using box-and-whisker plots. This poor man's approach is considered valid for this purpose as the AOD climatology is somehow known and documented, with little interannual variability [Queface et al., 2011]. WRF/Chem settings of the model are also compared to MODIS observed AOD through spatial maps as well as scatter plots [King et al., 2003].

A tool devised by Taylor [2001] – the *Taylor Diagrams* – able to derive information about pattern similarities among variables without spatial and/or temporal restrictions, by geometrically mapping a statistical summary of variable intercorrelation, RMSEs and ratio of respective variances on the same 2–dimensional diagram is also used in this part of the work to compare WRF/Chem simulated AOD against their corresponding observed MODIS datasets.

Identification of the local and external sources to BB aerosol concentrations in Southern Africa.

In this section, seasonal maps of GFED emissions of carbonaceous aerosols – used as tracers of biomass burning – are employed together with modeled transport pathways, to identify the sources of the carbonaceous aerosol burden found over Southern African atmosphere.

Firstly, the study investigates causal relationship between regional emissions and aerosol concentrations, and their links to the resultant AOD. Thus, intra-annual plots of area averaged regional aerosol emissions and concentration for the *Aitken*, accumulation and coarse mode aerosols are produced, including the resultant AOD (for the three ECHAM5-HAM simulations). These graphs are then employed to identify common trends in the variables aforementioned. It is expected that fluctuations of these variables follow a same trend.

Should an asynchronous peak of aerosol concentration (i.e., outside of the regional

aerosol emissions season) appear on any of the modes, then it is assumed as an external contribution to the aerosol burden. Zonally averaged vertical cross sections are employed to identify the altitudes where largest aerosol concentrations occur. Once the levels of maximum concentrations are identified, both vertical and horizontal winds overlaid onto aerosol concentrations are plotted. These plots give an indication of the local and external sources and transport mechanism of the BB aerosol burden found in the regional atmosphere at these levels.

Identification of synoptic conditions favourable for high atmospheric aerosol concentrations in Southern Africa

Synoptic conditions favourable for high atmospheric aerosol concentrations in Southern Africa are identified with the help of a neural network technique – Self–Organising Maps (SOMs) [Kohonen, 1982] – which is applied in several areas of research in order to reduce to human–readable dimensions the high dimensionality of data, while maintaining the structure of the data.

The SOM technique uses unsupervised learning Artificial Neural Network (ANN) algorithms to recognize data patterns, by keeping similar patterns adjacent to one another, while keeping very different types apart in the maps [see Hewitson and Crane, 2002, for instance]. The SOM technique is widely used in different areas and it has been demonstrated that it is more robust in extracting variability patterns than other clustering techniques such as the Empirical Orthogonal Function (EOF) or Principal Component Analysis (PCA) [see Liu et al., 2006; Reusch et al., 2005].

Crane and Hewitson [1994], Cavazos [2000] and Hewitson and Crane [2002], for instance, have extended the application of the SOMs by using them to identify the primary features of the synoptic-scale circulation over a region.

In this work, Sea–Level Pressure (SLP) is used as a proxy for regional atmospheric circulation as it was shown to be a good indicator of regional climate [Tyson et al., 1996a,b]. and trained together with modeled carbonaceous aerosol concentrations from the GLBLBB1 simulation, using the super–SOM algorithm, which is an extension of the SOM that allows multiple data layers to be trained at once after being normalised. A weighted distance over all layers is calculated to determine the winning units during training. Resulting SOMs maps are used to identify which circulation patterns prevail when aerosol concentrations

are high and the opposite. Detailed description on the implementation of the SOM training algorithm can also be found in Sang et al. [2009]. In this work, a 12-node SOM is used as this size is able to adequately represent all synoptic types in the region, as suggested in the latter reference. Data is trained in fifty thousand (50000) iterations until nodes converge and no significant changes in distances between the nodes are seen during the training process. Histograms of number of days mapped in each archetype per month for the modeling period as well as the average annual frequency of months with high carbonaceous aerosol mixing ratios averaged over nodes of concern are presented.

Daily averaged Geopotential heights and vorticity, wet and dry deposition velocities, as well as the SLP used before to train the SOMs, are extracted from the SOM nodes in which carbonaceous aerosols are widespread in the subcontinent, and are used to determine their partial impacts on carbonaceous aerosol concentrations. This is done by applying Generalised Additive Models (GAMs), which are mechanistic regression models in which the common linear predictors $\eta = \sum \beta_j X_j$ used in regression analysis, are replaced by splines of the form $\sum s_j(X_j)$ [Hastie and Tibshirani, 1986], in which s_j are smoothed exponential functions obtained from an automated scatter–plot smoother algorithm.

The GAM technique allows for complex relationships among variables to be unveiled without the requirement of prior knowledge of their structural linking mechanism and has broadly been used in several epidemiological studies to evaluate dose–response relationships [see Benedetti and Abrahamowicz, 2004; Preisler, 1989, for example], and is gradually being used in air pollution research [see Aldrin and Haff, 2005; Carslaw et al., 2007; Pearce et al., 2011a,b], where pollution concentrations are modeled as a function of meteorological variables written in the form:

$$\log(y_i) = \sum_{j=1}^{n} s_j(x_{ij}) + \epsilon_i \tag{3.4}$$

where y_i is the concentration at the i$^{\text{th}}$; $s_j(x_{ij})$ is a smooth function of covariate j, n is the total number of covariates, ϵ_i is the i$^{\text{th}}$ residual; and var(ϵ_i)=σ^2, assumed to be normally distributed.

Replacing the variables in Equation 3.4, the logarithm of carbonaceous aerosol mixing ratios is modeled as the sum of smoothed functions of the variables aforementioned and takes the form:

$$\log(\text{Mix.ratio}) = s(day) + s(SLP) + \sum_{i=1}^{n}[s(GPT) + s(SVO)] + s(WETDEPO) + s(DRYDEPO) \tag{3.5}$$

where $s(day)$ is the calendar day, introduced to account for seasonality and long–term trends [see Carslaw et al., 2007, for instance]; SLP is the sea level pressure; GPT and SVO are the geopotential heights and vorticity at the levels of interest (n); $WETDEPO$ and $DRYDEPO$ are the wet and dry deposition velocities. The logarithmic function for the predictand was used as, according to Aldrin and Haff [2005], for example, it ensures data to be evenly distributed and that predicted values are positive in the original scale.

Estimation of potential feedbacks between BB aerosols, the thermal structure, atmospheric circulation and precipitation development

To assess feedbacks between BB aerosols, the thermal structure, the atmospheric circulation and the precipitation, differences between the `GLBLBB1` and `RGNLBB0` simulation results are used.

In this part of the work, changes in the radiative impacts are presented alongside fire–induced changes of temperature, vertical velocity, aerosol number concentration and cloud cover are presented for the months with positive aerosol emission anomalies (identified by the SOM procedure).

SLP, temperature and precipitation patterns are investigated in both intra– and interannual time scale.

For atmospheric circulation and precipitation, the analyses are extended to a seasonal scale, making it possible to assess the change in the regional atmospheric dynamics caused by BB–induced changes in the radiative forcing over the region.

Chapter 4

Evaluation of models' performances against observations

In this section, the GLBLBB1 setting of the simulations is compared to the mean observed temperature and precipitation data from CRU [Mitchell and Jones, 2005]. Spatial and temporal analyses of both simulated and observed climate are plotted; RMSEs and correlation maps between the two are used to assess ECHAM5-HAM's performance in intra– and inter–annual scales. WRF/Chem simulated AOD is compared with both MODIS and AERONET observed AODs.

4.1 Comparison of ECHAM5-HAM with CRU temperature

The ability of the GLBLBB1 setting of the ECHAM5-HAM in simulating observed annual mean temperature is shown in Figure 4.1. The CRU observed annual mean temperature is shown in Figure 4.1a; the differences between GLBLBB1 simulated and CRU observed mean surface temperature are shown in Figure 4.1b. In Figure 4.1c, RMSE between simulated and observed mean surface temperatures are presented; Figure 4.1d shows the correlation map between simulated and observed values for the same variable.

Simulated spatial patterns of temperature somewhow match observations, with the module of the deviations mostly found below 1.5°C. Highest mean observed annual temperatures were around 25°C degrees over DRC, parts of Mozambique, Botswana and in regions following the bordering region between Zimbabwe and Zambia. Lowest values

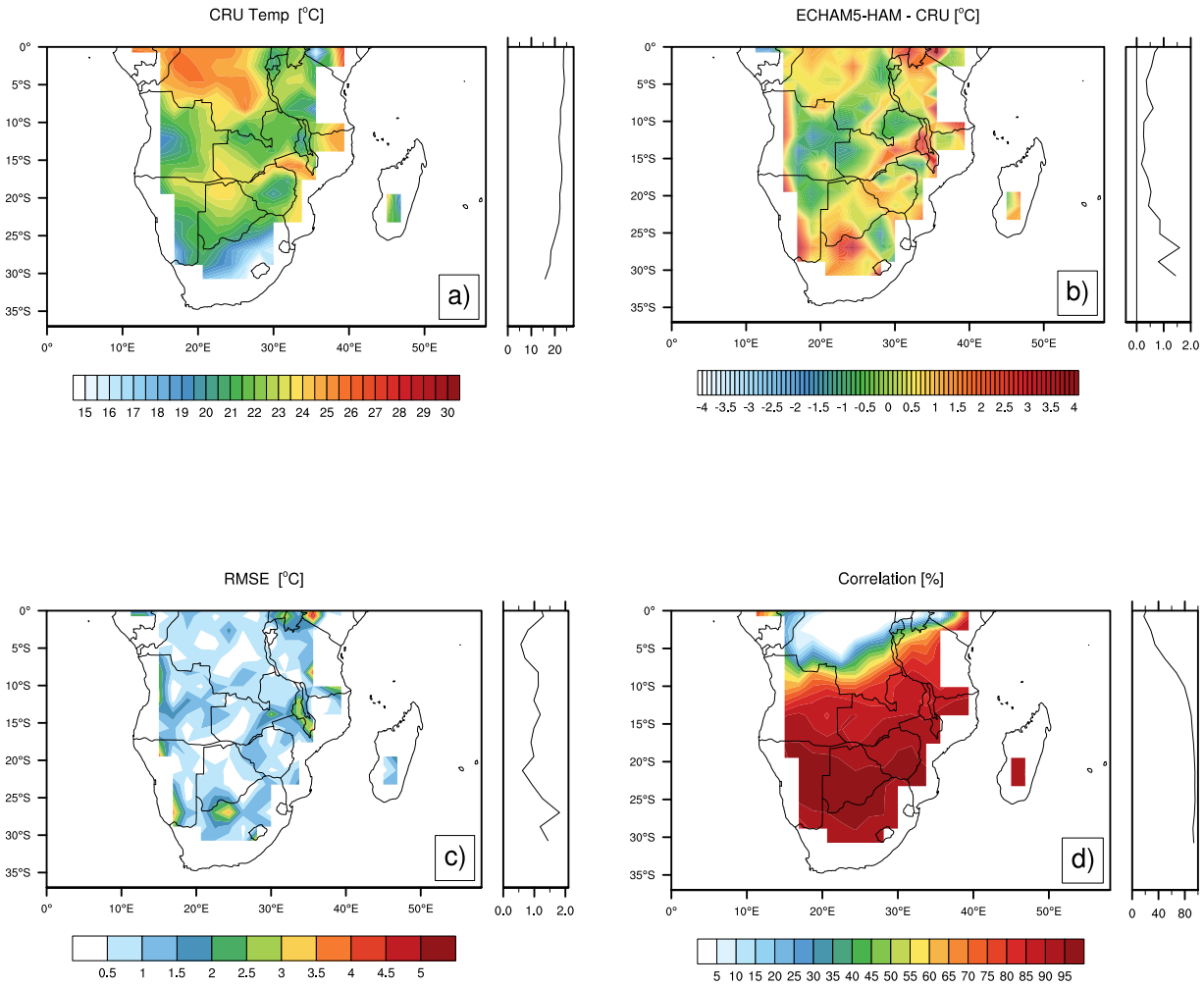

Figure 4.1: Comparison of simulated and observed annual mean temperature, including the corresponding zonal means. a) CRU observed; b) `GLBLBB1-CRU` simulated; c) RMSE between simulates and observed mean annual surface temperatures; and d) temporal correlation map between simulated and simulated and observed mean surface temperature.

of around 15°C were seen over the Drakensberg mountains in South Africa and Lesotho. A slight positive model bias of 1–2°C in magnitude, especially over the desert region in southern Namibia and also in parts of Zimbabwe and Tanzania, was also seen.

Analysis of the RMSE between simulated and observed mean temperature (Figure 4.1c) indicated that the model was able to capture the spatial pattern of mean temperature, showing a generalised pattern of average error of less than 2°C for the interior of the region; a larger value of RMSE was seen over the western part of south Africa and the west coast of the subcontinent, over the Namib Desert.

The model/observation correlation map of annual mean temperature (Figure 4.1d) shows values above 90% below 15°S; between 80% and 90% over parts of Angola, Zambia,

Malawi, northern Mozambique and Tanzania. However, this setting of the model poorly correlated to observed temperature data over most of the DRC, where negative correlations of up to 10% were observed. This is an expected result, as stated in Section 3.3, because this is a region of the world where observed climate data barely exist, leading to large uncertainties when comparison of observations and simulations is concerned.

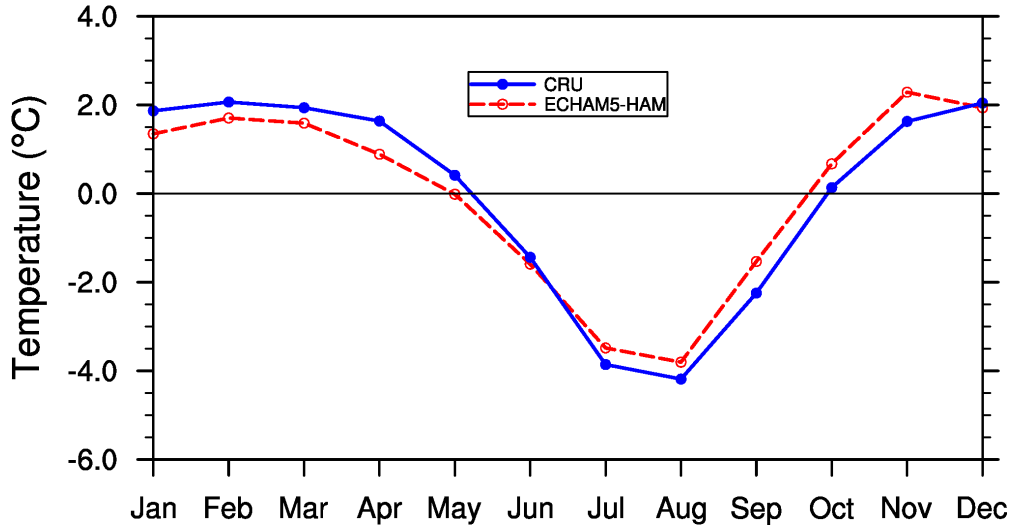

Figure 4.2: Simulated and observed monthly mean values of surface temperature deviations over land in Southern Africa averaged over 1991–1996. Simulated values are in a red dashed line and CRU–observed are in a blue solid line. The domain of comparison is comprised between 37°S – 0°S and 0°E – 60°E.

The deviations from the climatological monthly mean values of ECHAM5-HAM–simulated and CRU–observed surface temperature for the domain comprised between 37°S – 0°S and 0°E – 60°E are shown in Figure 4.2. The `GLBLBB1` setting of the model was able to capture the seasonality of mean temperature over the study region. The magnitude and signal of the simulated temperature deviation is very close to the observed values. The model exhibits a cold bias of around 0.5° between December and June, and a positive bias of the same magnitude over the rest of the year. Largest model deviations occur namely in April and November, when bias reached approximately –1°C and +1°C, respectively.

In Figure 4.3, seasonally averaged temperature differences between simulations and observations are shown, together with the corresponding zonal averages.

The predominant feature showed by the model in DJF and MAM was a slight cold bias of approximately 2°C over the central regions of the subcontinent, especially in parts of Namibia, Angola, southern DRC, western Zambia and a localized region in northern South

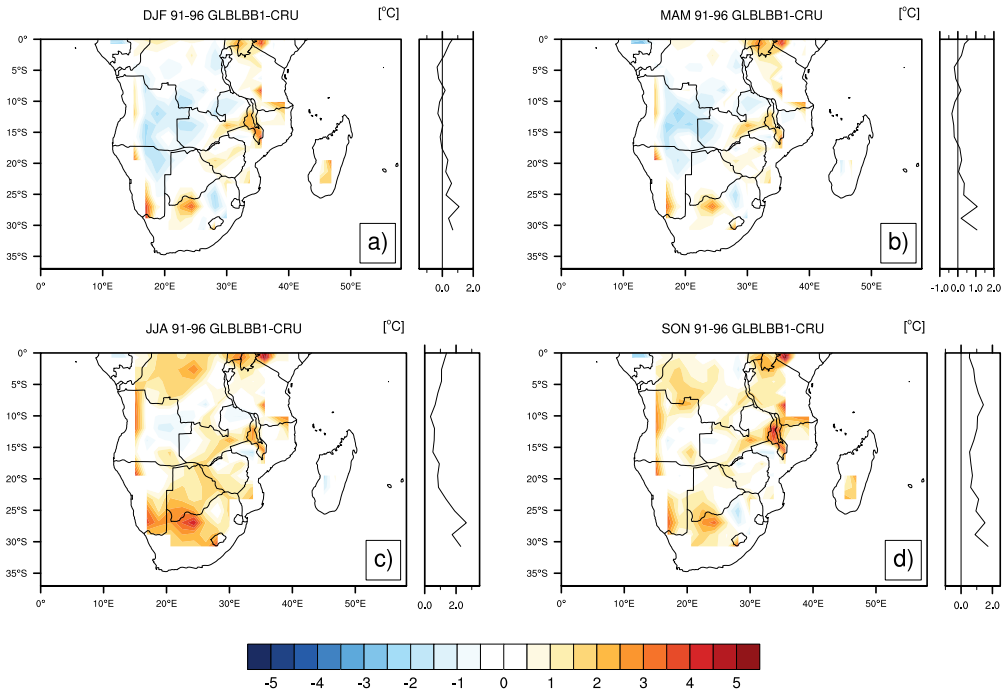

Figure 4.3: Seasonally averaged temperature differences between simulations and observations and corresponding zonal means for a) DJF; b) MAM; c) JJA; and d) SON seasons.

Africa. Zonally averaged temperatures for DJF and MAM seasons indicated a slight warm bias of less than a degree between 20°S–30°S, mainly caused by the model overestimating temperatures over north-western South Africa, and the Namib Desert. During JJA and SON seasons, the model showed a scattered pattern of a warm bias, with the JJA simulated temperature bias being more pronounced (especially over central and north-western South Africa) than the bias noted during SON.

Figure 4.4 shows the annual cycle of simulated (in red, dashed line) and observed (in blue, solid line) mean temperature for Southern Africa, over the five years analysed. The model and observations seemed to agree on the pattern of warm and cold cycles; however, while the model indicated annual mean winter temperatures would be between 17.5°C and 18.5°C, the actual observed temperatures were slightly warmer (between 18.5°C and 19.5°C). In relation to annual mean summer temperatures, no significant differences were devisable from the graph, with the exception of the summer of 93/94 when the model exhibited a cold upwards bias of approximately -1°C when compared to the observed data.

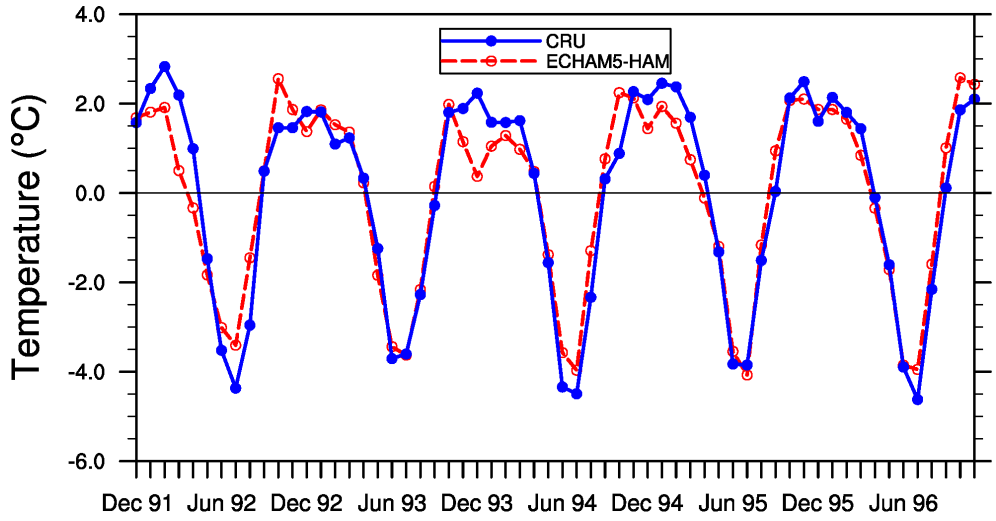

Figure 4.4: annual cycle of simulated (in red, dashed line) and observed (in blue, solid line) mean temperature for Southern Africa, over the five years analysed

4.2 Comparison of ECHAM5-HAM with CRU precipitation

Figure 4.5 shows the capability of the GLBLBB1 setting of the ECHAM5-HAM for simulating observed annual mean precipitation. Model simulated annual mean precipitation is shown in Figure 4.5a; the CRU observed annual mean precipitation is shown in Figure 4.5b. In Figure 4.5c, RMSE between simulated and observed annual mean precipitation are presented; Figure 4.5d shows the correlation map between GLBLBB1 and CRU values for the same variable.

Spatial distribution patterns of precipitation for both a) simulated and b) observed cases generally match in space and magnitude. In terms of magnitude, simulation and observation identify the same locations of minimum annual precipitation values: The lowest minimum precipitation areas (less than 200mm/yr) are located over the southern regions of the Namib and Kalahari deserts. For the maximum precipitation values, the model highlighted the wettest region as that within 15°E–30°E and spanning 15°S to the North of the study domain (with rainfall above 2000mm/yr); the observation depicted two regions as the wettest: one with mean annual rainfall close to 1600mm/yr, located within a zonal band between 15°S and 10°E stretching across from central Angola, crossing Zambia and ending in Tanzania and northern Mozambique; the other, with values around 400mm/yr higher that the previous, located over northern DRC and northwards.

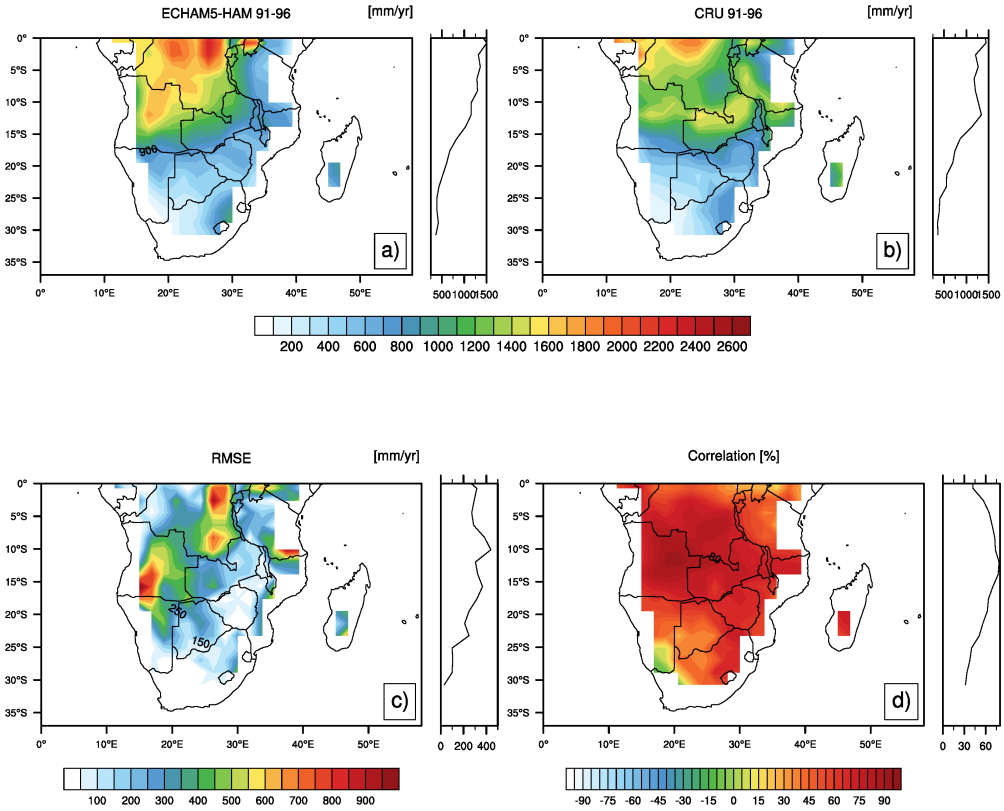

Figure 4.5: Comparison of 1991–1996 model mean annual rainfall with CRU observations. a) GLBLBB1 mean annual precipitation in mm/year; b) CRU mean annual precipitation in mm/year; c) RMSE between simulated and observed mean annual precipitation; and d) temporal correlation map between simulated and observed time series of annual precipitation.

Analysis of the RMSE map between simulated and observed mean temperature (Figure 4.5c) indicated that the model was able to capture the precipitation variability over the desert areas covering parts of Botswana, Namibia and South Africa, and over both the Limpopo and Zambezi basins. However, the model showed some localised deviations of mean precipitation (of up to 900mm/yr) in parts of Angola and the DRC. The RMSE is lowest (less than 200mm/yr) over most the south and the south–eastern part of the study domain.

To examine how well the model time series of annual precipitation correlated to observations, a temporal correlation map is presented in Figure 4.5d. Correlation coefficients exceeding 70% were the most predominant pattern over the region; however, some minor exceptions occurred in some places where the model seemed to demonstrate a low correlation of approximately –15% to 15% with observed rainfall. This low correlation occured in the same regions where the highest deviations from observed mean annual

temperature were seen (Figure 4.1c).

Climatological annual cycle of simulated and observed precipitation is shown in Figure 4.6. Both model and observations showed almost the same amplitude of variability, ranging from around -80mm/month for the model and -60mm/month for CRU (both in August) to around 80mm/month (in January) for the model and 70 mm/month (in February) for the observations. The monthly pattern of simulated precipitation was in good agreement with observations, although model precipitation showed slightly more month-to-month variability in austral Summer than CRU. In austral Winter, the model is able to follow the trend of observed precipitation, however with dry bias of up to 20mm/month (especially in August).

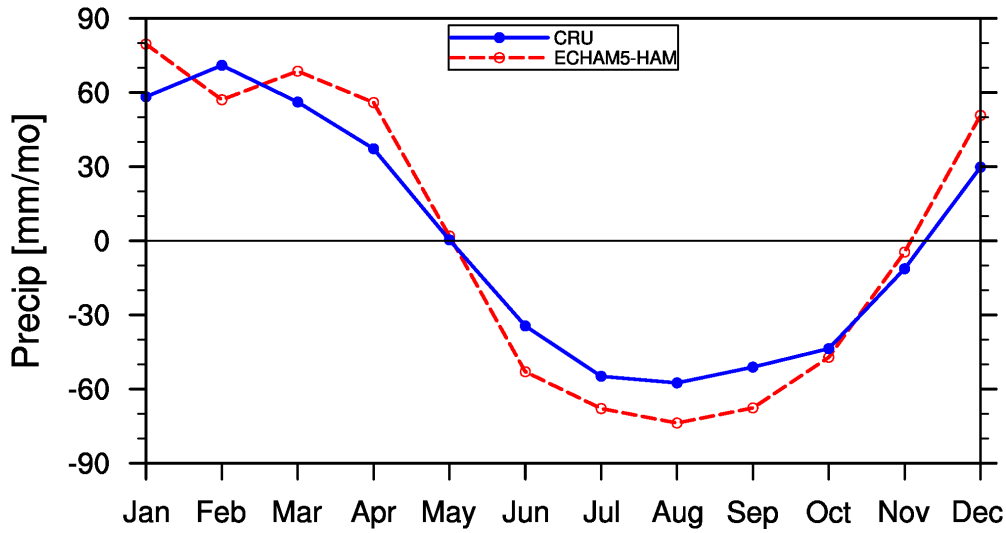

Figure 4.6: As in Figure 4.2 but for rainfall.

Seasonal precipitation differences between simulated and observed precipitation in mm/month are shown in Figure 4.7. Differences between simulation and observation were particularly notable during the DJF season, when the model overestimated by up to 100mm/month precipitation in the central region of the subcontinent (especially in DRC and Angola) but exhibited the opposite sign over Mozambique and south–eastern Zambia and Westen Tanzania. The same spatial pattern was seen in MAM; when values peaked ±80mm/month. During JJA no considerable deviations were seen in the simulated precipitation in comparison with observation becaused this corresponded to the dry season in the region. A subtle overestimation of precipitation occured again in southern DRC and eastern Angola. A negative bias of up to 50mm/month was seen over western Angola and DRC.

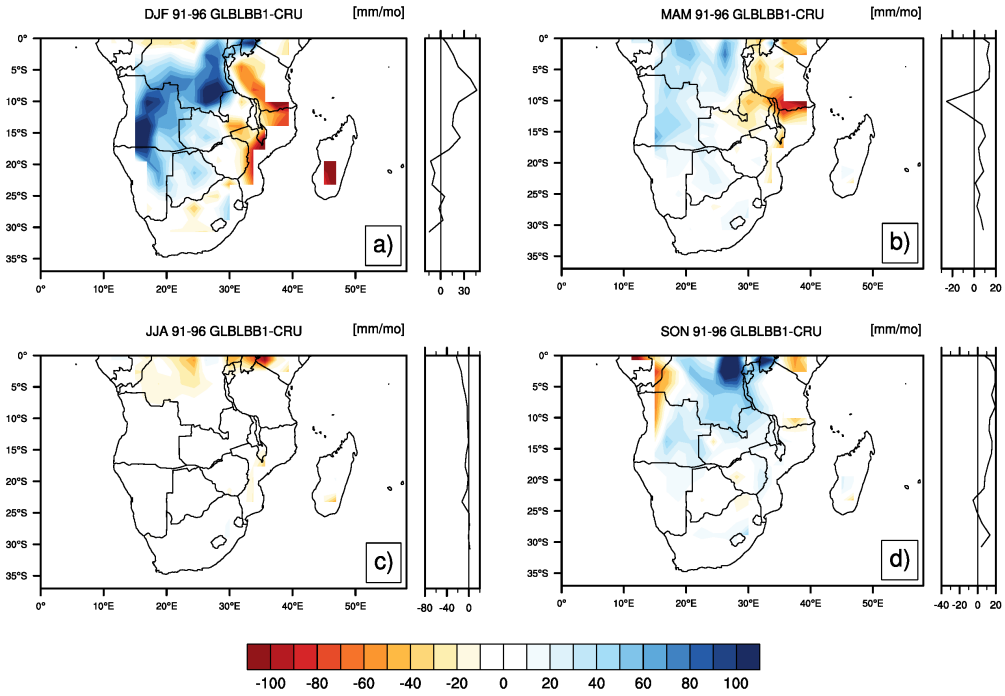

Figure 4.7: Comparison of simulated and observed seasonal precipitation in mm/month. The seasons are: a) DJF; b) MAM; c) JJA; and d) SON.

Figure 4.8 shows simulated (in red dashed line) and observed (in blue solid line) area–averaged deviations of monthly precipitation in Southern Africa for the analysis period (Dec 91–Nov 1996). Simulation and observations had the same cyclical pattern of precipitation values above mean in austral mid-Summer and below mean in austral mid-Winter. Simulated variability ranges from approximately –80mm/month in mid-Winter to 70-90 mm/month in mid- Summer; observed variability ranged from –80mm/month to 30–100mm/month in mid-summer. Simulation were able the capture the bell-shaped cycle of precipitation over Southern Africa. The model, however, exhibited a systematic dry bias in austral Winter (up to 15 mm/month in July); a wet bias was seen during the wet season of 94/95. Additionally, the model seemed to indicate the highest precipitation peak a month earlier than observations, with the exception of the wet seasons of 91/92 and 94/95, when it peaked two months later.

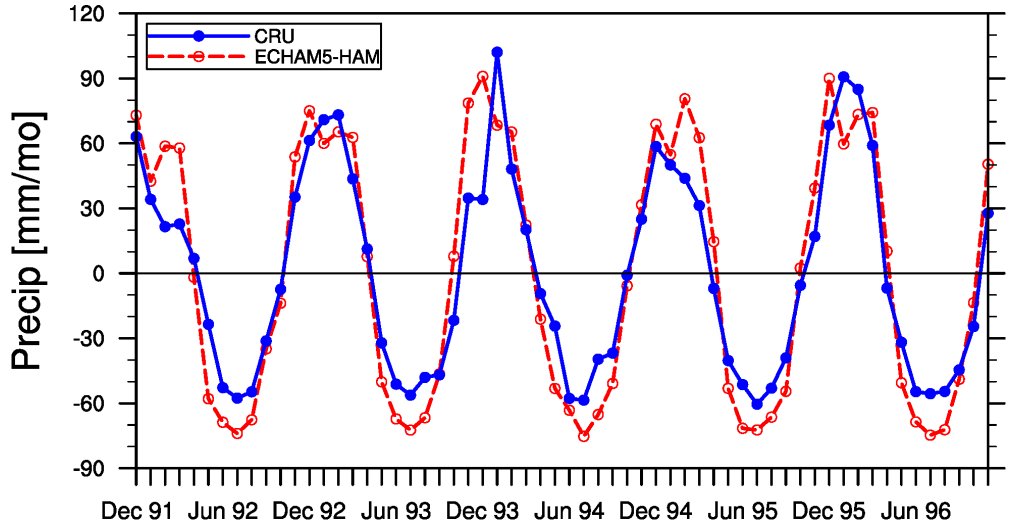

Figure 4.8: Simulated (red dashed line) and observed (blue solid line) area–averaged deviations of monthly precipitation in Southern Africa for the analysis period (Dec 91–Nov 1996).

4.3 Comparison of ECHAM5–HAM AOD with MODIS data

Figure 4.9 shows seasonal mean AOD maps of 1991–1996 ECHAM5–HAM simulations (left-hand side column) and 2000–2010 MODIS observations (right-hand side column) over Southern Africa for DJF [in a) and b)]; MAM [in c) and d)]; JJA [in e) and f)]; and SON [in g) and h)] seasons. For the reasons stated in subsection 3.3, the comparison of ECHAM5–HAM -simulated AOD with observations uses a poor man's approach, by evaluating the model against AOD climatology of a different period, namely 2001–2010.

During the DJF, the model (Fig. 4.9a) was able to replicate both the spatial pattern and the magnitude of the observations (Fig. 4.9b), especially over the northwestern portion of the domain where AOD values ranging from 0.2 to 0.6 are seen. However, over land in the central portion of the subcontinent (mostly over Angola, Zambia, Namibia and Botswana), the model underestimates AOD, with simulated values below 0.1 against observations between 0.1–0.4.

The MAM season exhibits a pattern not so much different from the one seen in DJF, with the model (Fig. 4.9c) simulating a noteworthy northward retraction of the peak AOD seen in DJF above 10°, while observations (Fig. 4.9d) still show AOD values between 0.3–0.4. It is important to mention that this is the period when BB emissions are mostly

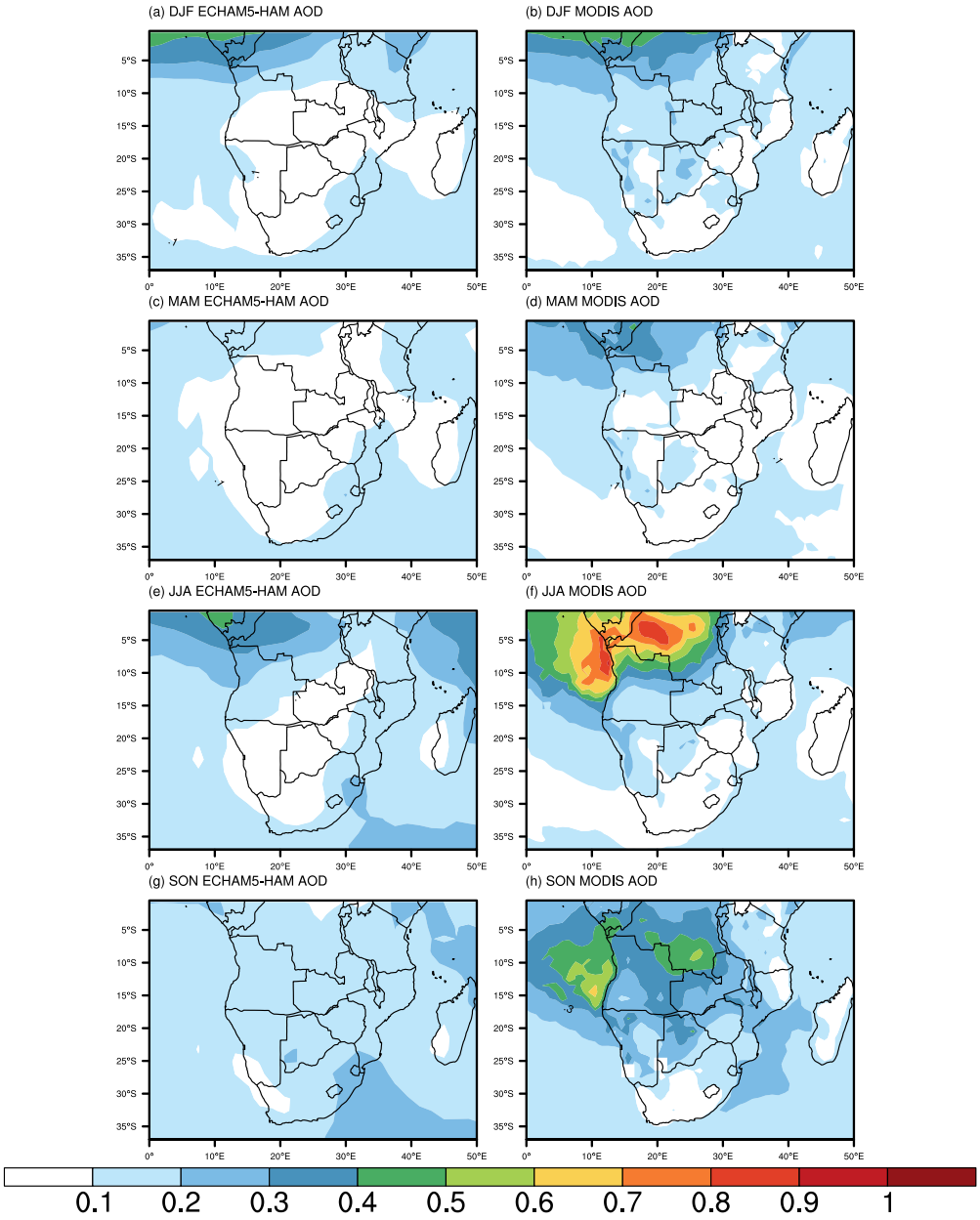

Figure 4.9: Seasonal mean AOD maps of 1991–1996 ECHAM5–HAM simulations (left-hand side column) and 2001–2010 MODIS observations (right-hand side column) over Southern Africa. Seasons depicted are DJF [in a) and b)]; MAM [in c) and d)]; JJA [in e) and f)]; and SON [in g) and h)].

occurring in the Equatorial forest over the African continent.

In JJA, during the onset of the biomass burning season in Southern Africa, the model (Fig. 4.9e) was somehow able to simulate the spatial pattern of the observed AOD (Fig. 4.9f), especially the location of the highest peak AOD. However, in this case the magnitude of the underestimation of the observed AOD is higher than in the previous cases. While simulated values barely reach 0.6 in the peak regions, the observations almost double

the simulated magnitudes.

In SON, the model (Fig. 4.9g) fails to accurately map the observed (Fig. 4.9h) AOD peaks over the central and the upper–left quadrant of the domain, showing simulated values below 0.2, while MODIS observations could reach up to 0.5–0.7 in these regions.

4.4 Comparison of WRF/Chem AOD with AERONET and MODIS data

Figure 4.10 shows PDFs of daily values of `WRFCHEMBB1` simulated (blue, dash-dot line) and AERONET observed AOD (red, solid line) over the four AERONET stations used in this study for the June–November 2001 period.

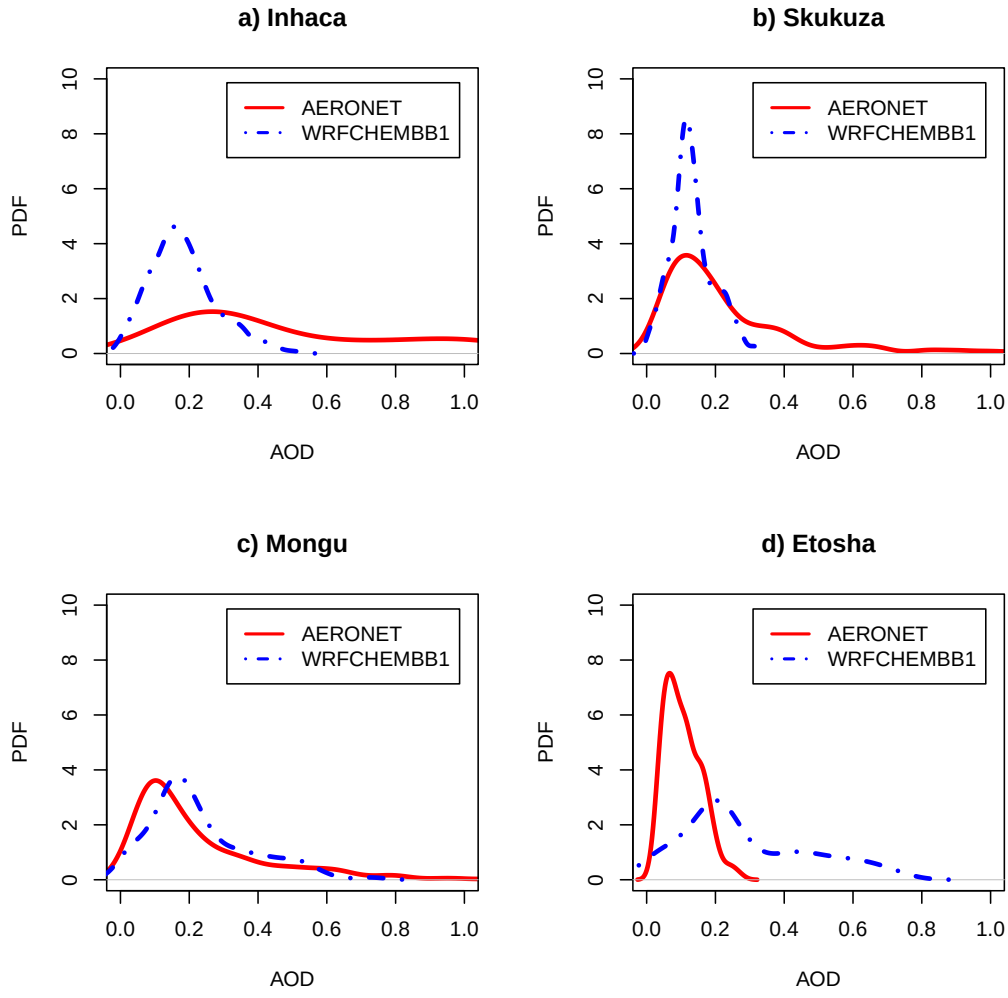

Figure 4.10: PDFs of `WRFCHEMBB1` simulated (dash–dot line) and AERONET observed (solid line) AODs over a) Inhaca; b) Skukuza; c) Mongu; and d) Etosha stations for June–November period.

At all stations, both the model and observations showed a quasi–gaussian distribution of AODs. At Inhaca (Mozambique) and Skukuza (South Africa), the modeled distribution was narrower than the observed, with a majority of the AODs values constrained within 0.0 – 0.6 (for Inhaca) and 0.0–0.4 (for Skukuza), against observed AOD values which spanned 0.0 to more than 1.0 in both locations. The simulated and observed distribution peaks were around 0.15 and 0.25 respectively at Inhaca and 0.15 for both simulated and observed at Skukuza. A contrasting behaviour of the distribution was seen over Mongu (Zambia) and Etosha (Namibia): At Mongu the modeled distribution was almost the same as the observed (both spreading from 0.0 to slightly over 0.8); at Etosha, the modeled distribution of AOD covered a similar interval to that of Mongu, whereas the observed distribution was constrained between 0.0 and close to 0.35. At these stations, the model shifted the peak of the AODs distribution to slightly higher values (close to 0.2) at both stations; observations were peaking slightly below 0.1.

Figure 4.11 shows June–November 2001 averaged spatial distribution of a) MODIS observations at 500nm; b) `WRFCHEMBB1`; and c) `WRFCHEMBB0` simulated AODs over Southern Africa.

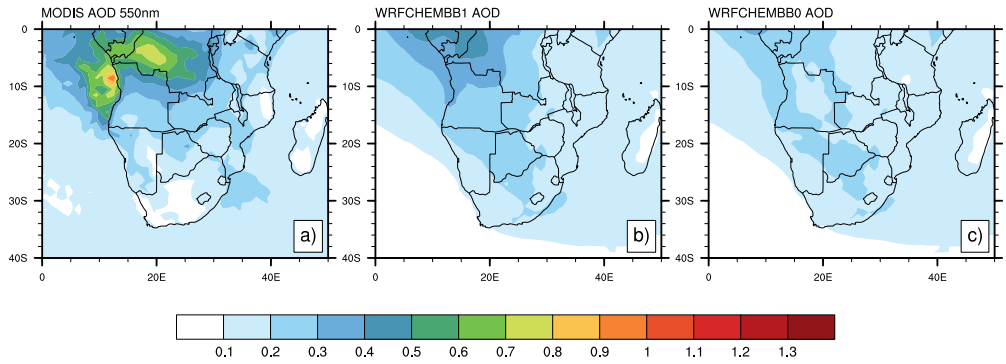

Figure 4.11: June–November 2001 averaged spatial distribution of a) MODIS observations at 500nm; b) `WRFCHEMBB1`; and c) `WRFCHEMBB0` simulated AODs over southern Africa.

Over land, both settings of WRF/Chem model were somehow able to replicate the spatial pattern of peak AODs retrieved by MODIS during the June–November 2001 period, especially the location of the maximum AOD. The areas over the DRC, Angola (and that part of the Atlantic Ocean close to Angola) where AOD values usually achieve maximum values during this period (from 0.8 to 1.2) were well represented on the `WRFCHEMBB1`

setting of the model, and fairly well represented in WRFCHEMBB0. In these regions, the simulations slightly underestimated observations, exhibiting values of 0.4–0.5 and 0.2–0.3 for WRFCHEMBB1 and WRFCHEMBB0, respectively. Additionally, simulations showed a slightly higher than observed AOD over Botswana and central South Africa, in which MODIS seemed to observe no AOD at all.

Analysis of the results above were supplemented by using the Taylor diagrams shown in Figure 4.12. In this figure, AOD correlations, standard deviations and RMSEs between the reference values from MODIS and the two settings of WRF/Chem simulations, namely the WRFCHEMBB1 (in red circles) and the WRFCHEMBB0 (in blue triangles), are presented for June–November 2001 period.

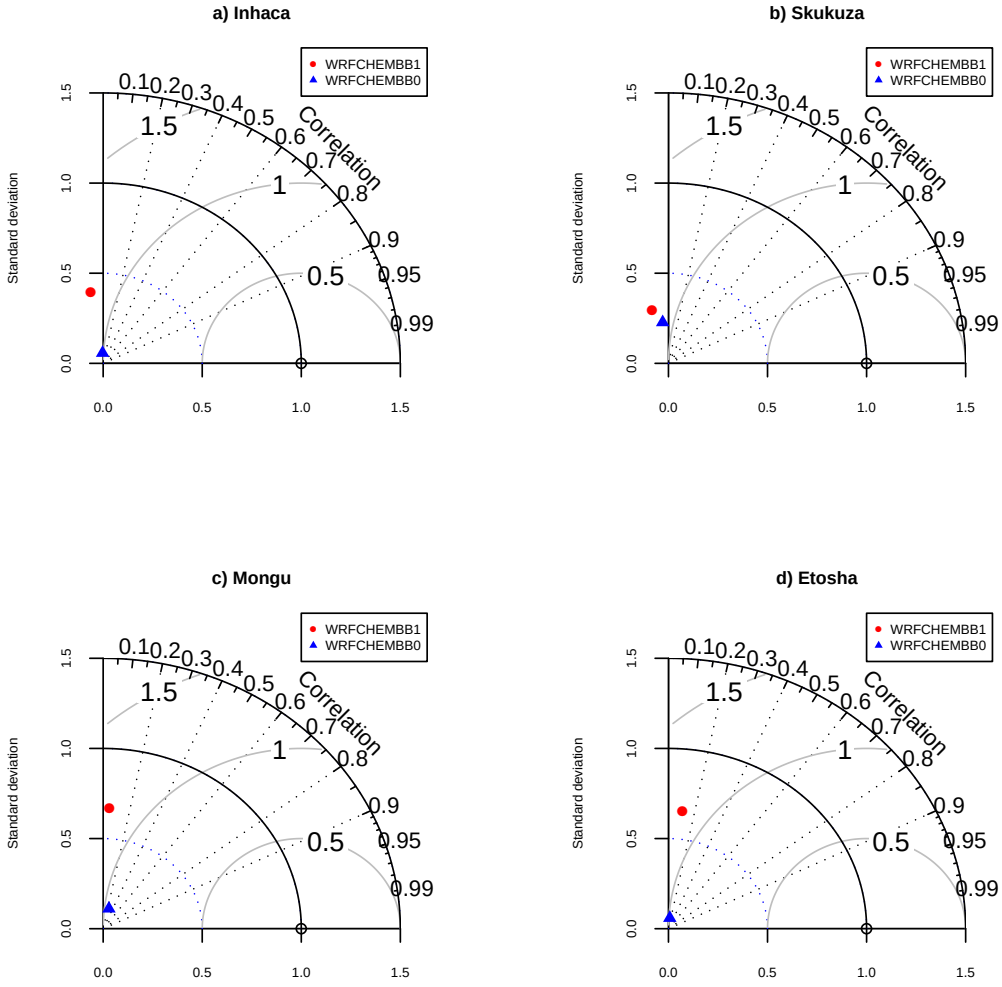

Figure 4.12: Normalised Taylor diagrams of June–November 2001 daily averages of WRF/Chem–simulated and MODIS–observed AODs over the four AERONET stations in Southern Africa, indicated in Figure 3.5, namely a) Inhaca; b) Skukuza; c) Mongu; and d) Etosha. Correlations, standard deviations and RMSEs between the two settings of WRF/Chem (WRFCHEMBB1, in red circles and WRFCHEMBB0, in blue triangles) and MODIS data are shown.

Based on the Taylor diagrams, poor correlation between simulations and observations were seen at all four study stations. In the southern stations (Inhaca and Skukuza) correlation values were negative; for their counterparts in the north values were also low but positive. The standard deviation, represented in the Taylor diagrams as the distance of the simulated values from the origin, was small ranging from 0.05 to 0.15, with the exception of the WRFCHEMBB0 over Skukuza. Here errors as large as five times those of the WRFCHEMBB1 over the same place were simulated. The normalised RMSEs for all models over all stations were close to 1 (or slightly above) for this period – in other words, the models simulated AOD error is about the same value as (or slightly larger than) the standard deviation of the MODIS observed.

4.5 Summary

The ability of the models to replicate observed climate was been examined by comparing simulated precipitation and temperatures with observed data from CRU and AOD with AERONET and MODIS datasets. The model showed good agreement in the spatial patterns of the variables, as well as in the variability and range of the magnitudes of the variables concerned. Although exhibiting some localised bias (especially over desert areas and areas where the observed data is scarce), the model was able to simulate with a good approximation the observed variability in these regions. Possible explanations for both temporal and spatial deviations are:

(a) Although aerosols are known to play a major in the radiative forcing and thus influencing surface energy balance and consequently climate variables such as temperature and precipitation, they are not yet properly accounted for in climate models, either because their properties are not well represented in the model equations or because they are not well quantified and characterised in regions such as Southern Africa.

(b) The resolution at which the model was being run (T63/L31), was relatively coarse when compared with that of the CRU datasets. At a such model resolution, some sub-grid scale features important for the evaluation of temperature were not well captured and, as was shown by Roeckner et al. [2006a], the RMSEs decrease monotonically with increasing horizontal resolution;

(c) The performance of a climate model over a region is highly influenced by the LSM coupled to it. In turn, the LSM itself is a function of the input fields and the highly variable surface water and energy states at the beginning of the simulation [Rodell et al., 2005]. As stated in Section 3.3, this region of the world has a scarcity of resolved spatio-temporal data. CRU data, for example, was found to have bias simply because of the scarcity of data (particularly over DRC), thereby making any comparison of variables nearly impossible [Tadross et al., 2006];

(d) Prescription of monthly mean aerosol emissions of year 2000 for all the simulation years, instead of the inter–annually varying emissions, which could allow the model to capture deviations caused by inter–annual variability of emissions [Aghedo et al., 2007];

(e) Both models use GFED2–based biomass burning emissions, which are known to be lower than other emission inventories (see for example Liousse et al. [2010]; Stroppiana et al. [2010]). In addition, the current setting of WRF/Chem, the possible loss of information during the interpolation of aerosol concentration from the GOCART model $2.5^{\circ} \times 2.5^{\circ}$ grid to the finer WRF/Chem 60km$\times$60km grid seems to also contribute to the underestimation of the AOD over most of the region, because of the high spacio-temporal variability which is smoothed out at the larger grid; and

(f) MODIS AOD algorithm is known to perform poorly over areas with high surface reflectances (e.g., deserts). Thus, poor model performance over desert areas in Southern Africa may have been caused by the comparison with an uncertain metric [Mahler et al., 2006].

Chapter 5

Contribution of local and external sources to biomass burning aerosol concentrations in Southern Africa

From the climate modeling perspective, it is necessary to know the exact location of the factor the impact of which on climate is to be studied. This ensures that sensitivity studies can be carried out by changing the level or quantity of the factor at the precise location. In this chapter, GFED emissions of carbonaceous aerosols – used as tracers of biomass burning – were employed together with modeled transport pathways, to identify the sources of the BB aerosol burden found over the Southern African atmosphere.

5.1 Global and regional sources of carbonaceous aerosols and their contribution to regional aerosol burden

Figure 5.1 shows 1991–1996 averaged monthly cycle of emissions, concentrations and the AODs in Southern Africa. Figure 5.1a) shows GFED combined BC and OC emissions; Figures 5.1b), c) and d) show model–derived vertically integrated burden of *Aitken*, accumulation and coarse modes BC and OC aerosols, respectively. Figure 5.1e) represents the modeled AODs caused by the presence of BC and OC aerosols.

From Figure 5.1b to Figure 5.1e, the `GLBLBB1` simulation is represented by a dashed

red line; the GLBLBB0 by a blue dash–dotted line; and the RGNLBB0 by a black dotted line. The concentrations in the *Aitken*, accumulation and coarse modes are on the same scale so that the magnitudes of the concentrations can be easily compared.

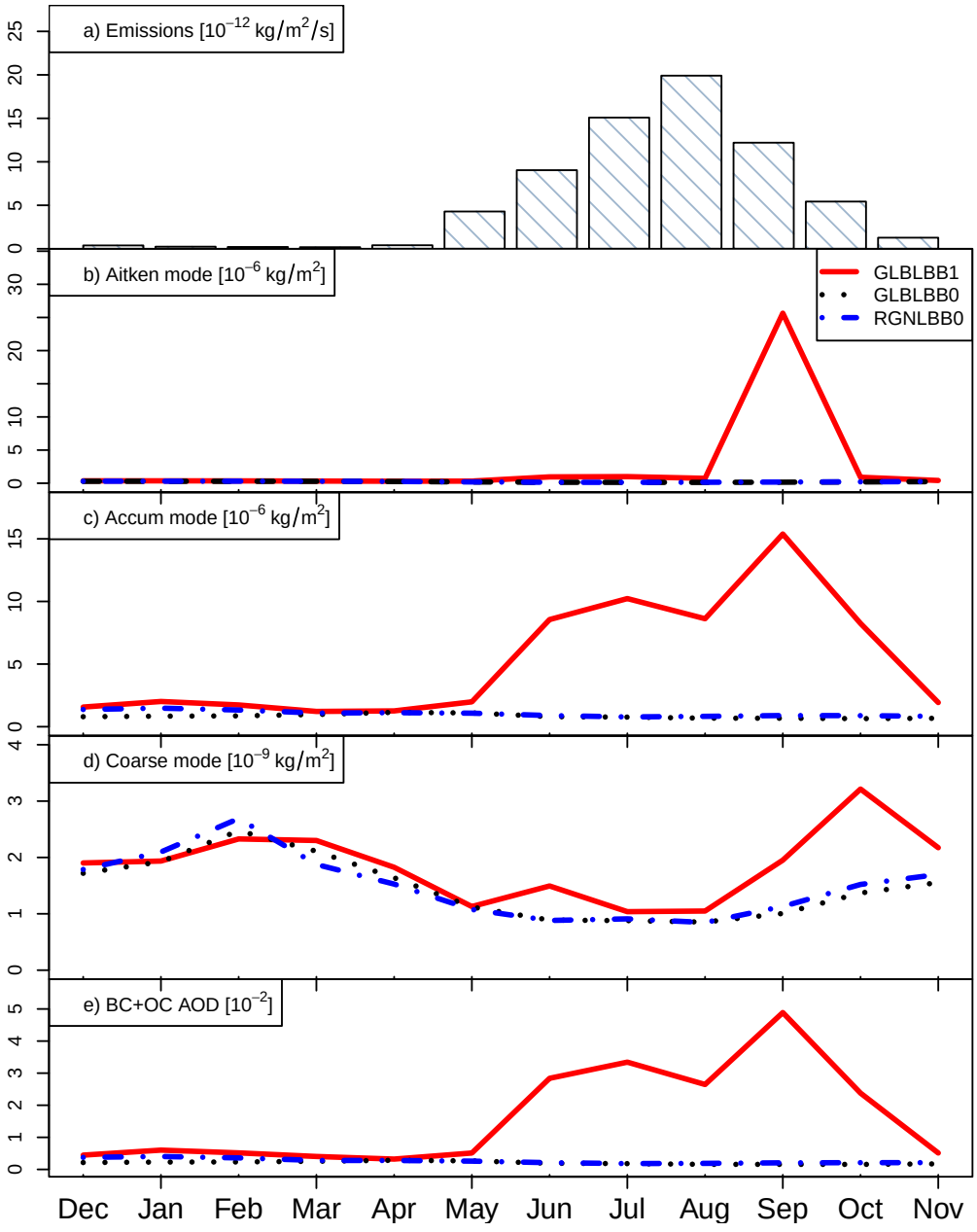

Figure 5.1: Intra–annual cycle of 1991–1996 averaged a) GFED emissions; and modeled inter–annual cycle of atmospheric burden of b) *Aitken*, c) accumulation, and d) coarse modes of BC and OC. In e) the modeled BC and OC AOD is presented. In all b), c), d) and e), GLBLBB1 is the red dashed line; GLBLBB0 is the blue dash–dotted line; and RGNLBB0 is the black dotted line.

BC and OC emissions from GFED [Figure 5.1a] built up around the onset of the austral dry season in April, reached their peak of around 2×10^{-11}kg/m^2/s in August and dissipated

later in December. The modeled regional atmospheric burden of *Aitken* mode aerosols (Figure 5.1b), also showed a mono-modal pattern as the emissions. This pattern showed an increase-to-reduction cycle from August to October, slightly after and for a shorter period than displayed by the GFED regional emissions cycle in the region. The modeled *Aitken* mode peak concentration was in October with values around 25×10^{-6}kg/m^2. By contrast, almost no *Aitken* mode BC and OC aerosols were found in the region's atmosphere throughout the year when BB emissions were switched off either regionally `RGNLBB0` or globally `GLBLBB0`.

Relative to the accumulation mode, the modeled inter–annual cycle of BC and OC aerosol burden in the region (Figure 5.1c), the `GLBLBB1` showed a major peak of the same order of magnitude and synchronised with that of the *Aitken* mode. Some additional variability is seen, caused by a minor increase/decrease cycle with a pattern close to that of regional emissions, followed by a larger increase and decrease between May and August, before the major peak of around 15mg/m^2 referred to earlier was also seen. Again, for this aerosol mode, `RGNLBB0` and `GLBLBB0` simulations were both close to zero throughout the year.

In Southern Africa, modeled concentrations of BC and OC aerosol in the coarse mode (Figure 5.1d), are three orders of magnitude smaller than in the *Aitken* and/or accumulation modes. Amplitudes of the cycle varied between 1 and 3 µg/m^2. The `GLBLBB1` simulations exhibited a trimodal distribution pattern, with 1 month lagged peaks when compared to the accumulation mode described before. In this case, the highest peak of the coarse mode BC and OC aerosol concentration is reached in October. The `RGNLBB0` and `GLBLBB0` simulations had an intra-annual cycle, as opposed to the previous cases, building up as early as September, with values close to 1.0µg/m^2 and increasing to peak around 2.5–3µg/m^2 in March, thereafter decreasing to the original minimum of around 1.0µg/m^2 in August, in a pattern much similar to that of `GLBLBB1`. A competition of the accumulation and coarse mode could also be seen during the onset of emissions in Southern Africa: while the concentration of accumulation mode particles increased (Figure 5.1c), the opposite took place for the coarse mode particles (Figure 5.1d)..

The modeled inter–annual cycle of the BC and OC contributions to the regional AOD (presented in Figure 5.1e), show the `GLBBLBB1` simulation largely dominating AOD levels throughout the year. The `GLBBLBB1` fraction of the AOD had a minute peak centred in

February, which dissipated in May. In June, the AOD rose to values an order of magnitude higher than the former and peaked in August (between 0.03 and 0.04), before decreasing slightly a month later, and peaking again (to a maximum value of 0.05) in October – a month later than the emissions counterpart (Figure 5.1a). The contributions of the two other simulations remained close to nil throughout the year, with the exception of the January–April period, when RGNLBB0 exhibited negligible concentration values, at levels almost half those of the GLBLBB1 model setting.

Figure 5.1 is intended to demonstrate the causal relationship between regional emissions and aerosol concentrations, and their links to the resultant AOD. Regional emissions were expected to cause increases in aerosol concentrations and thus increase the AOD within a short time–frame. The time–frame would be of the same order as the duration of emissions. This is confirmed by the similarity in the patterns exhibited by the emissions (Figure 5.1a) and the AOD (Figure 5.1a) graphs. AOD in the region can be attributted mostly to *Aitken* and accumulation mode particles, given their similar monthly pattern.

Nevertheless, there were situations in which peak atmospheric BC and OC aerosol concentrations existed outside the emissions cycle, namely in January, for the accumulation mode, and in March for the coarse mode. These peaks suggested that some sort of external sources brought in aerosols into the region through long–range transport mechanisms. Tyson and D'Abreton [1998]; Aghedo et al. [2007]; and Swap et al. [1996], have done extensive work, looking at the opposite situation, in which the contribution by African pollution to the air pollution in other regions has been studied.

The peculiar behaviour noted in Figure 5.1d) in which coarse mode mixing ratios in GLBLBB0 and RGNLBB0 simulations were found to be slightly larger than in GLBLBB1 around February, i.e., when concentration values became larger when emission sources had been removed (either regionally or globally) than when emissions were present, is addressed in the context of Chapter 7.

In order to investigate the provenance of the aerosols which caused increases of concentrations of fire–generated aerosols in the atmosphere of Southern Africa during the BB *off–season* period previously referred to, global sources of BC have been mapped in Figure 5.2 for seasonally averaged biomass burning emissions of BC (from the GFED–based AEROCOM reference emissions for year 2000). Detailed description of the inter–annual variability in global biomass burning emissions can be found in van der Werf et al. [2006].

In this study, only the location of the wildfire emissions were needed to identify the possible sources of fire emitted aerosols found in the study region.

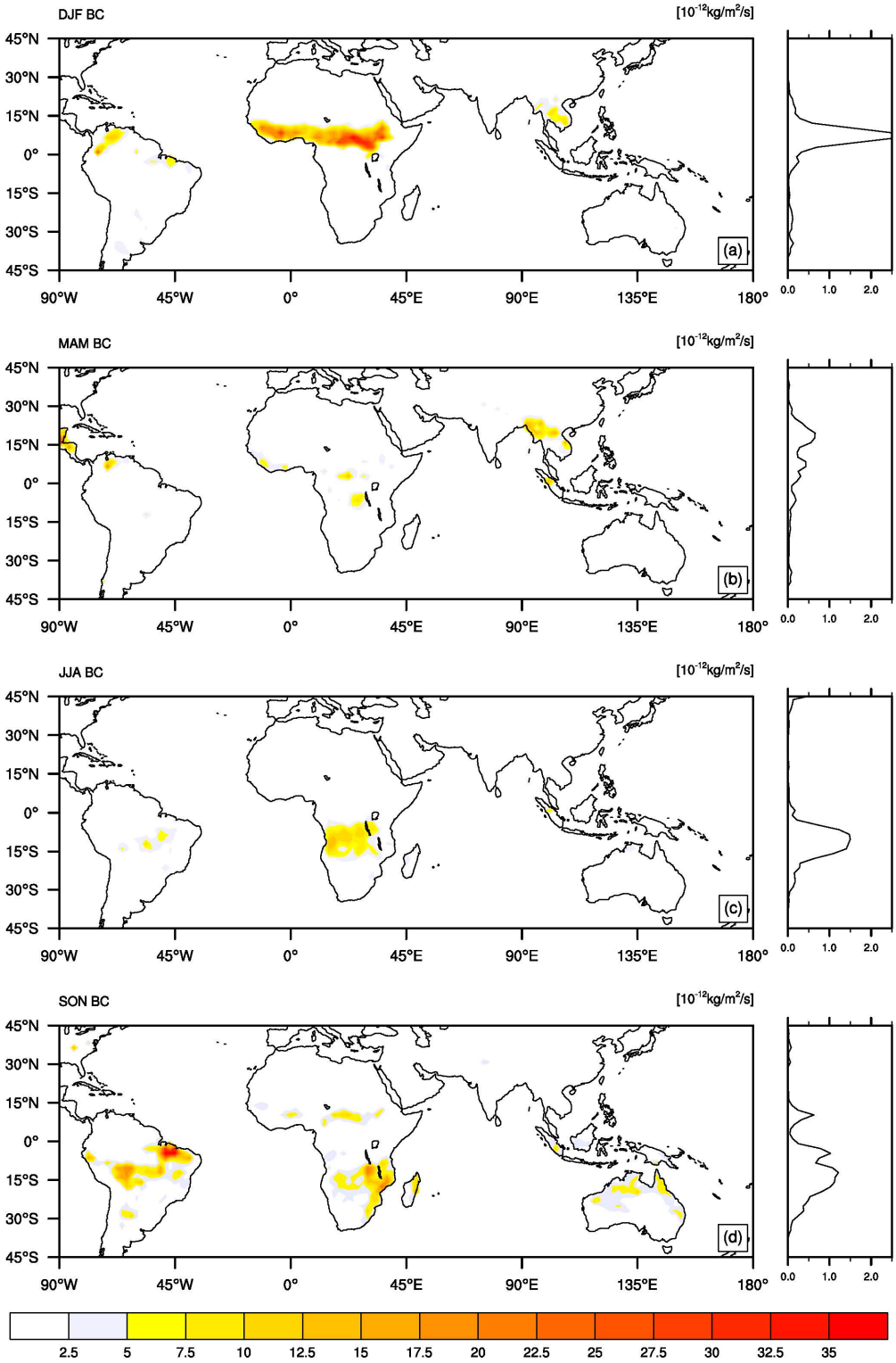

Figure 5.2: Seasonally averaged biomass burning emissions of BC from the GFED–based AEROCOM reference emissions for year 2000 in 10^{-12} kg/m^{2}s, together with the zonal means on the rhs of each map. Maps are for a) DJF; b) MAM; c) JJA; and d) SON respectively.

During DJF season, wild–fires were found in Central Africa; in a large and intense latitudinal band stretching between 0–15°N and extending from 15°E to 45°. Minor patches of wild–fires are found over Southeast Asia and around the Equator on the South American continent. The zonal mean showed peak emissions occurred between latitudes 0 to 15°N during the DJF season, mainly caused by the African contribution.

In MAM, wild–fires appeared to move to higher latitudes on the American continent, centred around 15°N, while on the African continent wild–fires are almost extinguished throughout the continent, apart from some localised burning which occurs in the western and central parts of the continent, and in the DRC. Over Southeast Asia, fires intensify and expand to the north and south of the areas affected during DJF season. The latter fires and the American contribution are responsible for the major zonal peaks between 0 to 30°N in this season, while the minor zonal peak seen between 15°S to 0°N is caused by the Congolese forest fires.

In JJA, the dominance of the African fires south of Equator takes effect. Except for minor hotspots in the Amazon forest and the initiation of fires in northern Australia, the African fires during this season dominates the global zonal mean of emissions, and the zonal mean curve has now moved to latitutes 30°S to 0°S.

Later, during SON, fires move further south and the whole southern hemisphere is burning almost over all the land areas namely, Amazon forest, Southern Africa and north-western and northern Australia. These fires contribute to the widespread zonal mean stretching from beyond 30°S to 0°S. Additional fires occuring during this season, over the African tropical forest between 0°N to 15°N, cause an additional peak on the zonal mean between these latitudes.

Zonal averages of modeled vertical profiles of BC and OC mixing ratios, overlaid by vertical winds, are presented in Figure 5.3, to clarify the behaviour displayed in Figure 5.1, and take into account the sources of wildfire aerosols presented in Figure 5.2.

Carbonaceous aerosols can be found over the region almost throughout the year, with maximum mixing ratios expanding and retracting according to each season. In the DJF season (Figure 5.3a), these aerosols were found in a very small location of the model domain, around 20°S, from the earth's surface to 500hPa. Mixing ratios were also low, with the maximum lower than 1×10^{-12}kg/kg. The aerosols were mostly found in the interface of a region where vertical winds indicated sinking air parcels south of 22°S (with speeds up to

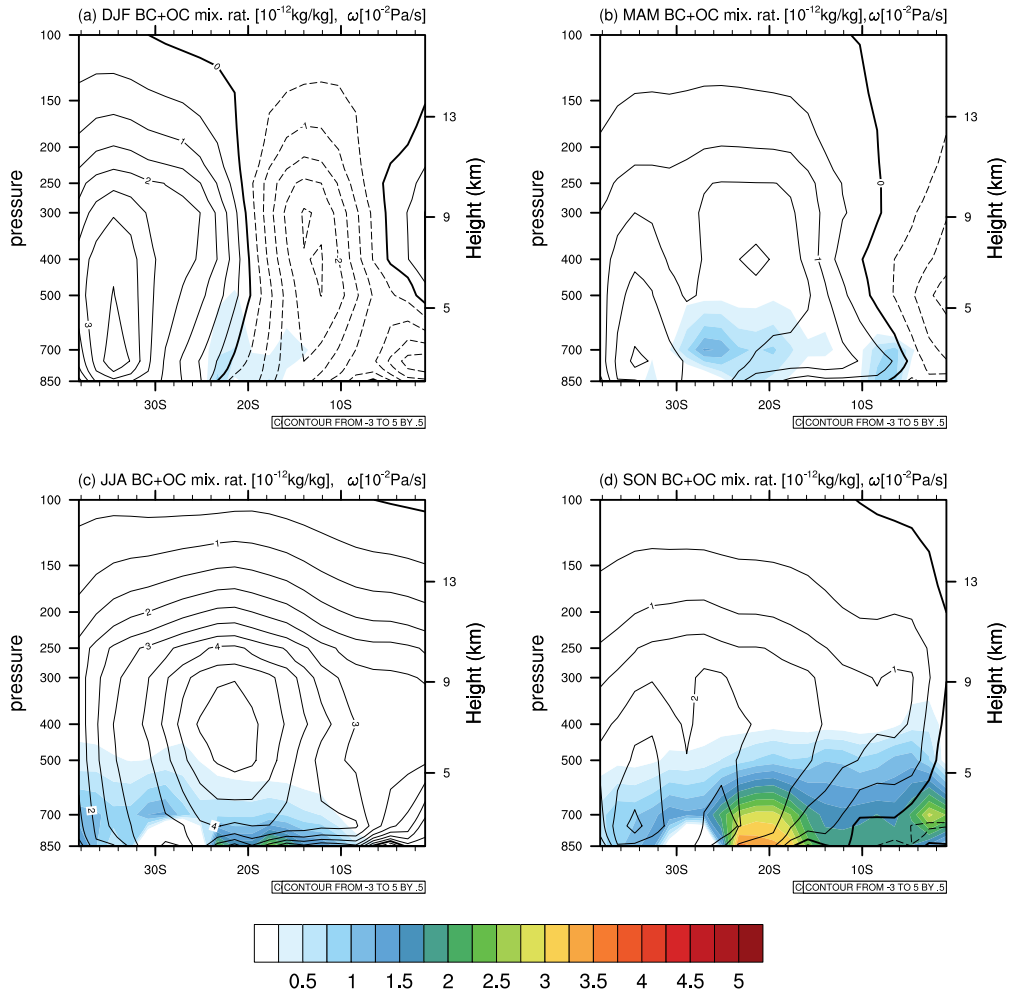

Figure 5.3: Zonal averages of seasonal vertical profiles of BC and OC concentrations for the GLBLBB1 case, overlaid to pressure–coordinate vertical winds. BC and OC mixing ratios are represented by shades, and vertical wind by contours. Positive values of vertical winds (indicating sinking) are the solid lines; negative ones (indicating rising) are dashed lines; and the zero contour is the black thick line. Seasons represented are (a) DJF; (b) MAM; (c) JJA; and (d) SON.

3 Pa/s) and rising air parcels between 22°S and the Equator (with speeds up to 2 Pa/s).

In MAM (Figure 5.3b), carbonaceous aerosol mixing ratios had pattern slightly similar to that of DJF; however the peak appeared to move southwards and hover at around 700hPa over 26°S. Additionally, a new and smaller peak appeared below 700hPa at latitudes between 5°S – 10°S. Convective activity during this season was only perceived above the latitude 8°S; below that latitude, sinking air masses predominate.

In JJA (Figure 5.3c), mixing ratios of carbonaceous aerosols were higher than in previous cases; they seemed to cover all latitudes from 8°S to the southern boundary of the study area, and tended to be constrained between the earth's surface and altitudes of 6 km.

Maximum mixing ratio values of around 1×10^{-12}kg/kg, were found close to the surface throughout most of the study area. Highly stable conditions prevailed during this season, with sinking air masses reaching up to 4 Pa/s.

Finally, for the SON season (Figure 5.3d), large carbonaceous aerosol mixing ratios were well established over the domain, from surface to ≈5km and ≈8km near the southernmost boundary and 20°S, respectively. All latitudes appeared to be equally covered by carbonaceous aerosols during this season and the largest peak was noted between 16°S and 24°S.

Although the convective activity is high in DJF, which injected/carried aerosol particles aloft from the surface, the absence of sources of carbonaceous aerosols during this season excluded the possibility of local production of the aerosols – as shown in Fig. 5.3a – and suggested the existence of a long–range transport mechanism. Additionally, during MAM, the presence of aerosols was noted as far away as 26°S, when the regional emissions were constrained in small cells in the Congo region, also suggesting a similar transport mechanism had moved particles as far as this distance in the atmosphere.

5.2 Major transport pathways of carbonaceous aerosols

The assumptions above were confirmed by global modeling of seasonal circulation patterns, shown in Figures 5.4 and 5.5, which present major transport pathways for each season at the levels at which maximum mixing ratios occured (at 850hPa and 700hPa).

Our model suggests that carbonaceous aerosols causing the off–season peaks in aerosol concentrations are derived from the following sources:

- In DJF, at both 850 and 700hPa levels, north–easterly trade winds added to intrusions from the Asian fires bringing carbonaceous aerosols from the tropical rainforest north of the Equator to the south. Then, south–easterly trade winds re-circulated matter inside the semi–permanent continental *gyre*. This re-circulation caused a peak concentration centred around the Drakensberg mountain region (close to 30°E/30°S), a result of accumulation of particles because of prevailing sinking motion, added to the effect of elevated orography, manifested by the inhibition of horizontal circulation at the 850hPa level. The end result was increased concentration values in the atmosphere. Choi and Choi [2008], for example, have presented a detailed explanation

of the pollution trapping effect caused by the shallow PBL close to mountains. However, this work was not able to include the important effect of the PBL *per se* – the model was too coarse for this effect to be explicitly treated. Thus, the increased aerosol concentration may possibly be explained in terms of nucleation processes [Makkonen et al., 2009].

- In MAM, the large peak close to 10°S is mostly associated with the Congolese fires; south–westerly winds were seen to be driving air-masses from over Brazil to merge with the Southern African gyre and, again, causing the peak over the Drakensberg mountains. Interestingly, using Light Detection And Ranging (LIDAR) observations together with off–line modelling, Bencherif et al. [2003], have only attributed the aerosols found over Durban (29.9S/31.0E), South Africa, to the air masses coming from the equatorial region close to Brazil; not taken into account was the contribution of the re-circulated matter. Another interesting fact was the existence of a minor *payback* mechanism (not visible in the maps because of the scale used), seen through a large-scale re-circulation system centred over sub-equatorial Atlantic, in which aerosols were taken from Central Africa by the north– and south–easterlies towards the Southern American region, and brought back by a band around 30S to Southern Africa by westerly winds.

Details of the behaviour in JJA and SON need no discussion here, since Southern Africa is the major contributor to the aerosol concentrations during this season, and this has been thoroughly discussed by Piketh and Walton [2004] and well as by Tyson et al. [1996a,b]. It is important to note the contribution of the north–easterlies and easterlies to the aerosol concentrations during SON, and, again, the role of the topography with the associated air sinking motion in trapping aerosols around the 850–700hPa levels in both the JJA and SON seasons.

To elucidate the role of topography on the concentrations found at lower levels around the Drakensberg region, WRF/Chem model was used to zoom into the area at a finer resolution and present the horizontal wind and temperatures profiles at 700hPa (Figure B.2, in Appendix B), and a vertical cross section (which crosses the mountains at an angle of 45° with the latitudes) of black carbon and temperature (Figure B.3). The JJA season was chosen from the available WRF/Chem simulations for its resemblances to the GCM simulated MAM and JJA winds over the region of concern.

WRF/Chem was used to zoom into the area (again, at a finer resolution) and produce the horizontal wind and temperatures profiles at 700hPa. Figure B.2 clearly shows winds in the Drakensberg region are a combination of westerlies and the continental anticyclone, reinforcing the assumptions previously made that aerosol concentrations in the region are a combination of locally generated aerosol particles and those coming from two different sources. Wind flow at this level in this region seems to be controlled by two geopotential lines that are very close together.

The vertical cross section in Figure B.3, also helped differentiate between two peaks of aerosol masses over the region. One peak, at the south, coming from the west at approximately 21°W, was located in the stable layer at around 4km above sea level (asl); the other peak, on the northern side of mountains peak, apparently undergoing a wake effect, was in the layer between 5km and 6km asl. The former was clearly the contribution of the westerlies; the latter represented the contribution of the gyre at this level. Concentration above the PBL was far larger than inside it; this allows the author to differentiate between local and non–local aerosol contributions over the Drakensberg Region, being local aerosols mostly trapped inside the PBL and non–local located above it.

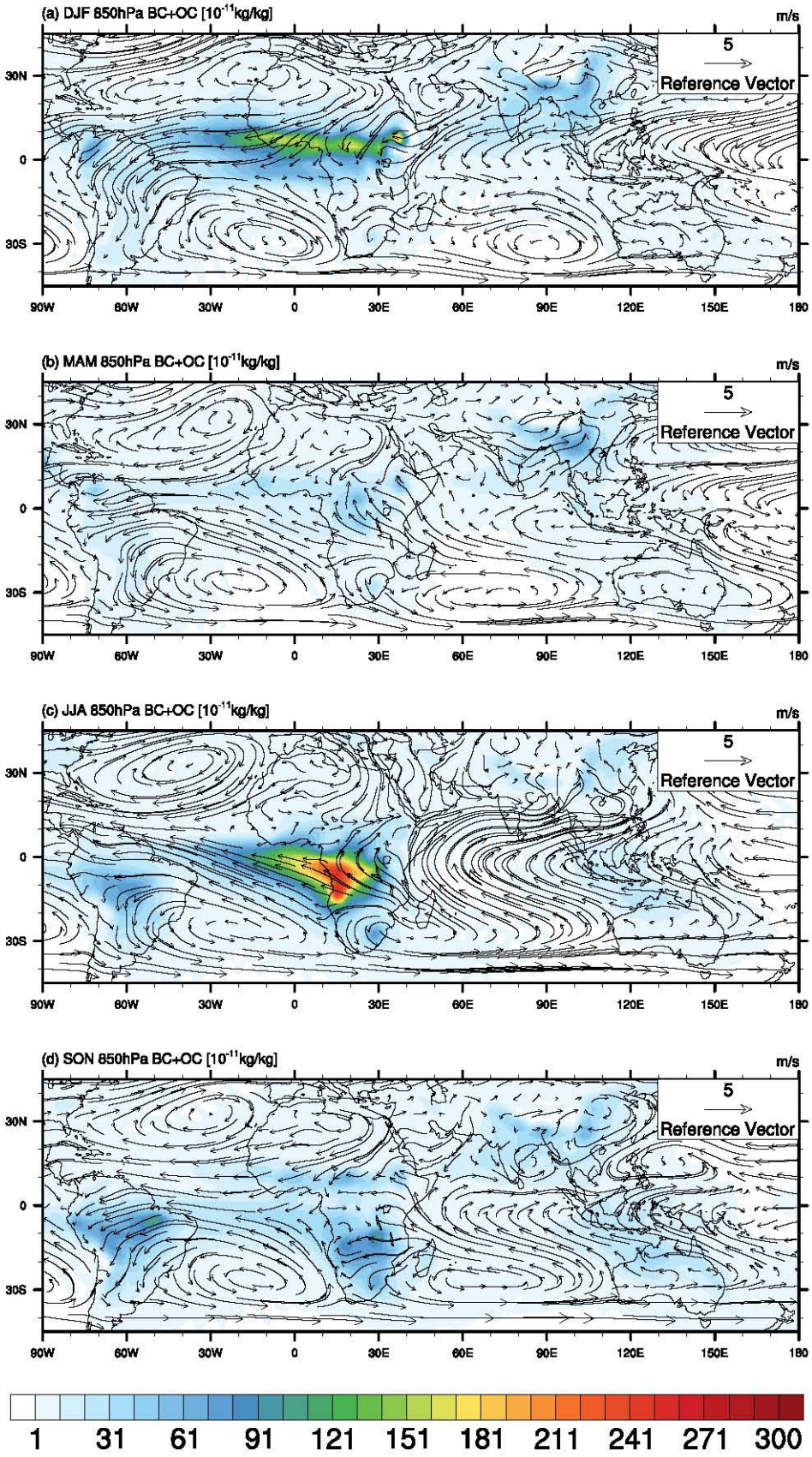

Figure 5.4: 850hPa streamlines overlaid to ultra–fine mode BC and OC aerosol concentrations. Seasons are (a) DJF; (b) MAM; (c) JJA; and (d) SON.

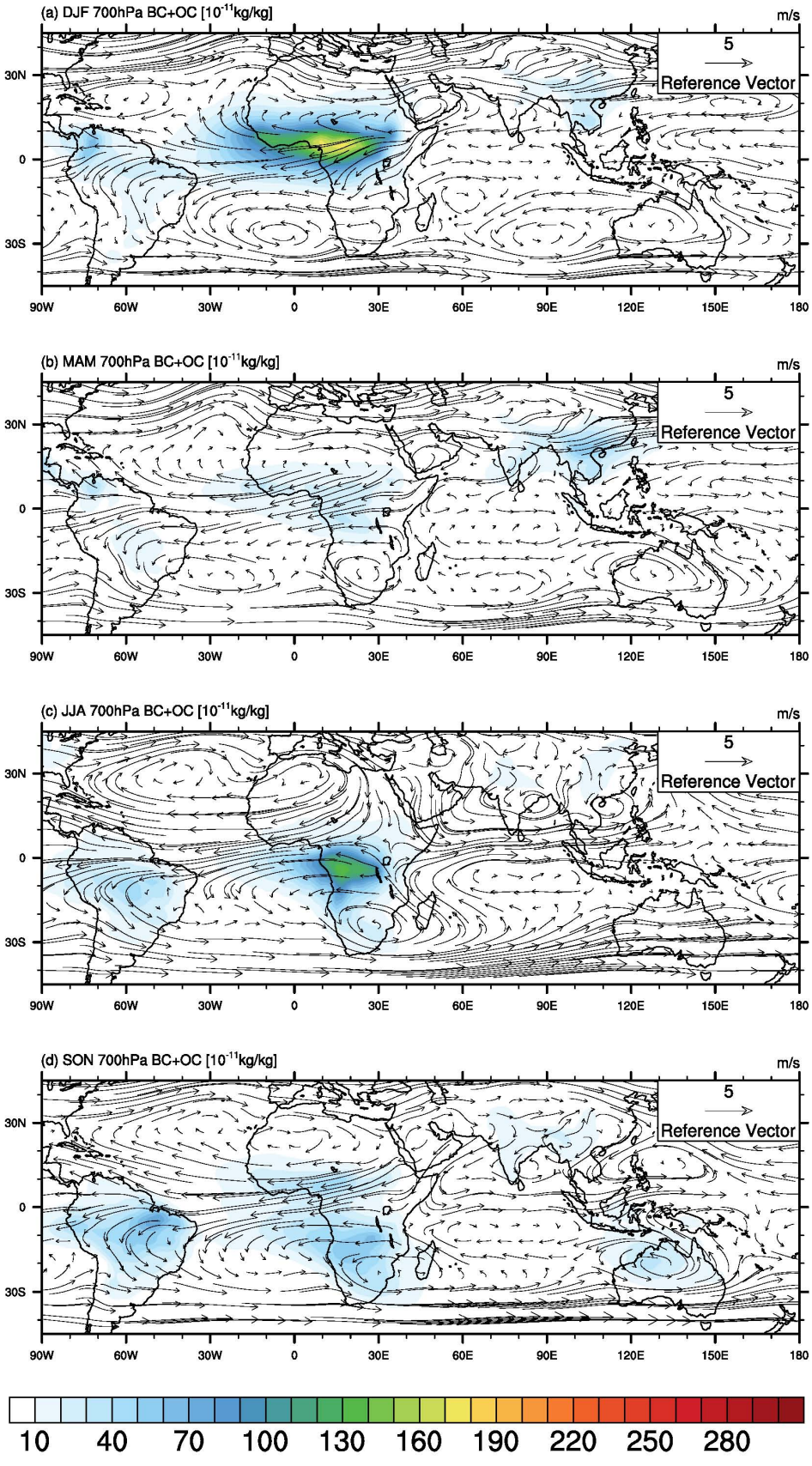

Figure 5.5: Same as Figure 5.4, but for 700hPa.

5.3 Summary

In this chapter an online aerosol–climate GCM has been used to identify major pollution sources contributing to the carbonaceous aerosol burden found over the Southern African atmosphere. Apart from the local sources (which have already been identified and have extensively been studied) external sources also exist, namely the African tropical forest fires north of the Equator and, to a lesser extent, the South American wildfires. The Equatorial fires contributed to the slight increase of concentrations in the northern part of the study area through south–easterlies; the latter region, together with the anticyclonic *gyre*, bring pollution from the Amazonian forest through westerlies to the southern region of the domain, which is then trapped by the combination of elevated orography in the Drakensberg mountains and the prevailing air sinking motion, added to possible local aerosol nucleation processes.

The impact on the concentrations of the existing aerosols when biomass burning emission modes are switched off both regionally (`RGNLBB0`) and globally (`GLBBLBB0`) was very low, and therefore, it can be expected that the impact on the direct and semi–direct effects (factors intrinsically linked to the aerosol optical properties) would also be low. This fact led the author to assume that the direct and semi-direct effects of carbonaceous aerosols in Southern Africa are primarily governed by local emissions, and, particularly biomass burning.

It was found almost irrelevant for the atmospheric concentrations of carbonaceous aerosols over Southern Africa that biomass burning was removed either globally (`GLBBLBB0`) or regionally (`RGNLBB0`). This indicated that local emissions were the largest contributors to the regional carbonaceous aerosol concentration. Thus, discussions on the next sections will mostly be based on differences between `GLBBLBB1` and `RGNLBB0`, rather than between `GLBBLBB1` and `GLBBLBB0`.

Finally, a peculiar behaviour was found from January to mid–February, when coarse mode mixing ratios were larger when fire emission sources were removed (either regionally or globally) than in the case when emissions were present. This indicated that complex changes in the aerosol growth dynamics is induced by the presence of BB aerosols (accumulation mode), causing the the concentrations of the course mode to be depleted during the BB season in Southern Africa. These changes might be linked to the increased probability of a particle coagulating with a smaller particle (in the accumulation mode) rather than

with a coarse mode particle. In fact, Porter and Clarke [1997] had already acknowledged that, on average, the peak diameter of the accumulation mode shifts to larger sizes as the concentration of this mode increases.

Chapter 6

Relevance of the synoptic variables in determining the aerosol concentrations in Southern Africa during the biomass burning season

In this chapter, SOMs were used to assess the relevance of circulation conditions influencing carbonaceous aerosol concentrations over southern Africa. Five-year daily averaged BC and OC aerosol mixing ratio are trained together with SLP, from the GLBLBB1, in a 32×21 grid covering 0°E-58°E and 38°S-1°S. Patterns have been analysed, based on the prevailing conditions, for occurrences of maximum concentrations. A 50 000–iteration SOM training process was found to be more than enough for convergence of the nodes on the SOM (A sample graph showing relative changes of Euclidean distances during the iterative training of the SOMs is presented in Appendix C). Once the high aerosol mixing–ratio nodes had been identified, geopotential heights, vorticity, wet and dry deposition velocities, and the SLP (previously used to train the SOMs) were used in GAM to assess their marginal impacts on mixing–ratios.

6.1 Identification of circulation conditions influencing biomass burning aerosol concentrations in Southern Africa using Self Organizing Maps (SOMs)

As shown in the Chapter 5, emissions of this type of aerosols are driven by anthropogenic activities regardless of the prevailing climate, and their occurrence is not intrinsically related to concentrations (Figure 5.1). Furthermore, the occurrence of emissions from outside the study area, which impacted on concentrations within the region, forced the author into finding relationships between the factors related to regional circulation patterns and the aerosol concentrations (rather than between the circulation patterns and emissions). Thus, emissions have not been accounted for in the SOM training process.

Figure 6.1 shows a 3×4 SOM composite map of archetypes resulting from a simultaneous training of SLP (shaded) and carbonaceous aerosols mixing ratios (contours). In the SLP shading, red represents higher pressure; blue represents lower pressure. In the contours, thicker lines represent larger mixing ratios; and thinner lines indicate the opposite. An additional table of graphs, Figure 6.2, is complementary to Figure 6.1, and was created to show the distribution of the number of days mapped in each SOM node per month for the ECHAM5-HAM modeling period. In these graphs, each season is depicted by a different colour (easing the interpretation of the seasonality of concentrations detailed in the graphs).

As for the SOM algorithm, opposed systems were mapped on diagonally opposite corners of the SOM map, with the transition states located in between [Hewitson and Crane, 2002]. In Figure 6.1, colour and contour patterns clearly show the archetypes evolving from the high–pressure system over the subcontinent and relatively high aerosol concentrations above 20°S (Node-01), to a low–pressure system over the whole subcontinent (together with weakening of the high–pressure systems over the Indian and Atlantic Oceans. Nodes located between Node-01 to Node-12 depict the evolution of the archetypes.

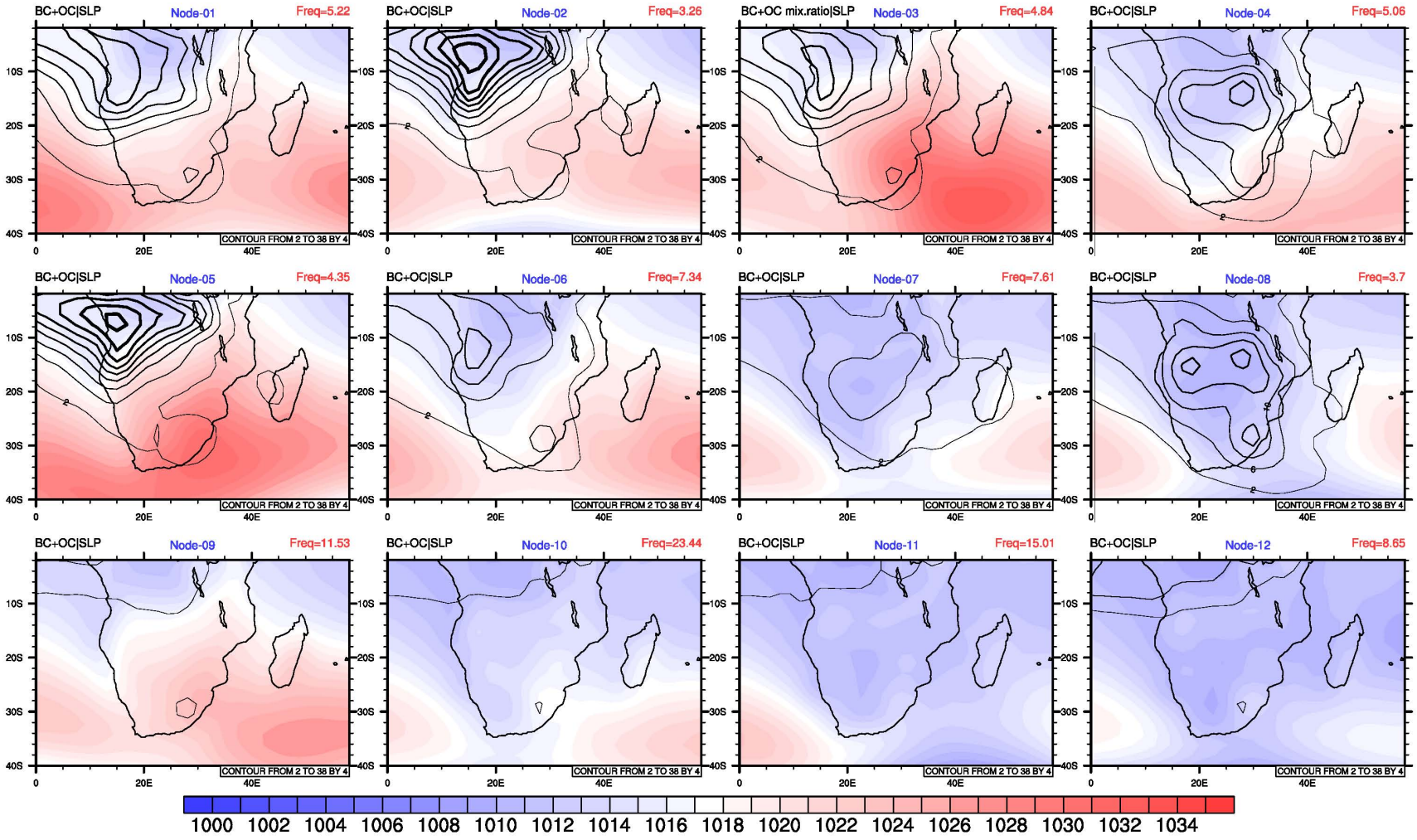

Figure 6.1: 3× 4 SOM map resulting from a simultaneous training of SLP, in hPa, and carbonaceous aerosol mixing ratio, in 10^{-10}kg/kg. SLP is shaded; mixing ratio is contoured.

Frequency distribution of the archetypes ranged from 3.26% (Node-02) to 23.44% (Node-10). These extremes, given their location on the SOM map, represented transitional states. Low frequencies were mainly located at the top portion of the SOM map (nodes 02, 03, 05, and 08); while high frequencies are mapped at the bottom portion of the same map (Nodes 09, 10, 11 and 12). Coincidentally, months with high aerosol mixing ratios are presented on the lhs while the opposite group is located on the rhs of the SOM map. Given that the SOM algorithm was trained using two variables with equal weights in the algorithm, one of which was of high variability and a short lifetime (the aerosol concentrations), the absence of the highest concentrations in the nodes with the highest frequencies was an expected result.

In the maps presented in Figure 6.1, areas with higher carbonaceous aerosol mixing ratios were associated, in general, with lower pressure systems, in general. The archetype shown in the `Node-01` (top–left), represents a high–pressure system over the southern and eastern part of the subcontinent, displaying the larger carbonaceous aerosols mixing ratios which had slotted into a relatively low pressure cell centred over Congo and part of the Atlantic coast (and, at lower levels, in a region over and around the Drakensberg mountains (Chapter 5)). This pattern, occurring approximately 5% of the simulated period, represents typical austral winter conditions, when the Indian Ocean high–pressure system, otherwise located below 30°S, is mirroring the Atlantic Ocean anticyclone on either side of the subcontinent. The two ocean high–pressure systems then merge into a single high–pressure system over the southern region of the subcontinent. In fact, counting the days in each month contributing to this node (as presented in `Node-01`, top–left graph in Figure 6.2) showed that this node (with 86 days) is mostly contributed for by July. The 86 days correspond to almost 90% of the total number of days in this node (June and August each contributed a marginal number of days to this node).

At the opposite end (denoted as `Node-12`, at the bottom–right of Figure 6.2), the Indian Ocean anticyclone had moved south and eastwards and had slightly weakened; the high–pressure system (once over the subcontinent) had now split into two systems, one on either side of the subcontinent; a low pressure system was well established over the subcontinental landmass. In this pattern, carbonaceous aerosol mixing ratio was almost non–existent over a large part of the subcontinent (with the exception of above 12°S). This archetype occurred in almost 9% of the simulated events and is was a pattern commonly

found over the region throughout the austral summer. This fact was confirmed through the results gained from the SOM mapping of 159 days in node Node-12 (bottom-right Figure 6.2). Node Node-12 was almost exclusively partitioned by DJF days. During the DJF season the Intertropical Convergence Zone (ITCZ) moves downwards, bringing convective rainfall which eventually rinses aerosols out of the atmosphere (by wet removal processes) and reduces the concentration of aerosols in the region.

Node-09 (bottom–left corner) of the SOM represents a situation similar to Node-01. However, carbonaceous aerosols were not yet well established over the subcontinent (apart from the Atlantic coast of Angola and the land regions in Angola and the DRC). Part of the Indian Ocean high was already over the south-eastern part of the subcontinent. Although it is still south (when compared to Node-01), the merging with the Atlantic high was visible. This circulation is typical of austral late autumn, when the single high–pressure system over the subcontinent starts to form and moves northwards. This was corroborated by the count of days in this node (bottom-left Figure 6.2), shown to mostly correspond to the MAM season (with more emphasis on May days which contributed 126 days (60%) of the 212 total count of days in this node). This was the period in which local emissions were initiated within the region.

Node-04 (top–right node of the SOM), represents the archetype in opposition to Node-09. In Node-04, the Indian Ocean high was retracting eastwards and splitting away from the Atlantic high; the continental low establishes itself over most of the sub–continent, with the exception of part of the south–eastern portion of the subcontinent. Carbonaceous aerosol mixing ratios accompanied the continental low, and even exhibited some intrusions over the Indian Ocean close to Madagascar. This period corresponds to austral spring, in which fires were active over most of Southern Africa (Chapter 5) and when the *River–of–Smoke* phenomenon is observed.

The transitional nodes with relatively high concentration of aerosols covering a large portion of the subcontinent (nodes 02, 03, 05, 06, 07, and 08) also represented the splitting of the continental high into separate Indian and Atlantic highs and the eastward displacement of the Indian Ocean high. Analysis of the occurrence days showed that these archetypes mostly fell in June, July, August, September, and, to a lesser extent, November days.

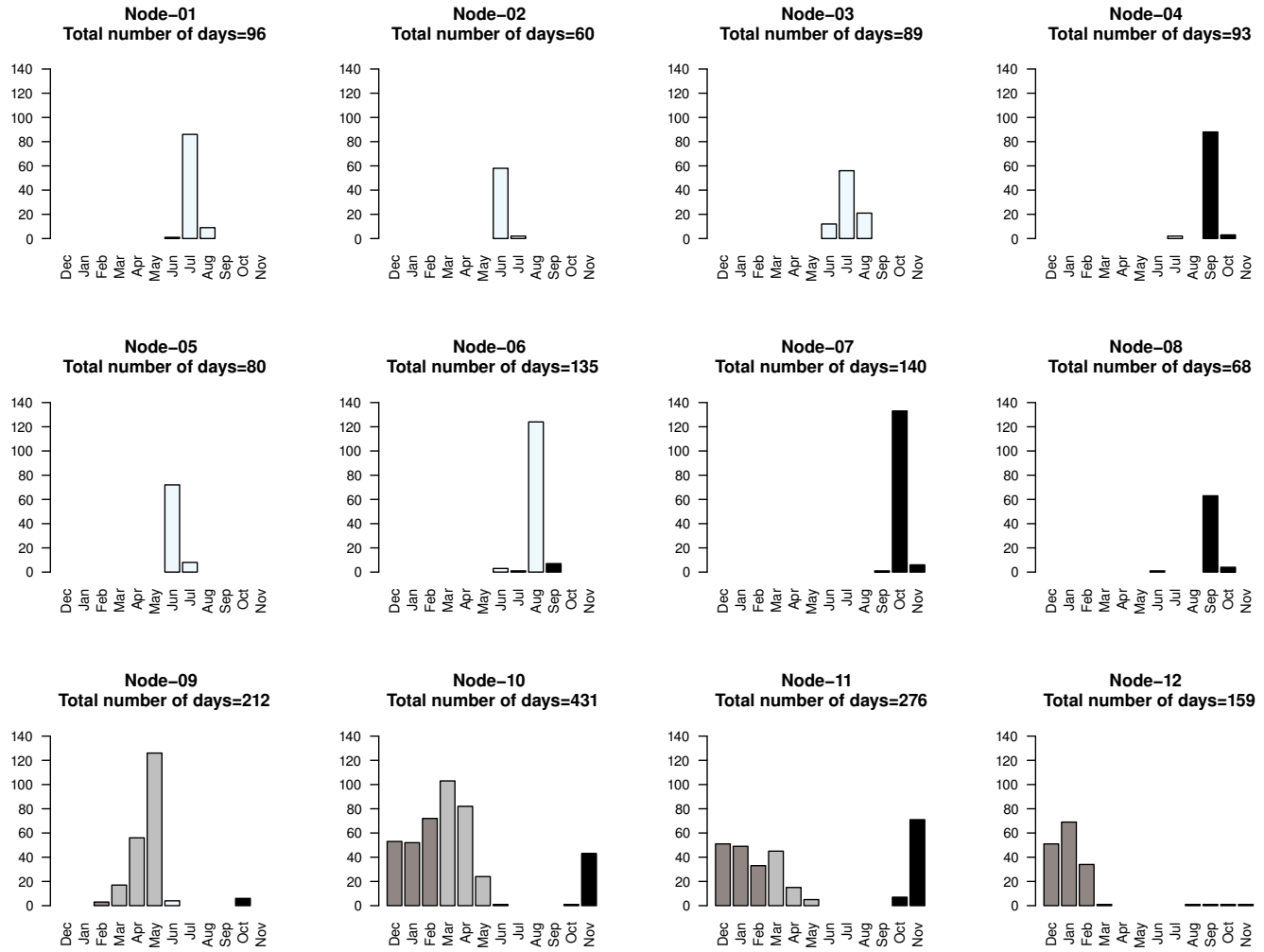

Figure 6.2: Distribution of number of days mapped in each SOM node per month for the ECHAM5-HAM modeling period.

Figure 6.3 shows the time evolution of the average number of days mapping per month for the nodes with both widespread and relatively higher aerosol concentrations (Nodes 01, 02, 05, 06, 09, 10 and 11).

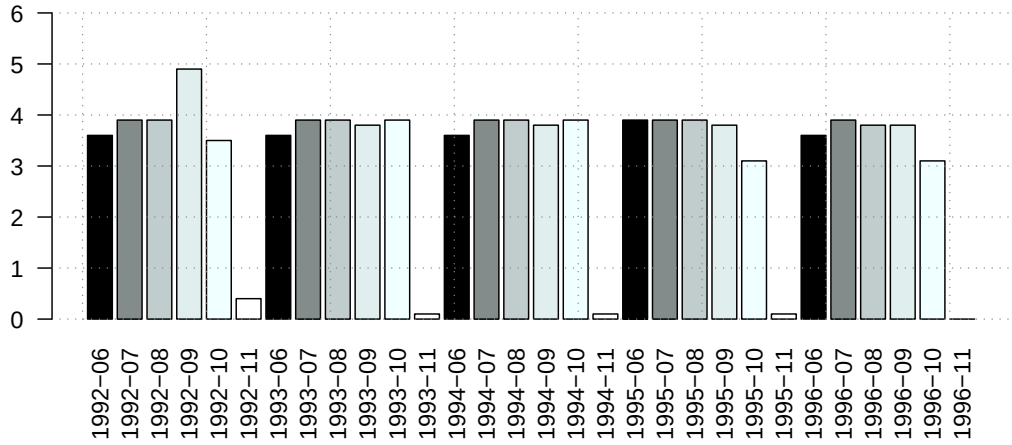

Figure 6.3: Annual frequency of months with high carbonaceous aerosol mixing ratios averaged over nodes 01, 02, 03, 04, 05, 06, 07 and 08. Each of the 6 colours represent a month, from June to November.

In Figure 6.3, the average number of appearances per node referred to above, varied between 3 and 5 for June to October, with very little internal variability. November, showed small values (below 1), with a decreasing trend along the time–line. The dry season of the 1992 showed the largest variability with September peaking at 5 appearances; November also exhibited the largest number of occurrences in the simulated period. October also showed some inter–annual variability, having increased in 1993 and 1994, then decreased to a steady value in 1995 and 1996. The overall picture was of steady behaviour throughout the modelling period, a likely effect of using monthly variations of emissions of a single year (year 2000) as reference for each year of the study period, as stated in Section 3.2.1. The relatively high peak in September occurrences in 1992 could be explained in terms of the dry conditions that prevailed in 91/92, which would favour the availability of biomass for burning [Tummon, 2010; van der Werf et al., 2006]. As stated before, these simulations used the year 2000 AEROCOM reference emissions and, therefore, other circulations factors have to be taken into account [Reid et al., 2012].

Table 6.1: Approximate significance of smooth terms.

	edf	Ref.df	F	p-value
s(SLP)	5.758	7.065	3.076	0.002955
s(850hPa Geopot)	6.965	8.072	2.947	0.002607
s(geopot700.gam)	3.839	4.961	1.723	0.126051
s(vorticity850.gam)	1.831	2.370	9.860e-01	0.384255
s(vorticity700.gam)	1.000	1.000	4.680e-01	0.493738
s(wetdepo.gam)	1.000	1.000	2.020e-01	0.653192
s(drydepo.gam)	4.650	5.733	9.480e-01	0.456370

6.2 Assessment of the relative importance of synoptic variables in the determination of aerosol concentrations in Southern Africa using Generalised Additive Models (GAMs)

The extent to which factors associated with atmospheric circulation individually affect carbonaceous aerosols concentrations over the region, is presented below using the GAM technique (Equation 3.5, Chapter 3).

The approximate significances of each of the smoothed terms, after GAM simulation with the covariates proposed by Equation 3.5, are summarised in Table 6.1, where "edf" values represent the estimated degrees of freedom for the model terms; "F" gives a rough estimate of the importance of each term; p-value is p-value for the test. Results indicated that the model was able to explain 94.2% of the variance, with SLP the most important circulation parameter influencing the mixing ratios ($F \approx 3.1$; $p < 0.005$); followed by the geopotential height at 850hPa ($F \approx 2.9$; $p < 0.005$). Other parameters (e.g., the 700hPa geopotential height; the vorticity and the deposition velocities) had a lower impact on the mixing ratios in the proposed model.

Figure 6.4 shows the partial response plots of carbonaceous aerosol mixing ratios relative to:

a) SLP;

b) 850hPa geopotential height;

c) 700hPa geopotential height;

d) Vorticity at 700hPa;

e) Wet deposition velocity;

f) dry deposition velocity.

The shaded region represents the 95% confidence interval for the GAM fits; the short vertical lines on the horizontal axis represent the data density used for the fitting.

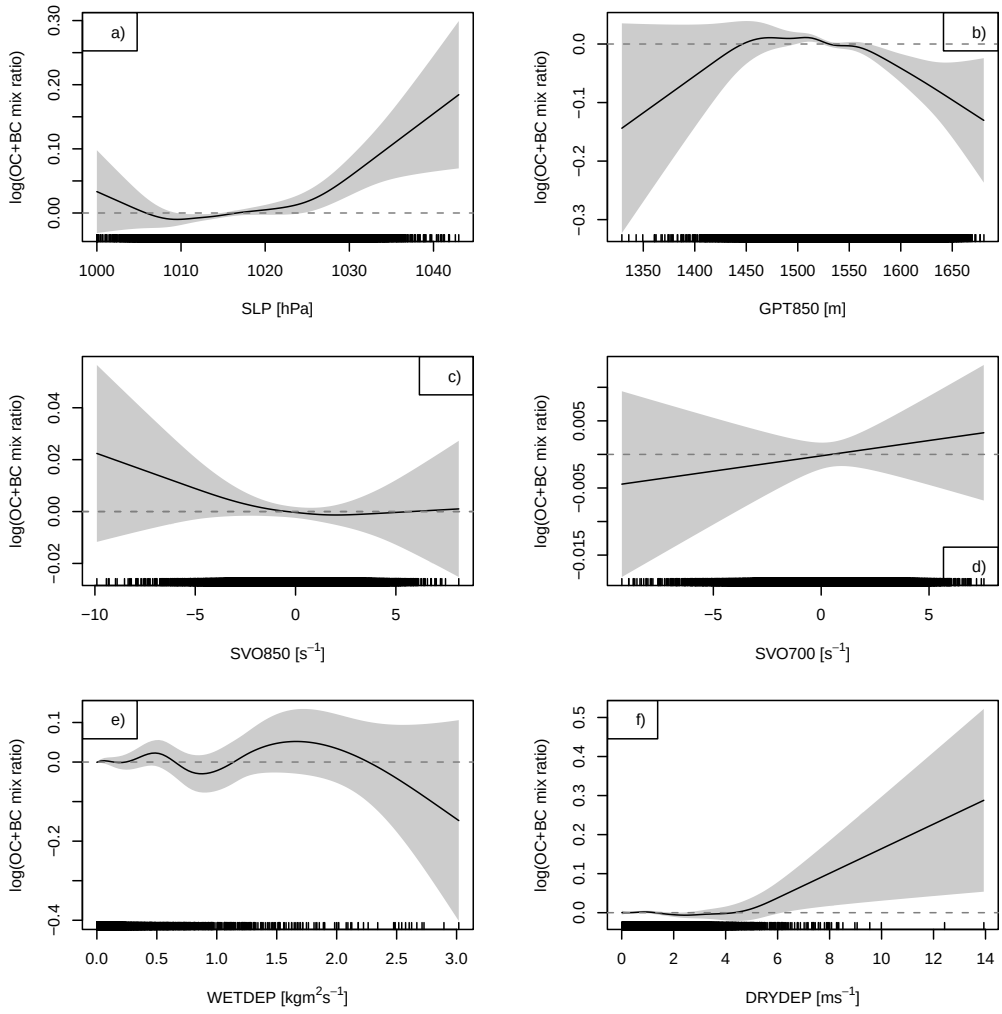

Figure 6.4: Partial response plots for carbonaceous aerosols for the nodes with days with large carbonaceous aerosol overcast. a) is for SLP; b) is 850hPa geopotential height; c)Vorticity at 850hPa; d) Vorticity at 700hPa; e) Wet deposition velocity; and f) dry deposition velocity. Shaded region shows the 95% confidence interval for the fits; short vertical lines at the horizontal axis represent data density.

The smoothed function $s(SLP)$ depicted in Figure 6.4a) relates the mixing ratios to SLP in a quasi–parabolic way so that a negative effect is seen as long as the SLP values

remain outside the range 1005hPa–1015hPa. Otherwise, the SLP slightly diminished the mixing–ratios. The slope of the increase was larger if SLP was above ≈1025hPa than when SLP was lower than ≈1005hPa. A change in SLP from 1000hPa to 1010hPa could reduce the mixing ratios by 5%; a change from 1015hPa to 1040hPa could increase the mixing ratio by ≈20%.

The behaviour of the 850hPa geopotential height (Figure 6.4b), is the inverse of SLP. The effect displays a convex curve, intersecting the horizontal axis at approximately 1450m and 1525m. The impact varied by almost -15% when the geopotential height varied between 1330m and the first intersection with the horizontal axis. Between the two interactions, the impact was slightly positive but vey close to nil. Thereafter, the height had further negative influences on the mixing height, with a similar slope to that seen at 1450m.

For vorticity at 850hPa, an apparently a positive impact occurred only if the circulation was anti–cyclonic in the region, with a maximum variation of approximately 2% at -10×10^{-5}s^{-1}. When vorticity was positive, no clear impact was seen. In relation to the 700hPa vorticity, very little changes of mixing–ratios were seen. Mixing ratios appear to be are linearly related to the vorticity at this level; the impact varied from 0.5%–0.5%.

The response of the mixing–ratios to the wet–deposition velocity is a complex function similar to an amplified oscillator, where the response fluctuates between positive and negative values, with increments in both amplitude and period throughout the cycle. The amplitudes of the impacts ranged from 0% (when wet–deposition velocity was nil) to close to -20% (when velocities were 3×10^{-10}kgm^2/s). The number of data elements of wet deposition velocity used in the model decreased substantially between 2 – 3×10^{-10}kgm^2/s.

In turn, mixing ratios responded to dry–deposition velocities in a positive manner. Generally, no considerable impact was seen until dry deposition velocities reached 4mm/s; at this point a linear positive response took place and, at 14mm/s, the response was approximately 30%. The uncertainty of the model is large especially in the range of 8–14mm/s, since very few data elements were found in this interval.

6.3 Summary

In order to identify circulation conditions which are likely to influence carbonaceous aerosol concentrations over Southern Africa, a SOM algorithm was applied simultaneously

to two variables (daily averages of BC and OC aerosol mixing ratios and SLP of a five-year period), in a 32×21 grid covering 0°E-58°E and 38°S-1°S.

Frequency distribution of the archetypes in the SOM indicated that extreme frequencies occurred in the transitional nodes, given their location in the map. This occurred mainly because one of the variables in the SOM training process – the aerosol mixing–ratio – was of high variability and short lifetime when compared with the SLP. As a consequence, the highest mixing–ratios were not located in the nodes with the highest frequencies.

Since the period of interest in this study is when Southern Africa is covered by carbonaceous aerosols, histograms of months mapped in the SOMs were produced and showed that the highest frequencies of months with large BB aerosol concentrations in the region correspond to the June–October period, with minor occurrences of November. This corresponds largely to the onset and offset of regional BB season. Additionally, no clear annual changes were discernible, presumably because each year of the modelling period is driven by the same year 2000 monthly averaged reference emissions from AEROCOM. This implies that the AEROCOM reference emissions may give a indication of the seasonality of the emissions, however, they fail to give annual variations in resulting BB aerosol concentrations in the region.

SLP appear to be a good indicator of where larger values of pollution are likely to be found over Southern Africa. In fact, according to the SOMs, modeled Southern African aerosol pattern seemed to be controlled by the Indian and Atlantic high–pressure systems with aerosols sitting inside the continental low, with some intrusions to the Indian Ocean below 20°S, when the Indian Ocean high retreats to the East. This period primarily corresponded to September, when the famous annual *River–of–Smoke* phenomenon occurs [Annegarn et al., 2001].

GAM was applied to evaluate the relative importance of the circulation variables on the regional concentrations of carbonaceous aerosols, during the months identified in the previous step. To confirm the suppositions, GAM simulated results showed that SLP was, in fact, the most important factor determining aerosol concentrations over Southern Africa, followed by the other factors such as geopotential heights, vorticity and wet and dry deposition. In fact, the deposition velocities seem to be largely uncertain as their confidence interval spans a large area in the graphs (Figures 6.4e,f), and, therefore, their results should be interpreted cautiously. Croft et al. [2010] have shown that uncertainties

in wet-deposition could be related to the representation of in–cloud scavenging processes; Grönholm et al. [2007] have shown that the dry deposition of aerosol particles is particularly highly dependent on either atmospheric turbulence or stability and the collecting properties of the surface, factors not accounted for in our GAM since circulation variables were of concern.

Nonetheless, the significance of dry deposition (F=0.95) is approximately five times higher than that of wet deposition. This was probably because wet deposition would occur mostly from the onset of the rain season in the region (October) onwards, however, the major source of aerosol emissions during that period is the Southern African subcontinent, as was seen in the previous section, and is ceasing the emissions, and, therefore, there are no considerable amounts of aerosols to be removed by wet–deposition, and thus the reason for the low significance in wet deposition.

Chapter 7

Potential feedbacks between biomass burning aerosols and the thermal structure, the atmospheric circulation and precipitation

Resulting differences from the GLBLBB1 and RGNLBB0 simulations have been used in this chapter to assess the feedback between BB aerosols, the thermal structure, atmospheric circulation and precipitation. Analysis of the impact of the BB aerosols on the thermal structure targeted the months with positive aerosol concentration anomalies and relatively large regional coverage(as identified by the SOM procedure in the previous chapter); for atmospheric circulation and precipitation the analysis was extended to all seasons of the year, making it possible to assess the change in the regional atmospheric dynamics caused by BB–induced changes in the radiative forcing over the region.

7.1 Direct and indirect effects

Figure-7.1 shows BB induced changes in the a) SSA and the impacts of BB aerosols on clear sky b) net top solar radiation; c) net atmosphere SW radiation; and d) net surface radiation for the June–October period. Corresponding zonal means are plotted on the righ hand side of each map. Blue tones indicate reduced impact; red tones indicate increased impact.

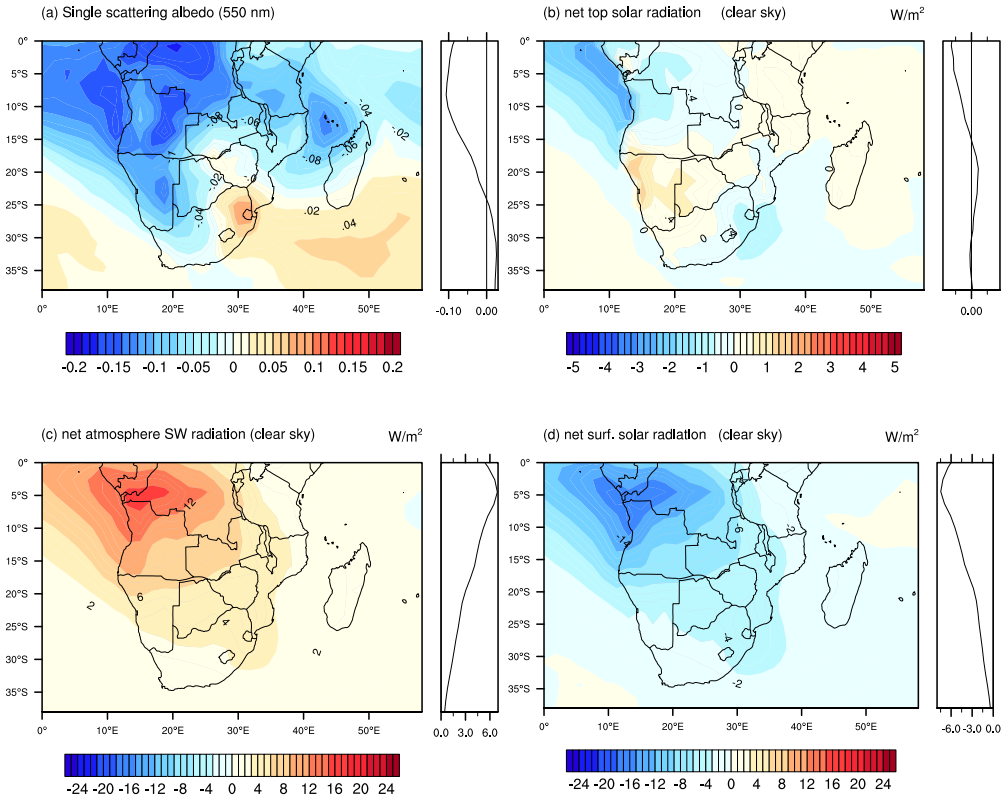

Figure 7.1: June–October averages of BB aerosol induced changes (GLBLBB1–RGNLBB0 difference) in a) SSA and b) clear–sky net TOA solar radiation; c)clear–sky atmospheric SW radiation; and d)clear–sky net surface solar radiation. Lines on the rhs of each map represent zonal averages.

BB aerosols mostly contributed to the decrease of the SSA over large parts of land in the subcontinent (Figure 7.1a), with maximum contributions occurring over the western region of the subcontinent, extending to the Atlantic Ocean and to the north–eastern part of the subcontinent. Figure A.2 presents SSA for the reference state (RGNLBB0), which shows that in the absence of BB emissions the region is somehow largely diffusive, with SSA values ranging from 0.9 to 1. When BB aerosols were added, the region mostly underwent an SSA decrease of around 0.02 to 0.08 mainly on the regions with the maximum BB aerosol emissions during this period. In turn, over land in north–eastern South Africa and southern Mozambique, and over the region where the Atlantic and Indian Ocean high pressure systems are generally located, dominance of scattering aerosols was clear, with largest SSA changes (between 0.02–0.05) found over a region centred in Swaziland, as well as over the Indian Ocean exit pathway of the *River–of–smoke*. This result implied that over and near the BB emission sources, absorption by accumulation and coarse mode BC aerosols dominates over scattering by OC aerosols; away from the sources, in the southern regions, fine mode

OC scattering aerosols dominated. The BB fine mode scattering OC aerosols tended to be located inside higher pressure systems rather than lower pressure systems (as demonstrated by the SOM and GAM algorithms for the carbonaceous aerosol in the previous chapter), this understanding is relatively new and will require further studies.

Modeled net top solar radiation (Figure 7.1b) showed a variation between -2.8 to $+2.2\mathrm{W/m^2}$, and appeared to respond negatively to the presence of BB aerosols, especially over ocean, where the AOD and radiative forcing maps matched. The largest negative forcing occured over water on the Atlantic coast (between 15°S and the Equator), followed by parts of the continent (over Angola and DRC and the south–eastern part of the continent over South Africa and southern Mozambique). The largest positive forcings occurred mainly over Namibia with the maximum over the Namib desert, followed by parts of Botswana, northern Mozambique and Madagascar, between 15°S-5°S.

Absorption and scattering processes in the atmosphere (Figure 7.1c) depleted large part of the solar radiation crossing it, and the overall effect on the direct radiative forcing of BB aerosols in the atmosphere was an increase of up to $16\mathrm{W/m^2}$. The largest changes occurred over the locations of maximum carbonaceous aerosol mixing ratios (as shown in the previous chapter). A similar pattern (both in space and magnitude) was also seen for net surface direct solar radiative forcing (Figure 7.1d); the latter presented slightly larger reduction values near the maximum mixing ratios, with some cancellations over the north–eastern and south–western portions of the analysis area.

The overall result was one of negative forcing of BB aerosols at all levels, mainly where the largest concentrations were seen (which is a known result from several studies cited in this thesis). However, for Southern Africa, the sudden appearance of positive clear–sky TOA SW forcing in certain areas was slightly different from the results obtained, for example, by Roeckner et al. [2006b] and Sakaeda et al. [2011]. Their studies only accounted for the optical properties of carbonaceous aerosols, leaving aside sulphate nucleated from BB SO_2. This aerosol is known to be highly reflective and, if over deserts, may enhance the already high desert albedo itself (as indicated by Power [2003]). Furthermore, with the addition of BB aerosols, the BC/OC (absorbing/reflecting) ratios may have a role top play in determining the SSA over these regions. This effect may also be an artifact of the model because of the existing complexities in estimating aerosol absorption over bright areas, caused by the Critical Surface Albedo (CSA) [Seidel and Popp, 2012].

The simulated role of cloud in the absorption and scattering of radiation, and the combined radiative effects of BB aerosols and clouds are presented in Figure 7.2.

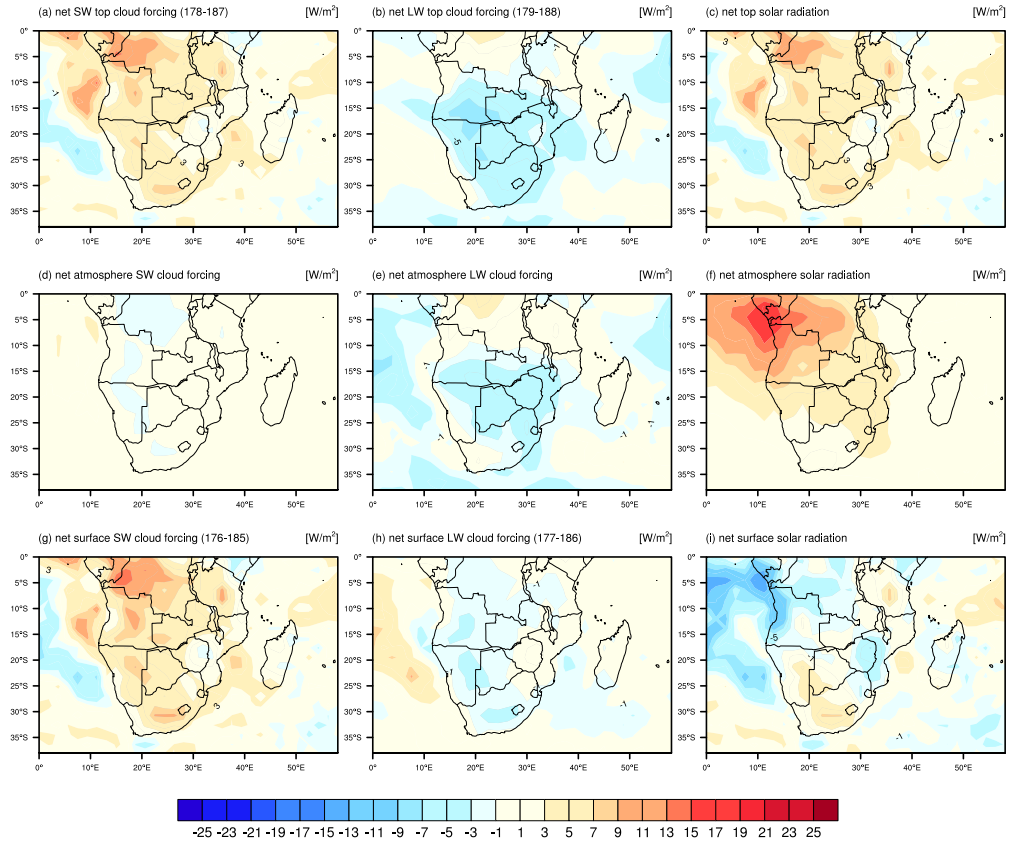

Figure 7.2: BB induced changes in radiative forcing components for cloud SW (lhs column); cloud LW (middle column); and net solar (rhs colum). Rows indicate TOA (top); atmosphere (middle); and surface (bottom). The third column indicate the all–sky radiative forcing. Units are in $\mathrm{W/m^2}$.

Model results indicated that the contribution of BB aerosol cloud forcing to the net forcing (top row) was mostly manifested through the SW component, with an order of magnitude larger than the contribution of the LW component, which does not seem to vary much over land, regardless of the level of the atmosphere (Figures 7.2b,e,h). Net top solar radiation (Figure 7.2c) was an unequivocal result of net SW TOA cloud forcing (Figure 7.2a). Although the negative values of the clear–sky net TOA solar radiation (Figure 7.1b), they were around an order of magnitude lower than the SW TOA cloud forcing and, thus, not enough dominant to compensate it at this level.

In the atmosphere (Figure 7.2 middle row), the cloud responses were around 10 times weaker than the clear sky atmospheric SW radiative forcing (Figure 7.1c). Thus, the net

atmosphere solar radiative forcing was mostly determined by the aerosol component. Both SW and LW cloud forcings were negative; although low in magnitude, LW radiation was larger than SW.

On the surface, competing negative SW clear–sky (Figure 7.1d), mostly positive cloud SW (Figure 7.2g), and mostly negative cloud LW (Figure 7.2h) forcings resulted in the complex pattern shown in (Figure 7.2i), in which parts of the continent received less radiation while other parts received more because of the combined effects of the BB aerosols and clouds (Figure A.5, in the Appendix, for the correlation of net surface forcing over two distinct regions - one region under the influence of aerosols only; the other with competition of aerosols and clouds). As a result, southern and southwestern parts of the subcontinent experience a increase of solar radiation of around 5–7 W/m^2; parts of Zimbabwe, central Mozambique and the north western region of the domain, where largest negative SSA values were registered, experienced a decrease of the same magnitude.

Modeled BB aerosol induced changes in near–surface temperature as a consequence of the forcings described above, as well as the resulting changes in SLP during June–October period, are shown in Figures 7.3a and b. In the graph, blue tones represent negative changes; red tones represent positive changes.

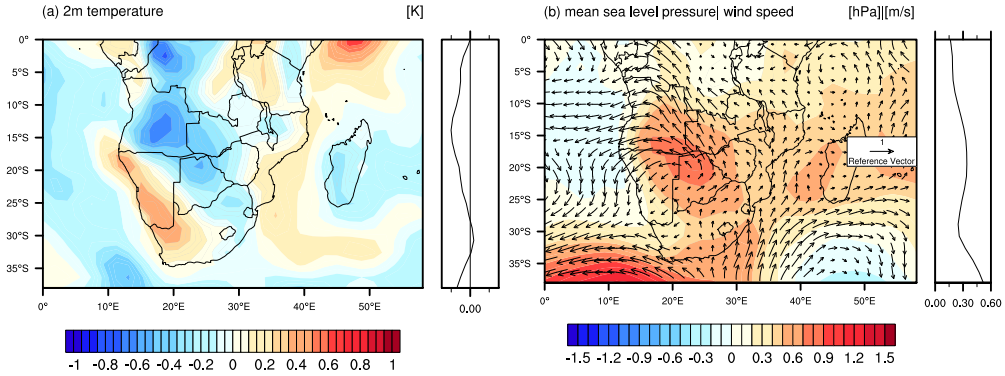

Figure 7.3: June–October BB induced changes in a) 2m temperature and b) mean SLP.

The net surface radiative forcing described above, caused the changes in near–surface temperature shown in Figure 7.3a during the June–October period. Over the oceans, opposite signs were seen for near–surface temperature: while the Atlantic cooled by up to –0.4K; the Indian Ocean side of the subcontinent warmed by the same magnitude. Over land, the largest cooling (of up to 1K, associated with the net atmospheric SW radiative forcing caused by absorption and reflection of the BB aerosols) occurred mostly over the regions

where the change of SSA was negative – from the DRC, crossing Angola to north–eastern South Africa and parts of north–western Mozambique.

Regions with a positive temperature response to the BB aerosols (specifically, the south–western portion of the subcontinent and Indian Ocean coast) were largely influenced by the positive net surface SW cloud forcing, suggesting that the suppression of clouds leads to an increase of SW radiation; added to the high albedo of the Kalahari desert and the scattering properties of the aerosols leaving the subcontinent through the Indian Ocean exit pathway. The zonal mean of regional surface temperature was consistent with the spatial map, showing the maximum reduction approximately at 15°S, with a slight increase around 30°S because of the responses of the desert and the Indian Ocean side of the subcontinent. The air warming pattern over the Indian Ocean side matched that observed during the *River–of–Smoke* phenomenon as discussed before, and is a signal typical of the fine mode biomass burning exiting the subcontinent, alongside the eastward displacement of the Indian Ocean high pressure cell. The spatial pattern of temperature obtained in this study, slightly differed with the results obtained for the same region by Sakaeda et al. [2011], in which the reduction of temperature was twice as high, and no increase in surface temperature was noticed on the Indian Ocean side and the south-western region.

As a result of the surface cooling/warming, mean SLP slightly increased/decreased throughout most of the study domain by approximately $\mp$0.3 to $\pm$0.6hPa (Figure 7.3b). The changes in SLP caused the wind convergence zone over land in Angola to move slightly from the inner continent to the Atlantic coastal region; an enhancement of convergence over DRC and, to a lesser extent, over the eastern part of the subcontinent. Over land, the overall impact of the BB aerosols was a reduction in the typical anticyclonic flow. The outer boundary of the Atlantic high intensified its anticyclonic speed by around 1m/s (i.e., the high pressure system slightly moved northwards), thus reducing the speed of westerlies; while the Indian high pressure system weakened by the same amount (i.e., slightly moved southwards). Over the eastern coast above 30°S, a lessening of up to -0.5m/s of the easterlies was seen, the likely cause of changes in the quantity of moisture advected from the Indian Ocean to the north–eastern part of the continent, and subsequently the cause of changes in precipitation (discussed in Section 7.2). These results are consistent with those obtained by Ming and Ramaswamy [2011] and Ming et al. [2011].

Modeled BB induced changes in the vertical profiles of temperature and vertical velocity

and cloud fraction and aerosol number for the JJASO period, averaged between 10–30°E over land (Figure 7.4); 0–10°E in the Atlantic Ocean side (Figure 7.5); and 30–50°E in the Indian Ocean side (Figure 7.6), respectively, were mapped. Averaging over these longitudes was considered appropriate to capture response of the troposphere to the different surface temperature settings (Figure 7.3).

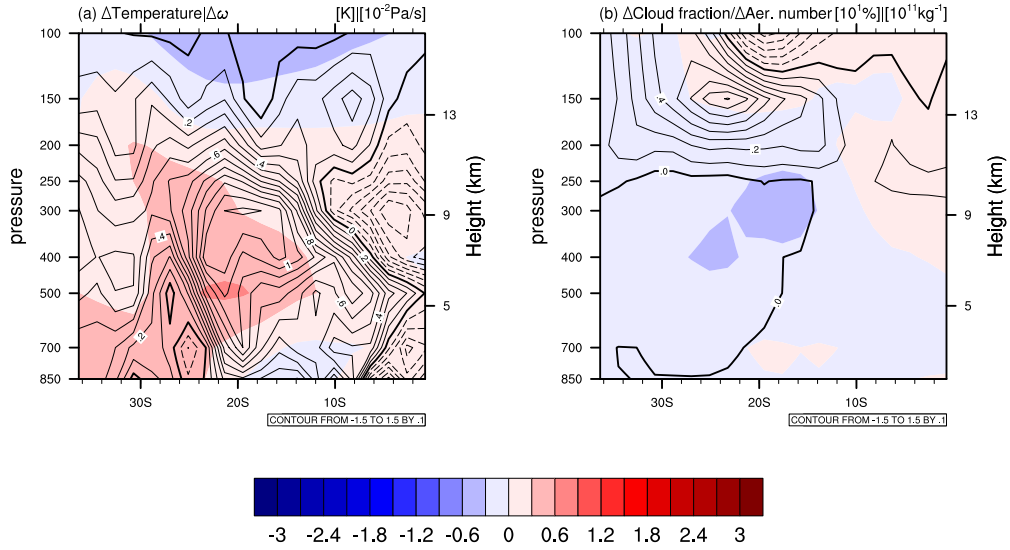

Figure 7.4: Modeled vertical profiles of BB induced changes in a) temperature (shaded) and vertical velocity ($\Delta\omega$) (contours) and b) cloud fraction (shaded) and aerosol number concentration (contours), over land (10E-30E), for June–October period. Red tones and full contour lines indicate positive values, while blue tones and dashed contour lines indicate upward directed/negative vertical velocities/aerosol numbers changes.

Over land in Southern Africa, mid–troposphere diabatic heating caused by absorbing aerosols, combined with the surface cooling, dampened vertical motion from surface, and, additionally, as the troposphere was almost well mixed with absorbing aerosols, a quasi–uniform heating profile was seen. This caused most of the troposphere to increase stability and, thus, induced a decrease of vertical velocity over large portions of the domain in consideration, with the exception of above 8°S, where velocity was slightly increased (Figure 7.4a).

At altitudes above 150hPa, a second inversion in the temperature profile was induced by BB aerosols; the maximum reduction of up to 0.6K occurred between 30°S–10°S. This was very close to the maximum where vertical velocities changed sign and enhanced upper level convection. The velocity changes caused the increase of up to 6% in cloud cover seen in Figure 7.4b over the same regions, while the remaining portions experienced a reduction

of similar magnitude.

The intense reduction of around 9% of cloud fraction, seen between 30°–15° at altitudes between 500hPa – 250hPa, was because of evaporation, since the aerosol concentrations do not change over this space. Above 15°, at altitudes between 500hPa and 150hPa, cloud fraction a to respond to the microphysics (with the aerosols acting as CCN), as with the increase in temperature over this region, a reduction of cloud fraction would have been expected. The overall pattern was one of decreased lower and mid-level clouds, compensated in some manner by increased upper level clouds; both changed by less than 6% in magnitude. Therefore, an insignificant negative impact on precipitation was to be expected over land during this period.

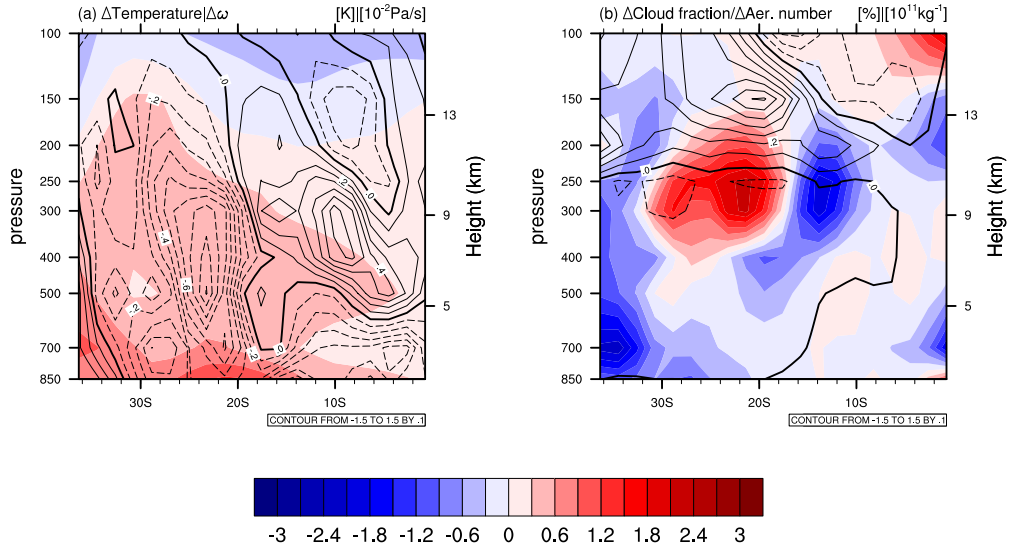

Figure 7.5: Same as Figure 7.4, but for the Atlantic Ocean side (0°E–10°E).

Over the Atlantic side, (Figure 7.5), the tropospheric temperature changes are larger than over land, with increases of up to 1K between 30–10°, at levels below 700hPa, because of absorbing aerosols. Below 30° the band with intermediate increases in temperature reached heights close to 400hPa, because of the contribution of scattering aerosols which dominated over absorbing aerosols in this region (Figure 7.1a), resulting in increased warming of upper levels by back–scattering of solar radiation. Vertical velocities were largely increased from the mid–troposphere to 100hPa height, at regions below 20°S. The velocity changes were caused caused by the large temperature gradients between the mid and the upper levels as compared to the case over land in Southern Africa. Between 20°S–5°S, differing vertical gradients of temperature anomalies caused the vertical velocities

changes to be stratified, with increased updrafts below 500hPa; reduced updrafts between 500–250hPa; and, further increased updrafts above 250hPa. In general, in this region, cloud fraction response and temperature display an inverse proportionality throughout all levels. However, the massive increase in cloud fraction between 32E–18E, at levels between 400–150hPa should to be attributed to microphysics and the shielding caused by an increase of upper level fine mode scattering aerosols, which appear to prevent cloud evaporation.

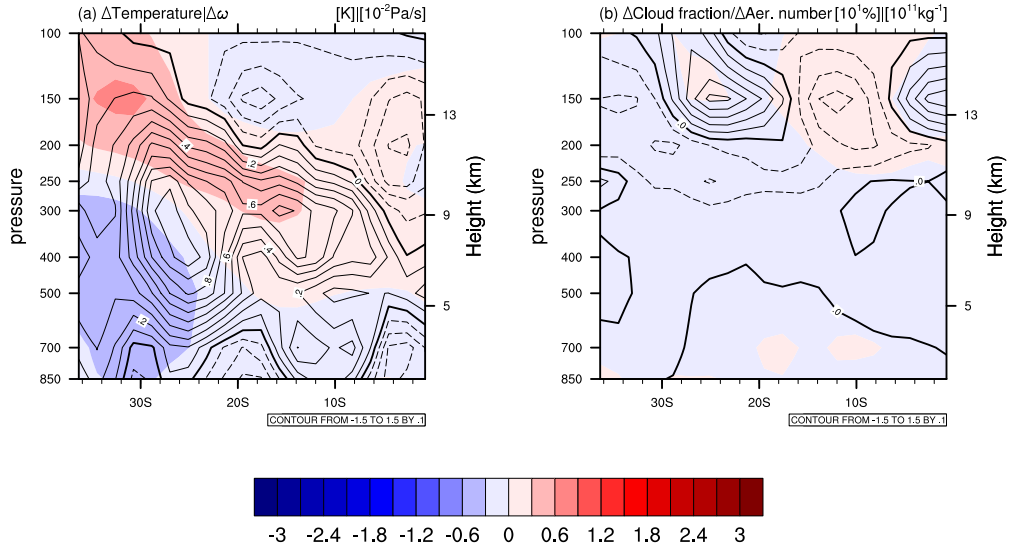

Figure 7.6: Same as Figure 7.4, but for the Indian Ocean side ($30°$E–$50°$E).

On the Indian Ocean side ($30°$E–$50°$E), temperature response was slightly weaker than on the Atlantic side, with the lower levels cooling even further, and reaching altitudes close to 9km below 20°S. A large cooling cell of up to –1K was found hovering above at approximately 32°S. The increased surface temperature (Figure 7.3a) added to the cooled lower level tropospheric layer (Figure 7.6a) (which was cooled due to scattering aerosols) caused an enhancement of lower level tropospheric convection; this was then suppressed at the mid-troposphere by an increase in temperature (caused through reduction in the number of scattering aerosols, and an eventual increase in concentration of the absorbing aerosols), which in turn caused reduction in cloudiness (Figure 7.3b). Eventually the CCN number concentration was also reduced. In the upper levels, temperature response was still positive below 25°S, while becoming negative above that latitude, thus favouring upper level convection. Aerosol numbers appeared to counteract the temperature induced cloud evaporation effect in the upper levels between 30°S–25°S. This reduction in temperature caused cloud fraction response to be slightly positive at these levels.

The overall impacts of BB aerosols and precursors over Southern Africa displayed increasing tropospheric temperature over regions where absorption dominated over scattering (i.e., over most of the northwestern region of the study domain), thus reducing cloud cover, a result consistent with studies carried out for the Southern African region by Tummon et al. [2010]. However, with the inclusion of sulphate aerosol nucleated from SO_2 from BB (known to be a hygroscopic and scattering aerosol [Boucher and Lohmann, 1995; Ramana et al., 2010]), the response of temperature and clouds on the Indian Ocean side presents a different behaviour from that documented by Roeckner et al. [2006b]; Sakaeda et al. [2011] and Tummon et al. [2010], once the semi–direct and first and second indirect effects began to play a role in the simulations. This finding was hypothesized by Randles and Ramaswamy [2010], where it was anticipated that a change in low–level circulation and increased subsidence would cause a decrease in cloudiness, precipitation and atmospheric water vapour, should the atmosphere be dominated by scattering aerosols.

Nevertheless, because changes caused by the indirect effect did not seem to fully compensate for the magnitude of those caused by the direct effect, it was expected that an increase in tropospheric temperature and a reduction in cloudiness would still prevail; and the consequences to precipitation would be low and limited to where there was considerable competition between the direct and indirect effects, and where considerable changes in circulation had occurred. Similar results on the magnitude of the response of clouds have been found over South America by Wu et al. [2011].

The impact of BB aerosols on a) convective and b) grid–scale precipitation is presented in Figure 7.10. Units are percentage departure of daily averaged precipitation in mm/day (averaged over June–October 1991–1996 period) and the shaded regions show precipitation where values were at the 90% confidence level.

As expected, low response in both convective and large scale precipitation was found during this period, mainly because the analysis period largely included the austral dry season. However, a modest negative response of around –25% was found for both convective and large-scale precipitation over Mozambique and Zimbabwe during this period; over Madagascar and parts of the Indian Ocean, and over the Atlantic coast, some localised increases of up to 80% in daily amount of precipitation were seen. The pattern of convective precipitation reduction seen over southern Tanzania and central Mozambique and Zimbabwe (Figure 7.7b) was probably associated with the second indirect effect, in

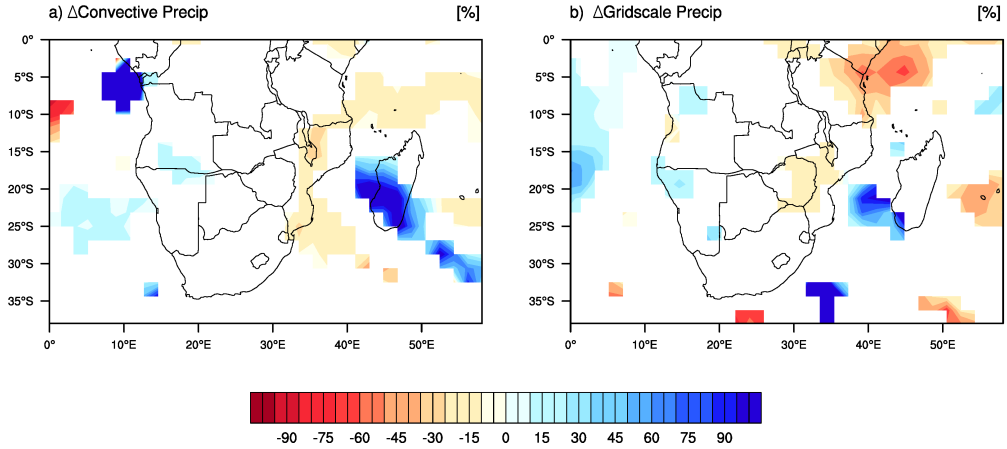

Figure 7.7: June–October fire induced departures in precipitation for a) convective; and b) grid–scale precipitation. Values are in percentage of [mm/day] and only those at 90% significance level, according to *Student's t-test*, are presented. Blue tones represent wet bias; red tones represent dry bias.

which increased concentration of sulphate CCN (Figure 7.8a) resulted in reduced nucleation rate (Figure 7.8b), and increased high cloud fraction (Figure 7.8c), suppressing precipitation formation (as hypothesized by Boucher and Lohmann [1995] and also discussed by Quaas et al. [2009], Takemura et al. [2005] and Myhre et al. [2007]). For the large-scale precipitation (Figure 7.7b), the pattern of precipitation reduction in Central Mozambique and part of Zimbabwe was largely associated with reduction of moisture convergence in this period. (Figure 7.3b).

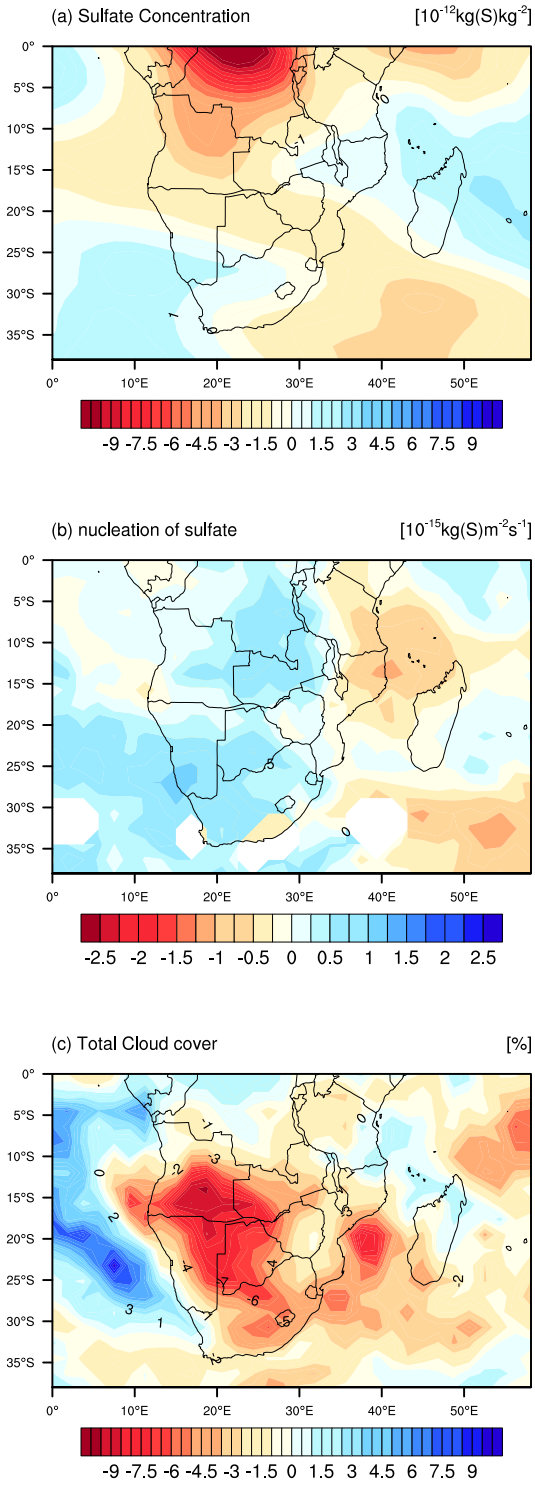

Figure 7.8: June–October BB induced changes in a) Sulphate concentration; b) Sulphate nucleation; and c) Total cloud cover.

7.2 Effects on circulation

What changes does a transient phenomenon such as biomass burning have in seasonal and inter–annual precipitation? In an attempt to answer this question, seasonal and

inter–annual maps of the extent of BB induced changes (GLBLBB1 – RGNLBB0) in temperature, mean SLP and total precipitation and circulation are presented below. Mean SLP is chosen to describe the effect of circulation because of its strong relationship with BB aerosol concentrations (Chapter 6).

Figure 7.9 shows seasonal changes in temperature (shaded) and mean SLP (contours) over the region. Blue tones indicate negative changes and red tones represent positive changes; the thick red line is the zero transition line The seasons represented are a) DJF; b) MAM; c) JJA; and d) SON. In Figure 7.10, the left-hand side column represents changes in precipitation, and the *Student*'s t-test 90% significance level seasonal precipitation differences maps are shown on the right-hand side (representing seasonal precipitation change (shaded) overlaid to streamlines at 850hPa (right-hand side column). The maps were defined for DJF (a and b); MAM (c and d) JJA (e and f); and SON (g and h) seasons. Precipitation unit is given as percentage of mm/day. Zonal means have also been included on the right-hand side of each map.

Seasonal changes shown in Figure 7.9 indicate that, in austral summer, there was a modest BB radiative forcing induced cooling/warming, of up to 1K in magnitude, over near land/ocean surfaces. While the mean SLP had diminished overall during this season, decreases over land were slightly less than over oceans. In MAM, the pattern was one of an accentuated decrease in surface temperature in the southern portion of the land, with no considerable changes noted over the ocean. Mean SLP had increased by 1.5hPa overall, slightly diminishing at both the Atlantic high and the Congo low by nearly the same magnitude. In JJA no considerable changes of temperature were seen over land; the Atlantic Ocean appeared to cool more than the Indian Ocean. Mean SLP had increased overall by 1.5–2.5hPa, with the largest increases located over the southern portion of the study domain. Finally, in SON, the temperature and pressure patterns were similar to that displayed in Figures 7.3a and b (thoroughly discussed in Section 7.1).

BB aerosol impact in precipitation showed a tendency to increase precipitation on the western portion of the subcontinent; a tendency to decrease precipitation was noted for the eastern portion during austral Summer, autumn and winter seasons (Figure 7.10a, and b). Slight changes towards the opposite direction were noted during the austral Spring (Figure 7.10g). A strong signal of precipitation increase of up to 80% was be found over the Atlantic Ocean, in the northwestern region of the domain; conversely, a prominent reduction

between 40–60% was seen in DJF (Figure 7.10b) over central and northern Mozambique, Malawi, Tanzania, Madagascar, as well as over the Mozambique Channel.

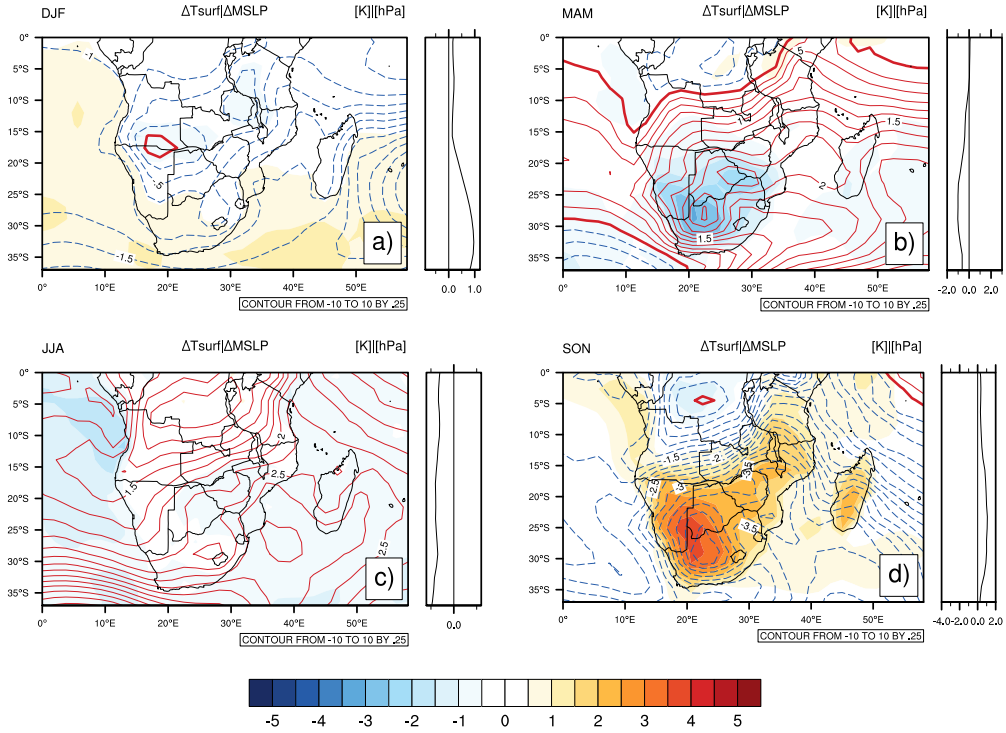

Figure 7.9: Seasonal changes (GLBLBB1-RGNLBB0) in Temperature (shaded) and mean SLP (contours) over the region. Blue tones indicate negative changes (shaded and dashed contours) and red tones (shaded and contours) represent positive changes. The thick red line is the zero transition line. Seasons represented are a) DJF; b) MAM; c) JJA; and d) SON.

In DJF (Figure 7.9a), the upper–level fine mode aerosol burden from northern Equatorial Africa was brought back into the subcontinent by an induced recirculation system over the Atlantic coast (Figure A.4, Appendix A). This burden, added to the precipitation increase, exerted a negative radiative forcing over the northern portion of the subcontinent, slightly reducing near–surface temperatures (by –1K) over the continent. Over the oceans, the radiative forcing was positive, slightly increasing surface temperatures by around the same magnitude. Although the mean SLP had, in overall, diminished during the DJF season, this pattern of surface temperatures caused decreases over land to be slightly lower than over the oceans, and thus, reducing the magnitude of the pressure gradients. Under these circumstances, the departures in precipitation, shown in Figure 7.10a and b, for the western and eastern regions of the subcontinent respectively, were probably caused by

i) an increased convergence over the Atlantic side (Figure A.10a), with wet flows from

the Equatorial Atlantic being mixed into the dry continental flows, added to the increased relative humidity;

ii) a reduction in the strength of the easterly trade winds which normally bring moisture from the Indian Ocean on to the land, thus lessening the contribution to the DJF rainfall over the continent.

iii) a positive soil moisture – precipitation feedback, i.e., if the antecedent summer season had a *deficit* of soil moisture (because of aerosol impact), precipitation in the following season would be reduced, and vice–versa [Tadross et al., 2010; Zhu et al., 2009]

iv) model's internal variability, associated to the response of the prescribed SSTs to the aerosol forcing within the mixed–layer ocean model [see for example Hagemann et al., 2006; Yue et al., 2011].

In MAM, the Atlantic wet signal moves southeastwards and over the bordering region between Namibia and Angola (Figure 7.10d); the dry signal retreated northwards to Tanzania and reduced in magnitude. The increase of precipitation simulated over the Namibia/Angola region was a result of BB radiative forcing induced changes in temperature, which caused an increase in relative humidity, adding to the new pressure gradients (weakening the Atlantic high pressure system, and enhancing the continental flow), causing the convergence of wet continental air masses (which appear to return to land after rotating over Ocean through this region (Figure A.10b), thus enhancing austral autumn rainfall. In Tanzania, analysis of the mean SLP in the surrounding areas, suggested the usual easterlies, which would bring moisture to the region, were weakened by an overall increase in mean SLP over this region. Radiative forcing induced changes caused temperature to rise over this region, thereby reducing the relative humidity. During this season it became apparent that the flow was dominated by north–easterlies, bringing dried air to the southern portion of the country.

Overall dry conditions were prevalent in this region during JJA and southerly winds were induced over the eastern portion of the subcontinent; the westerlies were generally weakened over the western coast (Figure 7.10f). Moist air was taken from the central region of the subcontinent to converge with the tropical Atlantic over the north–western region of the subcontinent (Figure A.10c), causing the slight increase in precipitation noted during this season between 10E-20E and 10S$^{\circ}$ and the Equator.

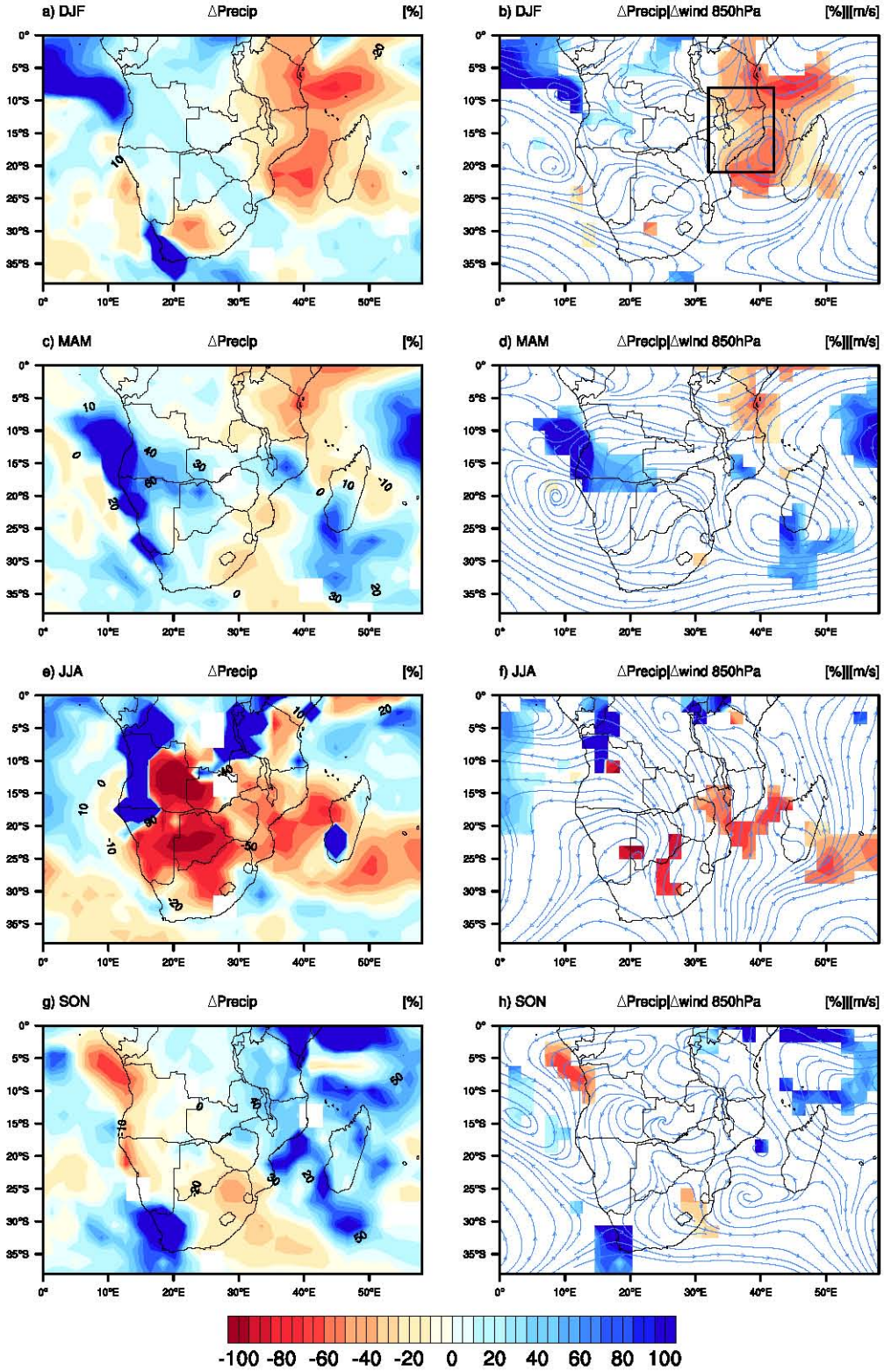

Figure 7.10: Seasonal fire induced changes in precipitation (lhs column) and 90% significance level changes in precipitation (shaded) overlaid to streamlines at 850hPa (rhs column) for DJF (a and b); MAM (c and d); JJA (e and f); and SON (g and h) seasons. Precipitation unit is given as percentage of mm/day. Blue tones represent wet bias; red tones represent dry bias.

In SON, no perceptible change in precipitation was seen over the region (Figure 7.10h), with the exception of a minor increase noted over the south–western tip of the subcontinent, caused by enhanced moisture convergence from the enhanced Atlantic anti–cyclone and the continental flow to this region (Figure A.10d).

Interest was focused on a specific region (inside the box in Figure 7.10h), representing the location where the largest precipitation reduction occurred during the DJF season. Corresponding intra–annual variability of vertical velocity and cloud cover are presented in a height–time Hovmöller diagram (Figure 7.11a,b); precipitation and surface temperature are in a line graph (Figure 7.11c).

The radiative impact of aerosols apparently caused a reduction in convection by reducing the vertical gradients of temperature, thus inhibiting convection, possibly contributing to the cloud fraction over this region in almost all the months of the year. Decreased cloudiness was notable around February, when the surface temperature increased by approximately 0.4K. Vertical velocity was reduced by increased stability from near surface to 150hPa; cloud fraction was reduced for both mid and high clouds. This reduction of cloudiness also caused precipitation to decrease over this period. It is the February signal which is being captured by the seasonal map presented in Figure 7.10b.

Later, in April, convection was slightly enhanced, also causing cloud cover to increase, because of the increased soil moisture stored during previous months. In May, with the onset of BB fires in Southern Africa, radiative forcing again caused a decrease in mid troposphere convection, apparently without a clear impact on the cloudiness, since the uplifted moisture was below the convective height. The June–August forcings, have been explained previously, and, by their characteristics, implied a reduction in precipitation as well. In November, a minor increase in mid altitude convection, seemed to have an equivalent impact on cloudiness at mid–level heights. This phenomenon appears to occur cyclically, but the magnitude of the convection and cloud cover signal was weaker in other months when compared to February.

Figure 7.12 shows the inter–annual (1991–1996) cycle of surface temperature (solid line) and precipitation (dashed line). In this graph, temperature variability exhibited an increasing amplitude trend, from ± 0.5K to ± 4K; the amplitude of the precipitation variability showed a slightly decreasing trend. The amplitude of the temperature anomaly ranged from 0.5K (in summer of 1991/92) to approximately between -3K and 4K (In summer of 1995/96

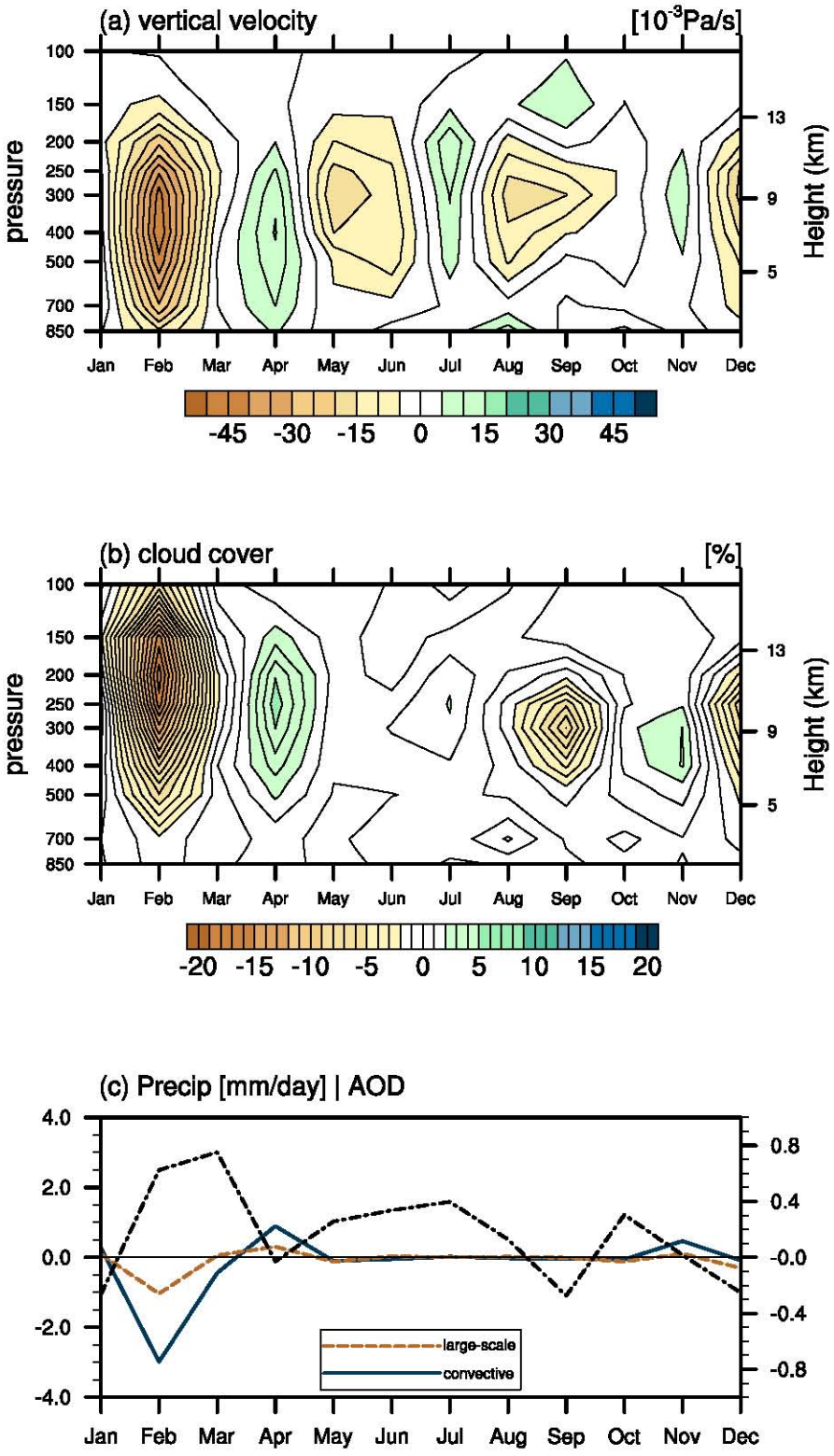

Figure 7.11: Hovmöller diagram of simulated BB radiative forcing induced changes in (a) vertical velocity in Pa/s; (b) hov-omega-clouds in percentage; and (c) convective (in continuous line) and intra–annual variability of large–scale (dashed line) precipitation in mm/day and surface temperature (dash–dotted lines) for the region marked by a box over Mozambique and Tanzania in Figure 7.10b.

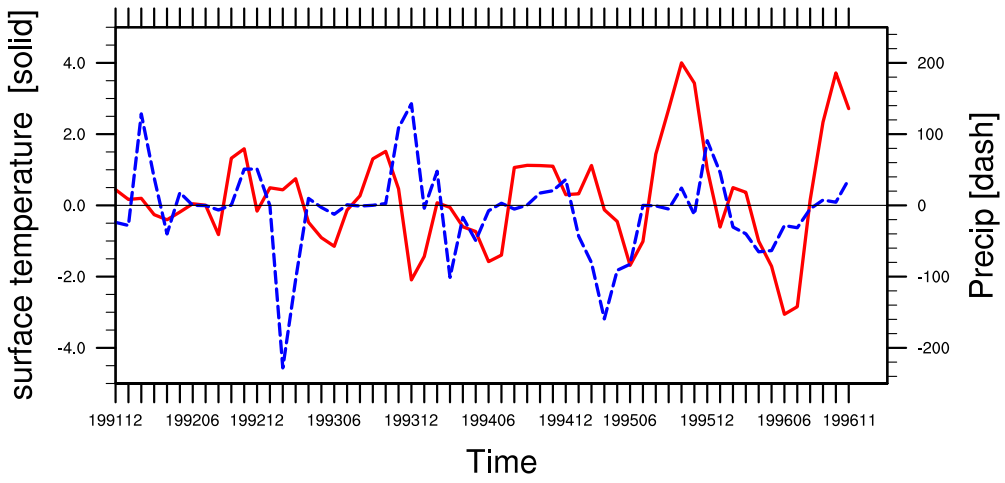

Figure 7.12: Inter–annual changes in monthly mean surface temperature (solid line) and rainfall (dashed line) for region depicted by a box over Mozambique and Tanzania in Figure 7.10b.

and in October 1996). Precipitation peak anomalies occurred around February and were lagging one month behind surface temperature peaks. Summer precipitation of 1992 had the maximum reduction of 220mm/month in this region. This reduction in precipitation can eventually be attributed to the 1991/92 drought in Southern Africa, which may have reduced the available soil moisture, required to spin–up precipitation in the following season (hinted at by Roeckner et al. [2006b]). In fact, the whole precipitation reduction trend can be explained in terms of a positive soil moisture – precipitation feedback, i.e., if the antecedent summer season had a *deficit* of soil moisture (because of aerosol impact), precipitation in the following season would be reduced, and vice–versa [Tadross et al., 2010; Zhu et al., 2009] as well as the model's internal variability, associated to the response of the prescribed SSTs to the aerosol forcing within the mixed–layer model [see for example Hagemann et al., 2006; Yue et al., 2011].

No clear explanation in terms of BB aerosols could be found for the amplitude–increasing pattern of the temperature variability. The model used only monthly aerosol emissions from the reference year 2000 and, therefore, inter–annual variability of emissions was excluded as a reason. It has been acknowledged that, over land, precipitation and temperature have strong negative correlation [van Dorland et al., 2007]. Thus, amplification of the temperature response in Fig. 7.12 is likely to be a consequence of precipitation increase caused by the model's internal variability and the response time of the prescribed SSTs to the aerosol forcing, as stated before. It is important to mention that ECHAM5–HAM has

a mixed layer which controls near–surface vertical mixing, which implies that the surface forcing of upper level aerosols is not well accounted for over oceans [see for example Yue et al., 2011].

Nevertheless, the overall impact of BB aerosol induced radiative forcing was one of reduced convergence, decreased convection and, therefore, reduced precipitation over the north–eastern region of the domain. In general, these findings are consistent with those obtained by Roeckner et al. [2006b]. They did, however, differ slightly at some locations where the inclusion of sulphate in the simulations changed the radiative forcing pattern and induced different circulation patterns (which can sometimes cause convergence to increase in some areas, therefore increasing precipitation, rather than diminishing it).

7.3 Summary

In this chapter, the potential feedbacks between biomass burning aerosols and the thermal structure, the atmospheric circulation and precipitation were assessed by analysing the differences between `GLBLBB1` and `RGNLBB0` results.

The direct and indirect impacts of BB aerosols were initially presented for the months identified by the SOM algorithm as being those with the largest aerosol concentrations over the region, namely from June to October. As the BB induced changes in radiative forcing were seen to cause changes in circulation patterns, the analysis of the impacts on circulation and precipitation was extended to other seasons of the year.

Thus, BB aerosols in Southern African atmosphere have been shown to influence the net top solar radiation through high cloud forcing; the net atmosphere SW radiation forcing was almost exclusively influenced by the absorption and scattering properties of aerosols. In turn, the net surface solar radiative forcing resulted from a combination of aerosol contribution (at the locations of largest concentrations), and the net surface SW radiative forcing (in the south and south–western region of the subcontinent).

The impacts of BB aerosols over Southern Africa were mostly manifested by increases in tropospheric temperature where absorption by BC dominated over scattering by OC and sulphate, and thus reducing cloud cover. Previous studies have demonstrated the consistency of these results; however, the inclusion of the hygroscopic and highly scattering sulphate aerosol (nucleated from SO_2 from BB) in the study, likely caused the temperature

and clouds response along the Indian Ocean portion of the study domain to be different from other studies. The semi–direct and first and second indirect aerosol effects began to play a role, although minor, in the simulations, just as Randles and Ramaswamy [2010] had hyphothesised.

Comparisons of temperature and precipitation from BB inclusive simulations (i.e., with fire emissions containing OC, BC, POM and the sulphate precursor SO_2) and simulations that excluded these factors demonstrated that some locations, returned different radiative forcing results when compared with previous studies of the region, where overall negative surface forcings were found. In this study, both negative and positive changes of surface temperature (and thus lower–level convergence) were also found.

However, because the June–October season largely includes the austral dry season, it was an expected result for a minor impact on precipitation through the indirect effects to be found. Special attention was paid to the region over central and northern Mozambique and Tanzania, where the most significant precipitation reduction was found.

Analyses of changes of temperature and precipitation in both seasonal and inter–annual scales showed that the impact of BB aerosol loading was not restricted to the June–October season. The precipitation reduction trend was accompanied by a temperature increase trend. The trend of the amplitude of precipitation variability was negative because of a memory of (low) antecedent soil moisture caused by BB aerosols; as a response, temperature amplitude increased. Large impacts on circulation and precipitation were found over land in DJF, with a significant reduction (of up to 60% in daily rainfall), caused by changes of radiative forcings induced by BB; this has impacted circulation patterns inside the Hadley cell region, and, in some cases, either favoured or inhibited moisture convergence.

This suggested that, despite the reduced occurrence of local BB aerosol emissions in other seasons, a minor disturbance of radiative forcing at the surface either caused by external aerosols brought into the region via any long–range transport mechanism or by a possible teleconnection mechanism, can lead to imbalances of SLP, causing convergence to change in direction and, thereby, impact on precipitation magnitude.

Chapter 8

Conclusions, Limitations of the study and Suggestions for Further Research

8.1 Conclusions

The aim of this study was to better understand the role of the aerosols, directly and indirectly generated from biomass burning emissions, on Southern African climate through using a state–of–the–art aerosol–climate model, namely ECHAM5–HAM. The WRF/Chem model was used as a support model to show some finer scale characteristics in the region in a shorter time–scale. The models are able to represent aerosol nucleation processes, both the direct and indirect aerosols effects, and, in the case of the latter model, chemistry. Simulation were run with and without BB emissions and, in particular, apart from the carbonaceous aerosols, the impact of which on climate has extensively been investigated by other authors before, fire emissions included SO_2 – a precursor gas of sulphate aerosols – which has different chemico–physical properties from the carbonaceous aerosols, and thus, has different radiative and microphysical properties. The specific objectives of the work were to:

- Identify the contribution of local and external sources to BB aerosol concentrations in Southern Africa;
- Assess the relevance of the synoptic variables in determining the aerosol concentrations in Southern Africa during the biomass burning season;
- Estimate potential feedbacks between the BB aerosols, the thermal structure and the

atmospheric circulation, and the consequent impacts on temperature and precipitation during austral spring, and their subsequent inter–annual variability.

Verification of the performance of the models against observed data

Initially, in order to assess the suitability of the models for the proposed study, comparisons were made between the model simulations and the actual observed climate and aerosol observations. Results have showed that ECHAM5–HAM was in good agreement with the spatio–temporal patterns of temperature and precipitation, and within the range of acceptable variability of these variables, although minor biases had been simulated by the model. Biases occurred mainly over desert areas and areas where observed data is scarce and may have been caused by the following:

(i) Although aerosols are known to play a major in the radiative forcing and thus influencing surface energy balance, they are yet properly accounted for in climate models, either because their properties are not well represented in the model equations or because they are poorly quantified and characterised in regions such as Southern Africa;

(ii) the relatively coarse resolution of the model was unable to reproduce some sub–grid scale features [Roeckner et al., 2006a];

(iii) the scarcity of good spatio–temporally resolved observational data, since CRU data itself was found to suffer from biases too, particularly over DRC [Tadross et al., 2006];

(iv) the prescription of using monthly mean aerosol emissions taken from the reference year 2000 for all the simulation years, instead of the inter–annually varying emissions [Aghedo et al., 2007]. Using the second option would have allowed the model to capture deviations in climate variables caused by inter–annual variability of emissions.

The model showed a relatively good performance in reproducing spatial distribution of observed AOD, however poor performance in representing the AOD magnitude over the region was exhibited. This was probably because simulated results were compared with uncertain observations. The uncertainties in the observations were probably caused by:

(i) the poor performance of the MODIS AOD algorithm for areas with high surface reflectances (e.g., deserts) is known [Mahler et al., 2006; Seidel and Popp, 2012];

(ii) the scarcity of good quality time–resolved observed AOD data over Southern Africa.

The models were considered to be in good overall agreement with observed climate variability in the study region. The major findings are summarised in the following subsections:

Identification of the contribution of local and external sources to BB aerosol concentrations in Southern Africa

To identify the sources of the aerosols contributing to the burden in Southern Africa, enabling sensitivity studies to be carried out (by switching these sources on and off), the ECHAM5-HAM was run with BB aerosols (`GLBLBB1` simulation). GFED emissions of carbonaceous aerosols - used as tracers of biomass burning – were employed together with modeled transport pathways, to identify the sources of the BB aerosol burden found over the Southern African atmosphere. Results indicated that the major pollution sources (in addition to the local sources of emissions) contributing to the aerosol burden over the Southern African atmosphere included the African tropical forest north of the Equator and, to a lesser extent, the South American fumes (especially during DJF and MAM seasons).

The African tropical forest fires contribute to the slight increase of concentrations in the northern part of the study area, carried by the south–easterly winds; the second, added to the local emissions and a continental anticyclonic flow, bringing pollution from the Amazonian forest, at higher levels, carried by westerly winds to the southern region of the domain, where aerosols are likely to be trapped by the combination of elevated orography in Drakensberg and the prevailing subsidence.

These results suggested that Southern Africa experiences external aerosol pollution during almost all seasons – i.e., and not only during the dry season (as studied by Chatfield et al. [1998]; Duncan et al. [2007]; Trentmann et al. [2002]. Therefore, to assess the feedbacks between aerosols and climate in the region, it is important to look at both local and external contributions to the aerosol burden.

Assessment of the relevance of the synoptic variables in determining the aerosol concentrations in Southern Africa during the biomass burning season

The role of synoptic conditions on atmospheric aerosol concentrations in Southern Africa and the relative importance of these synoptic variables on regional concentrations

of carbonaceous aerosols were investigated by using (Super–)SOMs (a type of SOM that allows multiple data layers to be trained simultaneously) and GAM. The (Super–)SOM was applied simultaneously in a 32×21 grid covering 0°E-58°E and 38°S-1°S over two variables: a) the daily averaged BC and OC aerosol mixing ratio and b) SLP. The latter variable was chosen to give a representation of the circulation patterns over the region; a 50 000 iteration GAM of the carbonaceous aerosol mixing–ratio as function of SLP, geopotential heights, vorticity and wet and dry deposition, was applied. Results of this section of the study are:

At a first glance, SLP appeared to be a good indicator of where larger values of pollution were likely to be found over Southern Africa; modeled aerosol patterns suggested that the Indian and Atlantic high–pressure systems delimited the aerosol burden area, with the largest aerosol concentrations found within a continental low, but displaying some intrusions into the Indian Ocean below 20°S, in the period when the Indian Ocean high retreated towards the East (this phenomenon generally occurs in September).

Histograms of months mapped in the SOMs demonstrated that the period when Southern Africa was overcast by carbonaceous aerosols corresponded to the June–October period (in agreement with results previously obtained by Tummon [2011]). It was also noted that no significant inter–annual variability existed, presumably because the model was driven with year 2000 monthly averaged reference emissions from AEROCOM.

The GAM procedure demonstrated that the choice of SLP as a representative of circulation patterns for the SOMs over the region was good; calculated significance revealed SLP as the most important circulation variable determining aerosol concentrations over Southern Africa, followed by other variables (e.g., geopotential heights, vorticity and wet and dry deposition).

Estimation of potential feedbacks between the BB aerosols and the thermodynamic structure during austral spring, and the implication thereof on temperature and precipitation during austral spring, and their subsequent seasonal and inter–annual variability

Feedbacks between the BB aerosols and (i) the thermal structure, (ii) atmospheric circulation and (iii) precipitation, were assessed by calculating differences between results from the `GLBLBB1` and `RGNLBB0` BB simulations.

Results indicated that the radiative impact of BB aerosols in Southern African, here assessed through the responses of clear–sky and cloudy radiative forcing components at varying levels (TOA, mid–level atmosphere and at the surface), exerted:

a) a mainly positive net radiative forcing at the TOA, with the contribution from cloud forcing compensating for the negative contribution of net TOA longwave (LW), with the exception of localised portions of the Atlantic Ocean;

b) a mainly positive net atmosphere radiative forcing, almost exclusively influenced by clear–sky radiation through the absorption and scattering properties of aerosols;

c) a competition between clear–sky and cloudy–sky shortwave (SW) and LW cloud forcings, resulting in a complex pattern of forcings over the region (where the negative clear–sky contribution was largest over the western and north–western portion of the sub–continent and parts of Zimbabwe and Mozambique); the positive cloud forcing at the surface was found to be responsible for the positive values of the surface RF elsewhere.

In general, impacts of BB aerosols over Southern Africa during June–October period were manifested by increases in tropospheric temperature when SSA values decreased because of the increase of BC/OC ratios, therefore increasing tropospheric absorption. This fact reduced cloud cover, in agreement with studies previously carried out for the Southern African region [Tummon et al., 2010]. However, the inclusion of BB–derived SO_2 and the CCN–active sulphate aerosol nucleated from SO_2 derived therefrom, induced a different radiative forcing, which caused temperature and clouds over the Indian Ocean portion of the study domain to respond differently from the behaviour expressed in other studies. The behaviour was different likely because sulphate aerosols are hydrophilic, highly scattering and serve as efficient CCN [Boucher and Lohmann, 1995], the evaporation of clouds through the semi–direct effect was compensated for by the first and second indirect aerosol effects, as these began to play a role in the simulations in sulphate dominated regions, increasing both near–surface temperature and high–clouds in some instances, a result expected by Randles and Ramaswamy [2010] and also investigated by Ramana et al. [2010], in experiments carried out over China.

Comparisons of temperature and precipitation from simulations with and without BB have shown that at some locations, because of the inclusion of BB SO_2 and sulphate, the

spatial pattern included regions with positive surface RF, a result completely different from that obtained by Sakaeda et al. [2011] and Tummon et al. [2010], in which only negative surface RF values were observed. This implied that both negative and positive changes of surface temperature and, thus, lower–level convergence, were also possible. However, during the June–October period, a minor impact on precipitation was found (this period largely includes the austral dry season), thus suggesting that the direct and semi–direct effects would be more important than the indirect effects during this period.

Analysis of the dynamic effects over Southern Africa indicated that BB induced changes in precipitation were primarily through circulation changes. Both positive and negative signs of the surface radiative forcing caused by different chemico–physical properties of the aerosol burden (as is the case with the inclusion of sulphate), induced different responses of the surface temperature, which in turn affected the SLP, the spatial differences of which would then determine the new circulation patterns and low-level convergence, and thus also affect precipitation.

Large impacts on circulation and precipitation were found over land in DJF, with a significant reduction of up to 90% in daily rainfall near Mozambique and Tanzania. These impacts, caused by BB, induced changes of radiative forcings resulting in an inhibition of moisture convergence over this region during this period. A study recently carried out by Rotstayn et al. [2012], proposed a mechanism involving changes in the Walker circulation or the local Hadley circulation to explain circulation trends caused by aerosol and GHG in the Australasian region.

The aerosol induced changed in circulation noted in DJF suggests that despite the reduced occurrence of local BB aerosol emissions in other seasons, a minor disturbance of radiative forcing at the surface caused by external aerosols (brought into the region via any long–range transport mechanism) or by a possible teleconnection mechanism, can lead to imbalances in SLP which will cause low–level convergence to change direction bringing more or less moisture and, therefore, impact on precipitation magnitude at a local scale. Additionally, the trends in the precipitation variability were found to be linked to the antecedent soil moisture conditions, and, the opposite response of temperature to precipitation was also found. A negative trend of the amplitude of precipitation variability (in the region with the significant precipitation reduction) was found. Apparently precipitation had a memory of the (low) antecedent soil moisture caused by BB aerosols. As a result,

temperature responded in the opposite direction (i.e., the trend of variability amplitude was positive).

It is important to look at the overall aerosol emissions from BB - from the aerosols directly released on the BB process to those nucleated from the precursor gases and the mixing of these, since different radiative forcings will be generated by different chemical species (see Jacobson [2001]), and, therefore, different circulation patterns will probably be induced. This implies that a more comprehensive model, which includes chemistry, (e.g. WRF/Chem) should be able to uncover the BB aerosol/climate feedbacks with reasonably good approximation.

8.2 Limitations of the study and Suggestions for Further Research

This study was carried out with some limitations and the interpretation of results should be done cautiously. The following limitations characterised the study and should be considered in future studies:

- The use of coarse resolution aerosol emission inventories may have masked out some key interactions between aerosol and climate on the finer scale. Given the short lifetime of aerosols, it would be advisable to integrate into the model a finer spatial resolution emissions database for the Southern African region.

- As different emission rates are known to exist in the inter–annual scale, the use of GFED–based AEROCOM monthly averaged reference emissions for year 2000 has caused the inter–annual variability of emissions to be masked out in the ECHAM5-HAM model. Therefore, it would be advisable to integrate inter–annual variability of emissions in the ECHAM5-HAM simulations.

- The ECHAM5-HAM model is driven by prescribed SSTs. Thus, the model does not include feedbacks between aerosols and the SSTs. However, it has been acknowledged that aerosols may alter the surface temperature of the ocean through their radiative forcing. Thus, it would be desirable for the model to include updates of the SSTs based on the forcing exerted by aerosols.

- It was shown that the inclusion of sulphur dioxide in the ECHAM5-HAM simulations led to different radiative forcing and, therefore, induced different circulations patterns which may have impacted on precipitation patterns. It is expected that, if the model had accounted for chemistry, the resultant chemical species would have displayed different roles in the interaction with radiation and clouds.

- Better results would be attainable by using the latest version of models (which have the capability to account for other parameterisation schemes together with aerosols). Updated versions of the models include suitable convection schemes, able to inject aerosols to appropriate heights in the troposphere.

- An attempt to include simulations of a state–of–the art model, which would help overcome part of the limitations presented above was made. Given that the simulation time required on the fastest computer cluster available and the size of data generated were unfavourable for the timely accomplishment of the tasks outlined for this study, WRF/Chem results are presented without further discussion in Appendix B to serve as support model for ECHAM5–HAM and a reference for further studies.

- It is important to understand the physical mechanisms by which the absence on BB aerosols (either globally or regionally) causes larger concentrations of coarse mode aerosols over the study region than the simulations with BB aeorols (Figure 5.1d).

- This work included sulphate aerosols nucleated from SO_2. Since not all SO_2 gas nucleates into sulphate aerosols, a further study aiming at understanding the possible impacts of the remaining SO_2 gas in regional climate is advisable.

- Another important aspect for further research is why BB fine mode scattering aerosols tended to be situated within high–pressure systems instead of low–pressure systems (as did carbonaceous aerosols).

Nevertheless, this study was able to show that BB aerosols can not be disregarded when a more comprehensive evaluation of the regional climate in Southern Africa is concerned. The complex impacts of aerosols on climate found in this study may help scientists understand more about the drivers of the climate dynamics in the region, and incorporate these drivers into seasonal forecast, thereby increasing the ability to predict certain anomalous climate patterns that, once established, would put the region at risk of disaster.

APPENDIX

Appendix A

Auxiliary results from ECHAM5–HAM

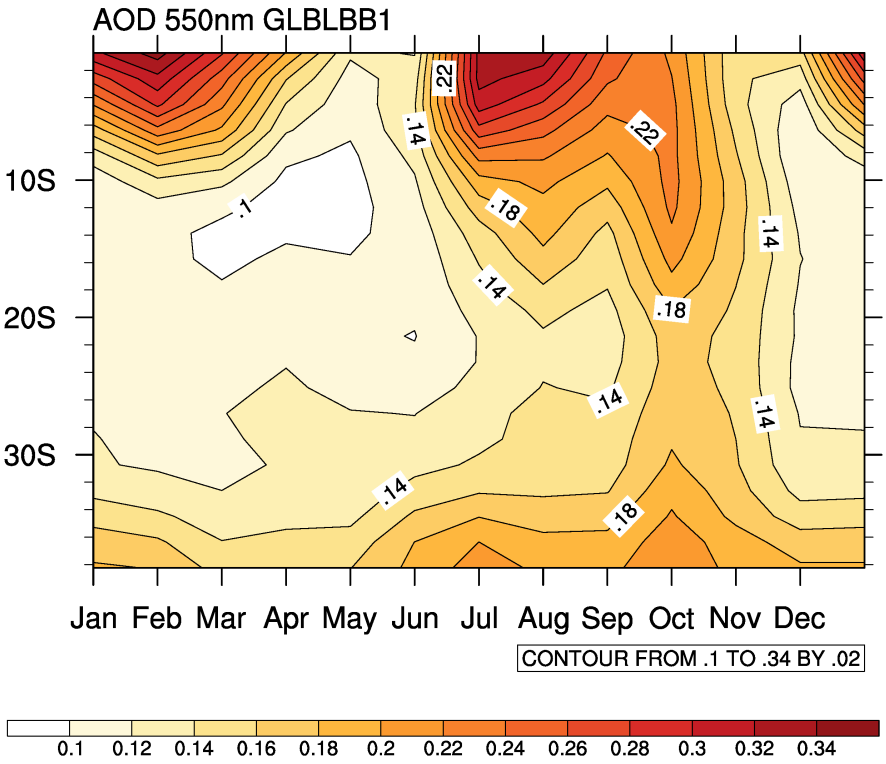

Figure A.1: Latitude–month Hovmöller diagram of 550nm AOD.

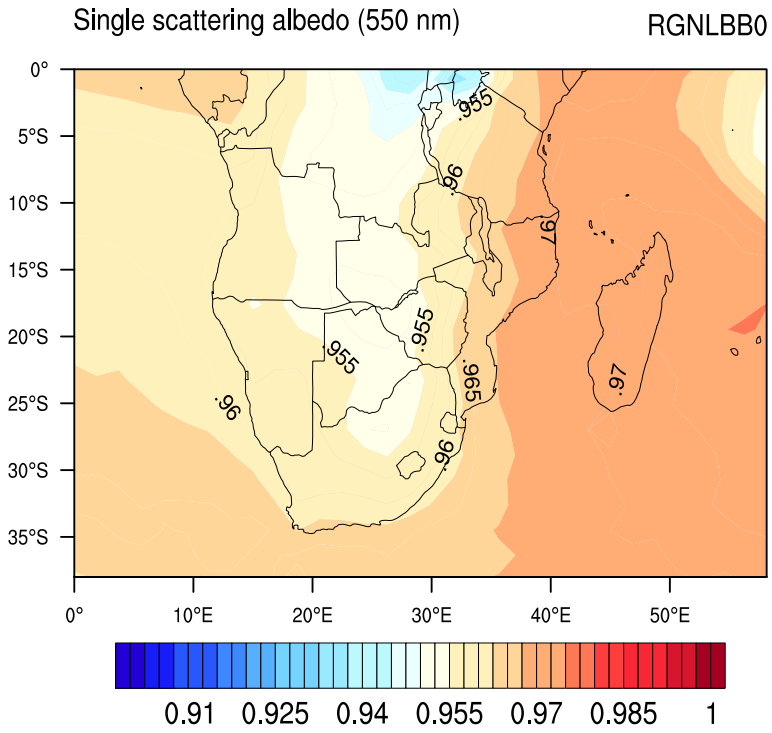

Figure A.2: JJASO average of simulated SSA in the `RGNLBB0` simulation

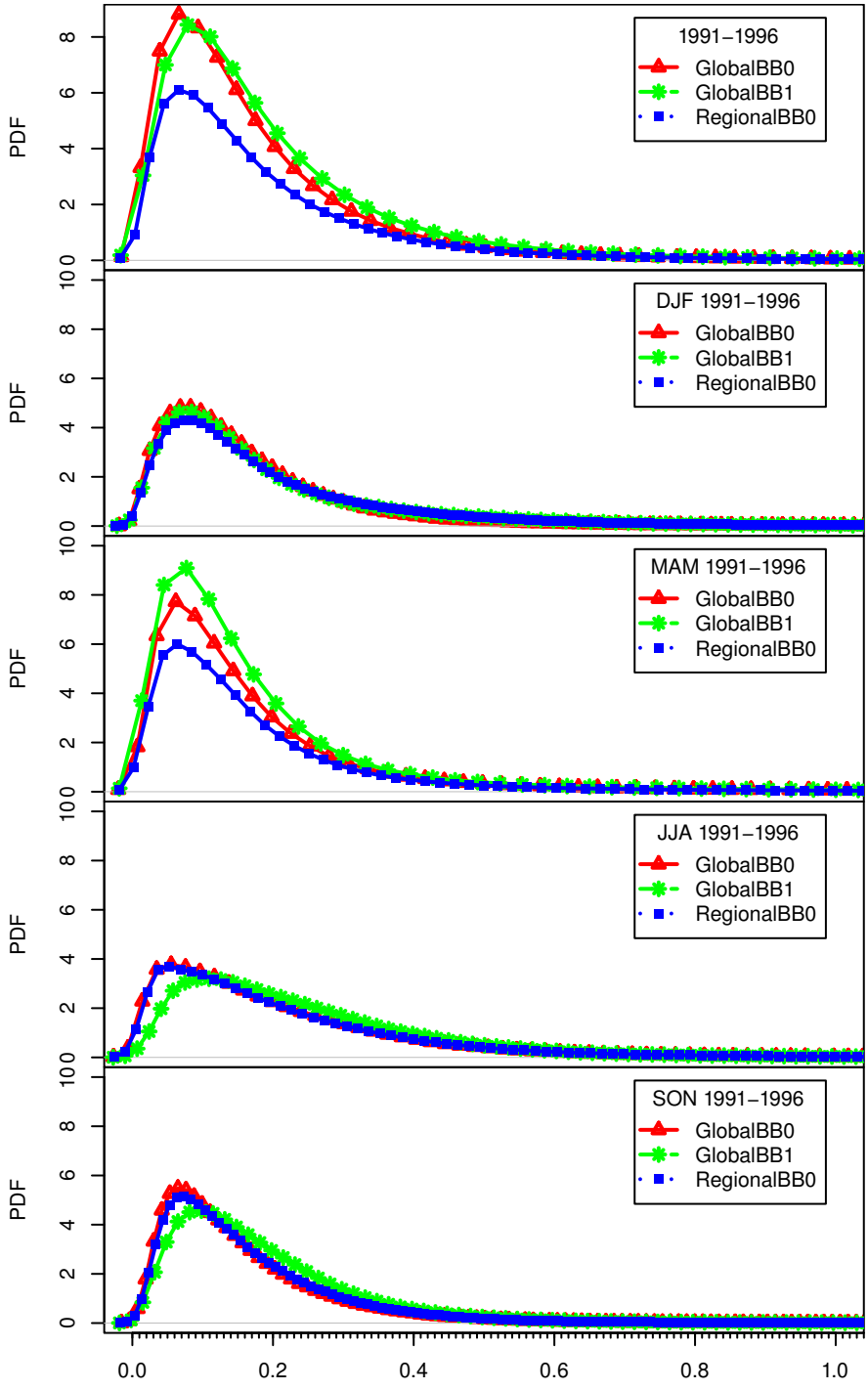

Figure A.3: Probability Distribution Functions of AOD's under different seetings of ECHAM5-HAM.

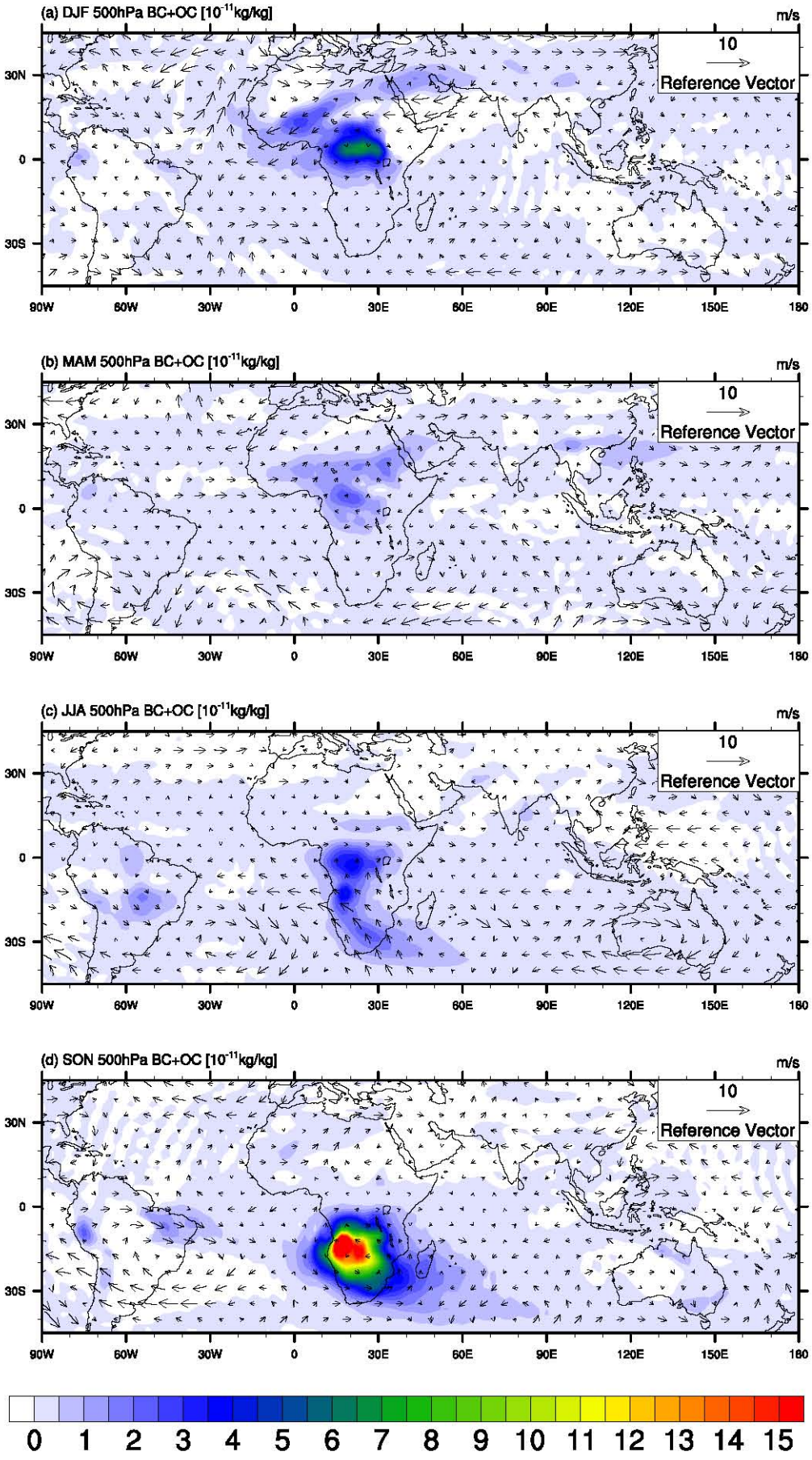

Figure A.4: Seasonal maps of ultra–fine mode BC and OC aerosol concentration overlaid to streamlines at 500hPa height. Seasons are (a) DJF; (b) MAM; (c) JJA; and (d) SON.

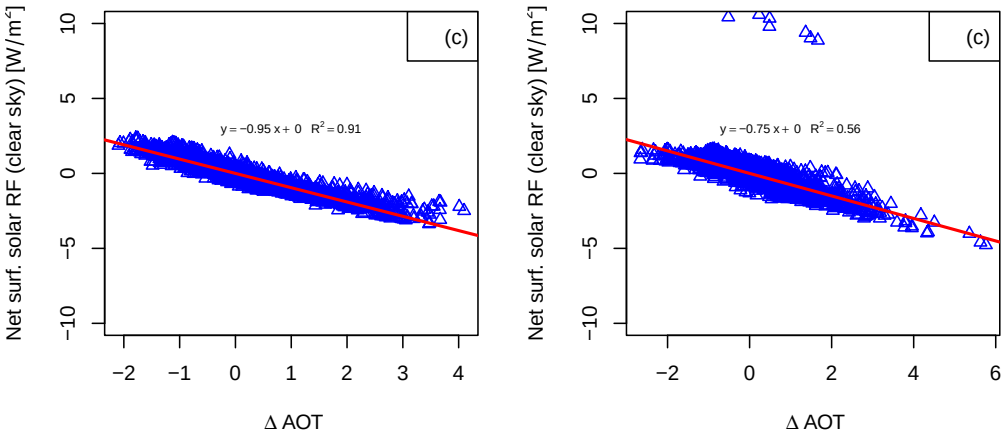

Figure A.5: Correlation of normalised net surface solar radiative forcing and AOD for 2 regions under different influences: a) Near largest emissions, where AOD dominates, b) In the north–eastern region where AOD and clouds compete.

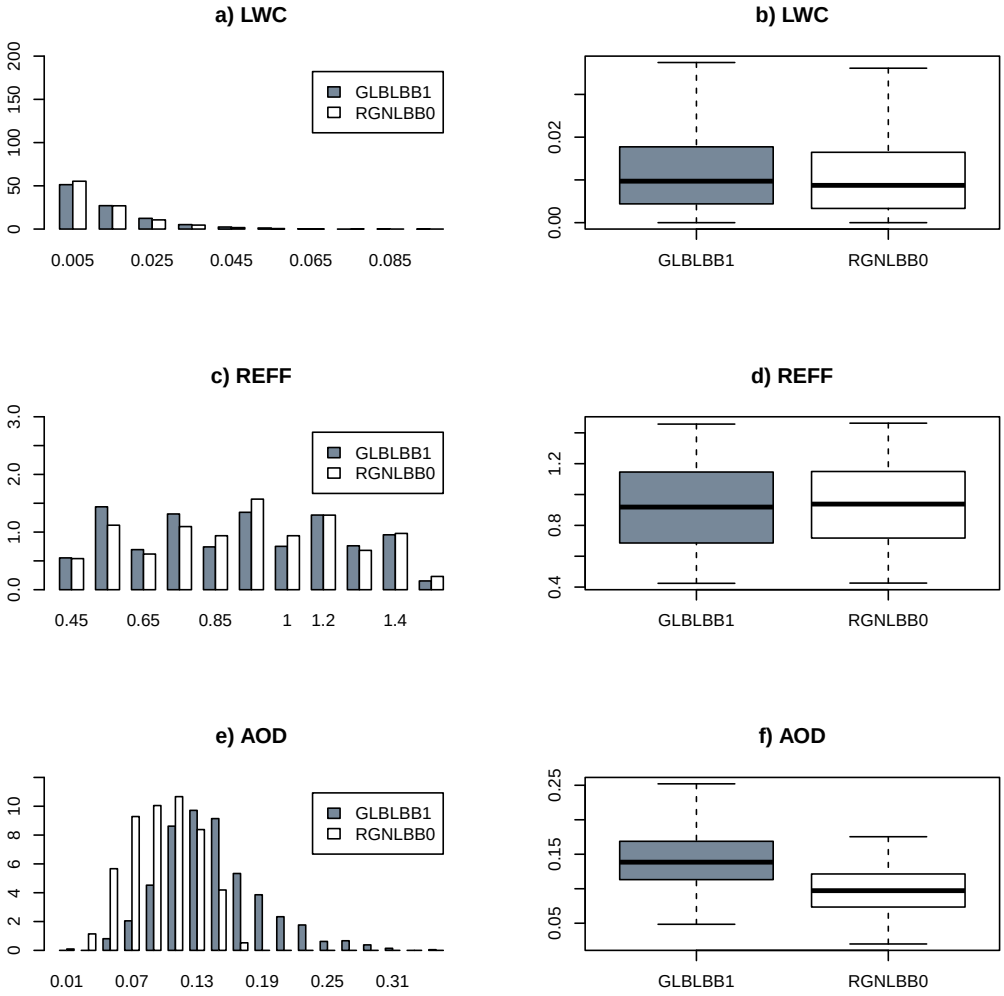

Figure A.6: Histograms and boxplots of Liquid water path (a,b); aerosol effective radius (c,d); and aerosol optical depth (e,f), in the simulations with and without BB over the region.

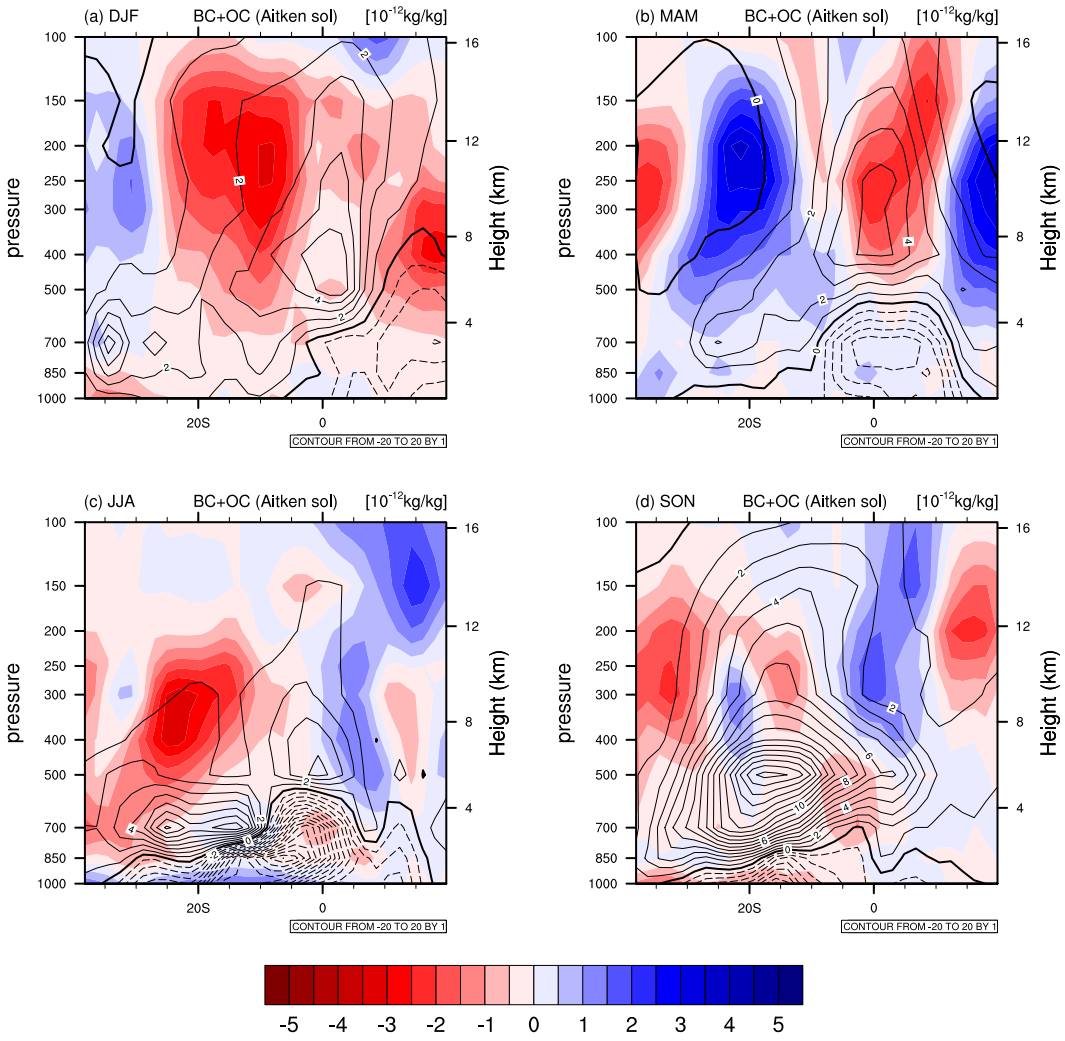

Figure A.7: Seasonal changes of mean cloud cover (coloured contours, in percentage) and mass mixing ratio of Aitken mode of soluble black and organic carbon (solid and dashed lines) for a) DJF; b)MAM; c) JJA; and d) SON seasons. In the line contours, dashed and solid lines indicate negative and positive anomalies, respectively.

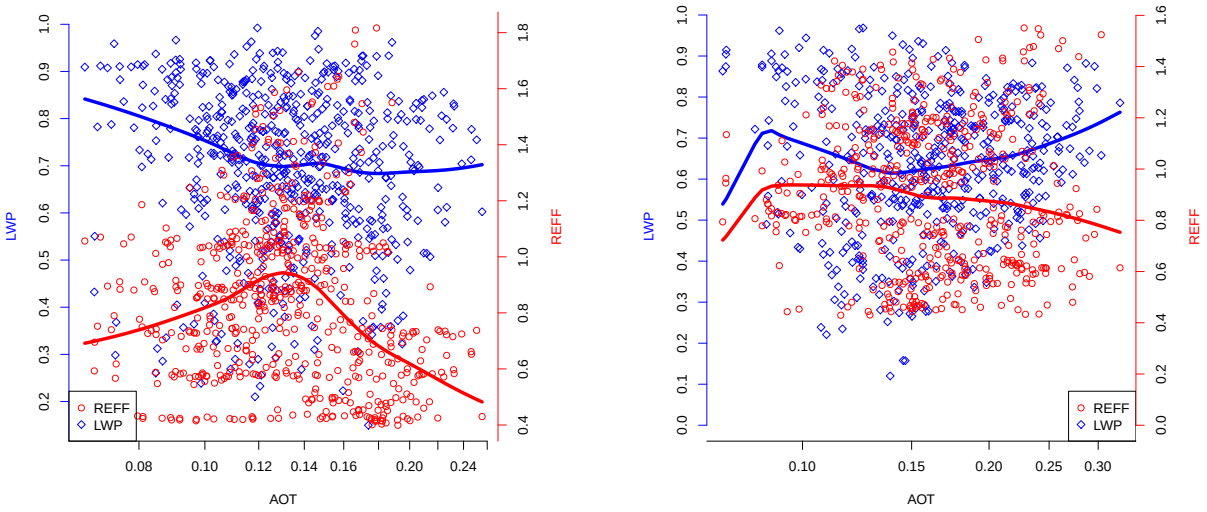

Figure A.8: Relationship between LWP and Effective Radius as a function of AOD for region with increased precipitation (lhs), and with decreased precipitation (rhs)

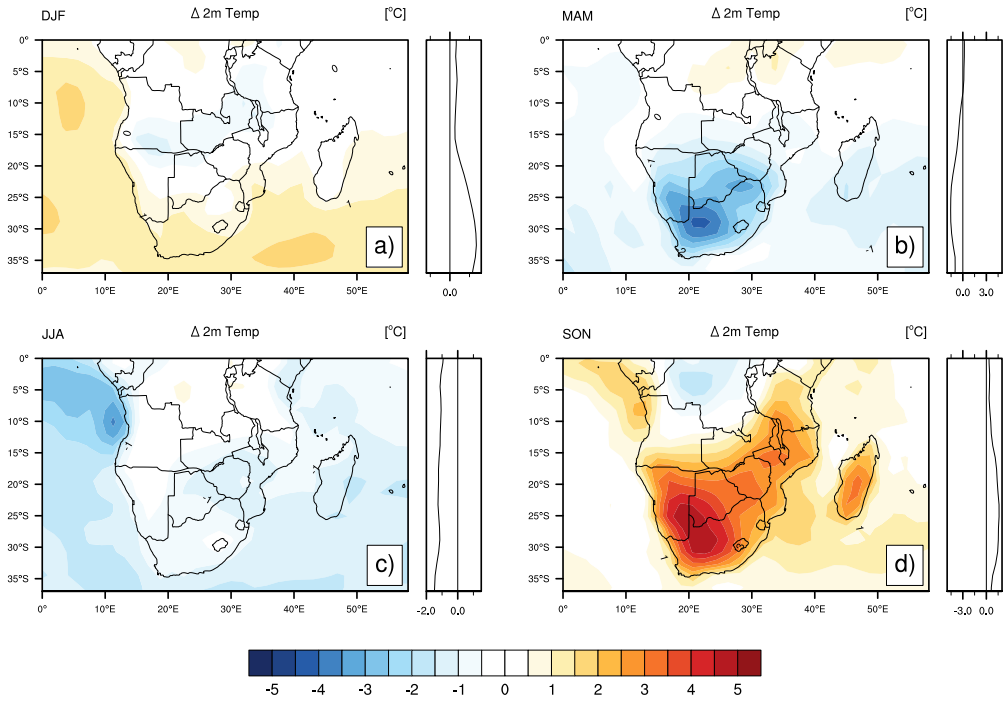

Figure A.9: Seasonal BB induced changes of 2m temperature

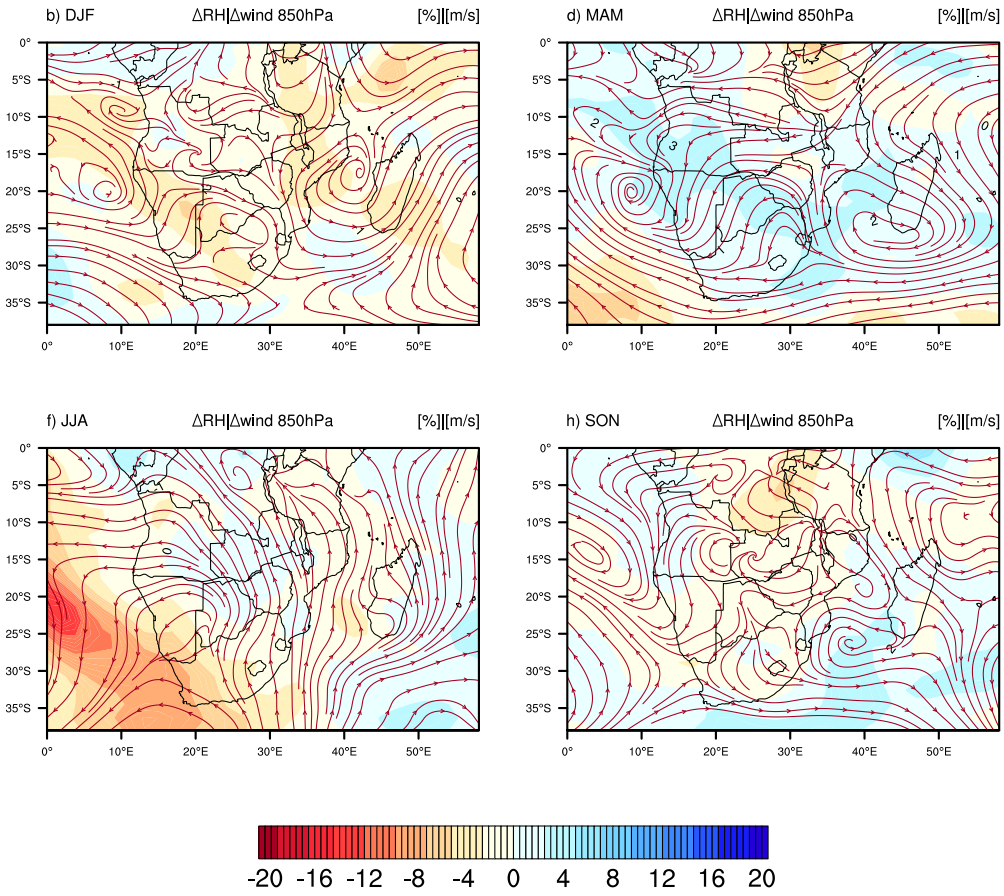

Figure A.10: Seasonal changes in relative humidity and 850hPa winds

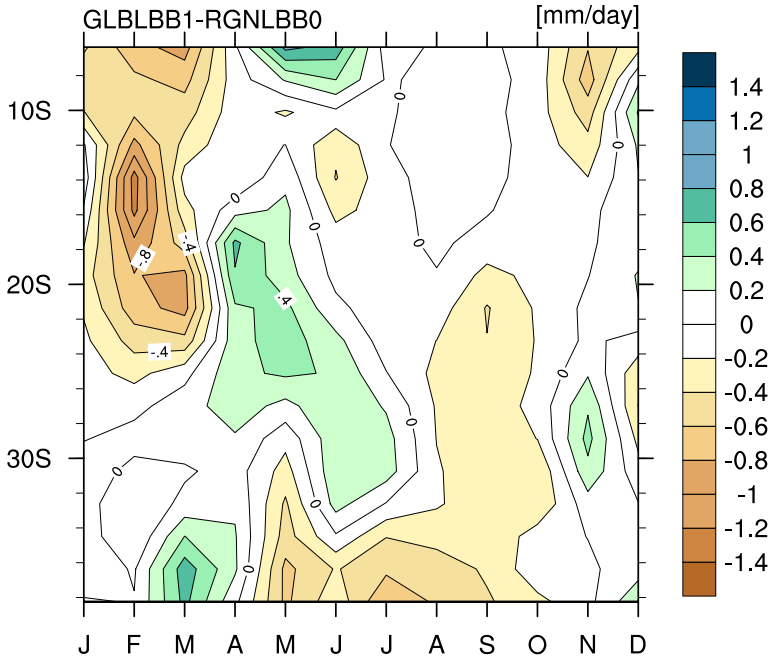

Figure A.11: Latitude–month Hovmöller diagram of precipitation changes.

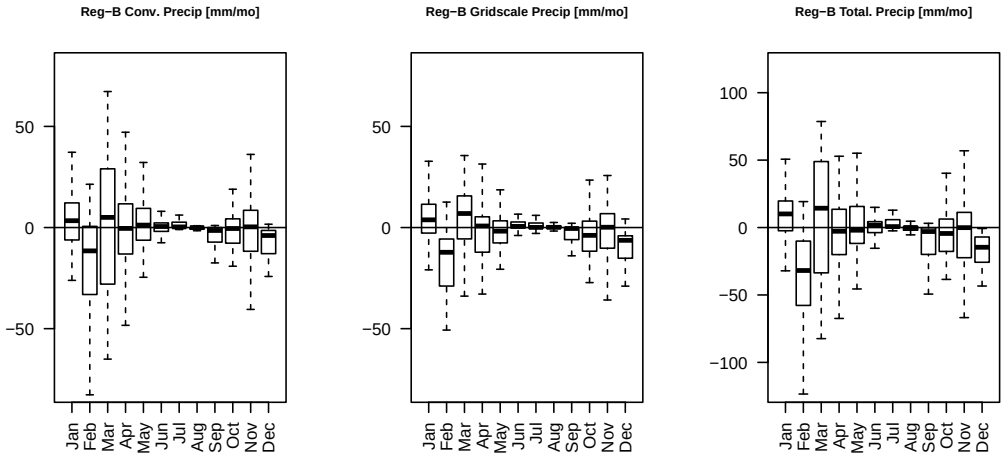

Figure A.12: Changes in monthly mean rainfall for the region over Mozambique and Tanzania where a significant reduction of precipitation was simulated.

Appendix B

WRF/Chem preliminary results

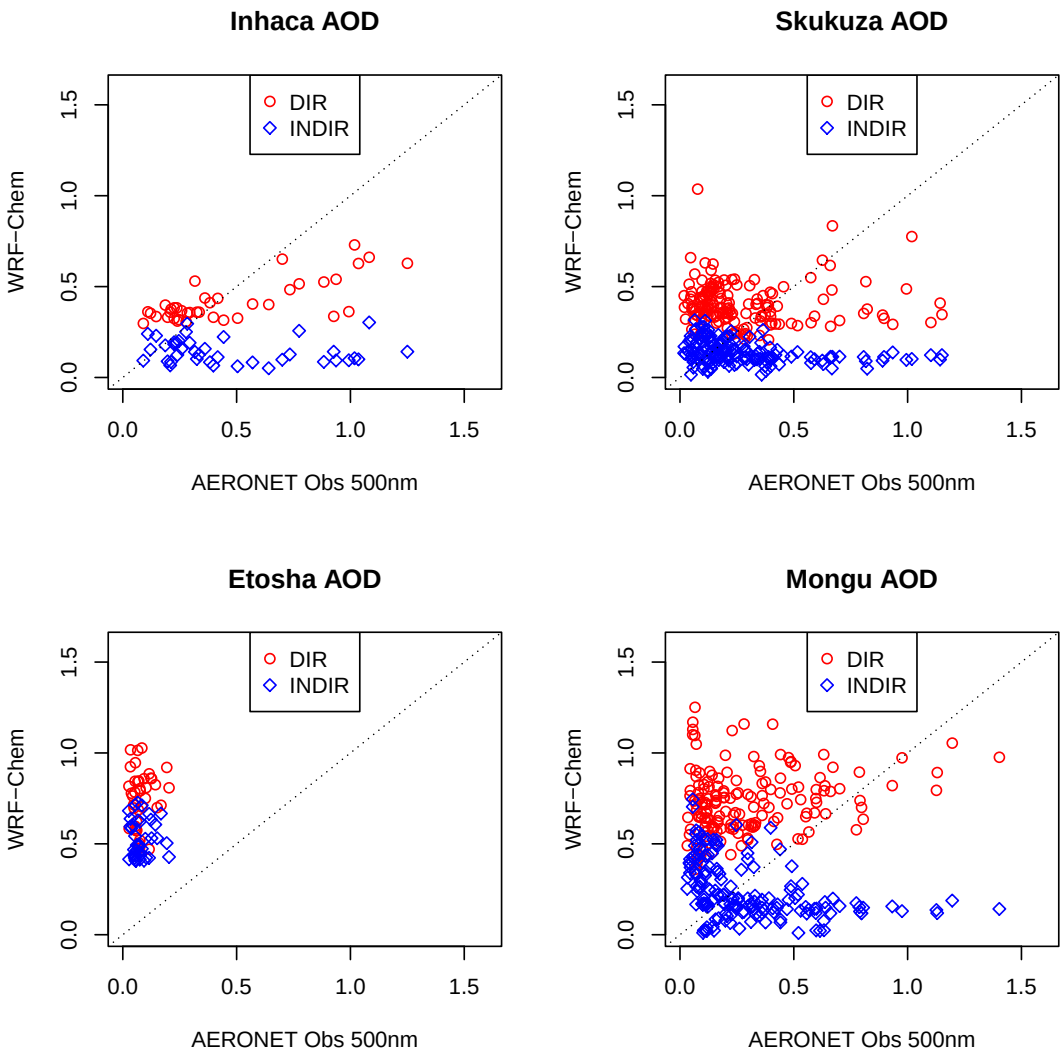

Figure B.1: Scatterplot of WRF-Chem modeled and AERONET observed AOD for Inhaca, Skukuza, Etosha and Mongu. Red circles correspond to WRF/Chem simulations in which only direct (DIR) effects were taken into account, while blue diamonds to those which both direct and indirect aerosols effects are considered (INDIR). Apparently the INDIR simulations underestimate AOD when compared with the DIR simulations. This may be cause by wet deposition of aerosols when the prognosis of cloud droplet number concentration is done via aerosol number concentration , as is the case of INDIR

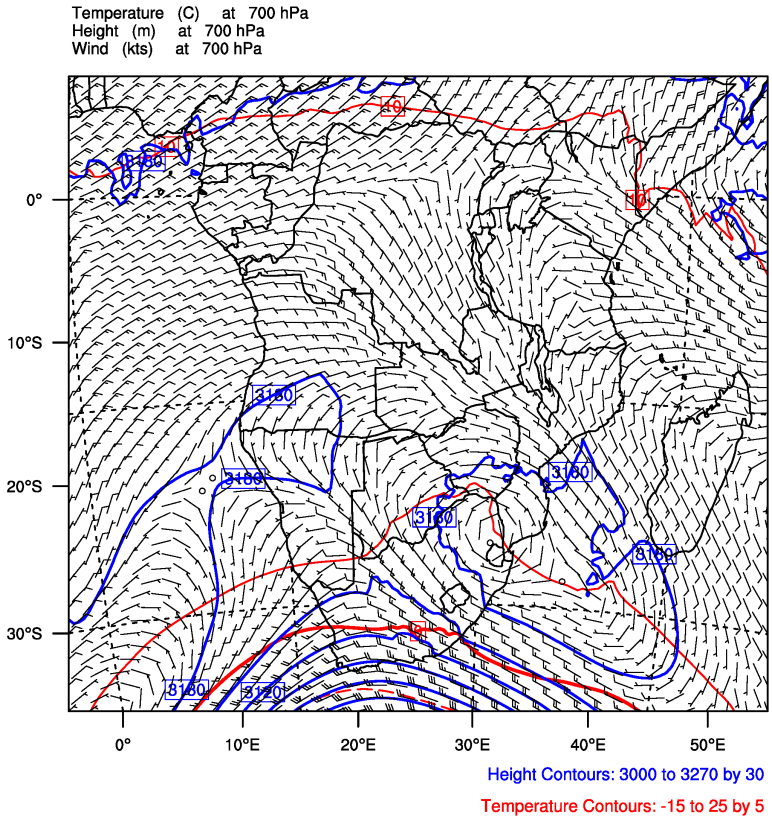

Figure B.2: JJA 2001 WRF/Chem simulated temperature, geopotential height and winds at 700hPa

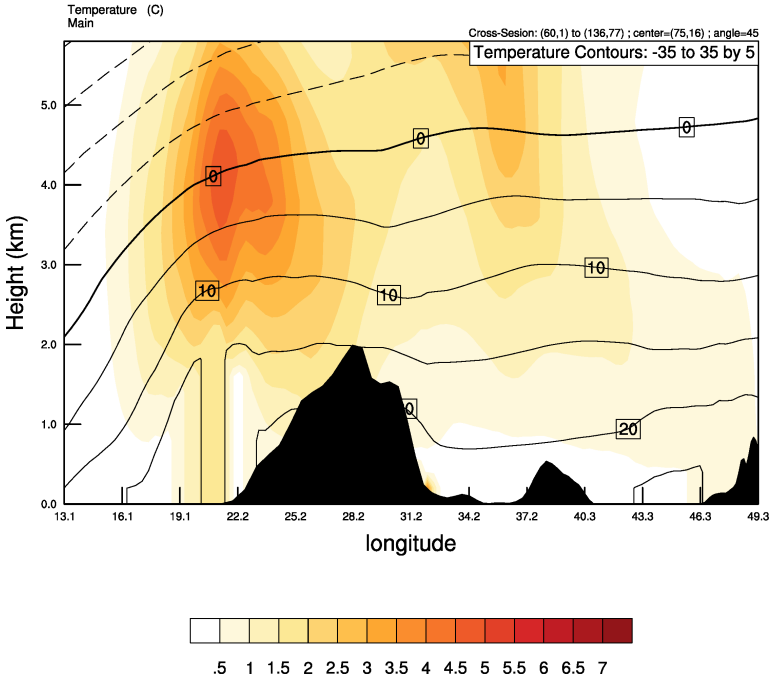

Figure B.3: WRF/Chem simulated vertical profile of black carbon and temperature, crossing Drakensberg region at 45° with the longitude axes

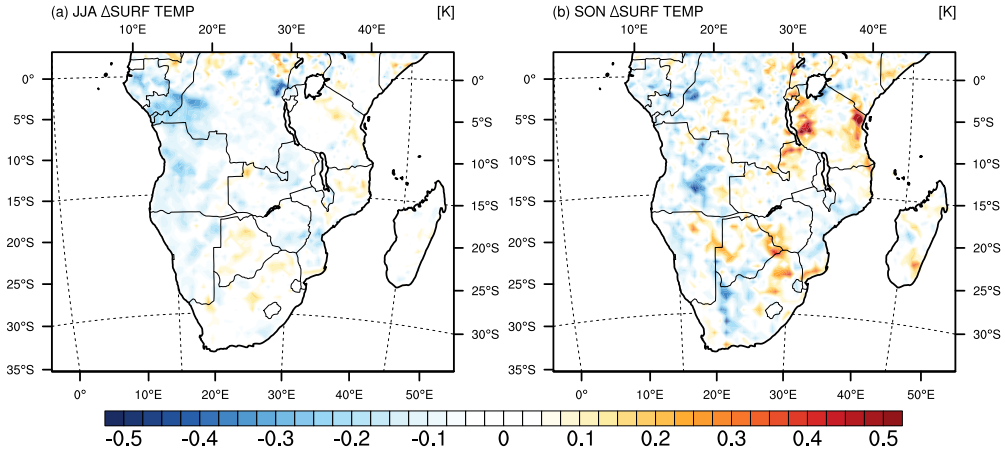

Figure B.4: BB aerosol induced changes in surface skin temperature for a) JJA and b) SON respectively. In JJA the general pattern is one of surface temperature reduction (up to -0.4K); Minor warming patches (up tp 0.2K) are noted over South Africa, Botswana and in the eastern coast of the subcontinent. In SON the warming and cooling patterns are mixed; the magnitude of the (JJA) warming has increased (up to 0.4–0.5K)

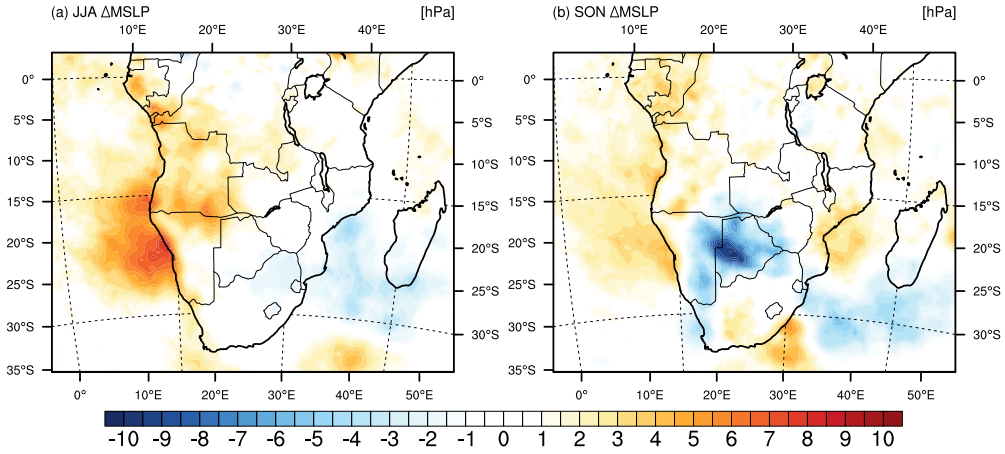

Figure B.5: BB aerosol induced changes in mean sea level pressure for a) JJA and b) SON respectively. The mean sea-level pressure (MSLP) signal appeared to contradict that of temperature (Figure B.4) in both seasons. In JJA, MSLP had increased by ≈10hPa on the western portion of Southern Africa; over the eastern side, including Indian Ocean, between 20°S–30°S, MSLP had slightly reduced by about 5hPa. In SON, a large decrease (up to -10hPa) was noted over Botswana and western South Africa. The pathway of the River–of–Smoke had also suffered a reduction in MLSP (uo to -5hPa). Pressure has also increase over the central parts of Mozambique and south-eastern South Africa

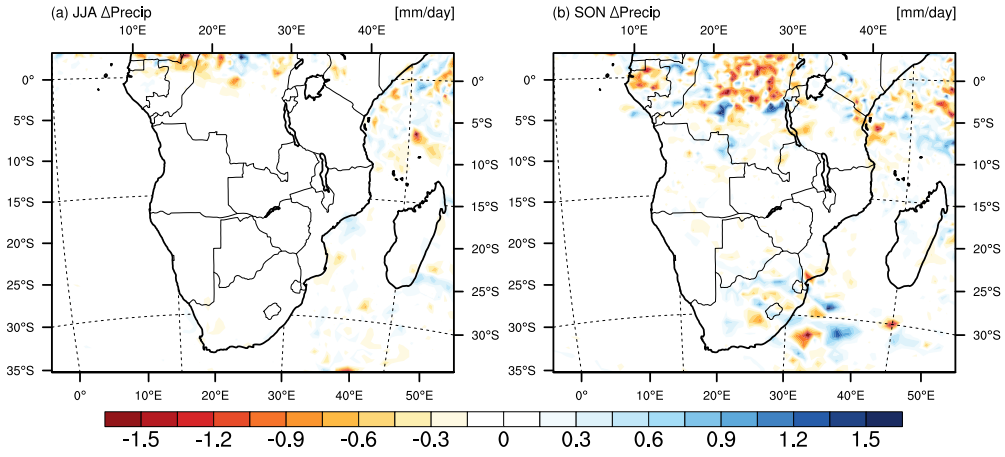

Figure B.6: The same as Figure B.4 but for precipitation. No clear signal of precipitation change is noted over the JJA season (this is the austral dry seasonn). In SON, with the initiation of the wet season in Southern Africa, concurrent patches of precipitation reduction and increase can be seen over the DRC and south Africa.

Appendix C

Changes during the iterative training process of SOMs

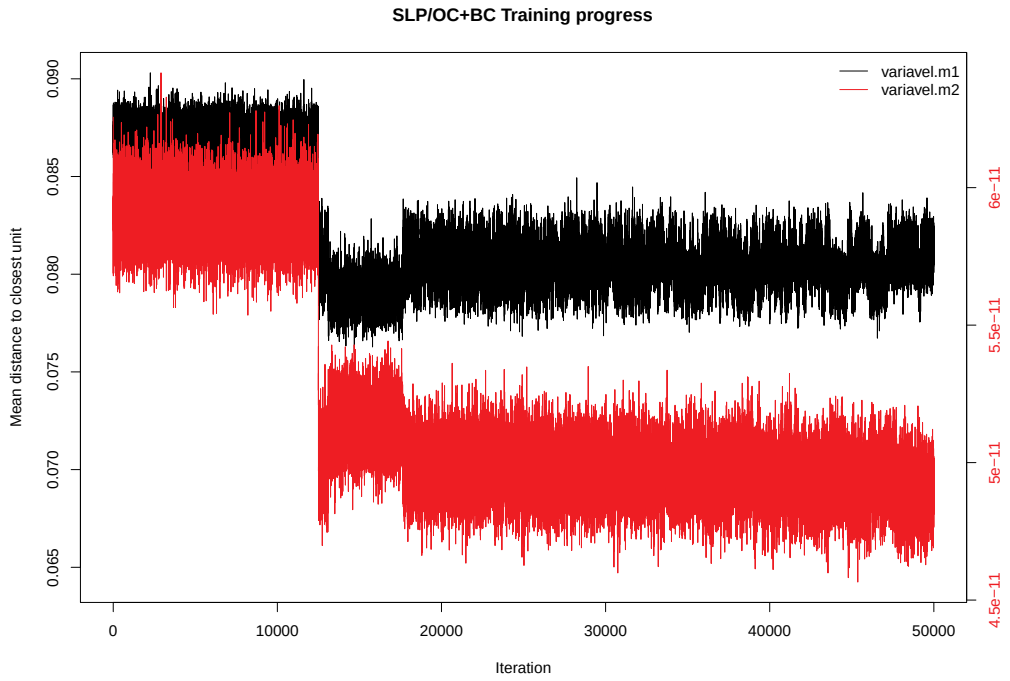

Figure C.1: SLP and OC+BC SOM training progress.

References

Abdul-Razzak, H. and Ghan, S. J. (2000). A parameterization of aerosol activation, 2, Multiple aerosol types. *J. Geophys. Res.*, 105:6837–6844.

Abdul-Razzak, H. and Ghan, S. J. (2002). A parameterization of aerosol activation 3. Sectional representation. *J. Geophys. Res.(Atmospheres)*, 107:4026.

Abel, S. J., Highwood, E. J., Haywood, J. M., and Stringer, M. A. (2005). The direct radiative effect of biomass burning aerosols over southern Africa. *Atmospheric Chemistry & Physics*, 5:1999–2018. http://adsabs.harvard.edu/abs/2005ACPD....5.1165A.

Aghedo, A. M., Schultz, M. G., and Rast, S. (2007). The influence of African air pollution on regional and global tropospheric ozone. *Atmospheric Chemistry and Physics*, 7(5):1193–1212.

Albrecht, B. A. (1989). Aerosols, cloud microphysics, and fractional cloudiness. *Science*, 245:1227–30.

Aldrin, M. and Haff, I. H. (2005). Generalised additive modelling of air pollution, traffic volume and meteorology. *Atmospheric Environment*, 39(11):2145 – 2155.

Andreae, M. O. and Crutzen, P. J. (1997). Atmospheric aerosols: Biogeochemical sources and role in atmospheric chemistry. *Science Magazine*, 276(5315):1052–1057.

Andreae, M. O. and Merlet, P. (2001). Emission of trace gases and aerosols from biomass burning. *Global Biogeochemical Cycles*, 15:955–966.

Andreae, M. O. and Rosenfeld, D. (2008). Aerosol–cloud–precipitation interactions. part 1. the nature and sources of cloud-active aerosols. *Earth-Science Reviews*, 89(1-2):13 – 41.

Andronache, C. (2003). Estimated variability of below-cloud aerosol removal by rainfall for observed aerosol size distributions. *Atmospheric Chemistry & Physics*, 3:131–143.

Annegarn, H., Swap, R. J., Swap, R. J., Piketh, S. J., Hobbs, P., Queface, A., Freiman, T., and Platnick, S. (2001). "River of Smoke" - Characteristics of the Southern African Springtime Regional Biomass Burning Haze. *AGU Fall Meeting Abstracts*, pages B4+.

Asa-Awuku, A. and Nenes, A. (2007). Effect of solute dissolution kinetics on cloud droplet formation: Extended Köhler theory. *J. Geophys. Res.(Atmospheres)*, 112(D11):22201.

Baklanov, A., Korsholm, U., Mahura, A., Petersen, C., and Gross, A. (2008). ENVIRO-HIRLAM: on-line coupled modelling of urban meteorology and air pollution. *Advances in Science and Research*, 2:41–46.

Barnaba, F., Angelini, F., Curci, G., and Gobbi, G. P. (2011). An important fingerprint of wildfires on the European aerosol load. *Atmospheric Chemistry and Physics Discussions*, 11(1):2317–2354.

Barrett, J. and Webb, N. (1998). A comparison of some approximate methods for solving the aerosol general dynamic equation. *Journal of Aerosol Science*, 29(1-2):31 – 39.

Barry, R. G. and Chorley, R. J. (1968). *Atmosphere, Weather and Climate*, volume 134. Routledge.

Batjes, N. H. (2006). Soil carbon stocks of Jordan and projected changes upon improved management of croplands. *Geoderma*, 132(3–4):361–371.

Bencherif, H., Portafaix, T., Baray, J., Morel, B., Baldy, S., Leveau, J., Hauchecorne, A., Keckhut, P., Moorgawa, A., Michaelis, M., and Diab, R. (2003). LIDAR observations of lower stratospheric aerosols over South Africa linked to large scale transport across the southern subtropical barrier. *Journal of Atmospheric and Solar-Terrestrial Physics*, 65(6):707 – 715.

Benedetti, A. and Abrahamowicz, M. (2004). Using generalized additive models to reduce residual confounding. *Statistics in medicine*, 23(24):3781–3801.

Bergstrom, R. W., Pilewskie, P., Schmid, B., and Rusell, P. B. (2003). Estimates of the spectral aerosol single scattering albedo and aerosol radiative effects during SAFARI 2000. *J. Geophys. Res.*, 108(D13):8474–+. doi:10.1029/2002JD002435.

Berk, A., Acharya, P., Anderson, G., and Gossage, B. (2009). Recent developments in the MODTRAN® atmospheric model and implications for hyperspectral compensation. 2:II–262–II–265.

Bhave, P. V., Pouliot, G. A., and Zheng, M. (2007). Source Apportionment of Primary Carbonaceous Aerosol Using the Community Multiscale Air Quality Model. In Borrego, C. and Norman, A.-L., editors, *Air Pollution Modeling and Its Application XVII*, pages 257–266. Springer US. 10.1007/978-0-387-68854-1_28.

Binkowski, F. S. and Roselle, S. J. (2003). Models-3 Community Multiscale Air Quality (CMAQ) model aerosol component 1. Model description. *J. Geophys. Res.(Atmospheres)*, 108:4183–+.

Boucher, O. and Lohmann, U. (1995). The sulfate-ccn-cloud albedo effect. *Tellus*, 47B:281–300.

Buseck, P. R. and Pósfai, M. (1999). Airborne minerals and related aerosol particles: Effects on climate and the environment. *Proc. Natl. Acad. Sci., USA*, 96(7):3372–3379.

Buseck, P. R. and Schwartz, S. E. (2003). Tropospheric Aerosols. *Treatise on Geochemistry*, 4:91–142.

Businger, J. A. (1986). Evaluation of the Accuracy with Which Dry Deposition Can Be Measured with Current Micrometeorological Techniques. *Journal of Applied Meteorology*, 25:1100–1124.

Carslaw, D. C., Beevers, S. D., and Tate, J. E. (2007). Modelling and assessing trends in traffic-related emissions using a generalised additive modelling approach. *Atmospheric Environment*, 41(26):5289 – 5299.

Cavazos, T. (2000). Using Self-Organizing Maps to Investigate Extreme Climate Events: An Application to Wintertime Precipitation in the Balkans. *Journal of Climate*, 13(10):1718–1732.

Chamberlain, A. C. (1967). Transport of Lycopodium Spores and Other Small Particles to Rough Surfaces. *Royal Society of London Proceedings Series A*, 296:45–70.

Chapman, E. G., Gustafson Jr., W. I., Easter, R. C., Barnard, J. C., Ghan, S. J., Pekour, M. S., and Fast, J. D. (2009). Coupling aerosol-cloud-radiative processes in the WRF-Chem model: Investigating the radiative impact of elevated point sources. *Atmospheric Chemistry and Physics*, 9(3):945–964.

Charlson, R. J., Schwartz, S. E., Hales, J. M., Cess, R. D., Coakley, Hansen, J. E., and Hofmann, D. J. (1992). Climate Forcing by Anthropogenic Aerosols. *Science*, 255(5043):423–430.

Chate, D., Rao, P., Naik, M., Momin, G., Safai, P., and Ali, K. (2003). Scavenging of aerosols and their chemical species by rain. *Atmospheric Environment*, 37(18):2477 – 2484.

Chatfield, R. B., Vastano, J. A., Li, L., Sachse, G. W., and Connors, V. S. (1998). The Great African plume from biomass burning: Generalizations from a three-dimensional study of TRACE A carbon monoxide. *J. Geophys. Res.*, 103(0148-0227):28059–28077.

Chen, B., Cheng, Y., and Yeh, H. (1984). Experimental responses of two optical particle counters. *Journal of Aerosol Science*, 15(4):457 – 464.

Chen, J.-P. (1994). Theory of Deliquescence and Modified Köhler Curves. *Journal of Atmospheric Sciences*, 51:3505–3516.

Chin, M., Rood, R. B., Lin, S.-J., Müller, J.-F., and Thompson, A. M. (2000). Atmospheric sulfur cycle simulated in the global model GOCART: Model description and global properties. *J. Geophys. Res.*, 105:24671–24688.

Choi, H. and Choi, D. S. (2008). Concentrations of PM10, PM2.5, and PM1 influenced by atmospheric circulation and atmospheric boundary layer in the Korean mountainous coast during a duststorm. *Atmospheric Research*, 89(4):330 – 337. Air Quality: Aerosols, Dust Storms, Photochemical Pollutants, 3rd International Symposium on Air Quality Management at Urban, Regional, and Global Scales (AQM2005).

Chylek, P., Dubey, M. K., Lohmann, U., Ramanathan, V., Kaufman, Y. J., Lesins, G., Hudson, J., Altmann, G., and Olsen, S. (2006). Aerosol indirect effect over the Indian Ocean. *Geophys. Res. Lett.*, 33:6806–+.

Clough, S. A., Iacono, M. J., and Moncet, J.-L. (1992). Line-by-Line Calculations of Atmospheric Fluxes and Cooling Rates: Application to Water Vapor. *J. Geophys. Res.*, 97:15761–15785.

Coakley, Jr., J. A., Cess, R. D., and Yurevich, F. B. (1983). The Effect of Tropospheric Aerosols on the Earth's Radiation Budget: A Parameterization for Climate Models. *Journal of Atmospheric Sciences*, 40:116–138.

Coakley, J. A. J. and Chylek, P. (1975). The two-stream approximation in radiative transfer: Including the angle of the incident radiation. *Journal of the Atmospheric Sciences*, 32:409–418.

Colman, R. (2003). A comparison of climate feedbacks in general circulation models. *Climate Dynamics*, 20(January 2002):865–873.

Colman, R. and McAvaney, B. (2009). Climate feedbacks under a very broad range of forcing. *Geophysical Research Letters*, 36(1):1–5.

Conant, W. C., Nenes, A., and Seinfeld, J. H. (2002). Black carbon radiative heating effects on cloud microphysics and implications for the aerosol indirect effect 1. Extended Köhler theory. *J. Geophys. Res.(Atmospheres)*, 107:4604.

Crane, R. G. and Hewitson, B. C. (1994). *Neural nets: Applications in Geography / Edited by Bruce C. Hewitson and Robert G. Crane*. Kluwer Academic Publishers, Dordrecht; Boston.

Crétat, J., Pohl, B., Richard, Y., and Drobinski, P. (2012). Uncertainties in simulating regional climate of Southern Africa: sensitivity to physical parameterizations using WRF. *Climate Dynamics*, 38:613–634.

Croft, B., Lohmann, U., Martin, R. V., Stier, P., Wurzler, S., Feichter, J., Hoose, C., Heikkilä, U., van Donkelaar, A., and Ferrachat, S. (2010). Influences of in-cloud aerosol scavenging parameterizations on aerosol concentrations and wet deposition in ECHAM5-HAM. *Atmospheric Chemistry & Physics*, 10:1511–1543.

Crutzen, P. J. and Andreae, M. O. (1990). Biomass Burning in the Tropics: Impact on Atmospheric Chemistry and Biogeochemical Cycles. *Science*, 250(4988):1669–1678. doi:10.1126/science.250.4988.1669.

Crutzen, P. J., Heidt, L. E., Krasnec, J. P., Pollock, W. H., and Seiler, W. (1979). Biomass burning as a source of atmospheric gases CO, H_2, N_2O, NO, CH_3Cl and COS. *Nature*, 282:253–256.

D'Alessio, A., D'Anna, A., Gambi, G., and Minutolo, P. (1998). The spectroscopic characterisation of UV absorbing nanoparticles in fuel rich soot forming flames. *Journal of Aerosol Science*, 29(4):397–409.

Debry, E. and Sportisse, B. (2007). Numerical simulation of the general dynamic equation (gde) for aerosols with two collocation methods. *Applied Numerical Mathematics*, 57(8):885 – 898.

DeCarlo, P., Slowik, J., Worsnop, D., Davidovits, P., and Jimenez, J. (2004). Particle morphology and density characterization by combined mobility and aerodynamic diameter measurements. part 1: Theory. *Aerosol Science and Technology*, 38(12):1185–1205.

Dentener, F., Kinne, S., Bond, T., Boucher, O., Cofala, J., Generoso, S., Ginoux, P., Gong, S., Hoelzemann, J. J., Ito, A., and et al. (2006). Emissions of primary aerosol and precursor gases in the years 2000 and 1750, prescribed data-sets for aerocom. *Atmospheric Chemistry and Physics Discussions*, 6(2):4321–4344.

Duhanyan, N. and Roustan, Y. (2011). Below-cloud scavenging by rain of atmospheric gases and particulates. *Atmospheric Environment*, 45(39):7201 – 7217.

Duncan, B. N., Strahan, S. E., Yoshida, Y., Steenrod, S. D., and Livesey, N. (2007). Model study of the cross-tropopause transport of biomass burning pollution. *Atmospheric Chemistry & Physics*, 7:3713–3736.

Dusek, U., Frank, G. P., Hildebrandt, L., Curtius, J., Schneider, J., Walter, S., Chand, D., Drewnick, F., Hings, S., Jung, D., Borrmann, S., and Andreae, M. O. (2006). Size matters more than chemistry for cloud-nucleating ability of aerosol particles. *Science*, 312(5778):1375–1378.

Ebert, E. E. and Curry, J. A. (1992). A parameterization of ice cloud optical properties for climate models. *Journal of Geophysical Research*, 97(D4):3831–3836.

Ebert, P., Kibler, M., Mainka, A., Tenberken, B., Baechmann, K., Frank, G., and Tschiersch, J. (1998). A field study of particle scavenging by raindrops of different sizes using monodisperse trace aerosol. *Journal of Aerosol Science*, 29(1-2):173 – 186.

Eck, T. F. (2003a). Variability of biomass burning aerosol optical characteristics in Southern Africa during the SAFARI 2000 dry season campaign and a comparison of single scattering albedo estimates from radiometric measurements. *J. Geophys. Res.*, 108(D13):8477–+. doi:10.1029/2002JD002321.

Eck, T. F. (2003b). Variability of biomass burning aerosol optical characteristics in Southern Africa during the SAFARI2000 dry season campaign and a comparison of single scattering albedo estimates from radiometric measurements. *J. Geophys. Res.*, 108(D13):8500–+. doi:10.1029/2003JD001606.

Eck, T. F., Holben, B. N., Reid, J. S., Dubovik, O., Smirnov, A., O'Neill, N. T., Slutsker, I., and Kinne, S. (1999). Wavelength dependence of the optical depth of biomass burning, urban, and desert dust aerosols. *J. Geophys. Res.*, 1043:31333–31350.

Ek, M. B., Mitchell, K. E., Lin, Y., Rogers, E., Grunmann, P., Koren, V., Gayno, G., and Tarpley, J. D. (2003). Implementation of Noah land surface model advances in the National Centers for Environmental Prediction operational mesoscale Eta model. *J. Geophys. Res.*, 108(D22):8851+.

Fast, J. D., Gustafson, W. I., Easter, R. C., Zaveri, R. A., Barnard, J. C., Chapman, E. G., Grell, G. A., and Peckham, S. E. (2006). Evolution of ozone, particulates, and aerosol direct radiative forcing in the vicinity of Houston using a fully coupled meteorology-chemistry-aerosol model. *J. Geophys. Res.(Atmospheres)*, 111:21305–+. doi:10.1029/2005JD006721.

Feichter, J., Roeckner, E., Lohmann, U., and Liepert, B. (2003). Nonlinear Aspects of the Climate Response to Greenhouse Gas and Aerosol Forcing. *Journal of Climate*, 17:2384–2398.

Feingold, G., Eberhard, W. L., Lane, D. E., and Previdi, M. (2003). First measurements of the indirect effect using ground-based remote sensors. *Geophys. Res. Lett.*, 30(6). http://adsabs.harvard.edu/cgi-bin/nph-bib_query?bibcode=2002AGUFM.A22E..11F&db_key=PHY.

Feingold, G., Yang, S., Hardesty, R. M., and Cotton, W. R. (1998). Feasibility of Retrieving Cloud Condensation Nucleus Properties from Doppler Cloud Radar,

Microwave Radiometer, and Lidar. *Journal of Atmospheric and Oceanic Technology*, 15(5):1188–1195.

Ferrare, R. A., Schwartz, S., Ogren, J., Schmid, B., Ghan, S., Daum, P., and Feingold, G. (2002). Intensive Airborne and Surface Measurements of Aerosol Microphysical and Optical Properties and Influences on Shortwave Radiation. *AGU Fall Meeting Abstracts*, pages C138+. http://adsabs.harvard.edu/cgi-bin/nph-bib_query?bibcode=2002AGUFM.A22C0138F&db_key=PHY.

Fishman, J., Hoell, J. M., Bendura, R. D., McNeal, R. J., and Kirchhoff, V. W. J. H. (1996). NASA GTE TRACE A Experiment (September-October 1992): Overview. *J. Geophys. Res.*, 101:23865–23880.

Fouquart, Y. and Bonnel, B. (1980). Computations of solar heating of the earth's atmosphere: A new parameterization. *Beitr Phys Atmos*, 53:35–62.

Freitas, S. R., Longo, K. M., Alonso, M. F., Pirre, M., Marecal, V., Grell, G., Stockler, R., Mello, R. F., and Sánchez Gácita, M. (2011). PREP-CHEM-SRC–1.0: a preprocessor of trace gas and aerosol emission fields for regional and global atmospheric chemistry models. *Geoscientific Model Development*, 4(2):419–433.

French, N. H. F., Goovaerts, P., and Kasischke, E. S. (2004). Uncertainty in estimating carbon emissions from boreal forest fires. *Journal of Geophysical Research*, 109(D14):1–12.

Frenklach, M. and Harris, S. J. (1987). Aerosol dynamics modeling using the method of moments. *Journal of Colloid and Interface Science*, 118(1):252 – 261.

Friedlander, S. K. (1977). *Smoke, dust and haze: Fundamentals of aerosol behavior*.

Garstang, M., Tyson, P. D., Swap, R., Edwards, M., Kllberg, P., and Lindesay, J. A. (1996). Horizontal and vertical transport of air over Southern Africa. *J. Geophys. Res.*, 101:23721–23736.

Gatebe, C. K., Tyson, P. D., Annegarn, H. J., Helas, G., Kinyua, A. M., and Piketh, S. J. (2001). Characterization and transport of aerosols over equatorial eastern Africa. *Global Biogeochemical Cycles*, 15:663–672. doi: 10.1029/2000GB001340.

Gates, W. L., Boyle, J. S., Covey, C., Dease, C. G., Doutriaux, C. M., Drach, R. S., Fiorino, M., Gleckler, P. J., Hnilo, J. J., Marlais, S. M., and et al. (1999). An overview of the results of the atmospheric model intercomparison project (amip i). *Bull. Amer. Meteorol. Soc.*, 80(1):29–55.

Gelbard, F. and Seinfeld, J. H. (1979). The general dynamic equation for aerosols. theory and application to aerosol formation and growth. *Journal of Colloid and Interface Science*, 68(2):363 – 382.

Ghan, S., Chung, C., and Penner, J. (1993). A parameterization of cloud droplet nucleation part i: single aerosol type. *Atmospheric Research*, 30(4):198–221.

Ghosh, S., Smith, M., and Rap, A. (2007). Integrating biomass, sulphate and sea-salt aerosol responses into a microphysical chemical parcel model: implications for climate studies. *Philosophical Transactions of the Royal Society Series A: Mathematical, Physical and Engineering Sciences*, 365(1860):2659–2674.

Giorgi, F., Bi, X., and Pal, J. S. (2004). Mean, interannual variability and trends in a regional climate change experiment over Europe. I. Present-day climate (1961–1990). *Climate Dynamics*, 22(6-7):733–756.

Girard, E. and Bekcic, B. (2005). Sensitivity of an arctic regional climate model to the horizontal resolution during winter: implications for aerosol simulation. *International Journal of Climatology*, 25(11):1455–1471.

Greenberg, J. P., Guenther, A., Harley, P., Otter, L., Veenendaal, E. M., Hewitt, C. N., James, A. E., and Owen, S. M. (2003). Eddy flux and leaf-level measurements of biogenic VOC emissions from mopane woodland of Botswana. *J. Geophys. Res.*, 108(D13):8466–+. doi:10.1029/2002JD002317.

Greenfield, S. M. (1957). Rain Scavenging of Radioactive Particulate Matter from the Atmosphere. *Journal of Atmospheric Sciences*, 14:115–125.

Grell, G. A. and Dévényi, D. (2002). A generalized approach to parameterizing convection combining ensemble and data assimilation techniques. *Geophys. Res. Lett.*, 29(14):1693.

Grell, G. A., Peckham, S. E., Schmitz, R., McKeen, S. A., Frost, G., Skamarock, W. C., and Eder, B. (2005). Fully coupled *online* chemistry within the WRF model. *Atmospheric Environment*, 39(37):6957–6975. doi:10.1016/j.atmosenv.2005.04.027.

Griffin, R. J., Dabdub, D., and Seinfeld, J. H. (2002). Secondary organic aerosol. Atmospheric chemical mechanism for production of molecular constituents. *J. Geophys. Res.(Atmospheres)*, 107:4332–+.

Grönholm, T., Aalto, P. P., Hiltunen, V., Rannik, Ã., Rinne, J., Laakso, L., Hyvönen, S., Vesala, T., and Kulmala, M. (2007). Measurements of aerosol particle dry deposition velocity using the relaxed eddy accumulation technique. *Tellus Series B Chemical And Physical Meteorology*, 59(3):381–386.

Guan, H., Chatfield, R. B., Freitas, S. R., Bergstrom, R. W., and Longo, K. M. (2008). Modeling the effect of plume-rise on the transport of carbon monoxide over Africa with NCAR CAM. *Atmospheric Chemistry and Physics*, 8(22):6801–6812.

Gustafson, W. I., Chapman, E. G., Ghan, S. J., Easter, R. C., and Fast, J. D. (2007). Impact on modeled cloud characteristics due to simplified treatment of uniform cloud condensation nuclei during NEAQS 2004. *Geophys. Res. Lett.*, 34:19809–+.

Hagemann, S., Arpe, K., and Roeckner, E. (2006). Evaluation of the hydrological cycle in the echam5 model. *Journal of Climate*, 19(16):3810–3827.

Han, Z., Ueda, H., Matsuda, K., Zhang, R., Arao, K., Kanai, Y., and Hasome, H. (2004). Model study on particle size segregation and deposition during Asian dust events in March 2002. *J. Geophys. Res.(Atmospheres)*, 109(D18):19205.

Hansen, J., Sato, M., and Ruedy, R. (1997). Radiative forcing and climate response. *J. Geophys. Res.*, 102:6831–6864.

Harrison, S. P., Kohfeld, K. E., Roelandt, C., and Claquin, T. (2001). The role of dust in climate changes today, at the last glacial maximum and in the future. *Earth-Science Reviews*, 54(1–3):43–80.

Hastie, T. and Tibshirani, R. (1986). Generalized additive models. *Statistical Science*, 1:297–310.

Haywood, J. and Boucher, O. (2000). Estimates of the direct and indirect radiative forcing due to tropospheric aerosols: A review. *Reviews of Geophysics*, 38:513–543. doi:10.1029/1999RG000078.

Haywood, J. M., Osborne, S. R., Francis, P. N., Keil, A., Formenti, P., Andreae, M. O., and Kaye, P. H. (2003). The mean physical and optical properties of regional haze dominated by biomass burning aerosol measured from the C-130 aircraft during SAFARI 2000. *J. Geophys. Res.*, 108(D13):8473–+. doi:10.1029/2002JD002226.

Heintzenberg, J. (1989). Fine particles in the global troposphere. *Tellus Series B Chemical and Physical Meteorology B*, 41:149–160.

Helas, G. and Pienaar, J. J. (1996). The influence of vegetation fires on the chemical composition of the atmosphere. *S. Afr. J. Sci.*, 92(3):132–136.

Henning, S., Rosenørn, T., D'Anna, B., Gola, A. A., Svenningsson, B., and Bilde, M. (2005). Cloud droplet activation and surface tension of mixtures of slightly soluble organics and inorganic salt. *Atmospheric Chemistry and Physics*, 5(2):575–582.

Herman, J. R., Bhartia, P. K., Torres, O., Hsu, C., Seftor, C., and Celarier, E. (1997). Global distribution of UV-absorbing aerosols from Nimbus 7/TOMS data. *Journal of Geophysical Research*, 102(D14):16911–16922.

Hess, M., Koepke, P., and Schult, I. (2010). Optical Properties of Aerosols and Clouds: The Software Package OPAC. *Bull. Amer. Meteor. Soc.*, 79(5):831–844.

Hewitson, B. C. and Crane, R. G. (2002). Self-organizing maps: applications to synoptic climatology. *Climate Research*, 22(1):13–26.

Hicks, B., Baldocchi, D., Myers, T., Hosker, R., and Matt, D. (1987). A preliminary multiple resistance routine for deriving dry deposition from measured quantities. *Water, Air and Soil pollution*, 36:311–330.

Ho, K. F., Lee, S. C., Chan, C. K., Yu, J. C., Chow, J. C., and Yao, X. H. (2003). Characterization of chemical species in PM2.5 and PM10 aerosols in Hong Kong. *Atmospheric Environment*, 37(1):31 – 39.

Hobbs, P. V. (2003). Clean air slots amid dense atmospheric pollution in Southern Africa. *J. Geophys. Res.*, 108(D13):8490–+. doi:10.1029/2002JD002156.

Holben, B. N., Tanré, D., Smirnov, A., Eck, T. F., Slutsker, I., Abuhassan, N., Newcomb, W. W., Schafer, J. S., Chatenet, B., Lavenu, F., Kaufman, Y. J., Castle, J. V., Setzer, A., Markham, B., Clark, D., Frouin, R., Halthore, R., Karneli, A., O'Neill, N. T., Pietras, C., Pinker, R. T., Voss, K., and Zibordi, G. (2001). An emerging ground-based aerosol climatology: Aerosol optical depth from AERONET. *J. Geophys. Res.*, 106:12067–12098.

Hong, G., Yang, P., Baum, B. A., Heymsfield, A. J., and Xu, K.-M. (2009). Parameterization of Shortwave and Longwave Radiative Properties of Ice Clouds for Use in Climate Models. *Journal of Climate*, 22:6287–+.

Huang, Y., Chameides, W. L., and Dickinson, R. E. (2007). Direct and indirect effects of anthropogenic aerosols on regional precipitation over east Asia. *J. Geophys. Res.*, 112:D03212.

Hulburt, H. M. and Katz, S. (1964). Some problems in particle technology: A statistical mechanical formulation. *Chemical Engineering Science*, 19(8):555–574.

Hulme, M., Doherty, R., Ngara, T., New, M., and Lister, D. (2001). African Climate Change: 1900–2100. In Desanker, P., editor, *Africa and global climate change*, volume 17, pages 145–168. Clim. Res.

Hutchinson, T. A. (2005). An adaptive time-step for increased model efficiency. *Europe*.

Ichoku, C., Kaufman, Y., Remer, L., Chu, D. A., Mattoo, S., Tanre, D., Levy, R., Li, R.-R., and Kleidman, R. (2001). MODIS Observation of Aerosols over Southern Africa During SAFARI 2000: Data, Validation, and Estimation of Aerosol Radiative Forcing. *Journal of Geophysical Research*, 108(D13):1–13.

Ichoku, C., Remer, L. A., Kaufman, Y. J., Levy, R., Chu, D. A., Tanré, D., and Holben, B. N. (2003). MODIS observation of aerosols and estimation of aerosol radiative forcing over southern Africa during SAFARI 2000. *J. Geophys. Res.*, 108(D13):8499–+. doi:10.1029/2002JD002366.

Ingmar J. Ackermann and Heinz Hass and M. Memmesheimer and A. Ebel and Francis S. Binkowski and Uma Shankar (1998). Modal aerosol dynamics model for Europe: development and first applications. *Atmospheric Environment*, 32(17):2981 – 2999.

IPCC-WGI (2001). *Climate Change 2001: The Scientific Basis*. Cambridge University Press, New York, Cambridge and New York.

IPCC-WGI (2007). *Climate Change 2007 - The Physical Science Basis: Working Group I Contribution to the Fourth Assessment Report of the IPCC*. Cambridge University Press, Cambridge, UK and New York, NY, USA.

Jacobson, M. Z. (1997). Development and application of a new air pollution modeling system–II. Aerosol module structure and design. *Atmospheric Environment*, 31(2):131 – 144.

Jacobson, M. Z. (2001). GATOR-GCMM: A global- through urban-scale air pollution and weather forecast model, 1. Model design and treatment of subgrid soil, vegetation, roads, rooftops, water, sea ice, and snow. *J. Geophys. Res.*, 106:5385–5402.

Jacobson, M. Z. (2001). Strong radiative heating due to the mixing state of black carbon in atmospheric aerosols. *Nature*, 409:695–697.

Jaenicke, R. and Hanusch, T. (1993). Simulation of the Optical Particle Counter Forward Scattering Spectrometer Probe 100 (FSSP-100). *Aerosol Science and Technology*, 18(4):309–322.

Janowiak, J. E. (1988). An Investigation of Interannual Rainfall Variability in Africa. *J. Climate*, 1(3):240–255.

Jin, J., Miller, N. L., and Schlegel, N. (2010). Sensitivity Study of Four Land Surface Schemes in the WRF Model. *Advances in Meteorology*, page 11 pp.

J.M. and Pacyna (2008). Atmospheric Deposition. In Jorgensen, S. E. and Fath, B., editors, *Encyclopedia of Ecology*, pages 275 – 285. Academic Press, Oxford.

Johnson, B. T., Shine, K. P., and Forster, P. M. (2004). The semi-direct aerosol effect: Impact of absorbing aerosols on marine stratocumulus. *Quarterly Journal of the Royal Meteorological Society*, 130:1407–1422.

Jones, A., Roberts, D. L., and Slingo, A. (1994). A climate model study of indirect radiative forcing by anthropogenic sulfate aerosols affects of sulfate aerosols. *Nature*, 370.

Joseph, J. H., Wiscombe, W. J., and Weinman, J. A. (1976). The Delta-Eddington Approximation for Radiative Flux Transfer. *Journal of the Atmospheric Sciences*, 33(12):2452–2459.

Jung, C. E. (1957). Chemical Analysis of Aerosol Particles and of Gas Traces on the Island of Hawaii. *Tellus*, 9(4):528–537.

Jung, C. H., Kim, Y., and Lee, K. (2002). Analytic solution for polydispersed aerosol dynamics by a wet removal process. *Journal of Aerosol Science*, 33(5):753 – 767.

Kanamitsu, M., Ebisuzaki, W., Woollen, J., Yang, S., Hnilo, J. J., Fiorino, M., and Potter, G. L. (2002). NCEP-DOE AMIP-II Reanalysis (R-2). *Bulletin of the American Meteorological Society*, 83:1631–1643.

Kanyanga, J. (2008). *El Niño Southern Oscillation (ENSO) and atmospheric transport over Southern Africa*. PhD thesis, University of Johannesburg.

Katoshevski, D. and Seinfeld, J. H. (1997). Analytical–numerical solution of the multicomponent aerosol general dynamic equation–with coagulation. *Aerosol Science and Technology*, 27(4):550–556.

Kaufman, Y. J., Fraser, R. S., and Mahoney, R. L. (1991). Fossil Fuel and Biomass Burning Effect on Climate–Heating or Cooling. *Journal of Climate*, 4(6):578–588. http://dx.doi.org/10.1175%2F1520-0442%281991%29004%3C0578%3AFFABBE%3E2.0.CO%3B2.

Kaufman, Y. J., Gitelson, A., Karnieli, A., Ganor, E., Fraser, R. S., Nakajima, T., Mattoo, S., and Holben, B. N. (1994). Size distribution and scattering phase function of aerosol particles retrieved from sky brightness measurements. *J. Geophys. Res.*, 99(D5):10341–10356.

Khvorostyanov, V. I. and Curry, J. A. (2006). Aerosol size spectra and CCN activity spectra: Reconciling the lognormal, algebraic, and power laws. *J. Geophys. Res.(Atmospheres)*, 111(D10):12202.

Kim, S.-W., Berthier, S., Raut, J.-C., Chazette, P., Dulac, F., and Yoon, S.-C. (2008). Validation of aerosol and cloud layer structures from the space-borne lidar CALIOP using a ground-based lidar in Seoul, Korea. *Atmospheric Chemistry and Physics*, 8(13):3705–3720.

Kim, Y. P. and Seinfeld, J. H. (1990). Simulation of multicomponent aerosol condensation by the moving sectional method. *Journal of Colloid and Interface Science*, 135(1):185 – 199.

King, M. D., Kaufman, Y. J., Tanré, D., and Nakajima, T. (1999). Remote Sensing of Tropospheric Aerosols from Space: Past, Present, and Future. *Bulletin of the American Meteorological Society*, 80:2229–2260.

King, M. D., Menzel, W. P., Kaufman, Y. J., Tanre, D., Gao, B.-C., Platnick, S., Ackerman, S. A., Remer, L. A., Pincus, R., and Hubanks, P. A. (2003). Cloud and aerosol properties, precipitable water, and profiles of temperature and water vapor from MODIS. *IEEE Transactions on Geoscience and Remote Sensing*, 41:442–458.

Kirchstetter, T. W., Novakov, T., Hobbs, P. V., and Magi, B. (2003). Airborne measurements of carbonaceous aerosols in southern Africa during the dry biomass burning season. *J. Geophys. Res.*, 108(D13):8476–+. doi:10.1029/2002JD002171.

Kirkevåg, A., Iversen, T., and Dahlback, A. (1999). On radiative effects of black carbon and sulphate aerosols. *Atmospheric Environment*, 33(17):2621 – 2635.

Knutson, E. and Whitby, K. (1975). Aerosol classification by electric mobility: apparatus, theory, and applications. *Journal of Aerosol Science*, 6(6):443 – 451.

Köhler, H. (1936). The nucleus in and the growth of hygroscopic droplets. *Transactions of the Faraday Society*, 32(184):1152–1161.

Kohonen, T. (1982). Self-organized formation of topologically correct feature maps. *Biological Cybernetics*, 43(1):59–69.

Kondratyev, K. Y., Binenko, V. I., and Melnikova, I. N. (1998). Absorption of solar radiation by clouds and aerosols in the visible wavelength region. *Meteorology and Atmospheric Physics*, 65:1–10. 10.1007/BF01030265.

Kourti, N. and Schatz, A. (1998). Solution of the general dynamic equation (GDE) for multicomponent aerosols. *Journal of Aerosol Science*, 29(1-2):41 – 55.

Kulmala, M., Korhonen, P., Laaksonen, A., and Charlson, R. J. (1997a). A generalized reformulation of the Köhler theory: effects of soluble trace gases and slightly soluble substances. *Journal of Aerosol Science*, 28, Supplement 1(0):S749 – S750.

Kulmala, M., Laaksonen, A., Aalto, P., Vesala, T., Pirjola, L., Kerminen, V. M., Korhonen, P., Hillamo, R., Virkkula, A., and Aurela, M. (1996). Formation, Growth, and Properties of Atmospheric Aerosol Particles and Cloud Droplets. *Geophysica*, 32(1-2):217–133.

Kulmala, M., T., M., and Toivonen, A. (1997b). The effect of ammonia and acids on cloud droplet formation. *Journal of Aerosol Science*, 28(1001):419–420.

Laaksonen, A., Korhonen, P., Kulmala, M., and Charlson, R. J. (1998). Modification of the Köhler Equation to Include Soluble Trace Gases and Slightly Soluble Substances. *Journal of Atmospheric Sciences*, 55:853–862.

Langmann, B., Zakšek, K., and Hort, M. (2010). Atmospheric distribution and removal of volcanic ash after the eruption of Kasatochi volcano: A regional model study. *J. Geophys. Res.(Atmospheres)*, 115(D14):0.

Lave, L. B. and Seskin, E. P. (1970). Air Pollution and Human Health. *Science*, 169:723–733.

Lee, S., Ghim, Y. S., Kim, S.-W., and Yoon, S.-C. (2010). Effect of biomass burning and regional background aerosols on CCN activity derived from airborne in-situ measurements. *Atmospheric Environment*, 44(39):5227–5236.

Levin, E. J. T., McMeeking, G. R., Carrico, C. M., Mack, L. E., Kreidenweis, S. M., Wold, C. E., Moosmüller, H., Arnott, W. P., Hao, W. M., Collett, J. L., and Malm, W. C. (2010). Biomass burning smoke aerosol properties measured during Fire Laboratory at Missoula Experiments (FLAME). *J. Geophys. Res.(Atmospheres)*, 115(D14):18210.

Levy, R. C., Remer, L. A., Martins, J. V., Kaufman, Y. J., Plana-Fattori, A., Redemann, J., and Wenny, B. (2005). Evaluation of the MODIS Aerosol Retrievals over Ocean and Land during CLAMS. *Journal of the Atmospheric Sciences*, 62(4):974–992.

Lin, S.-J. and Rood, R. B. (1996). Multidimensional flux-form semi-Lagrangian transport schemes. *Monthly Weather Review*, 124(9):2046–2070.

Lin, Y.-L., Farley, R. D., and Orville, H. D. (1983). Bulk Parameterization of the Snow Field in a Cloud Model. *Journal of Applied Meteorology*, 22:1065–1092.

Lindesay, J. A., Andreae, M. O., Goldammer, J. G., Harris, G., Annegarn, H. J., Garstang, M., Scholes, R. J., and van Wilgen, B. W. (1996). International Geosphere-Biosphere Programme/International Global Atmospheric Chemistry SAFARI-92 field experiment: Background and overview. *J. Geophys. Res.*, 101:23521–23530.

Lindley, S. J., Conlan, D. E., Raper, D. W., and Watson, A. F. R. (2000). Uncertainties in the compilation of spatially resolved emission inventories: evidence from a comparative study. *Atmospheric Environment*, 34(3):375–388.

Lioubimtseva, E., Cole, R., Adams, J., and Kapustin, G. (2005). Impacts of climate and land-cover changes in arid lands of Central Asia. *Journal of Arid Environments*, 62(2):285–308.

Liousse, C., Guillaume, B., Grégoire, J. M., Mallet, M., Galy, C., Pont, V., Akpo, A., Bedou, M., Castéra, P., Dungall, L., Gardrat, E., Granier, C., Konaré, A., Malavelle, F., Mariscal, A., Mieville, A., Rosset, R., Serça, D., Solmon, F., Tummon, F., Assamoi, E., Yoboué, V., and Van Velthoven, P. (2010). Updated african biomass burning emission inventories in the framework of the amma-idaf program, with an evaluation of combustion aerosols. *Atmospheric Chemistry and Physics*, 10(19):9631–9646.

Liousse, C., Guillaume, B., Konaré, A., Grégoire, J. M., Solmon, F., Poirson, A., Granier, C., Rosset, R., and Cachier, H. (2007). Fossil fuel, Biofuel and Biomass burning emission inventories for gases and particles in Africa with tentative validations with global TM4 and regional RegCM aerosol modeling for the year 2000. *Geophys. Res. Abstr.*, 9(03883). SRef-ID: 1607-7962/gra/EGU2007-A-03883.

Liu, B. Y., Berglund, R. N., and Agarwal, J. K. (1974). Experimental studies of optical particle counters. *Atmospheric Environment (1967)*, 8(7):717 – 732.

Liu, B. Y. and Kim, C. (1977). On the counting efficiency of condensation nuclei counters. *Atmospheric Environment (1967)*, 11(11):1097 – 1100.

Liu, Y., Weisberg, R. H., and Mooers, C. N. K. (2006). Performance evaluation of the self-organizing map for feature extraction. *Journal of Geophysical Research (Oceans)*, 111:5018.

Lohmann, U. and Feichter, J. (2001). Can the direct and semi-direct aerosol effect compete with the indirect effect on a global scale? *Geophys. Res. Lett.*, 28:159–162.

Lohmann, U. and Feichter, J. (2005). Global indirect aerosol effects: a review. *Atmospheric Chemistry & Physics*, 5:715–737.

Lohmann, U., Feichter, J., Penner, J., and Leaitch, R. (2000). Indirect effect of sulfate and carbonaceous aerosols: A mechanistic treatment. *J. Geophys. Res.*, 105(D10):12193–12206.

Lohmann, U., Stier, P., Hoose, C., Ferrachat, S., Kloster, S., Roeckner, E., and Zhang, J. (2007). Cloud microphysics and aerosol indirect effects in the global climate model ECHAM5-HAM. *Atmospheric Chemistry and Physics*, 7(13):3425–3446.

Loosmore, G. A. and Cederwall, R. T. (2004). Precipitation scavenging of atmospheric aerosols for emergency response applications: testing an updated model with new real-time data. *Atmospheric Environment*, 38(7):993 – 1003.

Magi, B. I., Hobbs, P. V., Schmid, B., and Redemann, J. (2003). Vertical profiles of light scattering, light absorption, single scattering albedo during the dry, biomass burning season in southern Africa and comparisons of in situ and remote sensing measurements of aerosol optical depths. *J. Geophys. Res.*, 108(D13):8504–+. doi:10.1029/2002JD002361.

Mahler, A.-B., Thome, K., Yin, D., and Sprigg, W. A. (2006). Dust transport model validation using satellite- and ground-based methods in the southwestern United States. In *Society of Photo-Optical Instrumentation Engineers (SPIE) Conference Series*, volume 6299 of *Society of Photo-Optical Instrumentation Engineers (SPIE) Conference Series*.

Makkonen, R., Asmi, A., Korhonen, H., Kokkola, H., Järvenoja, S., Räisänen, P., Lehtinen, K. E. J., Laaksonen, A., Kerminen, V.-M., Järvinen, H., Lohmann, U., Bennartz, R., Feichter, J., and Kulmala, M. (2009). Sensitivity of aerosol concentrations and cloud

properties to nucleation and secondary organic distribution in ECHAM5-HAM global circulation model. *Atmospheric Chemistry and Physics*, 9(5):1747–1766.

Marchisio, D. L., Pikturna, J. T., Fox, R. O., Vigil, R. D., and Barresi, A. A. (2003). Quadrature method of moments for population-balance equations. *AIChE Journal*, 49(5):1266–1276.

Maring, H. and Schwartze, G. (1994). A condensation particle counter for long-term continuous use in the remote marine environment. *Atmospheric Environment*, 28(20):3293 – 3298.

Martinsson, B., Cederfelt, S.-I., Svenningsson, B., Frank, G., Hansson, H.-C., Swietlicki, E., Wiedensohler, A., Wendisch, M., Gallagher, M., Colvile, R., Beswick, K., Choularton, T., and Bower, K. (1997). Experimental determination of the connection between cloud droplet size and its dry residue size. *Atmospheric Environment*, 31(16):2477 – 2490. The Great Dun Fell Cloud Experiment 1993, Eurotrac sub-project Ground-based Cloud Experiment (GCE).

Marufu, L., Dentener, F., Lelieveld, J., Andreae, M. O., and Helas, G. (2000). Photochemistry of the African troposphere: Influence of biomass-burning emissions. *J. Geophys. Res.*, 105:14513–14530.

Mason, S. J. and Joubert, A. M. (1997). Simulated Changes in Extreme Rainfall over Southern Africa. *International Journal of Climatology*, 17:291–301. doi:10.1023/A:1023630924100.

Max, M.-D. C. and Suarez, M. J. (1994). An Efficient Thermal Infrared Radiation Parameterization For Use In General Circulation Models. NASA Tech. Memo. 104606, 3, 85pp.

Maxey, M. R. and Corrsin, S. (1986). Gravitational Settling of Aerosol Particles in Randomly Oriented Cellular Flow Fields. *Journal of Atmospheric Sciences*, 43:1112–1134.

McFiggans, G., Artaxo, P., Baltensperger, U., Coe, H., Facchini, M. C., Feingold, G., Fuzzi, S., Gysel, M., Laaksonen, A., Lohmann, U., Mentel, T. F., Murphy, D. M., O'Dowd, C. D., Snider, J. R., and Weingartner, E. (2006). The effect of physical and

chemical aerosol properties on warm cloud droplet activation. *Atmospheric Chemistry and Physics*, 6(9):2593–2649.

McGraw, R. (1997). Description of aerosol dynamics by the quadrature method of moments. *Aerosol Science and Technology*, 27(2):255–265.

Meador, W. E. and Weaver, W. R. (1980). Two-stream approximations to radiative transfer in planetary atmospheres - a unified description of existing methods and a new improvement. *Journal of the Atmospheric Sciences*, 37(3):630–643.

Menghua and Wang (2003). An efficient method for multiple radiative transfer computations and the lookup table generation. *Journal of Quantitative Spectroscopy and Radiative Transfer*, 78(3–4):471 – 480.

Menon, S. (2004). Current Uncertainties in Assessing Aerosol Effects on Climate. *Annual Review of Environment and Resources*, 29(1):1–30. doi: 10.1146/annurev.energy.29.063003.132549.

Ming, Y. and Ramaswamy, V. (2011). A model investigation of aerosol-induced changes in tropical circulation. *Journal of Climate*, 24(19):5125–5133.

Ming, Y., Ramaswamy, V., and Chen, G. (2011). A model investigation of aerosol-induced changes in boreal winter extratropical circulation. *Journal of Climate*, 24(23):6077–6091.

Mircea, M. and Stefan, S. (1998). A theoretical study of the microphysical parameterization of the scavenging coefficient as a function of precipitation type and rate. *Atmospheric Environment*, 32(17):2931–2938.

Mitchell, T. D. and Jones, P. D. (2005). An improved method of constructing a database of monthly climate observations and associated high-resolution grids. *International Journal of Climatology*, 25:693–712.

Mlawer, E. J., Taubman, S. J., Brown, P. D., Iacono, M. J., and Clough, S. A. (1997). Radiative transfer for inhomogeneous atmospheres: RRTM, a validated correlated-k model for the longwave. *Journal of Geophysical Research*, 102(D14):16663–16682.

Montilla, E., Mogo, S., Cachorro, V., Lopez, J., and de Frutos, A. (2011). Absorption, scattering and single scattering albedo of aerosols obtained from in situ measurements in the subarctic coastal region of Norway. *Atmospheric Chemistry and Physics Discussions*, 11(1):2161–2182.

Morrison, H., Curry, J. A., and Khvorostyanov, V. I. (2005). A New Double-Moment Microphysics Parameterization for Application in Cloud and Climate Models. Part I: Description. *Journal of Atmospheric Sciences*, 62:1665–1677.

Murphy, D. M., Thomson, D. S., and Mahoney, M. J. (1998). In Situ Measurements of Organics, Meteoritic Material, Mercury, and Other Elements in Aerosols at 5 to 19 Kilometers. *Science*, 282:1664–+.

Myhre, G., Berntsen, T. K., Haywood, J. M., Sundet, J. K., Holben, B. N., Johnsrud, M., and Stordal, F. (2003). Modeling the solar radiative impact of aerosols from biomass burning during the Southern African Regional Science Initiative (SAFARI-2000) experiment. *J. Geophys. Res.*, 108(D13):8501–+. doi:10.1029/2002JD002313.

Myhre, G., Stordal, F., Johnsrud, M., Kaufman, Y. J., Rosenfeld, D., Storelvmo, T., Kristjansson, J. E., Berntsen, T. K., Myhre, A., and Isaksen, I. S. A. (2007). Aerosol-cloud interaction inferred from MODIS satellite data and global aerosol models. *Atmospheric Chemistry and Physics*, 7(12):3081–3101.

Nenes, A., Charlson, R. J., Facchini, M. C., Kulmala, M., Laaksonen, A., and Seinfeld, J. H. (2002). Can chemical effects on cloud droplet number rival the first indirect effect? *Geophys. Res. Lett.*, 29(17):170000–1.

Nenes, A. and Seinfeld, J. H. (2003). Parameterization of cloud droplet formation in global climate models. *J. Geophys. Res.(Atmospheres)*, 108:4415.

New, M., Hulme, M., and Jones, P. (1999). Representing Twentieth-Century Space–Time Climate Variability. Part I: Development of a 1961–90 Mean Monthly Terrestrial Climatology. *Journal of Climate*, 12(3):829–856.

New, M., Hulme, M., and Jones, P. D. (2000). Representing twentieth century space-time climate variability. ii: development of 1901-1996 monthly grids of terrestrial surface climate. *Journal of Climate*, 13(13):2217–2238.

Nicholson, S. and Entekhabi, D. (1986). The quasi-periodic behavior of rainfall variability in africa and its relationship to the southern oscillation. *Archives for Meteorology, Geophysics, and Bioclimatology, Series A*, 34(3-4):311–348.

Olivier, J. G. J., Bouwman, A. F., Vandermaas, C. W. M., and Berdowski, J. J. M. (1994). Emission database for global atmospheric research (EDGAR). *Environmental Monitoring and Assessment*, 31(1–2):93–106.

Otter, L., Guenther, A., Wiedinmyer, C., Fleming, G., Harley, P., and Greenberg, J. (2003). Spatial and temporal variations in biogenic volatile organic compound emissions for Africa south of the equator. *J. Geophys. Res.*, 108(D13):8505–+. doi:10.1029/2002JD002609.

Paeth, H. and Feichter, J. (2006). Greenhouse-gas versus aerosol forcing and African climate response. *Climate Dynamics*, 26:35–54. doi:10.1007/s00382-005-0070-z.

Pearce, J. L., Beringer, J., Nicholls, N., Hyndman, R. J., and Tapper, N. J. (2011a). Quantifying the influence of local meteorology on air quality using generalized additive models. *Atmospheric Environment*, 45(6):1328–1336.

Pearce, J. L., Beringer, J., Nicholls, N., Hyndman, R. J., Uotila, P., and Tapper, N. J. (2011b). Investigating the influence of synoptic-scale meteorology on air quality using self-organizing maps and generalized additive modelling. *Atmospheric Environment*, 45(1):128–136.

Peckham, S., Grell, G., McKeen, S., Fast, J., Gustafson, W., Ghan, S., Zaveri, R., Easter, R., Barnard, J., Chapman E Wiedeinmyer, C., and et al. (2010). WRF/Chem Version 3.2 Users Guide. *Atmospheric Research*, (July).

Penner, J. E. and Chuang, C. C. (1999). The role of entrainment and mixing in altering the relationship between aerosol concentration and cloud drop number concentration. *Weather*, pages 1–6.

Penner, J. E., Chuang, C. C., and Grant, K. (1998). Climate forcing by carbonaceous and sulfate aerosols. *Climate Dynamics*, 14:839–851. 10.1007/s003820050259.

Penner, J. E., Quaas, J., Storelvmo, T., Takemura, T., Boucher, O., Guo, H., Kirkevåg, A., Kristjánsson, J. E., and Seland, Ø. (2006). Model intercomparison of indirect aerosol effects. *Atmospheric Chemistry and Physics*, 6(11):3405.

Petters, M. D., Carrico, C. M., Kreidenweis, S. M., Prenni, A. J., DeMott, P. J., Collett, J. L., and Moosmüller, H. (2009). Cloud condensation nucleation activity of biomass burning aerosol. *J. Geophys. Res.(Atmospheres)*, 114(D13):22205.

Pierce, J. R., Chen, K., and Adams, P. J. (2007). Contribution of primary carbonaceous aerosol to cloud condensation nuclei: processes and uncertainties evaluated with a global aerosol microphysics model. *Atmospheric Chemistry and Physics*, 7(20):5447–5466.

Piketh, S. and Walton, N. (2004). Characteristics of Atmospheric Transport of Air Pollution for Africa. In Stohl, A., editor, *Air Pollution*, volume 4G of *The Handbook of Environmental Chemistry*, pages 173–195. Springer Berlin / Heidelberg.

Piketh, S. J., Annegarn, H. J., and Tyson, P. D. (1999). Lower tropospheric aerosol loadings over South Africa: the relative contribution of aeolian dust, industrial emissions, and biomass burning. *J. Geophys. Res.*, 104:1597–1608. doi: 10.1029/1998JD100014.

Platnick, S., King, M. D., Ackerman, S. A., Menzel, W. P., Baum, B. A., Riedi, J. C., and Frey, R. A. (2003). The MODIS cloud products: algorithms and examples from Terra. *IEEE Transactions on Geoscience and Remote Sensing*, 41:459–473.

Pleim, J. E. (2007). A combined local and nonlocal closure model for the atmospheric boundary layer. Part I: model description and testing. *J. Appl. Meteor. Climatol.*, pages 1383–1395.

Pope, C. (2000). Review: Epidemiological basis for particulate air pollution health standards. *Aerosol Science and Technology*, 32:4–14(11).

Popp, C., Hauser, A., Foppa, N., and Wunderle, S. (2007). Remote sensing of aerosol optical depth over central Europe from MSG-SEVIRI data and accuracy assessment with ground-based AERONET measurements. *Journal of Geophysical Research*, 112(D24):D24S11.

Porter, J. N. and Clarke, A. D. (1997). Aerosol size distribution models based on in situ measurements. *J. Geophys. Res.*, 102:6035–6046.

Pöschl, U. (2005). Atmospheric Aerosols: Composition, Transformation, Climate and Health Effects. *Angewandte Chemie International Edition*, 44(46):7520–7540.

Power, H. C. (2003). The geography and climatology of aerosols. *Progress in Physical Geography*, 27(4):502–547. doi: 10.1191/0309133303pp393ra.

Pratsinis, S. E. (1988). Simultaneous nucleation, condensation, and coagulation in aerosol reactors. *Journal of Colloid and Interface Science*, 124(2):416 – 427.

Preisler, H. K. (1989). Fitting dose-response data with non-zero background within generalized linear and generalized additive models. *Computational Statistics & Data Analysis*, 7(3):279 – 290.

Previdi, M., Feingold, G., Veron, D. E., and Eberhard, W. L. (2003). Ground Based Remote Sensing of the First Aerosol Indirect Effect: An Update. *AGU Fall Meeting Abstracts*, pages F1+.

Pringle, K. J., Carslaw, K. S., Spracklen, D. V., Mann, G. M., and Chipperfield, M. P. (2009). The relationship between aerosol and cloud drop number concentrations in a global aerosol microphysics model. *Atmospheric Chemistry and Physics*, 9(12):4131–4144.

Pruppacher, H. R. and Klett, J. D. (1978). *Microphysics of Clouds and Precipitation*. D. Reidel, Dordrecht Holland.

Quaas, J. and Boucher, O. (2005). Constraining the first aerosol indirect radiative forcing in the LMDZ GCM using POLDER and MODIS satellite data. *Geophys. Res. Lett.*, 32:17814–+. doi:10.1029/2005GL023850.

Quaas, J., Boucher, O., Dufresne, J.-L., and Treut, H. (2004). Impacts of greenhouse gases and aerosol direct and indirect effects on clouds and radiation in atmospheric GCM simulations of the 1930–1989 period. *Climate Dynamics*, 23:779–789. doi:10.1007/s00382-004-0475-0ELECTR: 7.

Quaas, J., Ming, Y., Menon, S., Takemura, T., Wang, M., Penner, J. E., Gettelman, A., Lohmann, U., Bellouin, N., Boucher, O., Sayer, A. M., Thomas, G. E., McComiskey, A., Feingold, G., Hoose, C., Kristjánsson, J. E., Liu, X., Balkanski, Y., Donner, L. J., Ginoux, P. A., Stier, P., Grandey, B., Feichter, J., Sednev, I., Bauer, S. E., Koch, D., Grainger, R. G., Kirkevåg, A., Iversen, T., Seland, Ø., Easter, R., Ghan, S. J., Rasch, P. J., Morrison, H., Lamarque, J.-F., Iacono, M. J., Kinne, S., and Schulz, M. (2009). Aerosol indirect effects – general circulation model intercomparison and evaluation with satellite data. *Atmospheric Chemistry and Physics*, 9(22):8697–8717.

Queface, A. J., Piketh, S. J., Annegarn, H. J., Holben, B. N., and Uthui, R. J. (2003). Retrieval of aerosol optical thickness and size distribution from the CIMEL Sun photometer over Inhaca Island, Mozambique. *J. Geophys. Res.*, 108(D13):8509–+. doi:10.1029/2002JD002374.

Queface, A. J., Piketh, S. J., Eck, T. F., Tsay, S.-C., and Mavume, A. F. (2011). Climatology of aerosol optical properties in Southern Africa. *Atmospheric Environment*, 45(17):2910 – 2921.

Raes, F., Liao, H., Chen, W.-T., and Seinfeld, J. H. (2010). Atmospheric chemistry-climate feedbacks. *Journal of Geophysical Research*, 115(D12):1–14.

Ramana, M. V., Ramanathan, V., Feng, Y., Yoon, S. C., Kim, S. W., Carmichael, G. R., and Schauer, J. J. (2010). Warming influenced by the ratio of black carbon to sulphate and the black-carbon source. *Nature Geoscience*, 3(8):542–545.

Ramanathan, V., Boucher, O., Haigh, J., Hauglustaine, D., Haywood, J., Myhre, G., Nakajima, T., Shi, G. Y., , and Solomon, S. (2001a). Radiative forcing of climate change. In et al., J. T. H., editor, *Climate Change 2001: The Scientific Basis*, pages pp. 349–416. Cambridge Univ. Press, New York.

Ramanathan, V. and Carmichael, G. (2008). Global and regional climate changes due to black carbon. *Nature Geoscience*, 1(4):221–227.

Ramanathan, V., Crutzen, P. J., Kiehl, J. T., and Rosenfeld, D. (2001b). Aerosols, Climate, and the Hydrological Cycle. *Science*, 294(5549):2119–2124. doi:10.1126/science.1064034.

Ramanathan, V., Crutzen, P. J., Lelieveld, J., Mitra, A. P., Althausen, D., Anderson, J., Andreae, M. O., Cantrell, W., Cass, G. R., Chung, C. E., Clarke, A. D., Coakley, J. A., Collins, W. D., Conant, W. C., Dulac, F., Heintzenberg, J., Heymsfield, A. J., Holben, B., Howell, S., Hudson, J., Jayaraman, A., Kiehl, J. T., Krishnamurti, T. N., Lubin, D., McFarquhar, G., Novakov, T., Ogren, J. A., Podgorny, I. A., Prather, K., Priestley, K., Prospero, J. M., Quinn, P. K., Rajeev, K., Rasch, P., Rupert, S., Sadourny, R., Satheesh, S. K., Shaw, G. E., Sheridan, P., and Valero, F. P. J. (2001). Indian Ocean experiment: An integrated analysis of the climate forcing and effects of the great Indo-Asian haze. *J. Geophys. Res.*, 106:28371–28398.

Rampino, M. R. and Self, S. (1984). Sulphur-rich volcanic eruptions and stratospheric aerosols. *Nature*, 310:677–679.

Randerson, J. T., Kasibhatla, E. S., Kasischke, E. J., Hyer, E. J., Giglio, L., Collatz, G. J., and Van Der Werf, G. R. (2005). Global Fire Emissions Database (GFED), Version 1. *Data set*.

Randerson, J. T., Van Der Werf, G. R., Giglio, L., Collatz, G. J., and Kasibhatla, P. S. (2007). Global Fire Emissions Database, Version 2 (GFEDv2.1). Data set. Available on-line. *Oak Ridge National Laboratory Distributed Active Archive Center Oak Ridge Tennessee USA*.

Randles, C. A. and Ramaswamy, V. (2010). Impacts of absorbing biomass burning aerosol on the climate of southern Africa: a Geophysical Fluid Dynamics Laboratory GCM sensitivity study. *Atmospheric Chemistry and Physics Discussions*, 10(4):9731–9752.

Rap, A., Ghosh, S., and Smith, M. H. (2009). Shepard and Hardy Multiquadric Interpolation Methods for Multicomponent Aerosol–Cloud Parameterization. *Journal of the Atmospheric Sciences*, 66(1):105–115.

Rashid and Mavliev (2002). Turbulent mixing condensation nucleus counter. *Atmospheric Research*, 62(3-4):303 – 314. Aerosol Number Concentration Measurement. International Workshop on Intercomparison of Condensation Nuclei and Aerosol Particle Counters.

Reid, J. S., Xian, P., Hyer, E. J., Flatau, M. K., Ramirez, E. M., Turk, F. J., Sampson, C. R., Zhang, C., Fukada, E. M., and Maloney, E. D. (2012). Multi-scale

meteorological conceptual analysis of observed active fire hotspot activity and smoke optical depth in the maritime continent. *Atmospheric Chemistry and Physics*, 12(4):2117–2147.

Remer, L. A. (2005). The MODIS aerosol algorithm, products and validation. *J. Atmos. Sci.*, 62:947–973.

Reusch, D. B., Alley, R. B., and Hewitson, B. C. (2005). Relative performance of self-organizing maps and principal component analysis in pattern extraction from synthetic climatological data. *Polar Geography*, 29(3):188–212.

Reynolds, R. W., Rayner, N. A., Smith, T. M., Stokes, D. C., and Wang, W. (2002). An Improved In Situ and Satellite SST Analysis for Climate. *Journal of Climate*, 15(13):1609–1625.

Richard, Y., Trzaska, S., Roucou, P., and Rouault, M. (2000). Modification of the southern african rainfall variability/enso relationship since the late 1960s. *Climate Dynamics*, 16(12):883–895.

Robert, A., Henderson, J., and Turnbull, C. (1972). An implicit time integration scheme for baroclinic models of the atmosphere. *Monthly Weather Review*, 100:329–335.

Rodell, M., Houser, P. R., Berg, A. A., and Famiglietti, J. S. (2005). Evaluation of 10 Methods for Initializing a Land Surface Model. *Journal of Hydrometeorology*, 6:146.

Roeckner, E., Bäuml, G., Bonaventura, L., Brokopf, R., Esch, M., Giorgetta, M., Hagemann, S., Kirchner, I., Kornblueh, L., Manzini, E., Rhodin, A., Schlese, U., Schulzweida, U., and Tompkins, A. (2003). The atmospheric general circulation model ECHAM 5. PART I: Model description. Technical report.

Roeckner, E., Brokopf, R., Esch, M., Giorgetta, M., Hagemann, S., Kornblueh, L., Manzini, E., Schlese, U., and Schulzweida, U. (2006a). Sensitivity of Simulated Climate to Horizontal and Vertical Resolution in the ECHAM5 Atmosphere Model. *J. Climate*, 19(16):3771–3791.

Roeckner, E., Stier, P., Feichter, J., Kloster, S., Esch, M., and Fischer-Bruns, I. (2006b). Impact of carbonaceous aerosol emissions on regional climate change. *Journal Climate Dynamics*, 27(6):553–571. doi:10.1007/s00382-006-0147-3.

Rosenfeld, D. and Feingold, G. (2003). Explanation of discrepancies among satellite observations of the aerosol indirect effects. *Geophys. Res. Lett.*, 30(14):1776. doi:10.1029/2003GL017684.

Ross, J. L., Hobbs, P. V., and Holben, B. (1998). Radiative characteristics of regional hazes dominated by smoke from biomass burning in brazil: Closure tests and direct radiative forcing. *J. Geophys. Res.- Atmospheres*, 103(D24):31925–31941.

Ross, K. E., Piketh, S. J., Bruintjes, R. T., Burger, R. P., Swap, R. J., and Annegarn, H. J. (2003). Spatial and seasonal variations in CCN distribution and the aerosol-CCN relationship over southern Africa. *J. Geophys. Res.*, 108(D13):8481–+. doi:10.1029/2002JD002384.

Rotstayn, L. D., Jeffrey, S. J., Collier, M. A., Dravitzki, S. M., Hirst, A. C., Syktus, J. I., and Wong, K. K. (2012). Aerosol- and greenhouse gas-induced changes in summer rainfall and circulation in the Australasian region: a study using single-forcing climate simulations. *Atmospheric Chemistry and Physics*, 12(14):6377–6404.

Rotstayn, L. D. and Lohmann, U. (2002). Tropical Rainfall Trends and the Indirect Aerosol Effect. *Journal of Climate*, 15:2103–2116.

Sakaeda, N., Wood, R., and Rasch, P. J. (2011). Direct and semidirect aerosol effects of southern African biomass burning aerosol. *J. Geophys. Res.*, 116(D12):D12205+.

Sang, H., Gelfand, A. E., Lennard, C., Hegerl, G., and Hewitson, B. (2009). Interpreting self-organizing maps through space–time data models. *The Annals of Applied Statistics*, 2(4):1194–1216.

Schell, B., Ackermann, I. J., Hass, H., Binkowski, F. S., and Ebel, A. (2001). Modeling the formation of secondary organic aerosol within a comprehensive air quality model system. *J. Geophys. Res.*, 106:28275–28294.

Schmid, B., Redemann, J., Russell, P. B., P. V. Hobbs, . D. L. H., McGill, M. J., Holben, B. N., Welton, E. J., Campbell, J., Torres, O., Kahn, R. A., Diner, D. J., Helmlinger, M. C., Chu, D. A., Gonzalez, C. R., , and de Leeuw, G. (2003). Coordinated airborne and spaceborne and ground-based measurements of massive thick aerosol

layers during the dry season in southern Africa. *J. Geophys. Res.*, 108(D13):8496–+. doi:10.1029/2002JD002297.

Scholes, R. J., Ward, D. E., and Justice, C. O. (1996). Emissions of trace gases and aerosol particles due to vegetation burning in southern hemisphere Africa. *J. Geophys. Res.*, 101:23677–23682. doi: 10.1029/95JD02049.

Schult, I., Feichter, J., and Cooke, W. F. (1997). Effect of black carbon and sulfate aerosols on the global radiation budget. *J. Geophys. Res.*, 102:30107–30118.

Schultz, M. G., Heil, A., Hoelzemann, J. J., Spessa, A., Thonicke, K., Goldammer, J. G., Held, A. C., Pereira, J. M. C., and van het Bolscher, M. (2008). Global wildland fire emissions from 1960 to 2000. *Global Biogeochemical Cycles*, 22:GB2002.

Schwarts, J. and Marcus, A. (1990). Mortality and Air Pollution in London: A Time Series Analysis. *American Journal of Epidemiology*, 131(1):185–194.

Seidel, F. C. and Popp, C. (2012). Critical surface albedo and its implications to aerosol remote sensing. *Atmospheric Measurement Techniques*, 5(7):1653–1665.

Seinfeld, J. H. and Pandis, S. N., editors (1998). *Atmospheric chemistry and physics : from air pollution to climate change*.

Seinfeld, J. H. and Pandis, S. N. (2000). *Atmospheric Chemistry and Physics, from Air Pollution to Climate Change*, volume 37. Journal of Atmospheric Chemistry.

Sellegri, K., Laj, P., Dupuy, R., Legrand, M., Preunkert, S., and Putaud, J.-P. (2003). Size-dependent scavenging efficiencies of multicomponent atmospheric aerosols in clouds. *J. Geophys. Res.(Atmospheres)*, 108:4334.

Sharma, V. and Patil, R. (1992). Size distribution of atmospheric aerosols and their source identification using factor analysis in Bombay, India. *Atmospheric Environment. Part B. Urban Atmosphere*, 26(1):135 – 140.

Simmons, A. J. and Burridge, D. M. (1981). An Energy and Angular-Momentum Conserving Vertical Finite-Difference Scheme and Hybrid Vertical Coordinates. *Mon. Wea. Rev.*, 109(4):758–766.

Skamarok, W. C., Klemp, J. B., Dudhia, J., Gill, D. O., Barker, D. M., Wang, W., and Powers, J. G. (2007). A Description of the Advanced Research Weather Research and Forecast (WRF) Model Version 2. Technical report, NCAR–Mesoscale and Microscale Meteorology Division, Boulder, Colorado, USA.

Smirnova, T., Brown, J. M., Benjamin, S. G., and Kim, D. (2000). Parameterization of cold-season processes in the MAPS land surface scheme.

Smirnova, T. G., Brown, J. M., and Benjamin, S. G. (1997). Performance of Different Soil Model Configurations in Simulating Ground Surface Temperature and Surface Fluxes. *Monthly Weather Review*, 125:1870.

Sotiropoulou, R.-E. P., Nenes, A., Adams, P. J., and Seinfeld, J. H. (2007). Cloud condensation nuclei prediction error from application of Köhler theory: Importance for the aerosol indirect effect. *J. Geophys. Res.(Atmospheres)*, 112(D11):12202.

Spencer, M. T., Shields, L. G., and Prather, K. A. (2007). Simultaneous measurement of the effective density and chemical composition of ambient aerosol particles. *Environmental Science & Technology*, 41(4):1303–1309.

Spracklen, D., Carslaw, K., Pöschl, U., Rap, A., and Forster, P. (2011). Global cloud condensation nuclei influenced by carbonaceous combustion aerosol. *Atmospheric Chemistry and Physics Discussions*, 11(3):6999–7044.

Stamnes, K., Tsay, S.-c., Wiscombe, W. J., and Laszlo, I. (2000). Disort, : Documentation of methodology. *Program*, pages 6–112.

Stier, P., Feichter, J., Kinne, S., Kloster, S., Vignati, E., Wilson, J., Ganzeveld, L., Tegen, I., Werner, M., Balkanski, Y., Schulz, M., Boucher, O., Minikin, A., and Petzold, A. (2005). The aerosol-climate model ECHAM5-HAM. *Atmospheric Chemistry and Physics*, 5(4):1125–1156.

Stroppiana, D., Brivio, P. A., Grégoire, J.-M., Liousse, C., Guillaume, B., Granier, C., Mieville, A., Chin, M., and Pétron, G. (2010). Comparison of global inventories of co emissions from biomass burning derived from remotely sensed data. *Atmospheric Chemistry and Physics*, 10(24):12173–12189.

Strow, L., Motteler, H. E., Benson, R. G., Hannon, S. E., and Souza-Machado, S. D. (1998). Fast computation of monochromatic infrared atmospheric transmittances using compressed look-up tables. *Journal of Quantitative Spectroscopy and Radiative Transfer*, 59(3–5):481 – 493. Atmospheric Spectroscopy Applications 96.

Suzuki, K., Nakajima, T., Numaguti, A., Takemurac, T., Kawamotod, K., and Higurashie, A. (2004). A study of the aerosol effect on a cloud field with simultaneous use of gcm modeling and satellite observation. *Journal of the Atmospheric Sciences*, 61(2):179–194. doi:10.1175/1520-0469(2004)061.

Swap, R., Garstang, M., Macko, S. A., Tyson, P. D., Maenhaut, W., Artaxo, P., Kllberg, P., and Talbot, R. (1996). The long-range transport of Southern African aerosols to the tropical South Atlantic. *J. Geophys. Res.*, 101:23777–23792. doi: 10.1029/95JD01049.

Swap, R. J., Annegarn, H. J., Suttles, J. T., King, M. D., Platnick, S., Privette, J. L., and Scholes, R. J. (2003). Africa burning: A thematic analysis of the Southern African Regional Science Initiative (SAFARI 2000). *J. Geophys. Res.*, 108(D13):8465–+. doi:10.1029/2003JD003747.

Szymanski, W. W. and Liu, B. Y. H. (1986). On the sizing accuracy of laser optical particle counters. *Particle & Particle Systems Characterization*, 3(1):1–7.

Tadross, M., Oliveira, I., Mdoka, M., Tummon, F., Maure, G., MacKellar, N., Browne, N., Crespo, O., Hachigonta, S., and Hewitson, B. (2010). Modelling the influence of vegetation, soil moisture and aerosols on early summer Southern African climate. Technical report, Water Research Commission, South Africa.

Tadross, M. A., Jr, W. J. G., Hewitson, B. C., Jack, C., and New, M. (2006). MM5 simulations of interannual change and the diurnal cycle of southern African regional climate. *Theor. Appl. Climatol.*, 86:63–80. doi:10.1007/s00704-005-0208-2.

Takemura, T., Nozawa, T., Emori, S., Nakajima, T. Y., and Nakajima, T. (2005). Simulation of climate response to aerosol direct and indirect effects with aerosol transport-radiation model. *J. Geophys. Res.(Atmospheres)*, 110(D9):2202–+.

Talukdar, S. S. and Swihart, M. T. (2004). Aerosol dynamics modeling of silicon nanoparticle formation during silane pyrolysis: a comparison of three solution methods. *Journal of Aerosol Science*, 35(7):889 – 908.

Taylor, K. E. (2001). Summarizing multiple aspects of model performance in a single diagram. *J. Geophys. Res.*, 106:7183–7192.

Tews, J., Esther, A., Milton, S. J., and Jeltsch, F. (2006). Linking a population model with an ecosystem model: Assessing the impact of land use and climate change on savanna shrub cover dynamics. *Ecological Modelling*, 195(3–4):219–228.

Thomas and Schumann (1991). Aerosol and hydrometeor concentrations and their chemical composition during winter precipitation along a mountain slope – III. size-differentiated in-cloud scavenging efficiencies. *Atmospheric Environment. Part A. General Topics*, 25(3-4):809 – 824.

Thorpe, A., Hemingway, M., and Brown, R. (1997). Experimental observation of the neutralisation of monodisperse aerosols by a small radioactive source. *Journal of Aerosol Science*, 28(2):334 –.

Tinsley, B. A., Rohrbaugh, R. P., Hei, M., and Beard, K. V. (2000). Effects of Image Charges on the Scavenging of Aerosol Particles by Cloud Droplets and on Droplet Charging and Possible Ice Nucleation Processes. *Journal of Atmospheric Sciences*, 57:2118–2134.

Tosca, M. G., Randerson, J. T., Zender, C. S., Flanner, M. G., and Rasch, P. J. (2010). Do biomass burning aerosols intensify drought in equatorial Asia during El Niño? *Atmospheric Chemistry and Physics*, 10(8):3515–3528.

Trentmann, J., Andreae, M. O., Graf, H.-F., Hobbs, P. V., Ottmar, R. D., and Trautmann, T. (2002). Simulation of a biomass-burning plume: Comparison of model results with observations. *J. Geophys. Res.(Atmospheres)*, 107:4013.

Tsang, T. H. and Brock, J. R. (1982). Simulation of condensation aerosol growth by condensation and evaporation. *Aerosol Science and Technology*, 2(3):311–320.

Tummon, F. (2010). Aerosol-climate interactions over southern Africa: the ENSO signal and interannual variability. *EGU General Assembly 2010, held 2-7 May, 2010 in Vienna, Austria, p.5920*, 12:5920–+.

Tummon, F. (2011). *Direct and semi-direct aerosol effects on the southern African regional climate during the austral winter season*. PhD thesis, University of Cape Town.

Tummon, F., Solmon, F., Liousse, C., and Tadross, M. (2010). Simulation of the direct and semidirect aerosol effects on the southern Africa regional climate during the biomass burning season. *Journal of Geophysical Research*, 115(D19):1–20.

Turco, R. P., Whitten, R. C., and Toon, O. B. (1982). Stratospheric Aerosols: Observation and Theory. *Reviews of Geophysics*, 20:233–279.

Turpin, B. J., Huntzicker, J. J., Larson, S. M., and Cass, G. R. (1991). Los Angeles summer midday particulate carbon: primary and secondary aerosol. *Environmental Science & Technology*, 25(10):1788–1793.

Twomey, S. A. (1959). The nuclei of natural cloud formation, Part II: The supersaturation in natural clouds and the variation of cloud droplet concentration. *Atmospheric Environment*, 43(243–249).

Twomey, S. A. (1974). Pollution and the planetary albedo. *Atmospheric Environment*, 8(1251–56).

Tyson, P. (1997). Atmospheric transport of aerosols and trace gases over southern Africa. *Progress in Physical Geography*, 21(1):79–101. doi: 10.1177/030913339702100105.

Tyson, P. D. (1981). Atmospheric circulation variations and the occurrence of extended wet and dry spells over Southern Africa. *International Journal of Climatology*, 1(2):115–130.

Tyson, P. D. and D'Abreton, P. C. (1998). Transport and recirculation of aerosols off southern Africa - Macroscale plume structure. *Atmospheric Environment*, 32(9):1511–1524.

Tyson, P. D., Garstang, M., and Swap, R. (1996a). Large-Scale Recirculation of Air over Southern Africa. *Journal of Applied Meteorology*, 35:2218–2236. doi: 10.1175/1520-0450(1996)035.

Tyson, P. D., Garstang, M., Swap, R., Kâllberg, P., and Edwards, M. (1996b). An Air Transport Climatology for Subtropical Southern Africa. *International Journal of Climatology*, 16:265–291. doi: 10.1002/(SICI)1097-0088(199603)16:3.

Tyson, P. D., Garstang, M., Thompson, A. M., D'Abreton, P., Diab, R. D., and Browell, E. V. (1997). Atmospheric transport and photochemistry of ozone over central Southern Africa during the Southern Africa Fire-Atmosphere Research Initiative. *J. Geophys. Res.*, 102:10623–10636. doi: 10.1029/97JD00170.

Upadhyay, R. and Ezekoye, O. (2003). Evaluation of the 1-point quadrature approximation in QMOM for combined aerosol growth laws. *Journal of Aerosol Science*, 34(12):1665 – 1683.

van De Hulst, H. C. (1981). *Light Scattering by Small Particles*, volume 1. Dover Publications.

van der Werf, G. R., Randerson, J. T., Giglio, L., Collatz, G. J., Kasibhatla, P. S., and Arellano Jr., A. F. (2006). Interannual variability in global biomass burning emissions from 1997 to 2004. *Atmospheric Chemistry and Physics*, 6(11):3423–3441.

van Dorland, R., Schulz, M., Raga, G., Prinn, R., Nganga, J., Myhre, G., Lowe, D., Lean, J., Haywood, J., Betts, R., Forster, P., Fahey, D., Ramaswamy, V., Artaxo, P., and Bernsten, T. (2007). *Changes in atmospheric constituents and in radiative forcing*. Cambridge University Press, Cambridge, UK and New York, NY, USA.

van Tienhoven, A., Zunckel, M., Emberson, L., Koosailee, A., and Otter, L. (2006). Preliminary assessment of risk of ozone impacts to maize (*Zea mays*) in southern Africa. *Environmental Pollution*, 140(2):220 – 230.

Vestin, A., Rissler, J., Swietlicki, E., Frank, G. P., and Andreae, M. O. (2007). Cloud-nucleating properties of the Amazonian biomass burning aerosol: Cloud condensation nuclei measurements and modeling. *J. Geophys. Res.(Atmospheres)*, 112(D11):14201.

Wang, Y., Leung, L. R., McGregor, J. L., Lee, D.-K., Wang, W.-C., Ding, Y., and Kimura, F. (2004). Regional Climate Modeling: Progress, Challenges, and Prospects. *Journal of the Meteorological Society of Japan*, 82(6):1599–1628.

Ward, D. E. and Hardy, C. C. (1991). Smoke emissions from wildland fires. *Environment International*, 17(2–3):117–134.

Ward, D. S., Eidhammer, T., Cotton, W. R., and Kreidenweis, S. M. (2010). The role of the particle size distribution in assessing aerosol composition effects on simulated droplet activation. *Atmospheric Chemistry and Physics Discussions*, 10(2):4189–4223.

Wesely, M. and Hicks, B. (2000). A review of the current status of knowledge on dry deposition. *Atmospheric Environment*, 34(12-14):2261 – 2282.

Whitby, E. R. and McMurry, P. H. (1997). Modal Aerosol Dynamics Modeling. *Aerosol Science and Technology*, 27(6):673–688.

Whitby, K. T. (1978). The physical characteristics of sulfur aerosols. *Atmospheric Environment (1967)*, 12(1-3):135 – 159. Proceedings of the International Symposium.

Whitby, K. T., Husar, R. B., and Liu, B. Y. H. (1971). The Aerosol Size Distribution of Los Angeles Smog. *Journal of Colloid and Interface Science*, 39(1):177–204.

Wild, O., Zhu, X., and Prather, M. J. (2000). Fast-J: Accurate Simulation of In- and Below-Cloud Photolysis in Tropospheric Chemical Models. *Journal of Atmospheric Chemistry*, 37:245–282. 10.1023/A:1006415919030.

Williams, C. R. and Gage, K. S. (2009). Raindrop size distribution variability estimated using ensemble statistics. *Annales Geophysicae*, 27:555–567.

Wilson, J. C. and Liu, B. Y. (1980). Aerodynamic particle size measurement by laser-doppler velocimetry. *Journal of Aerosol Science*, 11(2):139 – 150.

Winiwarter, W. and Schimak, G. (2005). Environmental software systems for emission inventories. *Environmental Modelling & Software*, 20(12):1469 – 1477. Environmental Knowledge and Information Systems.

Wong, M., Nichol, J., Lee, K., and Li, Z. (2009). High resolution aerosol optical thickness retrieval over the Pearl River Delta region with improved aerosol modelling. *Science in China Series D: Earth Sciences*, 52(10):1641–1649. 10.1007/s11430-009-0125-9.

Wu, C.-Y. and Biswas, P. (1998). Study of numerical diffusion in a discrete-sectional model and its application to aerosol dynamics simulation. *Aerosol Science and Technology*, 29(5):359–378.

Wu, J. and Menon, S. (2001). Aerosol dynamics in the near field of engine exhaust plumes. *Journal of Applied Meteorology*, 40(4):795–809.

Wu, L., Su, H., and Jiang, J. H. (2011). Regional simulations of deep convection and biomass burning over South America: 2. Biomass burning aerosol effects on clouds and precipitation. *Journal of Geophysical Research*, 116(D17):1–11.

Yokelson, R. J., Bertschi, I. T., Christian, T. J., Hobbs, P. V., Ward, D. E., and Hao, W. M. (2003). Trace gas measurements in nascent, aged, cloud-processed smoke from African savanna fires by airborne Fourier transform infrared spectroscopy (AFTIR). *J. Geophys. Res.*, 108(D13):8478–+. doi:10.1029/2002JD002322.

Yu, M., Lin, J. Z., and Chan, T. L. (2008). A new moment method for solving the coagulation equation for particles in Brownian motion. *Aerosol Science and Technology*, 42(9):705–713.

Yue, X., Liao, H., Wang, H. J., Li, S. L., and Tang, J. P. (2011). Role of sea surface temperature responses in simulation of the climatic effect of mineral dust aerosol. *Atmospheric Chemistry and Physics*, 11(12):6049–6062.

Zakey, A. S., Solmon, F., and Giorgi, F. (2006). Implementation and testing of a desert dust module in a regional climate model. *Atmos. Chem. Phys.*, 6:4687–4704.

Zaveri, R. A., Easter, R. C., Fast, J. D., and Peters, L. K. (2008). Model for Simulating Aerosol Interactions and Chemistry (MOSAIC). *J. Geophys. Res.(Atmospheres)*, 113(D12):13204.

Zaveri, R. A. and Peters, L. K. (1999). A new lumped structure photochemical mechanism for large-scale applications. *Journal of Geophysical Research*, 104(D23):30387–30415.

Zhang, Y. (2008). Online-coupled meteorology and chemistry models: history, current status, and outlook. *Atmospheric Chemistry and Physics*, 8(11):2895–2932.

Zhang, Y., Seigneur, C., Seinfeld, J., Jacobson, M. Z., and Binkowski, F. S. (1999). Simulation of aerosol dynamics: A comparative review of algorithms used in air quality models. *Aerosol Sci. Technol.*, 31:487–514.

Zhu, C., Leung, R., Gochis, D., Qian, Y., and Lettenmaier, D. (2009). Evaluating the influence of antecedent soil moisture on variability of the north american monsoon precipitation in the coupled mm5/vic modeling system. *Journal of Advances in Modeling Earth Systems*, 1(13).

Zunckel, M., Koosailee, A., Yarwood, G., Maure, G., Venjonoka, K., van Tienhoven, A., and Otter, L. (2006). Modelled surface ozone over southern Africa during the Cross Border Air Pollution Impact Assessment Project. *Environmental Modelling & Software*, 21(7):911 – 924.